Modeling of Mixing and Fuel-Air Ratio Fluctuations in Lean Premixed Flames

vorgelegt von
Diplom-Ingenieur
Christina K. Schrödinger
geb. in München

Von der Fakultät V – Verkehrs- und Maschinensysteme
der Technischen Universität Berlin
zur Erlangung des akademischen Grades

Doktor der Ingenieurwissenschaften
– Dr.-Ing. –

genehmigte Dissertation

Promotionsausschuss:

Vorsitzender: Prof. Dr.-Ing. Robert Liebich
Gutachter: Prof. Dr.-Ing. Christian Oliver Paschereit
Gutachter: Prof. Dr.-Ing. Michael Oevermann

Tag der wissenschaftlichen Aussprache: 20. März 2015

Berlin 2015

Danksagung

Diese Arbeit ist während meiner Zeit als wissenschaftliche Mitarbeiterin am Institut für Energietechnik und am Institut für Strömungsmechanik und Technische Akustik an der Technischen Universität Berlin entstanden.

Ich danke meinem Doktorvater Prof. Dr.-Ing. C. O. Paschereit, den ich bereits während meines Studiums und durch meine Anstellung als studentische Hilfskraft an seinem Institut kennengelernt habe, für seine Unterstützung und Förderung, ohne die diese Arbeit nicht verwirklicht hätte werden können. Ich habe bei Ihm enorm viel gelernt, nicht nur Fachliches. Ich möchte mich darüber hinaus für die Freiheiten, die er mir gelassen hat, und die Schaffung einer sehr angenehmen Arbeitsatmosphäre bedanken.

Bei Prof. Dr.-Ing. Michael Oevermann möchte ich mich für die gute Betreuung, die Unterstützung und das Vertrauen, das er mir entgegen gebracht hat, bedanken. Ich danke ihm außerdem für die gute Zusammenarbeit über die vergangenen Jahre. Die fachlichen Gespräche sowie die Besuche an der Chalmers University waren immer sehr inspirierend und zielführend.

Prof. Dr.-Ing. Robert Liebich möchte ich für die freundliche und unkomplizierte Ausführung des Promotionsvorsitzes danken.

Alan Kerstein hat mich während der gesamten Promotionszeit begleitet. Ich möchte mich für seine beispiellose Hilfsbereitschaft und den regelmäßigen Austausch bedanken. David Lignell möchte ich für die Bereitstellung seines ODT-codes und seine Unterstützung bei Fragen diesbezüglich danken.

Ich danke selbstverständlich unseren Sekretärinnen, Sandy, Kristin und insbesondere Lilli, die lange Zeit das Herz des Instituts darstellte. Sie haben mir die organisatorische Arbeit sehr erleichtert und mir bei bürokratischen Problemen immer geholfen.

Ganz herzlich möchte ich mich bei der IT und vor allem bei Frau Pätzold bedanken, die mir jederzeit bei meinen Computerproblemen zur Seite stand. Weiterhin möchte ich den Werkstattmitarbeitern und den technischen Mitarbeitern danken. Besondere Unterstützung bei elektronischen Fragestellungen habe ich von Heiko erhalten. Andy möchte ich für seine Hilfe, Lösungsvorschläge, Ideen und schnelle und gleichzeitig qualitativ hochwertige Arbeitsweise danken, die einen unersetzlichen Beitrag zum experimentellen Teil meiner Arbeit lieferten.

Ich möchte natürlich auch den wissenschaftlichen Mitarbeitern danken. Ich kann auf eine unbeschreiblich schöne Zeit mit Euch zurückblicken. Euch allen möchte ich für den abwechslungsreichen Arbeitsalltag, die erlebnisreichen Dienstreisen, und die vielen Unternehmungen außerhalb der Institutswelt danken. Sebastian G. und Joshua, mit denen ich mein Büro teilen durfte, danke ich, dass sie mir täglich eine angenehme, abwechslungsreiche und lustige Atmosphäre geboten haben. Olli, einer der wenigen anderen Numeriker, möchte ich für seine fachliche Unterstützung und gute Zusammenarbeit danken. Ich danke allen, die bei meinen experimentellen Untersuchungen und fachlichen Problemen hilfreich zur Seite standen, insbesondere Jonas, Arnaud, Katharina, Sebastian S., Holger und Steffen. Navid möchte ich für seine Hilfestellung bei sämtlichen fachlichen und organisatorischen Fragen danken. Für die freundschaftliche Zusammenarbeit und Unterstützung möchte ich mich außerdem bei meinen studentischen Mitarbeitern, und besonders bei David, Jan und Tim,

bedanken.

Für eine mein gesamtes Leben andauernde Unterstützung und Förderung danke ich meinen Eltern und meinem Bruder. Zuletzt möchte ich mich auch bei meinen Freunden bedanken, die mir meine Freizeit versüßt haben und auf die ich mich immer verlassen kann.

Zusammenfassung

Die Mischungsqualität von Brennstoff und Luft in Gasturbinenbrennern hat Einfluss auf wichtige Verbrennungsgrößen, wie Wärmefreisetzung, Flammenfronteigenschaften, Brenngeschwindigkeit, Emissionen und Zeitverzüge. Sie kann daher auch Verbrennungsinstabilitäten begünstigen, die sich bei einer Kopplung von Wärmefreisetzungs- und Druckschwankungen, insbesondere unter mageren Bedingungen, ausbilden. Somit ist es essentiell, turbulente Mischungsvorgänge modellieren zu können und ihren Einfluss auf Strömungs- und Vebrennungsvorgänge zu verstehen.

Die vorliegende Arbeit behandelt die Untersuchung von Mischungsvorgängen in einem Drallbrenner unter Verwendung von numerischen Strömungsberechnungen. Weitergehend wird die Auswirkung von Schwankungen im Brennstoff-Luft-Verhältnis auf Flammeneigenschaften und Emissionen mit einem eindimensionalen turbulenten Model berechnet. Experimentelle Untersuchungen an einem Staukörper-Brenner untermauern die Resultate dieser Berechnungen und gewähren einen tieferen Einblick in das Thema. Abschließend wird ein neuartiger Kopplungsansatz für ein Subgrid-Verbrennungsmodell vorgestellt, das auf die Brennerkonfiguration aus den experimentellen Untersuchungen angewendet wird.

Die Untersuchungen am Drallbrenner zeigen, dass die Position der Brennstoffeindüsung einen großen Einfluss auf die Mischungsqualität als auch die Flammmenform und -position hat. Axialsymmetrische Anregung der mittleren Strömung führt zu einer Überlagerung mit der helikalen Struktur der Strömung und beeinflusst so Mischungs- und Strömungsdynamik. Reynoldsgemittelte Simulationen waren in der Lage, wichtige Merkmale qualitativ, für die Mischung sogar quantitativ, wiederzugeben. Bezogen auf das Strömungsfeld haben sich Large Eddy Simulationen als deutlich genauer herausgestellt.

Die eindimensionalen Untersuchungen einer turbulenten, mageren Flamme zeigen steigende CO und NO Emissionen sowie Wärmefreisetzungsschwankungen mit steigender Anregungsamplitude. Nichtlineare Effekte bei hohen Amplituden werden mit Wechselwirkungen und einer Phasenabhängigkeit von Oszillationen im Brennstoff-Luft-Verhältnis und der Brenngeschwindigkeit assoziiert. Außerdem liegt ein Dämpfungseffekt der periodischen Anregung auf turbulente Schwankungen vor, der zu einer verminderten Brenngeschwindigkeit führt.

Die experimentellen Ergebnisse können viele Erkenntnisse der eindimensionalen Berechnungen bestätigen. Nichtlineares Verhalten der Wärmefreisetzungsschwankungen werden durch die Kopplung mit Brenngeschwindigkeit, Reaktionswärme und Strömungsfeld erklärt. Anregung bei niedrigen Frequenzen bzw. hohen Amplituden verursachen eine Dämpfung der turbulenten Fluktuationen und daraus resultierend einen Anstieg der turbulenten Flammendicke sowie eine Verringerung der Flammenoberflächendichte, welche auf eine Verringerung der Brennrate hinweist.

Mit dem Ziel, einige Probleme und Defizite herkömmlicher Verbrennungsmodelle zu überwinden, wird ein neuartiger Kopplungsansatz vorgestellt, der das eindimensionale Modell als Subgridmodell in Large Eddy Simulationen einbindet. Diese Kopplung verknüpft die thermochemischen Größen des Untergitters mit dem Geschwindigkeits- und Druckfeld des übergeordneten Gitters über eine Geschwindigkeitsdivergenzbedingung. Die Anwendung auf eine Staukörper-stabilisierte Flamme zeigt vielversprechende Ergebnisse, die Flammenfrontcharakteristika in guter Übereinstimmung mit Messergebnissen wiedergeben.

Abstract

The mixing quality of fuel and air in gas turbine burners has effects on important combustion properties such as heat release rate, flame front characteristics, burning velocity, emissions, and time delays. It such might promote combustion instabilities, especially under lean conditions, which are prone to evolve in the presence of heat release rate oscillations coupling with the acoustic modes of the combustion chamber. It is thus essential to understand mixing processes and their influence on the combustion process.

The present thesis studies mixing of fuel and air in a swirl burner by means of computational fluid dynamics. The impact of fuel-air ratio oscillations on flame characteristics and emissions is further evaluated with one-dimensional turbulence simulations. Validation of the one-dimensional studies and further insight into the topic is gained by experimental investigations of a bluff-body burner subjected to equivalence ratio fluctuations. Eventually, a novel coupling approach for a combustion subgrid model is introduced and applied in simulations of the experimental burner configuration.

The swirl burner mixing studies indicate that the fuel injection position has a major impact on the mixing quality and the flame shape and position. Axisymmetric forcing of the mean flow, inducing fuel-air ratio fluctuations, causes a superposition with the helical structure of the swirling flow and thus affects the flow and mixing dynamics. Reynolds-averaged simulations show the ability of qualitatively, and for mixing also quantitatively, reproducing important features. Regarding the flow field, large eddy simulations prove to be considerably more accurate.

The one-dimensional turbulent lean flame investigations reveal increasing emissions of CO and NO, as well as heat release rate fluctuations with increasing forcing amplitude of the equivalence ratio fluctuations. Nonlinear effects at high amplitudes are driven by the interaction and the phase-dependence of fuel-air ratio oscillations and burning velocity. Furthermore, a dampening effect of periodical forcing on turbulent fluctuations could be observed, leading to decreased burning velocities.

The experimental results confirm many of the findings from the numerical studies. Nonlinear behavior of heat release rate fluctuations were attributed to the coupling of the equivalence ratio oscillations with burning velocity, heat of reaction and flow field. Low-frequency high-amplitude forcing further causes a damping of turbulent fluctuations, in turn an increase in turbulent flame brush thickness and a decrease in flame surface density, indicating a decrease in burning rate.

To overcome shortcomings that are well known in three-dimensional combustion modeling, such as the lack of resolving turbulence-flame interaction, a novel coupling approach for the one-dimensional turbulence model as a subgrid model for large eddy simulations is presented. It relates the subgrid thermo-chemical properties to the supergrid velocity and pressure fields via a velocity divergence constraint. The model is applied to a bluff-body flame and shows promising results, reproducing flame front characteristics in good agreement with experimental results.

Contents

Zusammenfassung III

Abstract V

List of Figures XI

List of Tables XVII

Nomenclature XIX

1. General introduction 1
- 1.1. Swirling burner flows and mixing . . . 2
- 1.2. Computation of combustion and emissions . . . 3
- 1.3. Variations in fuel-air ratio . . . 6
- 1.4. Structure of the thesis . . . 8

I. Mixing in a swirl burner 9

2. Setup 13
- 2.1. The investigated burner . . . 13
- 2.2. Similarity of water and air flows . . . 14
- 2.3. Experimental setup . . . 14
  - 2.3.1. Combustion test rig & OH*-chemiluminescence measurements . . . 15
  - 2.3.2. Water test rig & concentration measurements . . . 15
  - 2.3.3. PIV setup . . . 15
- 2.4. CFD setup . . . 16
  - 2.4.1. Grid and time resolution . . . 17

3. Effect of fuel-staging on mixing quality and flame behavior 19
- 3.1. Cold flow investigations . . . 20
  - 3.1.1. Flow field validation . . . 20
  - 3.1.2. Mixing quality . . . 22
- 3.2. Reacting flow investigations . . . 24
  - 3.2.1. Flow field validation . . . 24
  - 3.2.2. Flame shape and position . . . 26
  - 3.2.3. Time delays . . . 32
- 3.3. Conclusion . . . 33

4. Effect of periodical flow forcing on fuel-air mixing 35
- 4.1. Definition of the forcing amplitude . . . 35

4.2. Forcing frequency . . . 36
4.3. Flow field . . . 37
4.4. Mixing quality . . . 39
4.5. Proper orthogonal decomposition . . . 42
4.6. Concluding remarks on the effect of periodical forcing . . . 45

II. Linear Eddy Modeling of fluctuations in fuel-air ratio 47

5. The Linear Eddy Model 51
5.1. One-dimensional transport equations . . . 51
5.2. One-dimensional turbulence modeling . . . 53
5.3. Code implementation . . . 54
5.3.1. Diffusive advancement . . . 54
5.3.2. Time integration . . . 54
5.3.3. Mesh adaption . . . 55
5.4. Subdomain decomposition . . . 56
5.4.1. Subdomain decomposition algorithm . . . 56
5.4.2. Parallelization issues . . . 58
5.4.3. Influence of turbulence parameters on the performance . . . 59
5.4.4. Validation . . . 62
5.5. Combustion mechanism . . . 63
5.5.1. Validation of the reduced mechanism . . . 64
5.6. Validation of the LEM code . . . 66
5.7. Impact of u' and L . . . 68
5.7.1. Variation of the turbulence intensity . . . 68
5.7.2. Variations of the integral length scale . . . 69
5.7.3. Turbulent flame speed . . . 71

6. Fuel-air-ratio fluctuations 73
6.1. Comparison of laminar and turbulent flames at constant equivalence ratio 74
6.2. Equivalence ratio oscillations . . . 75
6.3. Influence on NO and CO . . . 78
6.4. Influence on heat release . . . 81
6.5. Influence on burning velocity . . . 83
6.6. Concluding remarks on the effect of fluctuations in the fuel-air ratio . . . 87

III. Experimental investigations 89

7. Experimental setup 93
7.1. Burner . . . 93
7.2. Measurement techniques . . . 94
7.2.1. Particle Image Velocimetry (PIV) . . . 94
7.2.2. OH*-chemiluminescence . . . 94
7.2.3. OH-Planar Laser Induced Fluorescence (OH-PLIF) . . . 94
7.2.4. Emission analysis . . . 95
7.2.5. Hot-wire . . . 95

7.3. Measurement conditions 95

8. Impact of fuel-air ratio oscillation on a bluff body flame 99
8.1. Heat release rate 100
8.2. Coupling of the heat release rate and the velocity field 101
8.3. Flame front characteristics 104
8.3.1. Turbulent flame brush thickness 106
8.3.2. Flame surface density 107
8.4. Emissions 109
8.5. Summary on the experimental investigation of the effect of fuel-air ratio oscillations on a bluff-body stabilized flame 111

IV. The Linear-Eddy-subgrid-model 113

9. Coupling of LEM and LES 117
9.1. Large Eddy Simulations (LES) 118
9.2. LEMLES: general approach 119
9.3. LEMLES closure 120
9.4. Iterative solution procedure 121
9.4.1. Predictor 121
9.4.2. Corrector 122
9.5. Splicing 123
9.6. Subgrid Linear Eddy computations 125
9.7. Parallelization 125
9.8. Validation 126
9.9. Combustion mechanism 128

10. Simulations of a V-flame with LEMLES 131
10.1. Computational domain 131
10.2. Setup 131
10.2.1. Boundary conditions 132
10.3. Velocity fields 132
10.4. Heat release rate 134
10.5. Flame structure 135
10.6. Concluding remarks on the LEMLES simulations of a bluff-body burner . 136

11. Conclusion and outlook 139

Appendices 141

A. Reduced methane–air reaction mechanism 143

List of Figures

1.2.1. Borghi diagram with conditions typically encountered in gas turbine combustion indicated. . . . 4
1.3.1. Processes generating heat release rate oscillations caused by perturbations in fuel-air ratio adapted from Cho & Lieuwen (2005). . . . 7

2.1.1. Sketch of the swirl burner used for the present studies. . . . 13
2.1.2. Sketch of swirl induced burner with modified fuel injection. . . . 14
2.4.1. Meshing of fuel injection holes. . . . 18
2.4.2. Computational domain (not showing the complete combustion chamber considered for the LES and (U)RANS simulations). . . . 18

3.1.1. Isolines of axial velocity $u = 0$, cold case, simulation data for different β; measurements performed w/o injection. . . . 21
3.1.2. Axial velocity, cold case, simulation data for different axial positions and β; measurements for different axial positions, performed w/o injection. . 21
3.1.3. Intensity of turbulence, cold case, simulation data for different axial positions and β; measurements for different axial positions, performed w/o injection. . . . 22
3.1.4. Measures to evaluate the concentration in radial planes at different axial positions. . . . 23
3.1.5. Concentrations of fuel and their histograms from simulations in an axial plane at $x = 5$ mm, left: $\beta = 0.0$, middle: $\beta = 0.5$, right: $\beta = 1.0$. . . . 23
3.1.6. Temporal averaged concentrations of fuel and their spatial histograms from measurements in an axial plane at $x = 5\,\mathrm{mm}$, left: $\beta = 0.0$, middle: $\beta = 0.5$, right: $\beta = 1.0$. . . . 23
3.1.7. Spatial unmixedness vs. x, measurement (solid) and simulation data (dashed) for different β. . . . 24
3.1.8. Spatial unmixedness vs. β, measurement (solid) and simulation data (dashed) for different axial positions with fitted second-order polynomials. 25
3.2.1. Isolines of axial velocity $u = 0$, reacting case, measurement and simulation data for different β. . . . 25
3.2.2. Axial velocity, reacting case, measurement and simulation data for different axial positions and β. . . . 26
3.2.3. Radial velocity, reacting case, measurement and simulation data for different axial positions and β. . . . 26
3.2.4. Reaction rates from simulations, left $\beta = 0.1$, middle: $\beta = 0.5$, right:$\beta = 0.9$, view point: 45°, global color scale. . . . 27
3.2.5. Measured OH* intensities, left $\beta = 0.1$, middle: $\beta = 0.5$, right:$\beta = 0.9$, view point: 45°, global color scale. . . . 27

3.2.6. Reaction rates from simulations, left: $\beta = 0.1$, middle: $\beta = 0.5$, right: $\beta = 0.9$, view point: $-45°$, global color scale. 28
3.2.7. Numerical simulation of reaction rate in xy-plane, left: $\beta = 0.0$, middle: $\beta = 0.5$, right: $\beta = 1.0$, view point: $0°$, $\mathrm{Sc}_t = \mathrm{Pr}_t = 0.2$. 28
3.2.8. Numerical simulation of reaction rate in xy-plane, left: $\beta = 0.0$, middle: $\beta = 0.5$, right: $\beta = 1.0$, view point: $0°$, $\mathrm{Sc}_t = \mathrm{Pr}_t = 0.9$. 29
3.2.9. Numerical simulation of reaction rate in xy-plane, left: $\beta = 0.0$, middle: $\beta = 0.5$, right: $\beta = 1.0$, view point: $0°$, $\mathrm{Sc}_t = \mathrm{Pr}_t = 0.55$. 29
3.2.10. Numerical simulation of reaction rate, left: $\beta = 0.0$, middle: $\beta = 0.5$, right: $\beta = 1.0$, view point: $45°$, $\mathrm{Sc}_t = \mathrm{Pr}_t = 0.55$. 29
3.2.11. Integral values of OH*-intensities (measurement) and reaction rate (simulation) for different values of β. 30
3.2.12. Flame positions depending on β from experimental and numerical investigations. 31
3.2.13. Comparison of time delays for varying β. 32

4.2.1. Amplitude spectrum of the "fuel" concentration averaged in the crossflow-half-plane 5 mm downstream of the burner exit. 36
4.3.1. Mean profiles of the axial velocity (u) for different axial positions. 38
4.3.2. Mean profiles of the radial velocity (v) for different axial positions. . . . 38
4.3.3. Turbulence intensity for different axial positions. 39
4.3.4. Region of reverse flow defined by isolines of axial velocity $u = 0$. 39
4.4.1. Mean and RMS fuel concentration fields in the crossflow plane 5 mm downstream of the burner exit for unforced and forced (St = 1) cases; experimental results. 40
4.4.2. Mean and RMS fuel concentration fields in the crossflow plane 5 mm downstream of the burner exit for unforced and forced (St = 1) cases; LES results. 40
4.4.3. Mean and RMS fuel concentration fields in the crossflow plane 5 mm downstream of the burner exit for unforced and forced (St = 1) cases; URANS results. 40
4.4.4. Probability density functions for spatial mean (a) and rms (b) concentration distribution in the crossflow plane 5 mm downstream of the burner exit. 41
4.4.5. Spatial unmixedness determined for different axial positions. 41
4.5.1. Fluctuation energy captured by the POD modes for the concentration in the crossflow plane at the burner exit. 43
4.5.2. First five pod modes of "fuel"-concentration in the crossflow plane for unforced and forced (St = 1) cases. (a) & (b): LES; (c) & (d): URANS. 43

5.2.1. Triplet Map applied to a scalar gradient $c(x, t)$ 53
5.4.1. Regions of subdomain decomposition for $N = 4$ subdomains. 57
5.4.2. Evaluation of subdomain decomposition for different cases (Tab. 5.4.1), (a) run time normalized with corresponding single-domain run time; (b) average number of diffusion time steps. 60
5.4.3. Evaluation of subdomain decomposition for different cases (Tab. 5.4.1), (a) distributed maps normalized with total number of maps; (b) Cumulative distribution function for the eddy sizes. 62

5.4.4. Validation of subdomain decomposition for $N = 20$ and $N = 50$ against original code. Mean temperature and RMS are shown over the one dimensional domain for the cases with and without subdomain decomposition. 63
5.5.1. Comparison of original and reduced mechanisms. (a) CO; (b) NO; (c) v_b; (d) T profile. 64
5.5.2. Validation of the considered reduced mechanism. (a) laminar flame thickness; (b) laminar flame speed. 65
5.5.3. Laminar species profiles for a stoichiometric methane-air flame at atmospheric pressure and $T_u = 293K$; symbols: measurements, lines: reduced mechanism. 65
5.5.4. Laminar species profiles for a lean methane-air flame at $\phi = 0.86$, atmospheric pressure and $T_u = 293K$; symbols: measurements, lines: reduced mechanism. 66
5.6.1. Turbulent burning velocity, u_t, over turbulence intensity, u', both normalized by the laminar burning velocity, s_L. 67
5.7.1. Instantaneous Temperature profiles for different turbulence intensities u' and the same integral length scale $L = 0.025\,\mathrm{m}$. 69
5.7.2. Mean and RMS Temperature profiles for different turbulent velocity fluctuations u' and the same integral length scale $L = 0.025\,\mathrm{m}$. 69
5.7.3. Mean species profiles of emissions NO and CO for different turbulent velocity fluctuations u' and same integral length scale $L = 0.025\,\mathrm{m}$. 70
5.7.4. Instantaneous temperature profiles for different integral length scales L and same turbulent velocity fluctuation $u' = 10\,\mathrm{m/s}$. 70
5.7.5. Mean and RMS temperature profiles for different integral length scales and same turbulent velocity fluctuations $u' = 10\,\mathrm{m/s}$. 71
5.7.6. Mean species profiles of emissions NO and CO for different integral length scales and same turbulent velocity fluctuations $u' = 10\,\mathrm{m/s}$. 71
5.7.7. Mean turbulent flame propagation speeds for different integral length scales and different turbulence intensities plotted against turbulent Reynolds number Re_t. 72

6.0.1. Processes generating heat release rate oscillations caused by perturbations in fuel-air ratio. 73
6.1.1. Borghi diagram with classification of the investigated flame. 74
6.1.2. Comparison of laminar and turbulent one-dimensional flames. 75
6.2.1. (a) Diffusive amplitude attenuation, turbulent case (top) and position of laminar flame (bottom); (b) dissipation rate vs equivalence ratio 77
6.2.2. (a) Spatial equivalence ratio distribution from inlet to flame at different times; (b) equivalence ratio history at the inlet and shortly upstream of the flame (case: laminar, 30 Hz, relative amplitude 0.99). 78
6.3.1. Qualitative behavior of NO and CO vs. equivalence ratio. 78
6.3.2. Influence of forcing amplitude on mean emissions of NO and CO. 80
6.3.3. Influence of forcing frequency on mean emissions of NO and CO. 80
6.3.4. Phase averaged relation between CO fluctuations and equivalence ratio oscillations. 81
6.4.1. Amplitude and frequency dependence of the relative heat release rate fluctuations for laminar and turbulent flames (a)–(c) and the influence of forcing amplitude on the mean heat release rate (d). 82

6.5.1. Consumption speeds for CH_4 and O_2, averaged, for different forcing amplitudes and frequencies, normalized by the unforced burning velocity. . . 83
6.5.2. Consumption speeds for CO_2 and H_2O, averaged, for different forcing amplitudes and frequencies, normalized by the unforced burning velocities. 84
6.5.3. Histories of CH_4 and CO_2 consumption speeds at 30 Hz. (a) relative forcing amplitude of 0.16; (b) relative forcing amplitude of 0.83 85
6.5.4. Consumption speeds for NO for different forcing amplitudes and frequencies, normalized by the unforced burning velocities. 85
6.5.5. Consumption speeds for different forcing frequencies, divided into CH4 + O2, CO + H2O, and NO, normalized by the unforced burning velocities. . . . 86
6.5.6. Consumption speed fluctuations for different forcing amplitudes for 30 Hz, divided into reactants (CH_4 and O_2), products (CO_2 and H_2O), and NO 86

7.1.1. Sketch of the burner 93
7.3.1. Combustion regimes after (Peters 1999) (modified Borghi diagram). Markers indicate the regime of the studied flame. 96
7.3.2. Relative fuel flow oscillation amplitudes at fuel injection point (at the center-body) vs. forcing frequency. 96

8.1.1. Integrated OH* fluctuations vs amplitude for 20, 30, 60, and 90 Hz, normalized by their mean value; (a) rms of original signal, (b) rms of phase-averaged signal. 101
8.1.2. Integrated OH* fluctuations vs. frequency for maximum amplitude of forcing, normalized by their mean value. 102
8.1.3. Integrated phase-averaged OH* oscillations vs. phase-averaged equivalence ratio oscillations for different forcing frequencies at maximum forcing amplitude. 102
8.2.1. Comparison of mean Abel-deconvoluted OH*-chemiluminescence (a), axial (b) and radial (c) velocity fields without forcing and forcing at 20 Hz . 103
8.2.2. Phase-averaged Abel-deconvoluted OH*-chemiluminescence and phase-averaged axial velocity fields for forcing at 20 Hz and maximum amplitude. 103
8.2.3. Phase-averaged signals of normalized equivalence ratio oscillations at the fuel injection position, integrated OH* chemiluminescence, and axial and radial velocities at (41 mm, 19 mm) vs phase angle for (a) 20 Hz and (b) 60 Hz and maximum forcing amplitude. 104
8.2.4. Amplitude and phase angle of axial and radial velocity fluctuations for raw and phase-averaged signals vs frequency. 105
8.2.5. Phase-averaged velocity fluctuations versus phase-averaged equivalence ratio and heat release rate fluctuations for different frequencies and maximum forcing amplitudes. 105
8.3.1. Edge detection for OH-PLIF and Mie scattering. Left figures show the instantaneous intensities and right figures show the detected edges. . . . 106
8.3.2. Turbulent flame brush thickness vs. forcing frequency for three axial positions based on the RMS of the mean progress variable $\overline{c}$ and the flame front position x'_f. 107
8.3.3. Flame surface density vs mean progress variable $\overline{c}$. 108
8.3.4. Integral of the flame surface density over the mean progress variable space. 108
8.4.1. Molar fractions of emissions for different axial (x) and radial (y) positions. 110

8.4.2. Molar fractions of emissions vs. frequency for $x = 0.09\,\mathrm{m}$ and $y = 0.0\,\mathrm{m}$. 111

9.5.1. Illustration of splicing events. 123
9.8.1. Splicing of disk along grid orientation. (a) Initial field. (b) Convected field. 127
9.8.2. Splicing of disk diagonal to grid orientation. (a) Initial field. (b) Convected field. 127
9.8.3. Splicing of circle along grid orientation. Decomposed domain, computed in parallel mode. Domain borders are indicated by lines. (a) Initial field. (b) Convected field. 127
9.9.1. Validation of the employed mechanism. (a) laminar flame thickness; (b) laminar burning velocity. 128
9.9.2. Species profiles in a laminar premixed flame at $T_u = 293\,\mathrm{K}$, $p = 1\,\mathrm{atm}$. (a) $\phi = 1$; (b) $\phi = 1$; (c) $\phi = 0.86$. 129

10.2.1. Sketch of computational doamin. 132
10.3.1. Mean axial and radial velocities for different axial positions. 133
10.3.2. RMS axial and radial velocities for $x = 0.005\,\mathrm{m}$. 133
10.4.1. Mean OH*-chemiluminescence respectively heat release rates in xy-plane. 134
10.5.1. Instantaneous OH resp.temperature distributions (a-c) and detected edges (d-f). 135
10.5.2. Flame brush thickness (a) and flame surface density (b). 136

List of Tables

3.0.1. Operating conditions of experimental and numerical setup. 19

5.4.1. Test cases for subdomain decomposition. 59
5.4.2. Time scales for single-domain simulations. 61
5.6.1. Flame properties for the LEM validation case. 66
5.7.1. Turbulence properties for different u' and L. 68

6.2.1. Relative amplitudes at the flame for different frequencies and relative amplitudes at the inlet. 77
6.2.2. Strouhal numbers for laminar (L) and turbulent (T) flames. 78

7.3.1. Relative attenuation from fuel injection to flame and amplitudes at the flame for different frequencies. 97

9.9.1. 3-step mechanism. Units in cm, s, cal, mol 128

A.0.1. Reduced mechanism for lean premixed methane combustion, derived from GRI-mech 3.0. Units in cm, s, cal, mol 143
A.0.1. Reduced mechanism for lean premixed methane combustion, derived from GRI-mech 3.0. Units in cm, s, cal, mol 144
A.0.1. Reduced mechanism for lean premixed methane combustion, derived from GRI-mech 3.0. Units in cm, s, cal, mol 145

Nomenclature

Latin letters

A	area $\left(\mathrm{m}^2\right)$
C	volume concentration $(-)$
c	progress variable $(-)$
C_λ, C_η	constants for determinination of turbulence properties for the LEM $(-)$
D	(burner) diameter (m), diffusion coefficient $(\mathrm{m}^2/\mathrm{s})$
d	diameter (m)
Da	Damköhler number $(-)$
D_t	turbulent diffusivity $(\mathrm{m}^2/\mathrm{s})$
e	specific internal energy $(\mathrm{m}^2/\mathrm{s}^2)$
f	frequency (Hz)
h	specific enthalpy $(\mathrm{m}^2/\mathrm{s}^2)$
J	momentum ratio $(-)$
j	diffusive flux $(\mathrm{kg}/\mathrm{m}^2\mathrm{s})$
k	turbulent kinetic energy $(\mathrm{m}^2/\mathrm{s}^2)$
Ka	Karlovitz number $(-)$
L	integral length scale (m)
L_D	domain length (m)
$\dot{m}$	mass flow (kg/s)
M	molar mass $(\mathrm{kg}/\mathrm{mol})$
m	azimuthal wavenumber $(-)$
P, p	pressure (Pa)
Pr	Prandtl number $(-)$
q	heat flux $(\mathrm{W}/\mathrm{m}^2)$
Re	Reynolds number $(-)$
S	size of one-dimensional domain (m)
s_C	consumption speed (m/s)
Sc	Schmidt number $(-)$
s_L	laminar burning velocity (m/s)
St	Strouhal number $(-)$
s_T	turbulent burning velocity (m/s)
T	temperature, (K)
t	time (s)
Tu	turbulence intensity $(-)$
U	dilatational velocity (m/s)

u, v, w	velocity components (e.g. axial, radial, azimuthal) ($^{\mathrm{m}}/_{\mathrm{s}}$)
U_0	bulk velocity ($^{\mathrm{m}}/_{\mathrm{s}}$)
u_t	turbulent flame speed ($^{\mathrm{m}}/_{\mathrm{s}}$)
$U_{(x,t)}$	(spatial, temporal) unmixedness $(-)$
V	volume $\left(\mathrm{m}^3\right)$
x, y, z	coordinates (m)
Y	mass fraction $(-)$

Calligraphic letters

$\mathcal{S}$	Lagrangian system containing a fixed mass of fluid or species
$\partial\mathcal{S}$	Lagrangian system boundaries

Greek letters

β	parameter to characterize the fuel distribution between upstream and downstream injection in fuel-staging mode $(-)$
$\delta_{(T,Th)}$	flame thickness (based on temperature profile respectively thermal flame thickness) (m)
η	Kolmogorov scale (m)
λ	rate parameter for LEM ($^{1}/_{\mathrm{m\,s}}$)
ν	kinematic viscosity ($^{\mathrm{m}^2}/_{\mathrm{s}}$)
ω	reaction rate ($^{\mathrm{kg}}/_{\mathrm{m}^3\mathrm{s}}$)
ϕ	equivalence ratio $(-)$
ρ	density ($^{\mathrm{kg}}/_{\mathrm{m}^3}$)
Σ	flame surface density ($^{1}/_{\mathrm{m}}$)
τ	mean eddy occurence time (s)

Sub- and superscripts

b	burnt
ds	downstream
exp	experiment, expand (subdomain decomposition)
f	cell face
fl	left cell face
fr	right cell face
i	cell index
L, l	laminar
n	time step
sub	subdomain
T, t	turbulent
u	unburnt
us	upstream
α	diffusing species

Abbreviations

CFD	Computational Fluid Dynamics
CFL	Courant-Friedrichs-Levy number
DNS	Direct Numerical Simulation
ds	downstream
EDM/FRCM	combined Eddy Dissipation / Finite Rate Chemistry Model
exp	experiment
FSD	Flame Surface Density
LDA	Laser Doppler Anemometry
LEM	Linear Eddy Model
LES	Large Eddy Simulation
(P)LIF	(Planar) Laser Induced Fluorescence
PDF	Probability Density Function
PIV	Particle Image Velocimetry
POD	Proper Orthogonal Decomposition
rms	root mean square, standard deviation
sim	simulation
SST	Shear Stress Transport (turbulence model)
(U)RANS	(Unsteady) Reynolds Averaged Navier-Stokes-Equations
us	upstream
WALE	Wall-Adapted Local Eddy-viscosity (subgrid turbulence model)

Operators

$(\cdot)'$	perturbation from mean
$\bar{(\cdot)}$	mean state
$\langle(\cdot)\rangle$	mean state
$\tilde{(\cdot)}$	phase averaged state

1. General introduction

Premixed combustion with high air excess is used in modern gas turbines to operate under moderate temperatures and simultaneously low emissions of NO and CO. Strongly swirling turbulent flows that induce vortex breakdown in the combustion chamber and associated inner and outer recirculation zones are used in this application to stabilize the flame. The flame anchors in the shear layers conditioned by the recirculation zones. The highly turbulent swirling flow further leads to a compact flame and enhances the mixing of unburnt and burnt gases, which in turn promotes stability of the flame.

The major drawback of this kind of combustion systems is the susceptibility to disturbances, which may induce fluctuations in heat release rate, excite acoustic modes and eventually drive combustion instabilities. The disturbances can originate from turbulent fluctuations or coherent structures. Inhomogeneous mixing of fuel and air, arising due to short mixing lengths and being enhanced due to instabilities, has a major impact on the heat release rate, flame dynamics and emissions. Combustion instabilities might lead furthermore to increased emissions and acoustic fluctuations, incomplete combustion and thus less efficiency, flame extinction and, in the worst case, to mechanical failure. Hence, it is imperative to gain further knowledge on the mechanisms leading to combustion instabilities and their direct implications.

In this thesis, the mixing quality as well as the influence of inhomogeneous mixing on flame characteristics and emissions in lean premixed combustion is investigated. Given that experimental investigations are costly and time consuming and computer performance improved significantly during the last decades, numerical simulations have developed a wide prominence in modern engineering. Large eddy simulations (LES) are often used for academic purposes as they provide more accurate and reliable results than simulations based on the Reynolds-averaged Navier-Stokes (RANS) equations. However, LES remains time consuming when simulating complex flow configurations. Direct numerical simulations, which are still restricted to very small scale problems, are far from being employed for calculations of configurations with realistic geometries and boundary conditions.

The present studies make an effort to assess mixing properties in a swirl burner and evaluate the advantages and drawbacks of Reynolds-averaged Navier-Stokes equations (RANS) and Large Eddy Simulation (LES) methods. Detailed insight into the impact of variations in fuel-air ratio on heat release rate, flame dynamics, and emissions is provided employing the Linear Eddy Model (LEM) as stand-alone tool to a one-dimensional, turbulent, lean premixed flame. The LEM resolves all relevant length and time scales on a one-dimensional domain and can therefore be regarded as a one-dimensional analogue to direct numerical simulations. Furthermore, experimental investigations will support the findings from the LEM and give further information on the effects of fuel-air ratio oscillations. Finally, a novel coupling approach of the Linear Eddy Model with Large Eddy Simulations will be tested on the applicability to realistic processes of lean premixed combustion.

The following will give a literature survey on simulations conducted on burner flows and mixing characterization, the computation of combustion and pollutant emissions as well as studies on variations in fuel-air ratio.

1.1. Swirling burner flows and mixing

The mixing quality in a combustion system affects the propensity to unsteady heat release rate and emissions. It is controlled by fuel injection as well as flow field properties. The fuel injection position further affects the convective time delay. Mixing quality respectively fuel injection may thus act as a driving mechanism for combustion instabilities.

LES and in parts also unsteady RANS (URANS) have proven to be promising tools to investigate strongly swirling burner flows. Large Eddy Simulations of isothermal swirling flows showed good agreement with measurements for the mean and turbulent flow properties, the coherent flow structures and their characteristic frequencies (Wang et al. 2004, Duwig et al. 2007, Garcia-Villalba et al. 2007).

Wegner et al. (2004) studied the capability of URANS simulations to capture the precessing vortex core in comparison with experiments and LES and found that URANS with a full Reynolds Stress Model is able to reproduce the PVC (precessing vortex core) qualitatively and, to some extent, also quantitatively.

Investigations on the mixing of a turbulent jet in crossflow with numerical methods showed that the scalar fields computed with LES are in satisfactory agreement with measurements (Schlüter & Schönfeld 2000, Ivanova et al. 2010). Adapting the turbulent Schmidt number allows to achieve good results with URANS as well (Ivanova et al. 2010). Fröhlich et al. (2008) performed a LES of co-annular swirling jets. They found that the coherent structure has a strong impact on mixing.

Within the last few years the research activities in the field of periodical forcing of swirling flows and its influence on coherent structures increased considerably. This is because the topic is still not fully understood but crucial for the development of gas turbine burners with low NO_x emissions and reduced susceptibility to acoustic dynamics. Investigations were mostly performed experimentally but numerical studies have also been accomplished recently. Studies on the influence of forcing on the mixing characteristics of a swirl burner, in contrast, are rare. A brief overview of some experimental and numerical findings is given in the following.

Lacarelle et al. (2007) found that forcing at the frequency of the helical mode led to an increase in scalar mixing at the burner outlet. Phase-averaged measurements from PIV data showed that axial forcing at the natural frequency of the flow replaced a helical mode with an axisymmetric one. The impact of forcing on the flow field of a generic swirler was investigated by Khalil et al. (2006). They found that forcing frequency and amplitude have an influence on both the vortex shedding and the mean-field of the flow. Düsing et al. (2003) used LES to study two confined coaxial air jets with oscillating velocity inflow and observed that LES is able to retrieve the imposed frequencies in the flow and is therefore a useful tool to investigate instabilities in gas turbine combustors. Wang & Yang (2005) performed a LES of the axially forced flow of a swirl injector with radial entry. They focused on forcing frequencies below or equal to the natural flow frequency of the coherent structure.

The excitation of the flow generally had a small impact on the mean flow properties. When forcing was applied at a frequency matching the natural frequency of the flow, the mixing was dramatically enhanced.

Further numerical studies investigating the interaction of flame and flow field with external excitation are described in Iudiciani & Duwig (2011) and Palies et al. (2011). They show that forcing at frequencies lower than the PVC characteristic frequency moves the central recirculation zone upstream (Iudiciani & Duwig 2011). Vortex shedding taking place at the injector lip can induce flame roll-up which interacts with rotation rate fluctuations leading to enhanced or damped heat release rate fluctuations depending on the inlet acoustic wave frequency (Palies et al. 2011).

1.2. Computation of combustion and pollutant emissions of lean premixed flames

Restrictions for allowed pollutant emissions become more and more stringent for modern gas turbines. It is therefore important to reliably predict emissions in the design process of an engine. Especially NO and CO are of interest. For the formation of NO in lean premixed combustion, several pathways are of importance: thermal NO, formed mainly at high temperatures, NO formed through N_2O and NNH* as well as prompt NO (pathway via CH) when approaching stoichiometric and rich conditions in the mixture.

If NO and additionally CO are to be predicted, the chemistry has to be considered in detail, resulting in high computational cost. For complex flow configurations, such as strongly turbulent burner flows, the spatial as well as the temporal resolution has to be sufficiently fine allowing to accurately represent the interaction of flow field, turbulence and mixing characteristics with chemistry. This interaction may for specific conditions occur at the smallest turbulent and chemical scales. Such conditions might be present in gas turbine combustors which usually operate within the thin reaction zones / corrugated flamelets combustion regimes (Fig. 1.2.1).

In the following, a few modeling approaches and their applications on predicting emissions of CO and NO in lean premixed combustors are introduced and their benefits and drawbacks are discussed.

Eggels (2001) conducted a numerical study on the formation of NO in an industrial lean gas turbine burner. It consists of two stages between which the fuel was distributed. Variations in the fuel distribution in terms of minimizing the NO emissions were investigated with 2D and 3D simulations. The NO-formation was computed in a post-processing step. Eggels states that NO was considerably underpredicted in comparison with experimental findings when considering perfect mixing of fuel and air. A 2D-study with radial mixture fraction gradient at the fuel inlet indicated a strong influence on NO-emissions and enabled to estimate concentrations close to measured values.

Vicente et al. (2004) performed 2D simulations of the formation of NO and CO in the wake of a bluff-body stabilized flame. They employed a reduced mechanism including all relevant NO formation pathways and solved a Joint-PDF-equation system for five species based on the Monte Carlo method. The results of the simulated NO and CO distributions strongly deviate from measurements close to the symmetry axis, where the emissions are

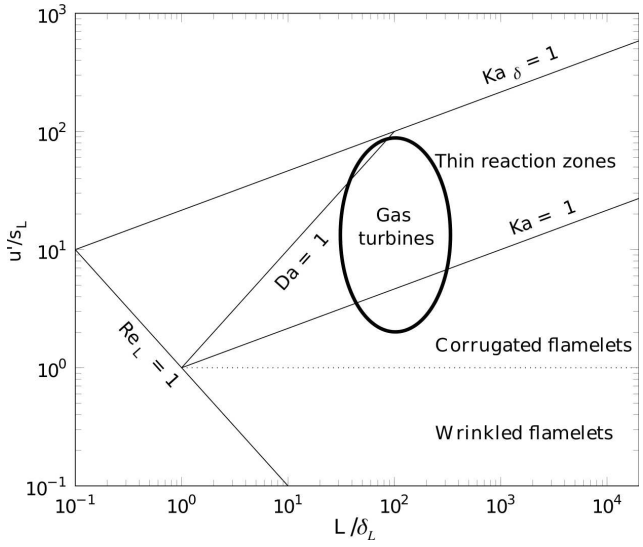

Figure 1.2.1.: Borghi diagram with conditions typically encountered in gas turbine combustion indicated.

underpredicted. Variations in the turbulent mixing or chemistry models or the inclusion of heat losses could not improve the results.

NO-emissions of a swirl-stabilized burner were investigated by Biagioli et al. (2005). The NO-formation was split into a fast (high Damköhler-numbers, prompt NO) and a slow (small Damköhler-numbers, post-flame region) part. Prompt-NO was assessed by coupling it to the heat release (type: flamelet-combustion model), whereas in the post-flame region NO was computed directly via the formation rate from the Zeldovich-mechanism integrated with a probability density function of the fuel mixture fraction. The NO-modeling was implemented in a 3D CFD code as well as a reactor network. The results agree qualitatively well with measurements. As the main reason for discrepancies the authors mention the inability of RANS to reproduce the flame position correctly.

Novosselov et al. (2006) introduced a combined reactor network-CFD ansatz to predict NO and CO emissions. A detailed reactor network resolving the different flow and reaction zones of the combustor was developed by means of CFD simulations. The CFD gives information on the flow field whereas the reactor network is used to analyze kinetics, employing a detailed combustion mechanism (GRI 3.0 mech. Smith et al. (1999)). The agreement of the results with measurements is good. To generate the reactor network for a (new) configuration a validated CFD simulation is needed. The effort for the computation of a new configuration is therefore quite high.

Syed et al. (2007) presented an algorithm to determine NO emissions which can be used in the burner development process or for online emissions prediction. The model was developed considering simplified fundamental processes that influence the formation of NO. It is divided in two parts: NO characteristics for ideal premixed conditions and statistics of fuel-air ratio in the NO formation zone. The model provides results in very good agreement with measurements in a high-pressure test rig. Drawbacks of the model are however the need of suitable empirical data as input and deviations from test results that were observed for high pressure loss.

Jella et al. (2010) described their experience with the commercial CFD-code Fluent to predict CO and temperature fields into a two stage Rolls-Royce burner. They considered the results from RANS and Large Eddy Simulations. RANS was not capable of reproducing the flame position in the second stage and thus the temperature and CO emissions at the exit. LES yielded considerably better results. The flame position and the exit temperature match measurement results. Discrepancies however occur in the CO concentrations, although the trend could be reproduced to some extent. Refinement of the grid affected the reaction zone and the highest reaction rates. An improvement of the results could however not be achieved, which was explained with the employed combustion model (Eddy-Break-Up-Model, EBU) introducing bigger errors than the grid resolution.

Wegner et al. (2010) presented a new model for the determination of CO that is based on the assumption of two separate time scales for the fast premixed flame stabilization zone and the slow burn out zone downstream of the flame. The combustion model was implemented in the commercial CFD code CFX. The flame position and reactive flow in a test case with atmospheric pressure as well as CO emissions at atmospheric and elevated pressure could be depicted correctly.

Bulat et al. (2014) studied the formation of emissions in an industrial gas turbine burner employing LES with an Eularian stochastic sub-grid pdf model with reduced chemistry. The influence of radiative heat losses and combustion mechanisms are evaluated. Velocity fields, temperatures and species in the inner shear layer as well as NO formation could be reproduced with good accuracy. Discrepancies were found in the outer shear layer.

Many of the investigations above emphasize the major role of turbulent mixing processes and turbulence-chemistry interaction for pollutant emission prediction. Their inclusion in the modeling process is however limited due to tremendous numerical costs. The slowly forming NO can, for certain circumstances, be computed in separate post-processing steps. This is not possible for CO so that often only one of the species is considered to keep the computational cost low.

The Linear Eddy Model, which we employ in the present studies, directly resolves the interaction of turbulent mixing, molecular diffusion and chemical reactions at all relevant physical length and time scales. Furthermore only few external data (integral and Kolmogorov length scales, turbulence intensity) is needed, which has to be generated empirically or obtained from measurements for a specific configuration. This gives an advantage over many of the presented methods and models. The Linear Eddy Model will be described in detail in Chapter 5.

Smith & Menon (1996) and Menon et al. (1994) showed in one-dimensional LEM studies on various turbulent premixed flames that key features of turbulent combustion and pollutant emissions are reproduced by the LEM. Three-dimensional simulations with the LEM implemented as a subgrid model for LES (LEMLES) show promising results in comparison with measurements and DNS. This is reported, for example, in the studies of Smith & Menon (1998) and Sankaran & Menon (2005). A more comprehensive overview on LEMLES will be given in Part IV.

Smith & Menon (1998) present a transient simulation of a premixed stagnation point flame employing LEMLES, which is in good qualitative agreement with experimental observations. Sankaran & Menon (2005) conduct a 3D-LEMLES of a freely propagating flame in the thin reaction zone combustion regime. Many important characteristics of the thin

reaction zone, for example, broadening of the flame structure, statistics of flame curvature, and the vorticity field, agree well with DNS studies.

1.3. Variations in fuel-air ratio

Combustion instabilities may be driven by various effects and their interaction (Huang & Yang 2009), including coherent flow structures (Paschereit et al. 1999, 2000), flame surface variation (Poinsot & Candel 1988) and equivalence ratio fluctuations (Lieuwen & Zinn 1998, Lieuwen et al. 1998). Equivalence ratio fluctuations originate from imperfect mixing of fuel and air at the injection point of fuel. Variations in the fuel-air mixture arriving at the flame front lead to heat release rate fluctuations. This mechanism was found to be one of the major causes for combustion instabilities at lean conditions (Lieuwen & Zinn 1998, Lieuwen et al. 1998). The reason for this lies in the relationship between equivalence ratio and chemical reaction time. The gradient of chemical reaction time and equivalence ratio increases significantly for premixed flames at lean conditions, as evidenced, for example, by the slope of the burning velocity with respect to the equivalence ratio. Moreover the chemical reaction time is inversely proportional to the reaction rate at lean conditions which amplifies the susceptibility to combustion instabilities.

There is a number of studies dealing with the investigation of the flame response to variations in mixture composition. Numerical investigations of premixed laminar and counterflow flames (Marzouk et al. 2000, Sankaran & Im 2002, Cho & Lieuwen 2005, König et al. 2009, Shreekrishna et al. 2010, Richardson et al. 2010, Zhou & Hochgreb 2013) as well as computational and experimental studies on bluff-body and swirl flames undergoing equivalence ratio variations (Balachandran et al. 2005, Birbaud et al. 2008, Altay et al. 2009, Balachandran et al. 2011, Kim et al. 2011, Bobusch et al. 2013, Cosic et al. 2015) have been performed.

Marzouk et al. (2000) investigated an axisymmetric stagnation-point flame in which a stream of reactants impinges a stream of burned combustion products. Equivalence ratio variations with small time scales were found to lead to reaction zone broadening, burning rate enhancement, and extension of the flammability region to lower equivalence ratios.

Sankaran & Im (2002) investigated unsteady methane-air flames in an opposed-flow configuration subject to time-varying composition fluctuations. They concentrated on the determination of the dynamic flammability limit and found that the flammability region is extended to lower equivalence ratios as the frequency of oscillation is increased (Zhou & Hochgreb 2013) while the mean equivalence ratio and temperature must be maintained higher than the critical value for steady flammability limit.

Analysis of the flame response to equivalence ratio fluctuations in terms of the flame transfer function (Cho & Lieuwen 2005, Shreekrishna et al. 2010) showed that the heat release response is controlled by superposition of three disturbances: heat of reaction, flame speed, flame area (Fig. 1.3.1). The influence of the particular disturbances varies with the oscillation frequency. Studies on the non-linearity of the heat release response identified two key mechanism (Shreekrishna et al. 2010): the flame-kinematic mechanism driven by fluctuations in flame position associated with oscillations in flame speed (Birbaud et al. 2008) and a mechanism due to the intrinsically non-linear dependence of flame speed and heat of reaction on equivalence ratio oscillations, which is especially pronounced for

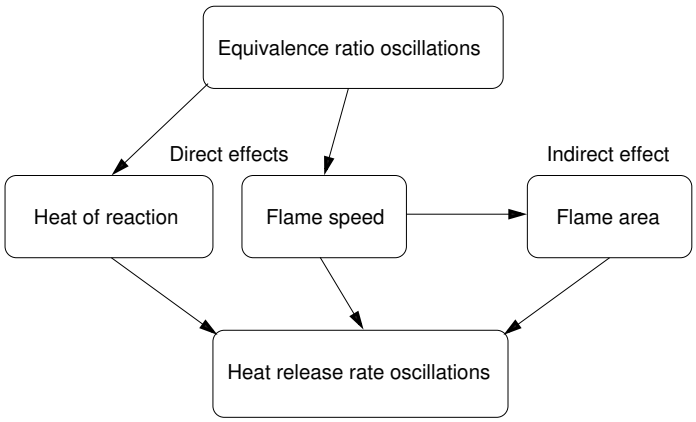

Figure 1.3.1.: Processes generating heat release rate oscillations caused by perturbations in fuel-air ratio adapted from Cho & Lieuwen (2005).

composition fluctuations varying between lean and rich values.

König et al. (2009) considered the response of laminar stretched premixed methane-air counterflow flames to periodical perturbations of mixture composition and inflow and observed that perturbations reach the flame only under certain conditions. The amplitude of perturbation reaching the flame decreases with increasing frequency due to diffusive processes and might even be completely damped before reaching the flame zone. They further stated that the equivalence ratio perturbations do not qualitatively influence the behavior of chemical kinetics.

Strained laminar premixed counterflow flames were numerically studied by Richardson et al. (2010) and Zhou & Hochgreb (2013), regarding the effect of equivalence ratio gradients and fluctuations. They found that back/front supported flames propagate faster/slower than their premixed counterparts. Moreover the stratified flame propagation was determined in terms of consumption speed of the mixture. Richardson et al. (2010) explain that reaction, diffusion and cross-dissipation components contribute to the consumption speed. Diffusion is thereby directly affected by strain responding most rapidly to strain variations whereas the reaction and cross-dissipation components' response is governed by flow and flame time-scales. Zhou & Hochgreb (2013) further state that under lean conditions the propagation is dominated by diffusion of heat and under rich conditions by diffusion of several major species.

The non-linear response of bluff-body respectively swirl-stabilized flames was experimentally investigated by Balachandran et al. (2005, 2011), Kim et al. (2011) and Cosic et al. (2015). Balachandran et al. found that the flame response depends on the strength of swirl (Balachandran et al. 2005) and the acoustic and convective compactness of the flame (Balachandran et al. 2011). For compact flames (low frequencies) the heat release rate fluctuations mainly depend on equivalence ratio variations whereas for higher frequencies the heat release is dominated by flame-vortex interaction. Kim et al. (2011) state that the non-linear response becomes more pronounced with increasing modulation frequencies and decreasing equivalence ratios. The phase between heat release and equivalence ratio oscillations was found to increase linearly with frequency. Balachandran et al. (2005) simulated a V-flame subjected to equivalence ratio fluctuations. The flame featuring wrinkles may inter-

act with the fresh mixture for sufficient large wrinkling amplitudes generating a non-linear heat release response. Furthermore high levels of modulation induce velocity perturbations, which in turn interact with the flame and modify its response. In an extensive experimental study of the nonlinear response of a partially premixed swirling flame, Cosic et al. (2015) found that there is little interaction between the velocity-fluctuation-induced response of the flame and the heat release rate fluctuations originating from perturbations in equivalence ratio. They suggested that the response of the flame to equivalence ratio fluctuations is reduced at higher oscillation amplitudes because of increased turbulent diffusion.

Altay et al. (2009) considered a backward-facing step combustor with and without oscillations in equivalence ratio and found that combustion dynamics are primarily controlled by flame-vortex interaction, while equivalence ratio oscillations show secondary effects although they could destabilize the flame and generate variations in the combustion dynamics.

1.4. Structure of the thesis

The thesis is structured in four parts.

The first part concentrates on the evaluation of mixing properties in a swirl burner. The setup of the combustor, the measurements and the numerics are explained (Chapter 2). The mixing characteristics and flame positions in a swirl burner for different fuel-staging configurations are investigated with steady RANS simulations in Chapter 3. Eventually, oscillations in the main flow through the swirl burner at the frequency of the helical coherent structure for isothermal conditions and their influence on the flow and mixing fields as well as the dynamics are studied by means of unsteady RANS and Large Eddy Simulations (Chapter 4).

Part II concentrates on stand-alone simulations with the Linear Eddy Model. In Chapter 5, the ansatz of the LEM, the code implementation and newly introduced methods as well as the employed combustion mechanism are described. The LEM code is validated against numerical and experimental data and the impact of turbulence intensity and integral length scale on flame characteristics and emissions is evaluated. Chapter 6 gives insight into periodical perturbations of fuel-air ratio oscillations and its implications on one-dimensional turbulent premixed flames. The effects are assessed by means of NO and CO emissions, heat release rate and flame propagation.

Results of experimental studies on equivalence ratio oscillations in a lean premixed bluff-body flame are given in Part III. The setup and measurement techniques are described in Chapter 7. The effects of fuel-air ratio fluctuations are characterized by velocity fields, heat release rates, flame front characteristics as well as emissions (Chapter 8).

Part IV introduces a new implementation approach for the Linear Eddy Model as a subgrid model for LES. Chapter 9 describes the coupling of the LEM with the LES; subgrid LEM computations, scalar transport across LES cell boundaries and the LEMLES closure are detailed. The implementation is validated for simple test cases. Chapter 10 assesses the performance of the LEMLES on a highly turbulent lean premixed bluff-body stabilized flame (as in Part III) in comparison with a standard combustion model and experimental studies. Velocity fields, heat release rates, emissions and flame structures are evaluated.

Part I.

Mixing in a swirl burner

Fuel injection plays an important role in gas turbine combustors as it influences the mixing quality as well as the time delay and thus affects dynamic stability of the combustion process. The position and configuration of fuel injection is directly coupled with the convective time delays, which have a major impact on the excitation of thermoacoustic instabilities as they influence fluctuations in heat release rate as well as the coupling of heat release rate and acoustic modes (Lieuwen et al. 2001). Fuel injection further affects the spatial and temporal mixing quality and thus has a major impact on pollutant emissions.

Furthermore, periodical flow patterns may have an influence on the stability and mixing of a burner. They may evolve through coherent structures in swirling flows or acoustic fluctuations which develop during combustion instabilities.

This part concentrates on the evaluation of mixing quality influenced by different fuel injection configurations respectively periodical flow excitation by means of (U)RANS and LES. The structure is as follows: Chapter 2 describes the investigated burner as well as the employed experimental and numerical setups. The impact of adapted fuel injection configuration on the mixing and combustion of a swirl burner is studied in Chapter 3. Chapter 4 reports on the impact of periodical flow forcing on flow fields and mixing characteristics.

The measurement data used in this part for comparison with the numerical results were obtained by Arnaud Lacarelle and Ahmed Emara at the water and combustion test rigs at the Chair of Experimental Fluid Mechanics, Institute of Fluid Dynamics and Acoustics, Technische Universität Berlin.

The findings of this part were published in Schrödinger et al. (2010), Schrödinger et al. (2011*c*), and Schrödinger et al. (2012*a*).

2. Setup

2.1. The investigated burner

The burner consists of two half cones that are shifted in radial direction forming two slots. The air stream through the slots generates a strongly swirling flow which induces a recirculation zone downstream of the burner outlet, where the combustion chamber is located (vortex breakdown). The flame stabilizes in the shear layers of the annular jet. Fuel is injected inside the slots, perpendicular to the air stream. Detailed information on the burner is given by Sattelmayer et al. (1992). A sketch of the burner with fuel injection is shown in Fig. 2.1.1.

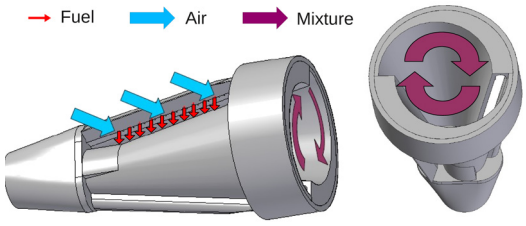

Figure 2.1.1.: Sketch of the swirl burner used for the present studies.

The fuel injection configuration used for the investigations in Chapter 3 is a secondary line of injection holes mounted upstream of the standard fuel injection line and is divided into a downstream (ds) and an upstream (us) part (Fig. 2.1.2). The two parts of the secondary injection line consist of two independent injection chambers. The upstream port features 16 and the downstream 14 injection holes of 0.7 mm diameter. The holes are directed in 45° angle to the air flow direction increasing the feasibility of influencing the convective time delay. Due to a high momentum of the fuel stream, in combination with the orientation of the fuel injection holes in flow direction, the convective time delays can be manipulated.

Since only the secondary injection line is used for investigations in Chapter 3 the fuel distribution among the upstream and downstream parts can be characterized by one parameter, β (Lacarelle et al. 2009*b*).

$$\beta = \frac{\dot{m}_{\mathrm{us}}}{\dot{m}_{\mathrm{all}}} \quad \text{with} \quad 0 \leq \beta \leq 1 \tag{2.1.1}$$

Here $\dot{m}_{\mathrm{all}}$ describes the overall fuel massflow with $\dot{m}_{\mathrm{all}} = \dot{m}_{\mathrm{us}} + \dot{m}_{\mathrm{ds}}$. The baseline configuration within Chapter 3 is referring to a fuel distribution of $\beta = 0.5$.

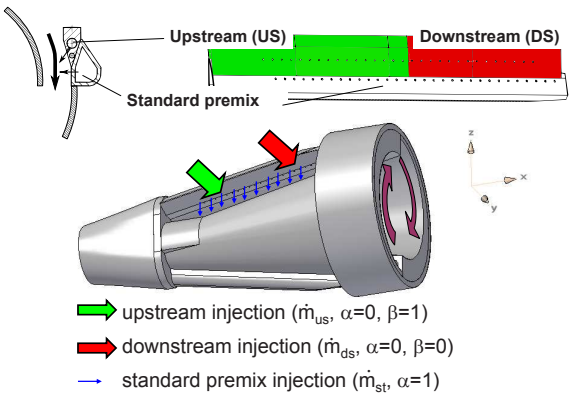

Figure 2.1.2.: Sketch of swirl induced burner with modified fuel injection.

2.2. Similarity of water and air flows

Part of the studies consider measurements in a water test rig. The corresponding simulations were also performed with water as fluid.

Similarity of water and air flows holds if the Reynolds number (Re) and the momentum ratio (J) are kept constant. Comparing the mixing quality in water and air is only meaningful for sufficiently high Reynolds numbers. For small Reynolds numbers, homogenization in gaseous flows is achieved earlier than in water flows. This is due to the high molecular diffusion in a gas. A parameter describing this behavior is the Schmidt number which is $\mathrm{Sc}_{\mathrm{gas}} \approx 1$ in gas while it is $\mathrm{Sc}_{\mathrm{water}} \approx 1\,000$ in water. At high Reynolds numbers, molecular diffusion is negligible compared to turbulent advection, and mixture processes in water and gas flows are similar (Miller 1991). For a Reynolds number of 35 000 considered in the present work, the mixing quality evaluations are therefore quantitatively transferable to air conditions.

The flow forcing in the experiments in previous studies (Lacarelle et al. 2009*c*) as well as in the present simulations is intended to emulate the action of acoustic waves during combustion instability. Although the speed of sound in water is much larger than in air, forcing studies in a water test-rig are still useful when considering frequencies for which the acoustic wavelength in air is much larger than the axial extent of burner and flame-stabilization domain. In this case, the burner flow is compact with respect to the acoustic wavelength and can be considered as incompressible.

2.3. Experimental setup

This section will give a brief overview of the experimental setups. For a detailed description we refer to Lacarelle et al. (2009*b*) and Emara et al. (2009). All investigations were performed under atmospheric conditions.

2.3.1. Combustion test rig & OH*-chemiluminescence measurements

The burner operated with natural gas was mounted into a cylindrical combustion chamber with a diameter of 200 mm made out of quartz glass. This enabled full optical access to the flame. An ICCD Camera (Imager + IRO of LaVision) equipped with a narrow bandpass filter centered around 312 nm was used to record the OH* chemiluminescence of the flame. The shutter time was set to 100 μs, and 100 pictures were taken to obtain the averaged pictures presented in this work. The camera was positioned perpendicular to the axial direction in 45° angle to the slot cross section of the burner.

2.3.2. Water test rig & concentration measurements

Cold flow investigations with High Speed Planar Laser Induced Fluorescence (LIF) in water can be used to evaluate the mixing quality of the burner. The combustion chamber and the burner with same physical dimensions as those of the combustion test rig were mounted in the water channel. For measurements inside the burner a Plexiglas model was used.

The main advantage of water investigations is the ease of using Laser Induced Fluorescence (LIF) and the high quality of the data. The mean velocity through the combustor geometry in water is reduced by more than one order of magnitude. This means for the LIF measurements that the frame rate of the camera can be decreased and a higher signal to noise ratio is obtained. The measurement system included a continuous wave laser at 532 nm wavelength and 4 W power, Rhodamin 6G as fluorescent tracer, and a Photron Fastcam PCI 1024 camera. A 1 mm thick laser sheet was generated with a combination of cylindrical lenses in different cross sections of the burner and combustion chamber. The laser excites the dye passing through the measurement plane, and the emitted light was filtered through a OG590 high-pass filter before being recorded by the camera. The intensity of the signal was transformed to concentrations by using an appropriate correction of the recorded intensity, which included background subtraction and absorption correction (Pan & Meng 2001).

To create a periodically forced flow, such as investigated in Chapter 4, a special mechanism was employed, which was located upstream of the test section, in the bypass of the pump. It consisted of a standard rotating valve driven by an electric motor. Depending on the preset parameters valve position, volume flow, frequency of forcing, and rotation of the pump, forcing amplitudes of up to 90% of the mean flow could be achieved. All chosen measurement points exhibited an almost sinusoidal excitation.

2.3.3. PIV setup

Flow field measurements of the reacting and cold flow were taken by Particle Image Velocimetry (PIV). A Continuum Minilite standard Nd:YAG PIV laser system was employed which generated a laser sheet of 1.5 mm in flow direction within the combustion chamber. The plane was positioned in 90° angle to the slot cross section of the burner. For the non-reacting investigations, liquid tracer particles were used in the combustion chamber and silver coated particles (15 μm) were used in the water test rig. Solid particles SiO2 were used for the reacting flow investigations. The whole combustion chamber cross section was recorded in the non-reacting investigations, while a half plane was recorded in the reacting

flow to increase the spatial resolution. For these cases, the velocity profiles were mirrored. Cold flow investigations were performed with 500 snapshots while only 250 snapshots were taken during reacting flow measurements due to the harsh environment. Both rates were sufficient to draw trends in mean and coherent quantities, but the latter was too low to obtain accurate turbulent quantities.

The two successive images recorded by the camera were computed with the software VidPIV of ILA GmbH. A cross correlation and 3 successions of adaptive cross correlation – local filter – local interpolation were used to compute the velocities in $16 \times 16\,\mathrm{px}^2$ windows with 50% overlap.

The error of the measurement was strongly dependent on the test rig. In air, non homogeneous seeding density, optical reflexions of the cylindrical wall as well as the low signal recorded led to significantly more velocity outliers and hence a higher error for instantaneous velocity estimation than in water (±16% against ±7.7%, procedure defined by ITTC (2008)). However, the error sources were slightly different: while the main error source in air is due to the post-processing of the velocities, a dominant error source in water is the oscillation of the main volume flow, higher than in air (±3.5% in water against ±1% in air). Further measurements performed with LDA in air (not shown here) present a degree of turbulence slightly higher than the air PIV measurement but still lower than the water measurement results. This confirms that the two test rigs present different degrees of turbulence and explains the higher turbulent values in the water test rig (see Fig. 3.1.3).

2.4. CFD setup

The CFD simulations were performed with the commercial ANSYS CFX 11/12/13 software. The Reynolds number of the computed flows corresponded to the one used in the experimental studies (Re = 35 000). Since the cold flow experiments were conducted in a water test-rig, the fluid properties in the corresponding simulations were also set to those of water, for the main flow as well as for the injected "fuel". The mean mass flow for the main inlet ("air") was set matching the Reynolds number of the experiment and the injection ("fuel") mass flow was determined by imposing a "fuel–air" mass flow ratio corresponding to an equivalence ratio of 0.6. The turbulence intensity at the inlet boundaries was set to 5% for the URANS/RANS simulations. An opening was used as outlet condition and no slip conditions were applied at all other boundaries.

For (unsteady) RANS simulations, the choice of the turbulent Schmidt number, defined as $\mathrm{Sc}_t = \nu_t/\mathrm{D}_t$, where ν_t is the turbulent viscosity and D_t the turbulent diffusivity, has a noticeable influence on the computed mixing quality (Ivanova et al. 2010). He et al. (1999) found a turbulent Schmidt number Sc_t of 0.2 to provide the best results in terms of mixing quality in comparison with measurements for a jet in cross-flow, while Schmitz et al. (2007) found best agreement in mixing properties for $\mathrm{Sc}_t = 0.35$ investigating a fuel–air premixer. Our own sensitivity tests showed that simulations with a turbulent Schmidt number of 0.2 provide results that were in best agreement with measurements with respect to mixing quality. Therefore, this value was chosen for the present (U)RANS calculations. For LES, the turbulent Schmidt number does not have a significant effect on the mixing characteristics (Ivanova et al. 2010, Schlüter & Schönfeld 2000).

Jiang & Campbell (2008) investigated the effect of turbulent Prandtl and Schmidt num-

bers on the reacting flow field properties of a propane diffusion flame combustor and found that the influence on the velocity is marginal while it shows a strong effect on the temperature and species fields. For the cases considered, the optimal turbulent Prandtl and Schmidt numbers for temperature and species prediction inside the combustor was 0.5 while it varied from 0.4 to 0.55 for wall temperature prediction.

We used a value of 0.2 for the turbulent Prandtl and Schmidt numbers in the reacting studies, as in the cold flow investigations. In addition, we performed the combustion simulations with $\mathrm{Sc}_t/\mathrm{Pr}_t = 0.55$ to improve the results on flame shape and position.

For the steady and unsteady RANS simulations, the Shear Stress Transport (SST) turbulence model was applied. The LES WALE (wall-adapted local eddy-viscosity, Nicoud & Ducros (1999)) model was used for the large eddy simulations. These models proved to give good results in earlier studies of the same burner.

The combustion model used for reacting flow simulations was the combined Eddy Dissipation / Finite Rate Chemistry Model (EDM/FRCM). Air and methane were employed for the oxidizer and fuel streams respectively.

ANSYS CFX uses a fully coupled solver, which solves the differential equations for the hydrodynamic variables (u, v, w, p) as a single system. This solution approach uses a fully implicit discretization of the equations at any given time step. For spatial discretization, the high-resolution advection scheme was used for all variables in the URANS and for the mass fraction in the large eddy simulation. For all other variables in the LES, the central difference advection scheme was applied. Second-order time discretization was used for LES as well as URANS.

2.4.1. Grid and time resolution

For the large eddy simulations, the computational domain, including the fuel and air supply, the burner, and the combustion chamber, was meshed with tetrahedrons. The grid was refined within the burner, at the burner outlet, and in the combustion chamber in the shear layer regions. The element volumes in these regions were smaller than $4 \times 10^{-9}\,\mathrm{m}^3$. Details of the fuel injection were included in the geometry. Altogether the mesh consisted of approximately 1.6 million nodes.

The mesh for the RANS respectively URANS simulations was divided into two parts. Upstream of the burner an unstructured tetrahedron grid with a prism layer was used while the burner itself and the combustion chamber were meshed with hexahedrons. The upstream and downstream parts were concatenated with a GGI-Interface. In contrast to the URANS and LES the RANS simulations employed a 180° model of the burner, the combustion chamber and the air and fuel supply. Periodic boundary conditions were applied at the azimuthal faces.

Details of the fuel injection were also included in the mesh for the (U)RANS simulations (Fig. 2.4.1). The extent of the combustion chamber was almost three times (URANS) respectively four times (RANS) that of the LES simulations. Furthermore, refinements in the hexahedron-mesh, needed to resolve the boundary layers at the burner walls, prolong through the complete combustion chamber. Due to these reasons the URANS mesh had around 3 million nodes and the RANS mesh even 3.7 million nodes, which is more than that of the LES grid. Nevertheless the resolution of the LES mesh (within the burner and

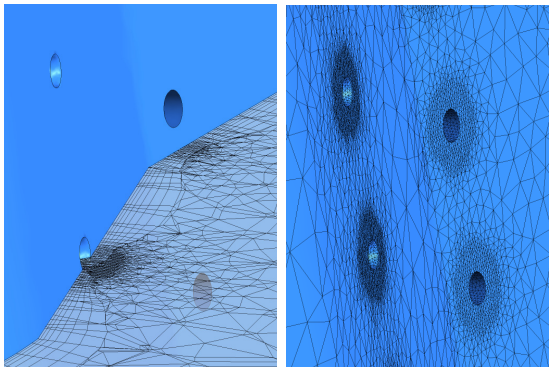

Figure 2.4.1.: Meshing of fuel injection holes.

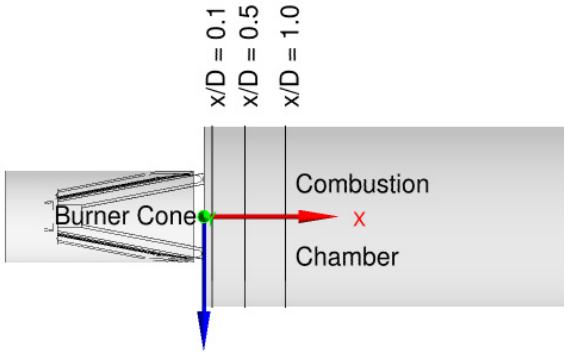

Figure 2.4.2.: Computational domain (not showing the complete combustion chamber considered for the LES and (U)RANS simulations).

the flame stabilization region) was significantly higher than that of the URANS mesh.

A sketch of the computational domain including plenum, burner and combustion chamber is shown in Fig. 2.4.2. Axial positions of cross sections used in the results section are indicated.

The time step taken for LES was set to 5×10^{-5} s so that the maximum Courant–Friedrichs–Levy (CFL) number in the whole domain was smaller than 2. The rms CFL number was smaller than 0.2, with the highest values being located at the fuel injection. The URANS simulations were conducted using a time step of 10^{-3} s, resulting in a rather high maximum CFL number. However, the maximum CFL number within the burner and combustion chamber was still smaller than 3. Convergence of all variables in each time-step was achieved within 10 loop iterations.

The time-averaged results and proper orthogonal decomposition (POD, see Section 4.5) were calculated for an overall time of approximately 10 periods of the dominant oscillation for the LES (period of dominant oscillation = 1/frequency of coherent structure). For URANS, a total simulation time of about 8 periods of dominant frequency was used for averaging. Regarding the averaged results and higher moments, no significant changes were observed for longer simulation times so that the numerical data sampling period was considered sufficient for evaluating data statistics.

3. Effect of fuel-staging on mixing quality and flame behavior

As explained in the main introduction (Chapter 1) and the beginning of this part (Part I), thermoacoustic instabilities may evolve under certain circumstances in lean premixed gas turbine burners and can lead to structural damage, increased emissions and flame extinction. Passive and active control mechanisms are capable of preventing thermoacoustic instabilities. One possibility of active control is *fuel-staging* which has been shown to operate successfully within single burners (Paschereit et al. 2003, Kokanovic et al. 2006, Bulat et al. 2007, Lacarelle et al. 2008) as well as multi-burner configurations (Kokanovic et al. 2006, Scarinci et al. 2004). In fuel-staging control the fuel injection configuration is adapted to the combustor operating parameters to adjust convective time delays and the mixing quality of the burner.

For the results presented in this chapter, we used steady RANS to simulate the flow and combustion of the swirl stabilized burner introduced in the previous chapter. The same burner was investigated numerically in previous studies, looking at time-delay modeling, stabilization mechanism, flame imaging, thermoacoustic behavior, mixing fields and pollutant formation (Flohr et al. 2001, 2002, Güthe et al. 2006, Biagioli 2006, Schmitt et al. 2007).

We performed simulations of fuel-staging and investigated its effect on the mixing quality, the flame shape and position and convective time delays. The numerical results are validated with experimental flow field, concentration, flame visualization and flame transfer function measurements. Firstly, cold flow investigations are evaluated. CFD simulations are compared to PIV-measurements of the water test rig and various cold flow configurations are considered (numerical and experimental) to characterize the mixing field. Secondly, reacting flow simulations are shown in comparison with data from the combustion test rig. Validation of the flow field as well as flame shapes and positions and convective time delays for varying fuel injection parameter β are investigated. For information on the effect of fuel staging on stability and NOx emission we refer to Lacarelle et al. (2009*b*).

The operation conditions considered in the studies are given in Table 3.0.1.

Table 3.0.1.: Operating conditions of experimental and numerical setup.

	Re	ϕ	$\mathrm{Tu}_{\mathrm{inlet}}$
water lab	$\sim 35\,000$	0.56	NA
comb. lab	$\sim 39\,000$	0.56	NA
cold flow sim.	$\sim 35\,000$	0.56	5%
reacting flow sim.	$\sim 39\,000$	0.56	5%

3.1. Cold flow investigations

Cold flow investigations can be considered with respect to reacting flows for the determination of physical properties upstream of the flame as Reynolds similarity is given there (Section 2.2). The simulations were performed with a turbulent Schmidt number of 0.2 (Section 2.4).

3.1.1. Flow field validation

The flow fields downstream of the burner in the combustion chamber were measured via PIV in the water test rig and the combustion test rig. The regarded plane was in both cases located in a 90° angle to the slot cross section of the burner. The measurements were taken to validate the computed CFD results. All resulting velocities are normalized by the mean bulk velocity calculated with the burner diameter. The axial and radial positions are normalized with the burner diameter. The burner exit is located at $x = 0\,\mathrm{m}$. The turbulence intensity Tu is calculated from the turbulent kinetic energy k for the CFD simulations and from the radial and axial velocity components for the experiments:

$$\mathrm{Tu}_{\mathrm{CFD}} = \frac{\sqrt{\frac{2}{3}k}}{U_0}, \tag{3.1.1}$$

$$\mathrm{Tu}_{\mathrm{exp}} = \frac{\sqrt{\frac{1}{3}(2\overline{u'^2} + \overline{v'^2})}}{U_0}, \tag{3.1.2}$$

where U_0 describes the mean velocity at the burner exit. As the measurements only provide two dimensional results we assume for the determination of Tu that fluctuations in the azimuthal component are similar to fluctuations in the axial velocity component u.

For cold flows, the experimental measurements were performed without fuel injection while the flow field was simulated for three fuel injection configurations ($\beta = 0$, 0.5, 1.0 (ds, us+ds, us)). The azimuthal fuel to air momentum ratio at the fuel injection is around 10% for $\beta = 0.5$ and up to 19% for $\beta = 0$ and 1. The effect of fuel injection on the flow field for comparing measurement and simulation at $\beta = 0.5$ is regarded to be insignificant. A comparison of the computed and measured recirculation zones is given in Fig. 3.1.1. The boundaries of the backflow regions are defined by isolines of the axial velocity u satisfying $u = 0$. Figure 3.1.2 shows the axial velocity u and Figure 3.1.3 shows the intensity of turbulence Tu at different axial positions. The cold case figures show, in addition to the comparison of simulation and measurement in water, the comparison to the non-reacting flow in air.

The results of water and air measurements support the assumption of similarity at the given Reynolds numbers. The axial velocity profiles (Fig. 3.1.2) are similar in both cases except for $x/D \geq 1$. For this region the air measurements show discrepancies from the water measurements also visible in Fig. 3.1.1. The discrepancies could originate from slight differences in the setups. The turbulence intensity is, as explained in Section 2.3.3, slightly higher in water than in air (Fig. 3.1.3).

The simulation results for the cold case are in best agreement with the measurements close to the burner exit. The axial velocity distribution is similar for $x/D = 0.1$ and 0.5

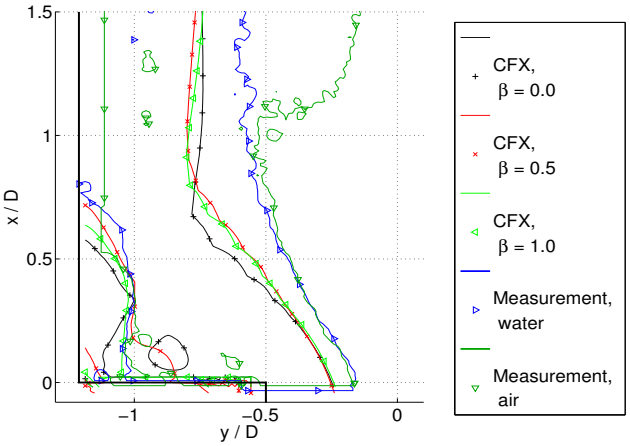

Figure 3.1.1.: Isolines of axial velocity $u = 0$, cold case, simulation data for different β; measurements performed w/o injection.

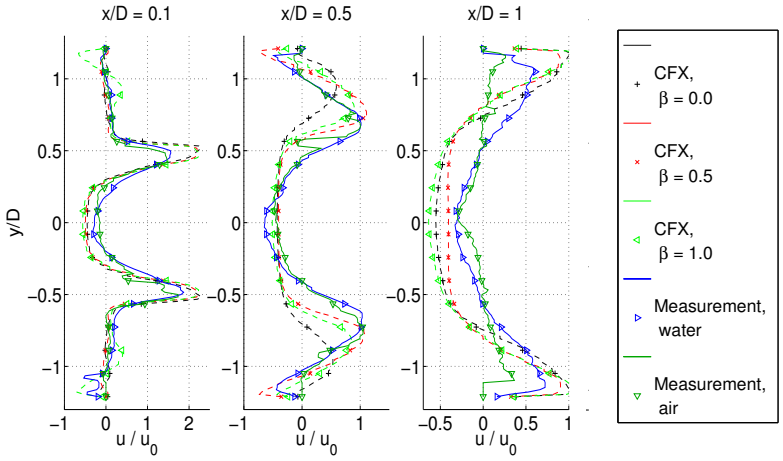

Figure 3.1.2.: Axial velocity, cold case, simulation data for different axial positions and β; measurements for different axial positions, performed w/o injection.

(Fig. 3.1.2) but the radial extent of the inner recirculation zone is too large for higher x/D. The outer recirculation zones of simulations and measurements are in closer agreement (Fig. 3.1.1). Even if stronger radial shear is obtained from simulations, the calculated turbulence intensity underpredicts the measured one despite depicting qualitatively similar distributions (Fig. 3.1.2). Flohr et al. (2002) investigated the flow field of a conical burner similar to present one. They also observed that steady RANS, employing the k-ϵ model, is not able to reproduce the level of turbulence correctly; in particular, it was underpredicted in the center of the flow.

Furthermore, the present simulations indicate that the flow field is, even if weakly, dependent on the fuel injection, as presented in Fig. 3.1.1, 3.1.2 and 3.1.3. Hence, the jet momentum induced by the fuel injection is able to influence the flow field. For $\beta = 0.0$ and 1.0, it leads to an increase of azimuthal momentum, which increases the recirculation

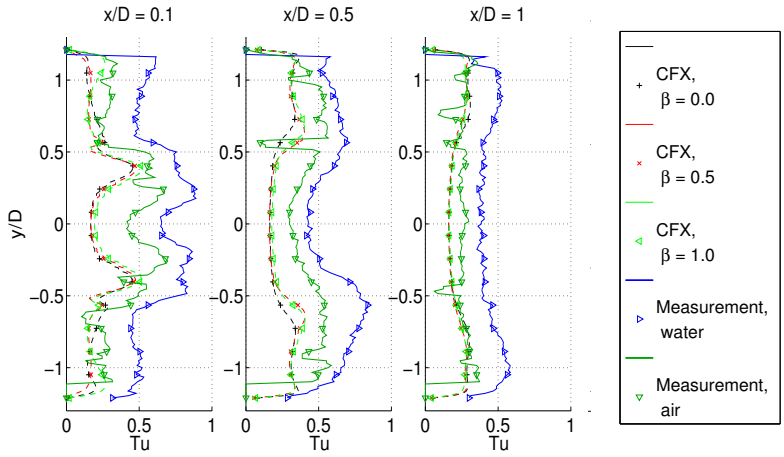

Figure 3.1.3.: Intensity of turbulence, cold case, simulation data for different axial positions and β; measurements for different axial positions, performed w/o injection.

zone size close to the burner outlet. At $\beta = 0.0$ this effect is more distinct since the fuel is injected downstream and therefore closer to the burner exit.

3.1.2. Mixing quality

The mixing quality of the burner is determined by a parameter describing the unmixedness of one substance (here: fuel) within another (here: air) which is defined as (Danckwerts 1952)

$$U = \frac{\sigma^2}{\overline{C}(1-\overline{C})}, \tag{3.1.3}$$

where σ^2 is the total variance of the volumetric fuel concentration and $\overline{C}$ denotes the mean fuel concentration. $\overline{C}(1-\overline{C})$ represents the maximum variance of the fuel concentration. The unmixedness can be determined for temporal as well as spatial dependencies, referred to as U_t and U_x. Since the studies in this chapter were performed with steady RANS we will only evaluate the spatial unmixedness U_x.

The unmixedness was calculated for three different axial positions, x = -24.9 mm, 5 mm and 19 mm. To only simulate the unmixedness of the mixture reaching the flame from the inlet and to exclude the backflow, the results were evaluated according to the measures given in Fig. 3.1.4; values within the half circles excluding the inner circle were used for the determination of U_x.

Fuel concentrations on the radial plane at $x = 5$ mm are given for three different values of *beta*, $\beta = 0.0$, 0.5 and 1.0, for simulations and measurements in Fig. 3.1.5 and Fig. 3.1.6, respectively. The figures further show the frequency distributions (histograms) of the concentrations. The concentration fields of the simulations are qualitatively and quantitatively in good agreement with measurements. For both, measurements and simulations, the variances of the histograms are smallest for $\beta = 0.5$. This indicates that mixing is better for $\beta = 0.5$ than for $\beta = 0.0$ and 1.0. The histograms of simulations and measurements display similar shapes of the distributions, especially for $\beta = 0.0$ and 0.5. For $\beta = 1.0$ the variance

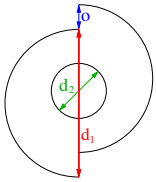

plane	d_1/mm	d_2/mm	o/mm
-24.9 mm	70.9	27.3	13.5
5 mm	91.7	34.166	6.59
19 mm	120	40	0

Figure 3.1.4.: Measures to evaluate the concentration in radial planes at different axial positions.

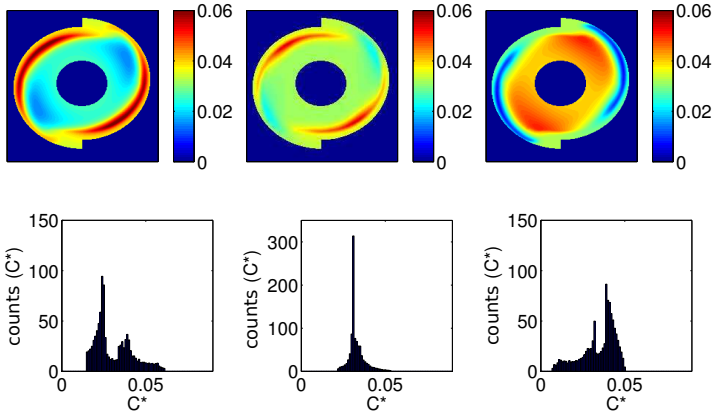

Figure 3.1.5.: Concentrations of fuel and their histograms from simulations in an axial plane at $x = 5$ mm, left: $\beta = 0.0$, middle: $\beta = 0.5$, right: $\beta = 1.0$.

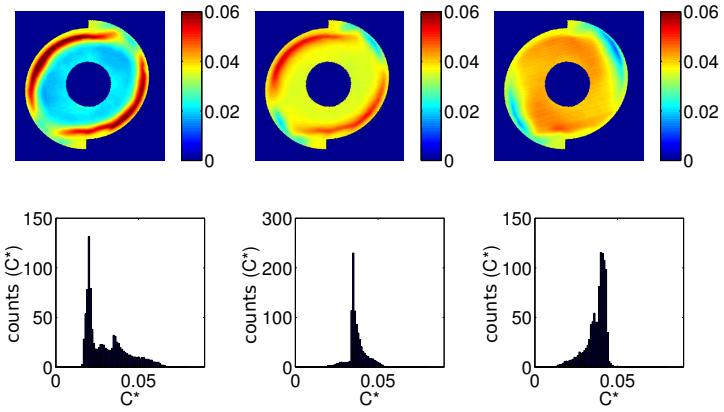

Figure 3.1.6.: Temporal averaged concentrations of fuel and their spatial histograms from measurements in an axial plane at $x = 5\,\text{mm}$, left: $\beta = 0.0$, middle: $\beta = 0.5$, right: $\beta = 1.0$.

in the concentrations is higher for the simulation results, indicating that the quality of mixing is underpredicted by the CFD for this injection case.

Figure 3.1.7 shows the spatial unmixedness depending on the axial position for different values of β ($\beta = 0.0$, 0.5 and 1) whereas Figure 3.1.8 shows the spatial unmixedness depending on β for different axial positions ($x = 5\,\text{mm}$ and $19\,\text{mm}$). Both figures compare simulated and measured results. Qualitatively, the simulations show reasonable results

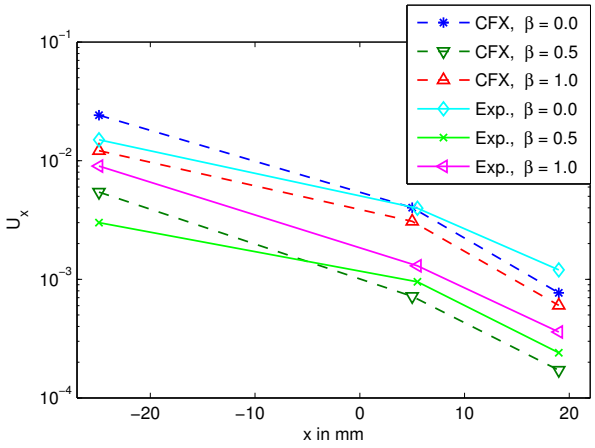

Figure 3.1.7.: Spatial unmixedness vs. x, measurement (solid) and simulation data (dashed) for different β.

predicting the decrease of the unmixedness in axial direction for all β (Fig. 3.1.7). The distribution of the unmixedness vs. β, fitted with a second-order polynomial, is very similar for measurements and simulations (Fig. 3.1.8). Quantitatively, we can observe from both figures that the values of the unmixedness determined from the simulations are very close to those of the measurements for axial positions $x = 5$ and 19 mm except for $\beta = 1.0$.

Generally, the mixing quality increases for more homogeneous ratios of upstream to downstream injection and also for larger time delays from the injection point to the monitor plane. Therefore, the best mixing quality establishes at $\beta \approx 0.7$, displayed by experimental and numerical data. This behavior is also consistent with the smaller variances for $\beta = 0.5$ compared to $\beta = 0.0$ and 1.0 depicted in Fig. 3.1.5 and 3.1.6.

Summing up, the cold case studies in water indicate that the steady RANS simulations are able to predict the qualitative as well as quantitative mixing behavior of the burner for various distributions of fuel injection using a turbulent Schmidt number of 0.2.

3.2. Reacting flow investigations

As the mixing was optimized for $\mathrm{Sc}_t = 0.2$, the reacting flow simulations were performed with the same turbulent Schmidt number. In addition, the influence of varying turbulent Schmidt/Prandtl numbers (0.55, 0.9) on flame shape and position is investigated.

3.2.1. Flow field validation

For the reacting case we compare simulation and experimental results for $\beta = 0.0$ and 0.5. In addition, we show results from a measurement with $\beta = 0.75$ where the flame is, in contrast to the other two cases, anchored within the burner cone. The resulting flow fields are similar for injection cases with $\beta > 0.75$. Computed flow field properties are given for $\beta = 1.0$.

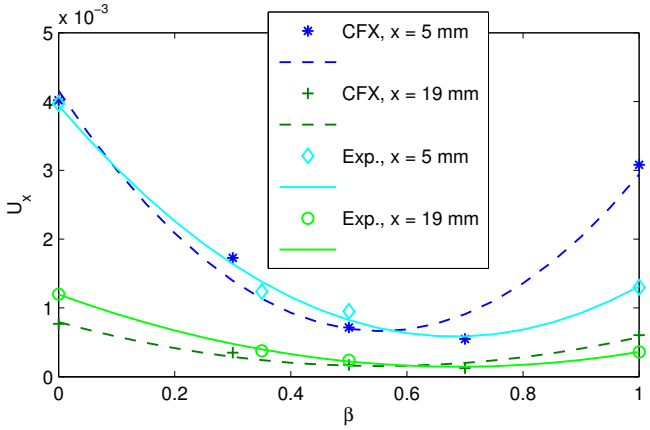

Figure 3.1.8.: Spatial unmixedness vs. β, measurement (solid) and simulation data (dashed) for different axial positions with fitted second-order polynomials.

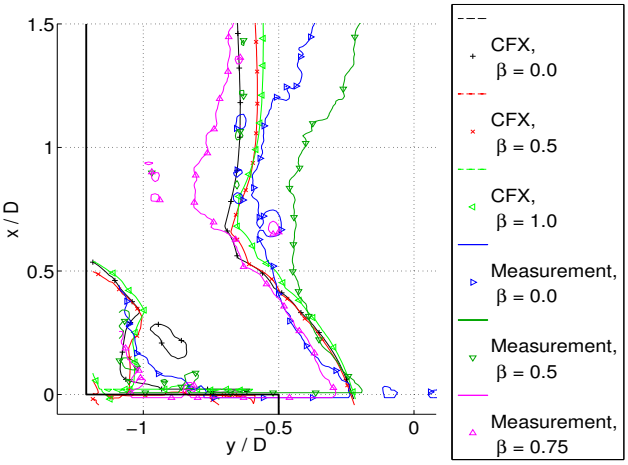

Figure 3.2.1.: Isolines of axial velocity $u = 0$, reacting case, measurement and simulation data for different β.

Figure 3.2.1 shows a comparison of the measured and simulated recirculation zones, and Fig. 3.2.2 and Fig. 3.2.3 show the axial u and radial v velocity components for the reacting case. The distributions of the velocity components are qualitatively in best agreement for $x/D = 0.1$ and 0.5, although the maxima of the simulated axial velocity compared to the measured results are higher and located closer to the center for $x/D = 0.1$ (Fig. 3.2.2 and 3.2.3). At this location the absolute values of u are overpredicted by the simulations.

The strong dependence of the boundaries of the recirculation zone on the fuel distribution observed in the measurements is not reproduced by the simulations, see Fig. 3.2.1. The velocity field and the flame are influencing each other. Since the flame changes its shape and position for different β, the velocity distribution and therefore the recirculation zone changes as well. As the computed boundaries of the recirculation zone do not change as much with β as in the experiment, it can be assumed that the computed flame shapes and

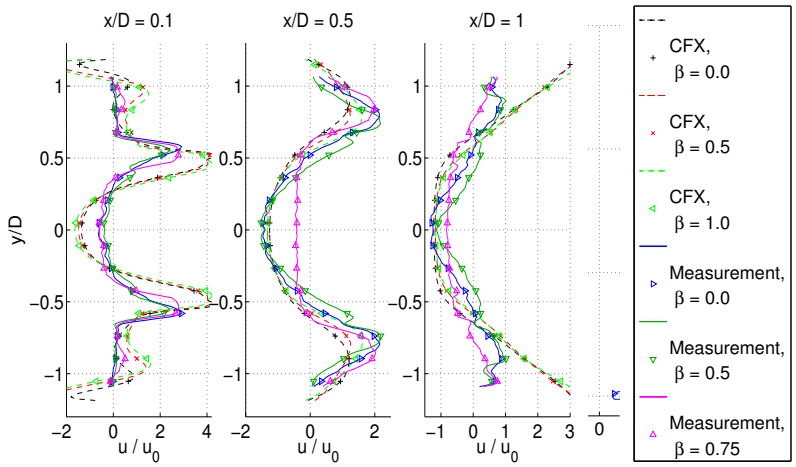

Figure 3.2.2.: Axial velocity, reacting case, measurement and simulation data for different axial positions and β.

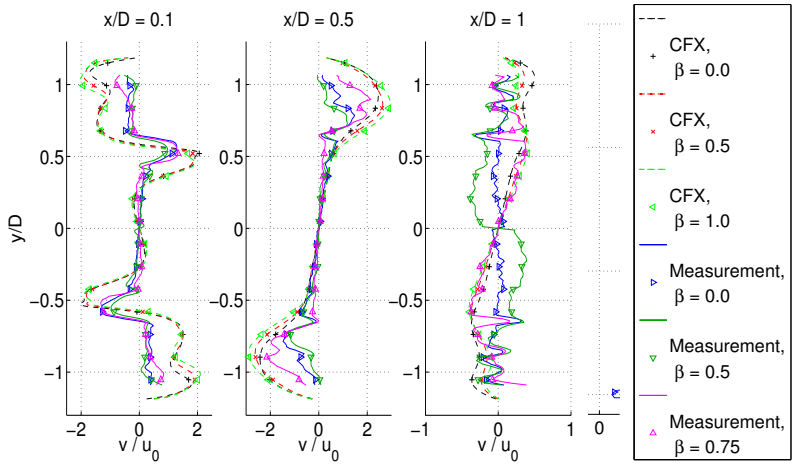

Figure 3.2.3.: Radial velocity, reacting case, measurement and simulation data for different axial positions and β.

positions will be less affected by various fuel injections than in the experiment, too. The interaction of flame and velocity field will be further discussed in the next section.

3.2.2. Flame shape and position

OH*-chemiluminescence from measurements is compared to reaction rates from CFD calculations. This is meaningful as excited OH radicals are formed in zones where the reaction rate is high (Güthe et al. 2006). However, one has to be aware of the limitations of this comparison since OH*-chemiluminescence and the reaction rate are not identical (for a more detailed discussion see Section 8.1).

In order to directly compare the CFD results with the experimental results, we used a method to generate CFD figures corresponding to projections of the flame from the same angle as the OH* images. We therefore rotated the flow field and integrated the reaction

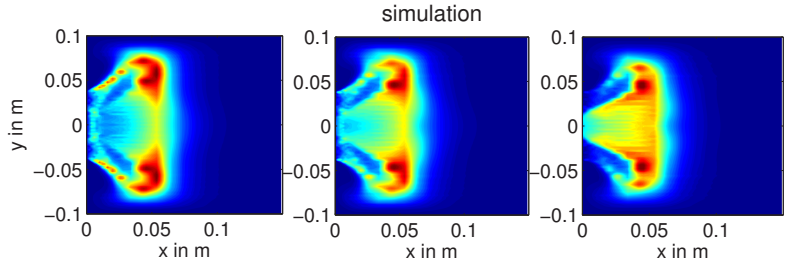

Figure 3.2.4.: Reaction rates from simulations, left $\beta = 0.1$, middle: $\beta = 0.5$, right:$\beta = 0.9$, view point: 45°, global color scale.

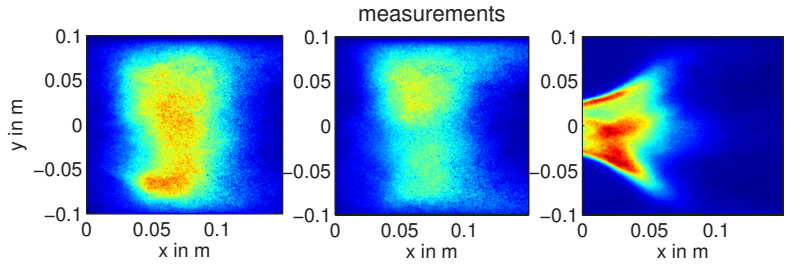

Figure 3.2.5.: Measured OH* intensities, left $\beta = 0.1$, middle: $\beta = 0.5$, right:$\beta = 0.9$, view point: 45°, global color scale.

rates along the radial axis. This implies parallel lines of view from the imaginary view point to the regarded domain which is a good approximation since the distance between camera and combustion chamber in the experimental setup was sufficiently large.

Figures 3.2.4 and 3.2.5 present the comparison of the flame images for $\beta = 0.1$, 0.5 and 0.9 from left to right for simulations and measurements. One global color scale is used for each the experimental and the numerical results. Dark blue represents zero and red the highest values. The burner exit is placed at $x = 0\,\mathrm{m}$.

For both, measurements and simulations, the flame shape changes with different β. The measured OH*-intensities show that the flame is wide spread and completely lifted from the burner for $\beta = 0.1$ and 0.5 while it is more compact and positioned inside the burner cone for $\beta = 0.9$. The intensity is highest for $\beta = 0.9$. The simulated reaction rate shows the tendency that the flame becomes more compact for larger β as well, although the flame is never completely lifted from the burner exit, and the flame shape does not change as much as seen in the experimental results. While the OH*-intensity is quite uniformly distributed in radial direction for low β, the reaction rate images feature distinct maxima in the outer regions of the flame. However, measurements with larger equivalence ratios (not shown here) show the two radial maxima depicted by the simulations, too.

Regarding the simulated flame from a viewpoint which is rotated by 90°, Fig. 3.2.6, the flame exhibits a different shape, with the maxima closer to the axis. The highly three dimensional shape of the flame agrees with experimental observations.

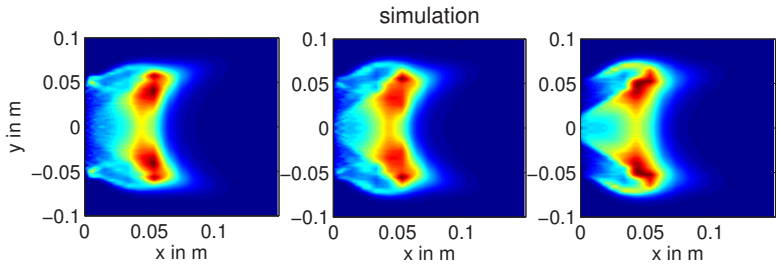

Figure 3.2.6.: Reaction rates from simulations, left: $\beta = 0.1$, middle: $\beta = 0.5$, right: $\beta = 0.9$, view point: $-45°$, global color scale.

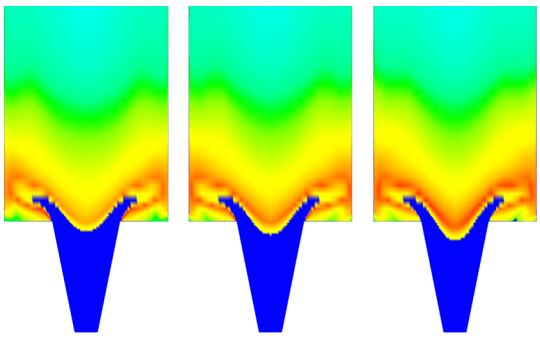

Figure 3.2.7.: Numerical simulation of reaction rate in xy-plane, left: $\beta = 0.0$, middle: $\beta = 0.5$, right: $\beta = 1.0$, view point: $0°$, $\mathrm{Sc}_t = \mathrm{Pr}_t = 0.2$.

Impact of $\mathrm{Sc}_t/\mathrm{Pr}_t$ on flame shape and position

Figure 3.2.7 shows the simulated reaction rates in the xy-plane for $\beta = 0.0$, 0.5 and 1.0 for $\mathrm{Sc}_t = \mathrm{Pr}_t = 0.2$ whereas Fig. 3.2.8 shows the reaction rate for $\mathrm{Sc}_t = \mathrm{Pr}_t = 0.9$ which corresponds to the standard CFX settings. Comparing the two figures we observe that the turbulent Schmidt respectively Prandtl number has a huge impact on the flame anchoring point. The flame is never anchored in the burner for the first case but always for the second. Besides, the reaction zone is much more compact in axial direction for $\mathrm{Sc}_t = \mathrm{Pr}_t = 0.2$ than for $\mathrm{Sc}_t = \mathrm{Pr}_t = 0.9$. This is most likely caused by the better and therefore more homogeneous mixing for $\mathrm{Sc}_t = 0.2$. The simulations with $\mathrm{Sc}_t = \mathrm{Pr}_t = 0.2$ are optimized for mixing determination. To optimize the simulations with respect to Sc_t and Pr_t for combustion, we simulated the reacting flow for turbulent Schmidt and Prandtl numbers of 0.55; the results are shown in Fig. 3.2.9. For this case the flame is positioned outside the burner for $\beta = 0$ and moves inside the burner for increasing β until it is completely anchored within the burner for $\beta = 1$. This behavior shows that the flame anchoring location strongly depends on turbulent Schmidt and Prandtl numbers and that it is possible to determine the flame shifting observed from experiments adapting these parameters.

Regarding the projection of the simulated flame for $\mathrm{Sc}_t = \mathrm{Pr}_t = 0.55$ in Fig. 3.2.10, the differences in flame shape for varying β are much more distinct than for $\mathrm{Sc}_t = \mathrm{Pr}_t = 0.2$. The flame features similar behavior as the experimental counterpart; it is wide spread for $\beta = 0.0$ and 0.5 and very compact and closer to the burner exit for $\beta = 1.0$.

In order to predict the flame position, the OH*-intensities and the reaction rates were

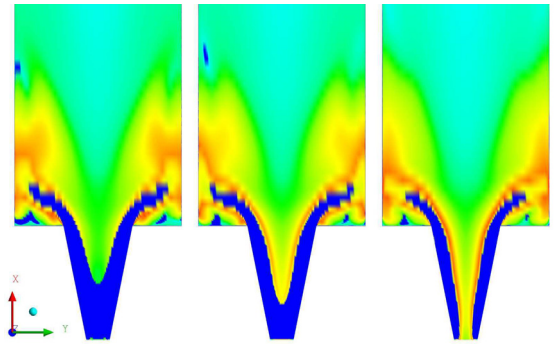

Figure 3.2.8.: Numerical simulation of reaction rate in xy-plane, left: $\beta = 0.0$, middle: $\beta = 0.5$, right: $\beta = 1.0$, view point: 0°, $\mathrm{Sc}_t = \mathrm{Pr}_t = 0.9$.

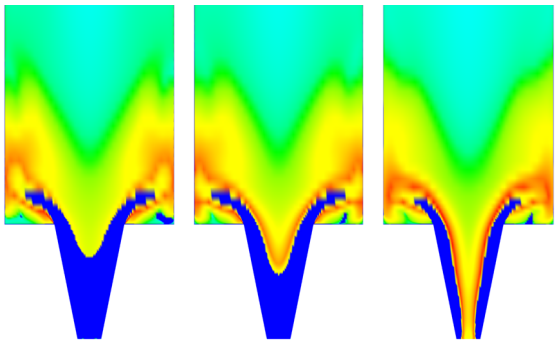

Figure 3.2.9.: Numerical simulation of reaction rate in xy-plane, left: $\beta = 0.0$, middle: $\beta = 0.5$, right: $\beta = 1.0$, view point: 0°, $\mathrm{Sc}_t = \mathrm{Pr}_t = 0.55$.

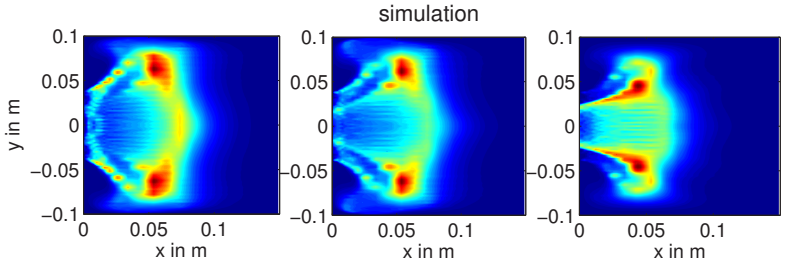

Figure 3.2.10.: Numerical simulation of reaction rate, left: $\beta = 0.0$, middle: $\beta = 0.5$, right: $\beta = 1.0$, view point: 45°, $\mathrm{Sc}_t = \mathrm{Pr}_t = 0.55$.

integrated perpendicular to the axial direction. The flame position was then assumed to be at the maximum of the integral value. The integrated intensities and reaction rates as a function of the axial position are shown in Fig. 3.2.11 for different values of β. For measurements the shape of the distributions is similar for $\beta = 0.1$ to 0.7. For $\beta = 0.9$ the amplitude gets larger and the maximum is clearly shifted in upstream direction. For simulations with $\mathrm{Sc}_t = \mathrm{Pr}_t = 0.2$ the distributions are alike for all β. For simulations with $\mathrm{Sc}_t = \mathrm{Pr}_t = 0.55$, however, we can observe a change in the distributions. The maximum moves in upstream direction with increasing β, particularly strong between $\beta = 0.7$ and 1.0. The growth in amplitude seen from experiments cannot be reproduced.

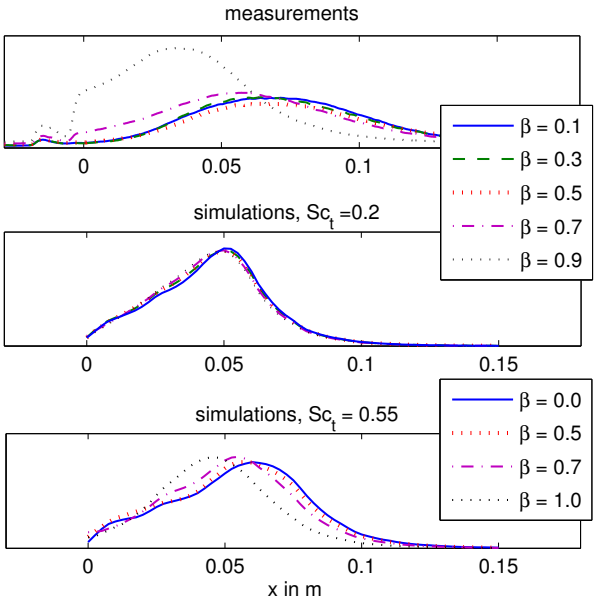

Figure 3.2.11.: Integral values of OH*-intensities (measurement) and reaction rate (simulation) for different values of β.

The axial extent of the reaction zones determined from measurements is, in general, larger than that determined from simulations. However, this could partly result from the differences in OH*-chemiluminescence and reaction rates.

Regarding the flame positions given in Fig. 3.2.12 it can be assessed from experimental results that for values of β smaller than 0.8 the flame remains more or less at the same position ($0.6 < x < 0.7$). For $\beta = 0.8$, it is shifted in upstream direction. The flame position determined from simulations with $\mathrm{Sc}_t = \mathrm{Pr}_t = 0.2$ lies around $x = 0.5$ for all β. The movement of the flame in upstream direction cannot be predicted here. For $\mathrm{Sc}_t = \mathrm{Pr}_t = 0.55$ the characteristics of flame shifting can be determined by CFD although it is weaker than observed in the experiment.

We observed from measurements that the fuel staging parameter at which the flame anchoring point moves into the burner cone can vary but always lies within $\beta = 0.65$ and 0.8. These values concur with fuel distributions of best mixing quality, which lies around $\beta = 0.7$ (Fig. 3.1.8). The flame shifting in upstream direction is most likely governed by the mixing quality, which increases, in combination with the fuel injection position, which moves further upstream with β.

As already mentioned, the flow fields determined from experimental investigations are highly dependent on the fuel injection position. For $\beta = 0.0$ and 0.5, where the flame position is outside the burner, the recirculation zones are significantly smaller in radial as well as axial direction than for $\beta = 0.75$. The differences in the velocity fields of these two cases could result from differences in flame shape which could arise from a rotation of the flame with β. This in turn could be influenced by the differing mixing characteristics. However, it is hard to draw any further conclusions without having more detailed insight into the 3D flow field and flame shape.

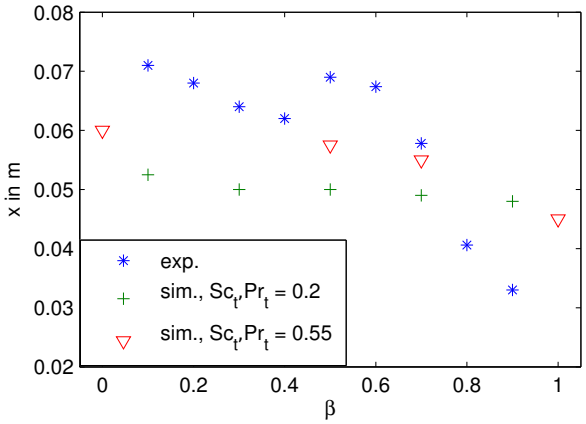

Figure 3.2.12.: Flame positions depending on β from experimental and numerical investigations.

The inability of the simulations to reproduce the interaction of flow field and flame behavior may be due to both insufficiency in turbulence and combustion modeling. Biagioli (2006) compared the flame positions for different equivalence ratios from CFD simulations and Güthe et al. (2006) compared the flame shapes computed with steady RANS for different burner variants with measured OH*-chemiluminescence images. They both observed that the flame simulated by steady RANS is anchored in the burner for all investigated configurations. Güthe et al. also observed that the flame shape remains similar in contradiction to experimental findings. They explained this behavior with the insufficiency of steady RANS to model the flow properties especially the strongly swirling flow field sufficiently accurate. They suggest that the flame position is mainly governed by the flow field and not the reactivity or fuel injection. Biagioli further concludes that RANS methods do not predict the distribution of the rate at which reactants are radially fed into the flame well. He states that this situation makes the flame quickly move inside the burner, driven by the excess of turbulent consumption rate over reactant feeding rate.

Considering the results from the flow field studies and from the investigations of flame shape and position, we can assume that the explanations found by Güthe et al. (2006) partly apply here as well. We also obtain similar flow fields for all considered cases, and the flame shapes and position vary though not as much as observed from measurements; nevertheless, we could reproduce the flame shifting. For our investigations with a turbulent Schmidt number of 0.2 and 0.55 Biagioli's (Biagioli 2006) statement does not entirely apply as the flame is not always anchored in the burner cone. However, the flame is positioned closer to the burner exit than the measured one and therefore the described phenomenon could, even though weaker, appear here as well.

Furthermore, we could show that the flame characteristics are not only governed by the flow field, which does not change much with varying injection configurations in our simulations, but are also strongly dependent on the turbulent Schmidt and Prandtl numbers, which affect the mixing quality and the heat transfer, respectively. This behavior clearly manifests the importance of suitable turbulence and combustion models and indicates a close interaction of mixing (molecular and turbulent) and combustion. In strongly turbu-

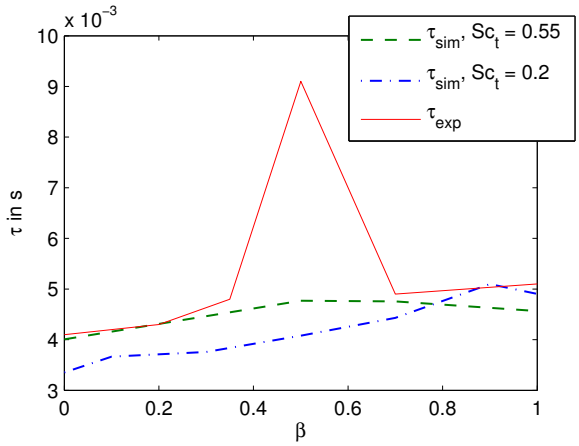

Figure 3.2.13.: Comparison of time delays for varying β.

lent lean premixed flames within the corrugated flamelet / thin reaction zones combustion regimes, this interaction may occur at very small scales and is therefore difficult to model. In Part II and Part IV we make an effort of including these characteristics in our studies by employing the Linear Eddy Model.

3.2.3. Time delays

The convective time delays were determined from reacting CFD as the time a fluid element needs to travel from the fuel inlet to the flame. We only considered streamlines reaching the flame from the upstream direction avoiding to include the flow recirculating back to it. The flame position was defined in terms of a progress variable at a value of 0.5. The progress variable was calculated from the temperature according to

$$c = \frac{T - T_{\min}}{T_{\max} - T_{\min}}. \tag{3.2.1}$$

Experimental data on time delays was gathered in the combustion lab from measurements of the flame transfer function for varying β (Lacarelle et al. 2009*a*). The time delays were then determined from the phase of the transfer function in the range of 0 to 150 Hz. In both cases, experimental and numerical, the determined time delays are estimated time-averaged values. Figure 3.2.13 shows the comparison of the time delays from measurements and simulations.

The time delays determined from measurements remain at an almost constant level for $\beta = 0 - 0.35$. At $\beta = 0.5$ the time delays reach their maximum which is about a factor of two higher than for the other cases. The time delay for the standard burner injection configuration under same conditions is approximately 9 ms and similar to the $\beta = 0.5$ case. The increase in time delay is due to the combination of low injection momentum as the fuel is distributed over all (upstream and downstream) injection holes and downstream stabilization of the flame. For $\beta = 0.7$ and 1 the time delays are smaller which is caused by the flame moving upstream into the burner and the higher fuel momentum. Due to the inability of reproducing the flame position correctly, the time delays determined from CFD

using a turbulent Schmidt respectively Prandtl number of 0.2 increase steadily with β and do not show the variance observed in the experimental results. For $\mathrm{Sc}_t = \mathrm{Pr}_t = 0.55$ the trend that the time delay is highest for $\beta = 0.5$ can be captured but the absolute value at this fuel injection configuration is much lower than the measured one. The differences in the computed time delays are not as distinct as in the experiment since there is also less variance in flame position. Quantitatively, the values of the time delays determined from simulations agree well with those of the measurements, except for $\beta = 0.5$.

From the experimental results we can conclude that the investigated fuel staging allows to decrease the convective time delay by a factor of two without a major change in mixing quality.

3.3. Conclusion

In this chapter we investigated the feasibility of steady RANS simulations to predict the mixing quality as well as the flame positions and shapes and the convective time delays of a swirl burner for different fuel injection configurations. The mixing quality was determined from cold flow simulations using water, and the flame position and shape as well as the time delays were computed for reacting flow with air and methane. The results were compared to measurements from water and combustion test rigs.

Simulations of the flow field are qualitatively similar to the experimental data, but are not satisfactory on a quantitative basis. Nevertheless, the studies on mixing quality show that steady RANS is capable of reproducing the influence of the fuel distribution on the mixing quality when a turbulent Schmidt number of 0.2 is used. Absolute values for the unmixedness downstream of the burner exit agree for simulations and measurements and predict the best mixing quality for a fuel distribution corresponding to $\beta \approx 0.7$.

Flame shape and position can be qualitatively well predicted by the simulations using a turbulent Schmidt/Prandtl number of 0.55. Experimental investigations show a flame which is lifted from the burner and widespread for fuel distributions with low upstream percentage and a flame which is anchored inside the burner and more compact for fuel distributions with high upstream percentage. The simulated flames show a similar behavior, although the characteristics and variances are not as distinct as observed in the measurements. Since the flame position cannot be predicted accurately, the strong variance in time delays with changing fuel injection configuration is not reproduced by the simulations. However, qualitative trends agree.

Altogether, we could demonstrate that RANS in combinations with the EDM/FRCM combustion model is able to capture the mixing behavior and the qualitative flame characteristics of a swirl burner with fuel staging and is therefore applicable as a fast and cheap tool for parametric studies. In the future, it would be interesting to put further effort in the investigation of the flame shifting behavior with a more sophisticated combustion model. The Linear Eddy Model, which we employed for one-dimensional studies on the impact of fuel-air ratio inhomogeneities in Part II and as a subgrid model to study a turbulent bluff body flame in Part IV, appears to be a very promising tool.

4. Effect of periodical flow forcing on fuel-air mixing

Large coherent structures resulting from flow instabilities of the annular swirling jet and acoustic forcing lead to periodical oscillations of velocity and, in case of technical premixing, concentration profiles. In turn this results in fluctuations of heat release rate, which can excite acoustic modes of the combustor and thus may induce combustion instabilities. Different coherent structures have been identified in experimental and numerical studies of swirling flows (Panda & McLaughlin 1994, Syred 2006, Lucca-Negro & O'Doherty 2001, Wang & Yang 2005, Duwig et al. 2007). Most of these investigations revealed a helical mode, manifested as a precessing vortex core (PVC).

To avoid instabilities driven by coherent structures, it is essential to understand their generation mechanism as well as their evolution in the case of forced flows. The forcing applied in the current investigation approximates the impact of axial acoustic modes related to combustion instabilities on the flow field and mixing characteristics of the burner. Numerical simulations, URANS and LES, are employed for the investigations.

The objective of the present work is to understand the impact of strong forcing on the flow field and the mixing quality at the exit of a swirl burner and to examine the capability of unsteady RANS simulations and LES to capture these effects. The focus on mixing characteristics is chosen since the mixing quality directly influences the flame and has a strong effect on heat release dynamics as well as pollutant formation. The heat release rate fluctuations may then couple with the acoustic modes of the chamber promoting combustion instabilities.

The flow forcing for the underlying studies is applied at a frequency close to the natural frequency of the coherent structure. The investigations are conducted for cold flow conditions using water to represent air and fuel flows. First, the results for the flow and concentration fields obtained by measurements and simulations are shown. The calculated mean velocity fields are validated with measurements, and the influence of forcing is assessed. Subsequently, the mixing quality is determined by mean and rms concentration fields and their unmixedness. The unforced and forced flows are eventually characterized by proper orthogonal decomposition (POD).

4.1. Definition of the forcing amplitude

A local definition of the forcing amplitude F_a was chosen. It was constructed using the ratio of the fundamental amplitude of the azimuthal velocity to its mean value at an arbitrarily

chosen position in the slot of the burner:

$$F_a = \frac{|\tilde{u}_t|}{\overline{u}_t}. \tag{4.1.1}$$

With this definition, the forcing amplitude for the given Strouhal number St ≈ 1 was found to be $F_a = 0.5$. The velocity at the "air"-inlet for the simulations with forcing was then set to $u_{\text{in}} = \overline{u}_{\text{in}}(1 + F_a \sin \omega t)$, where ω describes the angular frequency. The corresponding forcing Strouhal number St was based on the forcing frequency f, the burner outlet diameter D, and the mean bulk velocity U_0 based on this diameter (St $= \frac{fD}{U_0}$).

4.2. Forcing frequency

The present cold flow investigations of a swirl burner were conducted for unforced boundary conditions and for forcing close to the natural frequency at St $= 1$. Figure 4.2.1 shows a discrete Fourier transform of spatially averaged "fuel" concentration fluctuations in the crossflow half-plane shortly downstream of the burner outlet ($x/D = 0.1$). The simulations show peak frequencies close to a Strouhal number St $= 1$ for the unforced and forced cases, confirming the forcing close to the natural frequency. The large eddy and URANS simulations are able to capture the frequency of the coherent flow structure that was observed in the measurements (Lacarelle et al. 2009*c*). In the unforced case, this corresponds to a helical structure as will be shown by applying proper orthogonal decomposition in Section 4.5.

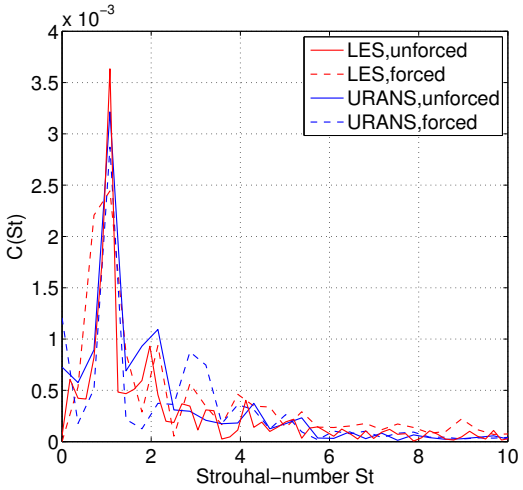

Figure 4.2.1.: Amplitude spectrum of the "fuel" concentration averaged in the crossflow-half-plane 5 mm downstream of the burner exit.

4.3. Flow field

The unforced flow field downstream of the burner in the combustion chamber was measured by PIV in the water test rig. The measurement plane was located in the slot cross section (xz-plane) of the burner. The measurements were taken to validate the CFD results. Furthermore, the simulated velocity distributions of the unforced and forced cases are compared.

All resulting mean velocities are normalized with the mean bulk velocity based on the burner hydraulic diameter; axial and radial positions are normalized with the burner diameter. The burner exit is located at $x = 0\,\mathrm{m}$. The turbulence intensity Tu is calculated from the turbulent kinetic energy k for URANS simulations and from the radial, axial (and tangential) velocity components for LES and experiments:

$$\mathrm{Tu}_{\mathrm{URANS}} = \frac{\sqrt{\frac{2}{3}k}}{U_0}, \tag{4.3.1}$$

$$\mathrm{Tu}_{\mathrm{LES}} = \frac{\sqrt{\frac{1}{3}(\overline{u'^2} + \overline{v'^2} + \overline{w'^2})}}{U_0}, \tag{4.3.2}$$

$$\mathrm{Tu}_{\mathrm{exp}} = \frac{\sqrt{\frac{1}{3}(2\overline{u'^2} + \overline{v'^2})}}{U_0}, \tag{4.3.3}$$

where U_0 denotes the mean velocity at the burner exit. As the measurements only provide two dimensional results, it is assumed that the azimuthal velocity rms is similar to the axial velocity rms. This assumption was confirmed by comparing Tu calculated from radial and axial velocity fluctuations only and from all three velocity components for the LES results.

Figures 4.3.1 and 4.3.2 show averaged axial (u) and radial (v) velocities, and Fig. 4.3.3 shows the turbulence intensity Tu at different axial positions. A comparison of the computed and measured backflow regions is given in Fig. 4.3.4. The boundaries of the backflow region are defined by isolines of the axial velocity satisfying $u = 0$. For the unforced case, the simulations, LES as well as URANS, predict the axial and radial velocity distributions downstream of the burner exit in satisfactory agreement with the measurements. Generally, the LES results are closer to the experimental results. Regarding the regions of reverse flow in Fig. 4.3.4, it can be observed that the inner backflow region obtained from URANS for the unforced case has a too low radial extent for x/D larger than 0.5. The shape of the outer backflow region is not well recovered by the simulation. The LES in contrast reproduces the inner and outer regions of reverse flow quite well. The turbulence intensity calculated from URANS underestimates the measured one but shows qualitatively similar distributions (Fig. 4.3.3). Flohr et al. (2002) investigated the flow field of a conical burner similar to the present one with CFD. They also found that RANS is not able to reproduce the level of turbulence correctly. The LES shows good agreement with measurements for the turbulence intensity although it is slightly underpredicted in the whole domain. Stronger discrepancies occur in the outer backflow region for an axial position $x/D = 0.1$. In addition to numerical shortcomings, this discrepancy could be related to experimental uncertainties due to difficult measurement conditions close to the wall caused by reflections from the glass cylinder.

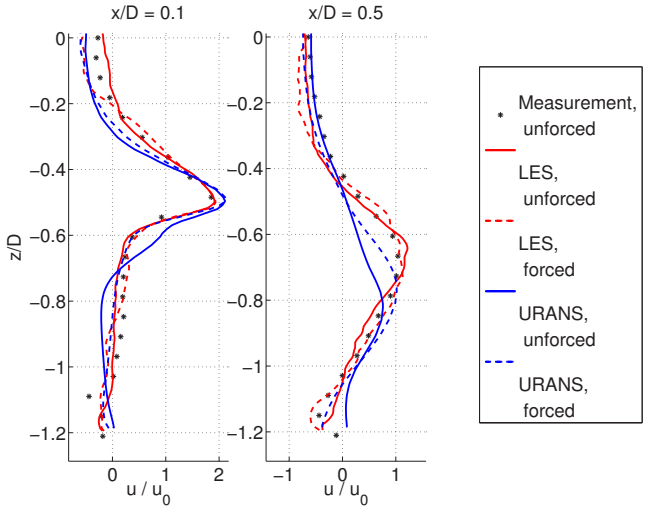

Figure 4.3.1.: Mean profiles of the axial velocity (u) for different axial positions.

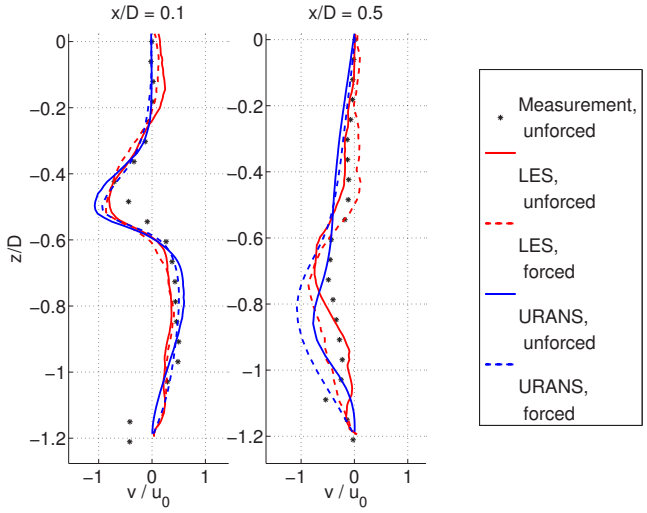

Figure 4.3.2.: Mean profiles of the radial velocity (v) for different axial positions.

A comparison of the unforced with the forced distributions indicates that the forcing has a negligible impact on the mean velocity field at the burner outlet. The LES results show that the extension of the inner recirculation zone slightly shrinks when forcing is applied, and the axial velocity on the centerline near the burner outlet decreases a little. Besides these minor changes, the mean flow field remains mostly unaffected. This is in agreement with measurements conducted with the same burner but unconfined boundaries by Lacarelle et al. (2009*c*).

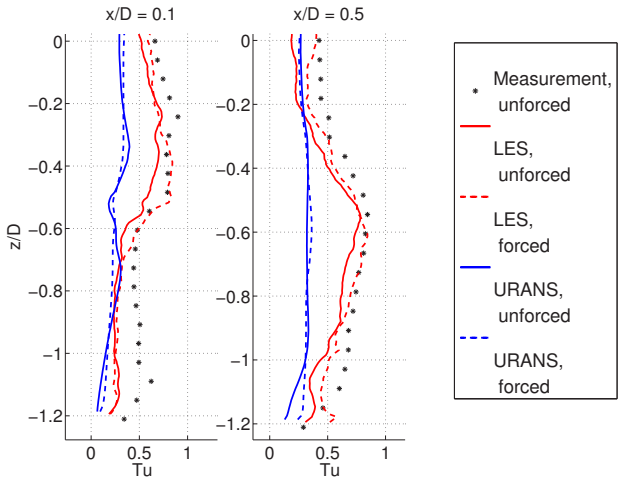

Figure 4.3.3.: Turbulence intensity for different axial positions.

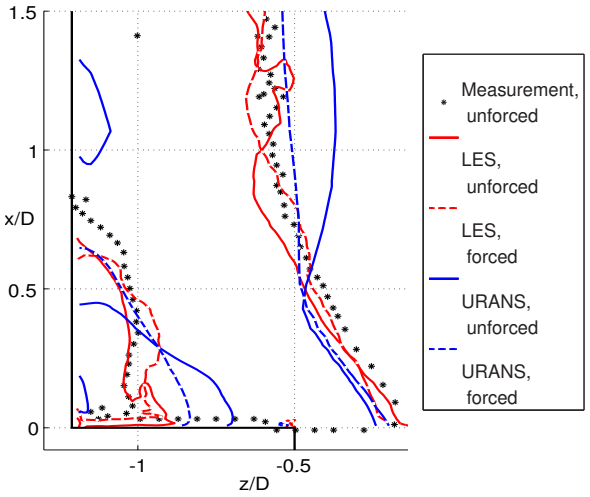

Figure 4.3.4.: Region of reverse flow defined by isolines of axial velocity $u = 0$.

4.4. Mixing quality

The mixing quality of the burner was evaluated on the basis of the spatial unmixedness, as in Section 3.1.2.

Before considering the unmixedness, the mean and rms fuel concentrations in the cross-flow plane at $x = 5\,\text{mm}$ are examined, comparing the unforced and forced cases given in Fig. 4.4.1, Fig. 4.4.2, and Fig. 4.4.3, for measurements, LES, and URANS respectively. Figure 4.4.4 displays the spatial probability density function in the same plane for the mean and rms concentrations.

The mean fuel concentrations determined by the simulations are in good qualitative agree-

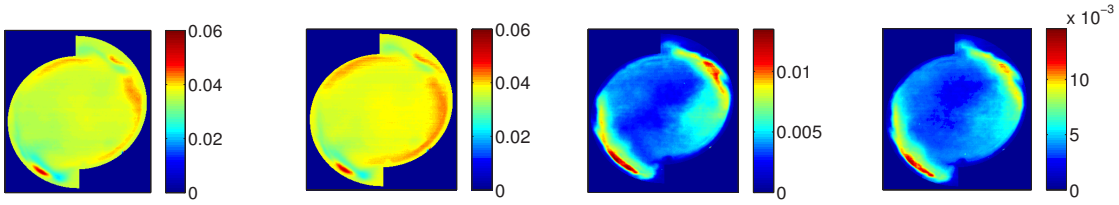

(a) C_{mean}, unforced (b) C_{mean}, forced, St=1 (c) C_{rms}, unforced (d) C_{rms}, forced, St=1

Figure 4.4.1.: Mean and RMS fuel concentration fields in the crossflow plane 5 mm downstream of the burner exit for unforced and forced (St = 1) cases; experimental results.

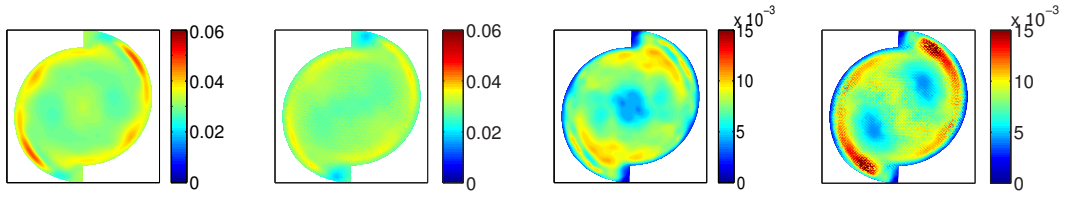

(a) C_{mean}, unforced (b) C_{mean}, forced, St=1 (c) C_{rms}, unforced (d) C_{rms}, forced, St=1

Figure 4.4.2.: Mean and RMS fuel concentration fields in the crossflow plane 5 mm downstream of the burner exit for unforced and forced (St = 1) cases; LES results.

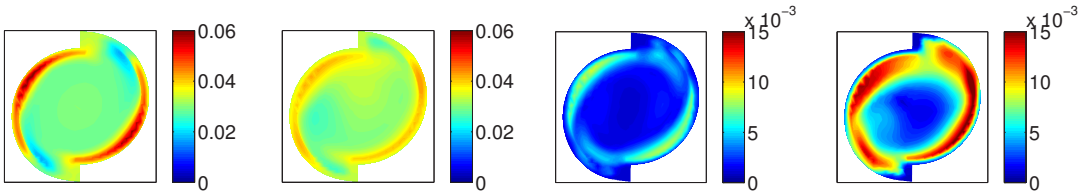

(a) C_{mean}, unforced (b) C_{mean}, forced, St=1 (c) C_{rms}, unforced (d) C_{rms}, forced, St=1

Figure 4.4.3.: Mean and RMS fuel concentration fields in the crossflow plane 5 mm downstream of the burner exit for unforced and forced (St = 1) cases; URANS results.

ment with the measurements, although quantitatively, the measurements show a slightly more homogeneous mean concentration field. This is also reflected in the probability distributions, which in case of the experiments exhibit less deviation from the peak concentration than the computational results. The measured mean peak concentration is slightly higher than the calculated ones. Both measurements and simulations predict a slightly higher peak concentration for the case with forcing at the natural frequency. With forcing, the simulations show furthermore a smaller deviation from the peak value, which is consistent with better mixing as will be discussed later again by considering the spatial unmixedness. The asymmetry in the measured mean concentration fields is caused by a slightly asymmetric "fuel"-injection. The previous studies in Chapter 3 showed that simulations are also

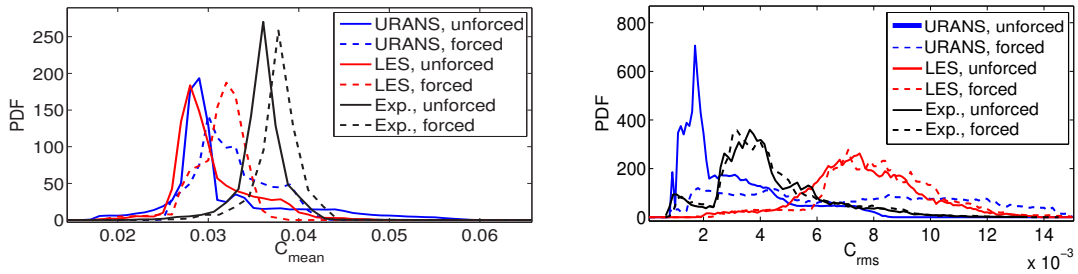

(a) PDF(C_{mean}) (b) PDF(C_{rms})

Figure 4.4.4.: Probability density functions for spatial mean (a) and rms (b) concentration distribution in the crossflow plane 5 mm downstream of the burner exit.

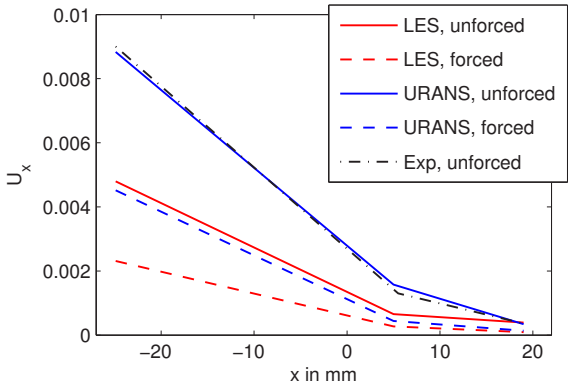

Figure 4.4.5.: Spatial unmixedness determined for different axial positions.

capable of capturing the mean concentration fields quantitatively well.

The rms fuel concentration fields are also qualitatively similar for measurements and simulations. Regarding the URANS simulations, there are quantitative discrepancies compared to the experimental data in the peak rms concentration in the probability distributions and the values in the inner region. This can be attributed to the non-resolved turbulent fluctuations which do not contribute to the rms in the simulations. The measured rms concentration fields are similar for the unforced and forced cases, whereas the URANS simulations show much higher rms concentrations in the outer region of the regarded plane with forcing. Apparently the forcing shows a stronger influence in this region than observed in the experiment. For the LES, the shapes of the probability distributions for the rms concentrations are in better agreement with the measurements than for the URANS simulations, although they are shifted to higher values of rms concentrations, and the deviations from the peak value are also higher. Furthermore, the rms concentration fields are quite similar for the unforced and forced cases, which agrees with the experimental findings; however, with forcing, higher rms concentration values in the peripheral region can be seen here as well.

The spatial unmixedness was calculated in planes at different axial positions $x = -24.9\,\mathrm{mm}$, 5 mm, and 19 mm (Fig. 4.4.5). The unforced simulation results are compared to unforced

measurements. Additionally, simulation results are shown for the forced case. The unmixedness determined from URANS simulations is qualitatively and quantitatively in very good agreement with the measurements. In Section 3.1.2 it was already shown that RANS simulations are able to quantitatively predict the spatial unmixedness using a value of 0.2 for the turbulent Schmidt number.

Forcing close to the natural frequency decreases the spatial unmixedness, implying improved spatial mixing. This is in agreement with cold flow measurements by Lacarelle et al. (2007) in the same water test-rig under similar conditions but different fuel injection configurations. The large eddy simulations show qualitatively the same trends but overpredict the mixing within the burner cone and at the burner exit. The decrease of spatial unmixedness with forcing is however captured by the LES.

4.5. Proper orthogonal decomposition

A low-dimensional characterization of the fluctuating concentration fields is obtained by proper orthogonal decomposition. POD decomposes the space and time dependent field into spatial modes and time-dependent Fourier coefficients. The decomposition represents the field in an optimally compact fashion in the sense that $\overline{\parallel C_{\text{fluc}}(\mathbf{x},t) - \sum_{j=1}^{N} a_j(t) C_j(\mathbf{x}) \parallel^2}$ is minimal for any N over the class of all orthonormal bases C_j. The fluctuating field is decomposed as follows:

$$C_{\text{fluc}}(\mathbf{x},t) \approx C_{\text{fluc}}^{(N)}(\mathbf{x},t) = \sum_{j=1}^{N} a_j(t) C_j(\mathbf{x}), \tag{4.5.1}$$

where N is the number of modes, C_j are the POD modes, and the mode coefficients are labeled a_j. The optimality condition leads to the following eigenproblem:

$$\int_{\Omega} \overline{C_{\text{fluc}}(\mathbf{x}) C_{\text{fluc}}(\mathbf{x}')} C_j(\mathbf{x}') d\mathbf{x}' = \lambda_j C_j(\mathbf{x}), \tag{4.5.2}$$

where Ω is the considered flow domain. The λ_j are the eigenvalues corresponding to the eigenfunctions C_j and $\overline{C_{\text{fluc}}(\mathbf{x}) C_{\text{fluc}}(\mathbf{x}')}$ is the two-point correlation. The eigenvalues λ_j can be interpreted as the contribution of mode j to the total fluctuation energy of the concentration field. The modes are ordered by decreasing energy contribution (optimality condition). The time coefficients can be obtained by taking the inner product with the corresponding mode

$$a_j(t) = \int_{\Omega} C_{\text{fluc}}(\mathbf{x},t) C_j(\mathbf{x}) d\mathbf{x}. \tag{4.5.3}$$

A full discussion of the POD framework may be found in Holmes et al. (1998).

Figure 4.5.1 shows the energy captured by the POD modes for the concentration in the crossflow plane at the burner exit in percent, comparing the unforced and forced cases. The first mode determined from URANS simulations for the unforced case carries approximately 65% of the energy, the first five modes more than 90%. The LES predicts a captured energy for the first mode of about 30%. POD analysis of measured velocity fields in the streamwise plane for the same burner but unconfined boundaries revealed that the first mode captures around 10% and the first five modes 25% of the energy (Lacarelle et al. 2009*c*). This

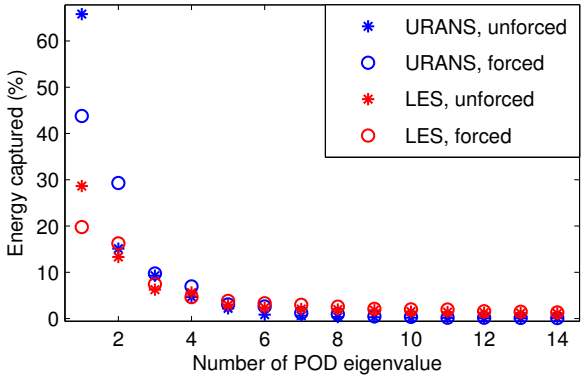

Figure 4.5.1.: Fluctuation energy captured by the POD modes for the concentration in the crossflow plane at the burner exit.

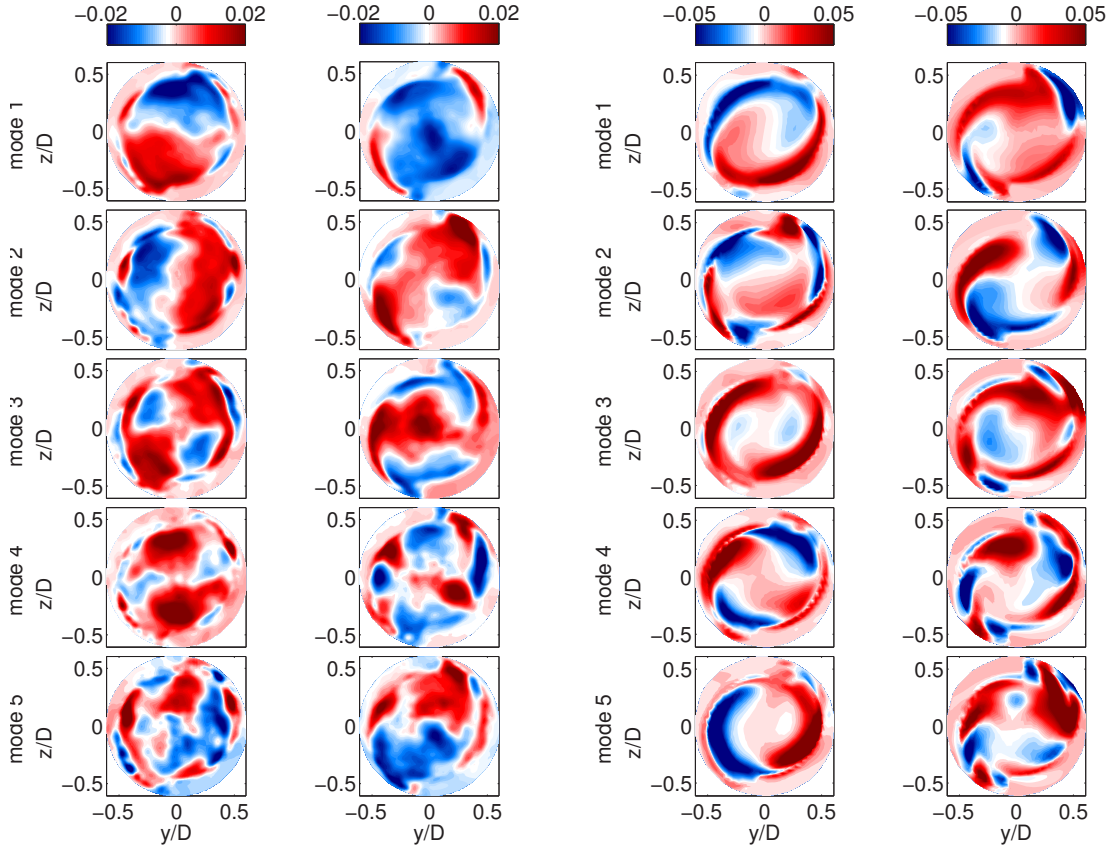

(a) LES, unforced (b) LES, St = 1 (c) URANS, unforced (d) URANS, St=1

Figure 4.5.2.: First five pod modes of "fuel"-concentration in the crossflow plane for unforced and forced (St = 1) cases. (a) & (b): LES; (c) & (d): URANS.

observation was also reproduced by Duwig et al. (2007) with large eddy simulations.

Moreover it has to be considered that the first two modes in the crossflow plane contain a significantly higher amount of energy (about twice) than the corresponding modes in the streamwise plane (Oberleithner et al. 2011). Taking this into account, the LES of the present investigations is able to reproduce the magnitude of the modal energy distribution quite accurately. The URANS simulation, however, is not capable of predicting the energy distribution of the POD modes, which is related to the inability of URANS to resolve detailed flow structures. Nevertheless URANS is able to reproduce the major modes in agreement with measurements and LES as was shown by Ferrand et al. (2006). Comparing the unforced and forced cases, a reduction of captured energy by the first POD mode can be observed whereas the second POD mode exhibits a higher energy content when forcing is applied. This characteristic is present in both URANS and LES results.

The studies of Oberleithner et al. (2011) on an unconfined swirling jet revealed that the first two spatial POD modes in the crossflow plane exhibit an antisymmetric shape describing a helical wave represented by a $\pi/2$ phase shift between the modes. Furthermore, they found that the fourth and fifth modes resemble one another, having a $\pi/4$ shift between them. The first two modes represent a traveling helical wave with azimuthal wavenumber $m = 1$, whereas the fourth and fifth modes represent a higher harmonic of the fundamental mode with an azimuthal wavenumber $m = 2$. The third POD mode features an axisymmetric structure, which Oberleithner et al. associated with axial fluctuations of the recirculation zone.

For the present studies, the first five spatial POD modes of the unforced case are displayed in Fig. 4.5.2(a) for LES and Fig. 4.5.2(c) for URANS. The first, third, and fourth mode, taking an $m = 1$, $m = 0$ and $m = 2$ shape, respectively, coincide with the findings of Oberleithner et al. The third mode, however, exhibits tendencies for an $m = 2$ shape, more pronounced in the LES results. For the URANS simulations, modes two and five do not resemble modes one and four. For LES the agreement is better; however, similar albeit weaker discrepancies than in the URANS POD can be observed. For the URANS simulations, the second POD mode features an $m = 3$ azimuthal wave. The fifth mode resembles an $m = 1$ structure but with much less energy captured than the first POD mode. The structures of all modes, particularly two and five, may originate from the interaction of the traveling helical wave and the flow through the two slots of the burner. This interaction also seems to affect the modal energy distribution. Generally, modes one and two form a pair and hold comparable amounts of energy (Oberleithner et al. 2011). The present investigations, in contrast, evidence a much higher amount of energy captured by POD mode one than two.

Addressing the forced cases in Fig. 4.5.2(b) for LES and Fig. 4.5.2(d) for URANS, it can be observed that the first POD mode changes its shape from an antisymmetric to a symmetric structure. Generally, one would expect to obtain an axisymmetric shape for mode one when harmonically forcing the axial flow with sufficiently high amplitudes (Lacarelle et al. 2009*c*, Iudiciani & Duwig 2011). The structures for the first POD modes which are present in the LES and URANS results for the forced case are governed by different effects.

First of all, a coupling of the axial flow forcing with the characteristic helical structure of the flow field takes place. The influence of the azimuthal wave decreases with increasing forcing amplitude, whereas the influence of the axial wave increases. Experimental and numerical investigations on swirl flames have shown that the axial forcing at high amplitudes generally tends to suppress the helical mode (Moeck et al. 2012, Iudiciani & Duwig 2011).

In the present case, a helical structure can still be observed in the first POD mode. This indicates that the forcing amplitude may not be sufficiently high to fully suppress the helical mode and evolve an axisymmetric structure.

Secondly, there is the impact of the two slots of the burner which was already held responsible for the anomalous structures in POD modes for the natural flow. The geometry of the double-cone burner investigated in the present work deviates significantly from axisymmetric configurations studied in the literature. This concurrence of various factors appears to be responsible for the complex structures of the POD modes with forcing. To gain further insight into the influence of the different effects, further studies with forcing at different amplitudes and frequencies may be considered for future work.

4.6. Concluding remarks on the effect of periodical forcing

The impact of axial forcing at the natural frequency on the flow and mixing fields of a swirl burner was studied by experimental and numerical means. The main emphasis was put on the examination of the ability of unsteady RANS and large eddy simulations to capture the characteristics of the mixing behavior and flow structures for the different cases, as these play an important role regarding pollutant emissions and combustion dynamics in gas turbines.

The numerical simulations are in reasonable agreement with measurements, although the turbulence intensity was underestimated by the URANS simulations. Mean velocity fields are only slightly influenced by the forcing. The mean and rms concentration fields could be qualitatively and mostly quantitatively reproduced by the simulations. The analysis of the concentration fields and the spatial unmixedness shows a more homogeneous mixing for the case with forcing than without. The unforced flow features a helical structure represented by antisymmetric shapes of the first POD modes which change to symmetric structures when forcing is applied. URANS and LES show similar characteristics of the POD modes, although the URANS simulations are not able to capture the modal energy distribution correctly.

Conducting numerical studies on the flow and mixing fields of a gas turbine burner, it was found that URANS is capable of reproducing mean flow properties at the burner exit in satisfactory qualitative and quantitative agreement with measurements. Regarding higher moments, URANS cannot be considered as a tool providing reliable results. Characterizing the coherent structure of the burner, URANS gives reasonable predictions for the first POD modes. Being able to predict mean velocity distributions more precisely and to capture turbulence characteristics, LES can be recommended as numerical tool.

The next step is to shed light on the influence of forcing not only on flow and mixing fields but also on flame characteristics. Since combustion modeling in three dimensions remains challenging and highly cost-intensive, especially if considering detailed chemistry and parametric studies, we chose to conduct these studies in one-dimension, allowing for high spatial and temporal resolution, detailed species information and parametrical evaluation at the same time. The employed methodology based on the Linear eddy Model and the results on the impact of periodical oscillations in equivalence ratio on the combustion process will be presented in Part II.

Part II.

Linear Eddy Modeling of fluctuations in fuel-air ratio

As explained in the Introduction (Chapter 1.3), fluctuations in fuel-air ratio may play a crucial role in the occurrence of instabilities and thus are an important field of study. This part concentrates on the investigation of the impact of fluctuations in fuel-air ratio on flame characteristics, i.e. heat release rate, emissions, and flame propagation speed (Chapter 6). Strongly turbulent calculations of lean premixed one-dimensional flames are performed. For the turbulent simulations the Linear Eddy Model is employed, which resolves the relevant length and time scales on a one-dimensional domain, and is therefore applicable to the whole range of combustion regimes. Due to its one-dimensional nature it is computationally relatively cheap, and parametric studies are feasible.

Chapter 5 explains the Linear Eddy Model, describes the implementation, special features in the code, and applied techniques respectively mechanisms. Additionally, the influence of varying input parameters, turbulent fluctuation level and integral length scale, on flame structure and emissions is illustrated.

The findings detailed in this part were published in Schrödinger et al. (2011*a*,*b*, 2012*b*, 2013*b*, 2014) and Oevermann et al. (2015).

5. The Linear Eddy Model

A one-dimensional approach for the investigations of mixing inhomogeneities was chosen within this work since it combines the advantages of reduced computational cost and the potential of a high spatial as well as temporal resolution. In particular, the Linear Eddy Model developed by Kerstein (1989, 1991) resolves all physically relevant length (for turbulent flows: Kolmogorov scale, η, to integral length scale, L) and time scales on a one-dimensional domain. It is thus applicable to all combustion regimes and masters flame-turbulence interaction which plays an important role within the considered combustion processes.

The one-dimensional domain can be considered as a line of sight through a three-dimensional turbulent domain. In the case of premixed combustion, the domain represents a statistical cut perpendicular to a three-dimensional turbulent flame front.

5.1. One-dimensional transport equations

In the following the underlying transport equations for a thermo-chemical system, mass, species, and energy equations, will be presented for three dimensions and subsequently reduced to one dimension. The equations are presented in a Lagrangian formulation. $\mathcal{S}$ denotes the Lagrangian system containing a fixed mass of fluid or species without any mass crossing the system boundaries $\partial\mathcal{S}$. The quantities are generally evaluated at the cell center. Flux terms or other quantities given at the cell faces are labeled with subscripts fl and fr for left and right cell faces, respectively.

The pressure equation will not be described, as in the current work, with focus on gas turbine combustion, the pressure is assumed constant in space and time. For a detailed derivation of the transport equations we refer to Lignell et al. (2013).

Continuity equation

The Lagrangian formulation of the continuity equation reads

$$\frac{d}{dt}\int_{\mathcal{S}} \rho dV = 0. \tag{5.1.1}$$

In one dimension and with constant properties in the control volume, Equ. (5.1.1) becomes

$$\frac{d}{dt}(\rho\Delta x) = 0, \quad \rightarrow \quad \rho\Delta x = \text{const.} \tag{5.1.2}$$

Species equations

The Lagrangian conservation equation for a diffusing species α is given by

$$\frac{d}{dt}\int_{\mathcal{S}} \rho Y_\alpha dV = \int_{\mathcal{S}} \omega_\alpha dV, \tag{5.1.3}$$

where Y is the mass fraction and ω is the reaction rate. Considering the Reynolds transport theorem and Equ. (5.1.2) and assuming uniform properties in the control volume, Equ. (5.1.3) can be written as

$$\frac{dY_\alpha}{dt} = -\frac{1}{\rho\Delta x}(j_{\alpha,\mathrm{fr}} - j_{\alpha,\mathrm{fl}}) + \frac{\omega_\alpha}{\rho}. \tag{5.1.4}$$

$j_\alpha = \rho Y_\alpha v_\alpha^D$ denotes the diffusive flux, where v_α^D is the species diffusion velocity. The diffusive flux of species α is expressed by a variation of Fick's law:

$$j_\alpha = -\rho D_\alpha \frac{dY_\alpha}{dx} - \frac{\rho D_\alpha Y_\alpha}{M}\frac{dM}{dx}, \tag{5.1.5}$$

where D_α is the species diffusion coefficient and M is the mean molar mass.

Energy equation

The energy equation expressed in terms of the internal energy e in Lagrangian formulation is

$$\frac{d}{dt}\int_{\mathcal{S}} \rho e dV = \dot{Q} + \dot{W} = -\int_{\partial\mathcal{S}} \mathbf{q}\cdot\mathbf{n} dA - \int_{\partial\mathcal{S}} \mathbf{F}\cdot\mathbf{v}_{\mathrm{sys}} dA, \tag{5.1.6}$$

where $\mathbf{q}$ is the heat flux vector, $\mathbf{F}$ is the surface force per unit area, $\mathbf{n}$ is the normal vector, and $\mathbf{v}_{\mathrm{sys}}$ is the system velocity vector. Assuming pressure work as the only surface force, integration over the one dimensional control volume gives

$$\frac{de}{dt} = -\frac{1}{\rho\Delta x}(q_{\mathrm{fr}} - q_{\mathrm{fl}}) - \frac{P}{\rho\Delta x}(U_{\mathrm{fr}} - U_{\mathrm{fl}}). \tag{5.1.7}$$

U denotes the dilatational velocity and P the pressure, which is uniform in the control volume. Substituting e with enthalpy $h = e - P/\rho$ and rearranging yields

$$\rho\Delta x\frac{dh}{dt} = -(q_{\mathrm{fr}} - q_{\mathrm{fl}}) + \Delta x\frac{dP}{dt} + \underbrace{P\frac{d\Delta x}{dt} - P(U_{\mathrm{fr}} - U_{\mathrm{fl}})}_{=0}, \tag{5.1.8}$$

$$\frac{dh}{dt} = -\frac{1}{\rho\Delta x}(q_{\mathrm{fr}} - q_{\mathrm{fl}}) + \frac{1}{\rho}\frac{dP}{dt}. \tag{5.1.9}$$

The heat flux vector is of the form of Fourier's law:

$$q = -\lambda\frac{dT}{dx} + \sum_\alpha h_\alpha j_\alpha. \tag{5.1.10}$$

It includes thermal conduction (λ is the thermal conductivity) and enthalpy transport through diffusive fluxes.

5.2. One-dimensional turbulence modeling

Turbulence, its production and dissipation are a highly three-dimensional processes, not represented by the one-dimensional transport equations. The main idea behind the concept of the Linear Eddy Model is to treat molecular diffusion processes and turbulent advection separately. Molecular diffusion is implemented deterministically (solving the transport equations in Section 5.1) whereas turbulent stirring is represented by a sequence of statistically independent rearrangement events. The rearrangement events can be regarded as the one dimensional analog of turbulent eddies. They are expressed by triplet maps, which compress the scalar field within a chosen segment by a factor of three. The original field is then replaced with three adjacent copies of the compressed field, with the middle copy spatially inverted (Fig. 5.2.1). The maps are measure preserving and do not introduce dis-

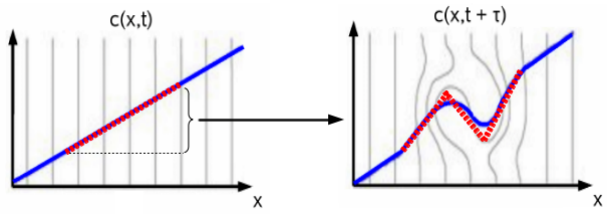

Figure 5.2.1.: Triplet Map applied to a scalar gradient $c(x,t)$

continuities into the scalar profiles. Each event is governed by three random variables: the time of eddy occurrence, the location of the eddy, and its size. The location is chosen randomly. The size of the eddy is chosen from a distribution of domain sizes which is obtained by applying Kolmogorov scaling laws. Identifying that the rearrangement events induce a random walk of one particle on a line, a rate parameter, λ, with dimensions $[l^{-1}t^{-1}]$ and a pdf describing the length distribution, $f_1(l)$, can be determined. The diffusivity of the random walk is then interpreted as the turbulent diffusivity D_t:

$$\lambda = \frac{54}{5} D_t L^{-3} \frac{1-(\eta/L)^{-5/3}}{(\eta/L)^{4/3}-1}, \tag{5.2.1}$$

$$f_1(l) = \frac{-5/3}{L^{-5/3}-\eta^{-5/3}} l^{-8/3}. \tag{5.2.2}$$

The eddy occurrence time is calculated from a Poisson process:

$$f_2(t) = \frac{1}{\tau}\exp(-t/\tau), \tag{5.2.3}$$

where τ denotes the mean eddy occurrence time $< t >= \tau = \frac{1}{\lambda S}$, with S being the size of the one-dimensional domain. Considering Equ. (5.2.1), (5.2.2), and (5.2.3), three input parameters are needed for the model, namely the integral length scale L, the Kolmogorov scale η, and the turbulent diffusivity D_t. η and D_t can be derived from the turbulence intensity and the integral length using the relations $\eta = C_\eta L \mathrm{Re}_t^{-3/4}$ and $D_t = {}^{u'L}/_{C_\lambda}$; Re_t is the turbulent Reynolds number and C_η, and C_λ are constants determined for a wide range of turbulent premixed flames in Smith & Menon (1996).

The LEM reproduces important key features of turbulent mixing (Kerstein 1991) and proved itself to be a valid model in studies on various research fields, amongst them LEM simulations on turbulent premixed combustion and pollutant formation by Smith & Menon (1996) and Menon et al. (1994).

5.3. Code implementation

The utilized code is based on an implementation developed by Lignell et al. (2013) for diffusion flames and One Dimensional Turbulence (ODT) (Echekki et al. 2011), which is closely related to LEM, but also considers velocity field. The code was refined within the present work to be suitable for one-dimensional turbulent premixed flames employing the Linear Eddy Model. In the following, the code implementation will be described in detail.

5.3.1. Diffusive advancement

The diffusive advancement is implemented using a Lagrangian formulation. This implies no mass fluxes across the cell boundaries, which leads to expansion and contraction of cells. The Lagrangian formulation treats one dimensional advection originating from dilatation in variable density flows implicitly. This is a huge advantage over an Eulerian formulation since the dilatation velocity is generally much larger than diffusion velocities. The Eulerian formulation is therefore controlled by the advection process causing very small advancement time steps. The Lagrangian formulation in contrast is controlled by the diffusion process, allowing for larger time steps.

5.3.2. Time integration

To cope with the complexities arising due to the treatment of premixed combustion, some changes in the time integration process were introduced. The solutions of the ordinary differential equations in time are treated individually. The enthalpy equation is solved explicitly using a first-order Euler method while the species equation is solved implicitly. For this purpose, the species equation is splitted using the Strang-splitting method. The diffusive term of the species equation (5.1.4) is solved in the first splitting step for $\Delta t/2$. Then the source term is calculated in the second step for Δt, and in the third step the diffusive term is again solved for $\Delta t/2$. Since the system of equations with detailed chemistry is usually stiff, which causes the necessity of very small time steps for explicit treatment, implicit integration of the chemical source term is used. The integration is performed with CVODE (Cohen & Hindmarsch 1996). In premixed combustion, the diffusion terms turn out to be quite stiff as well. Hence, this part is integrated implicitly using the Thomas Algorithm, also known as tridiagonal matrix algorithm (TDMA).

The overall solution procedure for the diffusive advancement for one time step ($t_n \rightarrow t_{n+1}$) can be summarized with the following steps:

1. Calculation of fluxes (mass j, heat q).
2. Advancement of species equation using Strang splitting to obtain Y_α at t_{n+1}.
3. Advancement of energy equation to obtain h at t_{n+1}.

4. Calculation of M and T from Y_α and h at t_{n+1}.
5. Utilization of the ideal gas law to obtain ρ at t_{n+1}.
6. Solution of Equ. (5.1.2) ($(\rho\Delta x)_{n+1} = (\rho\Delta x)_n$) to obtain Δx at t_{n+1}.

The solution procedure including molecular diffusion and turbulent stirring (triplet mapping) for the case of premixed combustion with outflow boundary conditions (Neumann boundary condition) is implemented such that

1. the eddy time, position and size are computed,
2. the eddy/triplet map is applied,
3. diffusion is updated to the eddy time, and
4. eventually the domain is shifted so that the flame remains at the same position.

When shifting the LEM domain, a new cell at the inflow side is created with predefined inflow properties. The outflow side is cut off to conserve the original domain size. The shifting length is calculated from the consumption speed which is determined for each species α from (Oevermann et al. 2008)

$$s_C = \frac{1}{\rho_u(Y_{\alpha,b} - Y_{\alpha,u})} M_\alpha \int \omega_\alpha dx. \tag{5.3.1}$$

Subscripts u and b denote the unburnt and burnt states, and the integration is performed over the entire one dimensional domain.

For discretization of spatial derivatives central differences are used. The software Cantera (Goodwin 2009) is employed to calculate thermodynamic variables, reaction rates, and transport coefficients. Transport properties are determined using the mixture-averaged model.

5.3.3. Mesh adaption

The Linear Eddy domain is descretizised on a non-uniform mesh. The domain $[0, S]$ consists of n cells with cell faces $x_{f,i}$ and cell centers x_i, where $x_{f,1} = 0$ and $x_{f,n+1} = S$ (domain length). The property profiles are assumed uniform in each cell. The number of cells varies due to the triplet mapping and mesh adaption procedures. Applying a triplet map, the number of grid points for the considered section is tripled. As this may imply an inappropriate discretization for the property profiles, very small cells which could impose stringent time-step constraints or large size ratios of adjacent cells, mesh adaption of this region has to be applied. On the other hand, diffusive evolution necessitates mesh adaption. Diffusive advancement smoothes property gradients and might lead to an over-resolved field. Furthermore, solving for reactive flows (with a scalar source term) may produce increased gradients. In combination with the Lagrangian formulation of the equation system, this may result in expanded or contracted cell sizes.

The mesh adaption is performed by splitting or merging cells conserving mass. It is based on one or more property profiles; in the current work it is based on the temperature profile. The adaption of the profiles follows several rules explained in the following. The cell size should not be larger, respectively smaller, than a given maximum, respectively minimum, cell size. The cell size is further bound to minimum and maximum gradients and curvatures

which are also predefined. Eventually, a cell should feature a cell size ratio of less than 2.5 to its adjacent cells. The last constraint prevents irregularities in the mesh which could affect the accuracy of the diffusive process. For further information on the choice of the factor 2.5 we refer to Lignell et al. (2013).

The benefit of the adaptive-mesh implementation is the strong reduction of the number of grid cells required to discretize a given domain with large gradients due to reaction and turbulent eddies.

5.4. Subdomain decomposition

To speed up the code, a mesh decomposition routine suggested by Kerstein (2010) was implemented. Although LEM is one dimensional, some problems with large domains or high turbulent Reynolds numbers might be computationally expensive.

The subdomain decomposition divides the domain in sub-regions which can be run on different processors to speed-up the simulations. But even for an execution in serial mode, as it was used in the present studies, the performance can be increased for cases with high turbulence. As explained in Sec. 5.3, the transport equations within the LEM are only updated up to an eddy occurrence, that is the diffusion process is constantly interrupted by triplet maps. This can be very time consuming especially if the diffusion time step is much larger than the eddy turnover time. On the smaller subdomains, only a fraction of the overall triplet maps occurs and so the diffusion time between the eddies and in turn the performance increases.

The implementation is done such that each subdomain works as an individual LEM line with its own grid, variables and functions. Each subdomain is run independently until it has to communicate with its neighbors. The LEM domain is decomposed into N subdomains. These subdomains consist of solution regions and guard regions (Fig. 5.4.1). The solution regions are of size $S = D/N$, where D is the overall domain size, whereas the guard regions on each side of the solution regions, except at the boundaries of the LEM domain, are of size $S/2$, overlapping their neighboring subdomain solution region. Every point on the domain D is thus in one solution region and one guard region except at the boundaries of the LEM domain. The necessity for guard regions is owed to non-physical boundary conditions of the subdomains, set as no-flux boundaries. Except for the real boundaries of the LEM domain these boundaries are artificial and lead to non-physical solutions which have to be prevented from propagating into the solution region.

5.4.1. Subdomain decomposition algorithm

The subdomain decomposition algorithm is structured in the following forms:

Initialization of the LEM domain At the beginning of the simulation one LEM line with initial conditions is created.

Initialization of the subdomains The LEM line is split into N subdomains with solution and guard regions as explained above.

Determination of maps The sizes, positions, and occurrence times of all triplet maps for

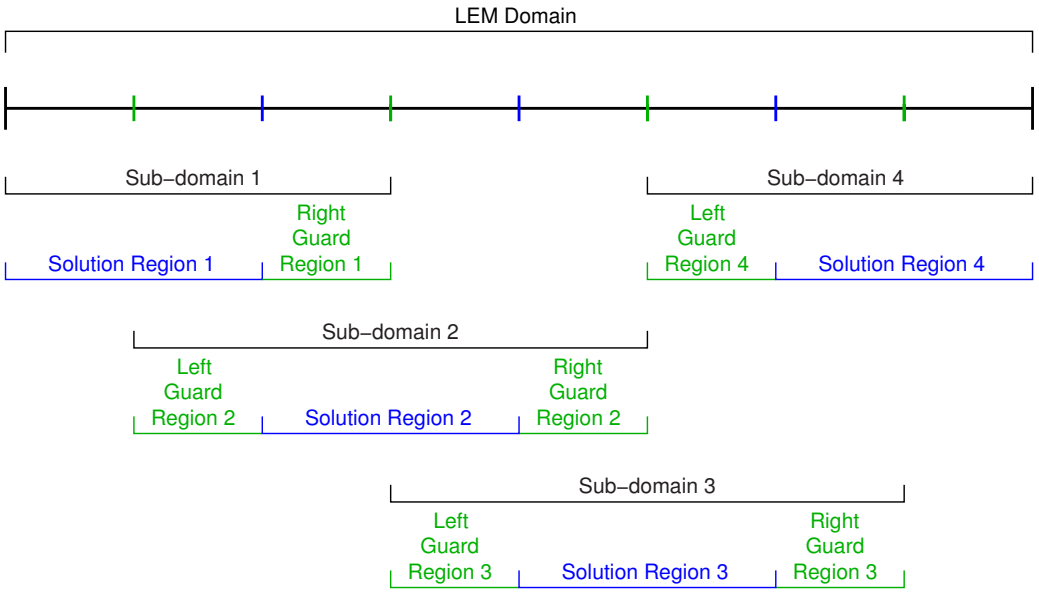

Figure 5.4.1.: Regions of subdomain decomposition for $N = 4$ subdomains.

a certain time period (e.g. a distinct time step until the solution is stored) are determined. This is possible since maps in LEM are mutually independent and do not depend on the state of the system.. Thus, they can be created in advance.

Distribution and execution of maps The maps are subsequently assigned to the subdomains. Two kinds of maps, independent and dependent maps, are distinguished. Independent maps, which lie within one solution region only, do not need communication between different subdomains and thus can be applied independently without communication of subdomains. A dependent map, in contrast, cannot be applied to a single subdomain, since it overlaps two or more solution regions. In this case a *stop event* is created. The *stop event* receives a certain stop number value which is then distributed to the corresponding map, and the map is distributed to all affected subdomains. The stop events are counted in ascending order. If a subdomain hits a stop event, it checks if the other affected subdomains are ready for gathering and applying the map (i.e. they are at the same map/time). If they are not, the stop number of the subdomain is set to the value of the map's stop number, and the subdomain waits for its neighbor(s). When the last subdomain is ready for the dependent map, it calls a function that gathers the solution regions of the affected subdomains, applies the map, and redistributes the solution to the subdomains. The subdomains then get new maps on their stack and run independently again until they hit another stop event.

Note that the maps are only distributed to the solution regions. A map that is entirely in a guard region of one subdomain is not distributed to this subdomain but only to its neighbor in whose solution region it lies. If a map overlaps a solution and guard region of one subdomain, it will also affect the neighbor's solution region and therefore is a dependent map requiring communication.

Another situation where subdomains need to communicate is when they run too long on their own. In this case the time it takes for the scalars to bridge the guard region is exceeded. This time is governed by the molecular diffusion (with the molecular

diffusivity D_M), respectively the heat transfer, since we are regarding thermo-chemical conditions, and the turbulent advection, which in turn is determined by the turbulent diffusivity D_t. A condition for the time limit can be derived from the fundamental solution of the diffusion equation:

$$\Phi(x,t) = \frac{1}{\sqrt{4\pi Dt}} \exp\left(-\frac{x^2}{4Dt}\right), \tag{5.4.1}$$

where D denotes the diffusivity. The time interval it takes for a perturbation to travel a distance Δx is thus given by:

$$\Delta t = \frac{(\Delta x)^2}{4D}. \tag{5.4.2}$$

For simulations run with LEM, generally $D_t \gg D_M$ holds true and D is therefore set equal to the turbulent diffusivity.

Since we consider premixed flames, propagating into the unburned mixture, another time constraint has to be formulated. The flame travels with the burning velocity v_b. The time that is needed for the flame to propagate over the distance Δx is

$$\Delta t = \frac{\Delta x}{v_b}. \tag{5.4.3}$$

Δx is set to a fraction of the guard region to ensure that the non-physical boundary conditions of the subdomains do not influence the solution regions.

The Lagrangian formulation of a thermo-chemical system, as in the current code (Sec. 5.3), can cause expansion and contraction of cells and domains. To prevent the subdomains from being assembled at wrong positions, a variable dx_{exp} was introduced for each subdomain. dx_{exp} considers the change in subdomain size up to the position where the next subdomain's solution region starts and is updated every diffusion time step, as is the position of the successive solution region. When gathering subdomains the solution regions are assembled such that every solution region is positioned at its original position plus the changes in size dx_{exp} of all preceding subdomains. After gathering and redistribution, dx_{exp} of all involved subdomains are set to 0 again.

Gathering of all subdomains for output After a predefined time step, the subdomains are gathered to store the solution.

5.4.2. Parallelization issues

Although parallelization was not used in the present work, some related issues shall be discussed here. A simple way of parallelizing the code would be to parallelize the loop over the subdomains which can be, for example, easily done with OpenMP. However, following issues have to be kept in mind. As explained above, a subdomain hitting a stop event, i.e. the occurrence of a dependent map, needs to communicate with its neighbor(s). First it needs to be check if the other subdomains are at the same time. In parallel, this could cause a race condition, when two or more subdomains try to check each other at the same time. The program can then either hang-up, i.e. it is not able to go further, or try to gather the remaining subdomains at the same time, which may result in an abend.

Table 5.4.1.: Test cases for subdomain decomposition.

case	Re_t	u'	L_D	L	η	D_t	λ	nb of maps
	-	in ms^{-1}	in m	in m	in m	in $\mathrm{m}^2\mathrm{s}^{-1}$	in $\mathrm{m}^{-1}\mathrm{s}^{-1}$	-
1	8603	10	0.25	0.025	$3.011{\cdot}10^{-4}$	0.01667	$18{\cdot}10^{6}$	227816
2	34412	10	1	0.1	$4.295{\cdot}10^{-4}$	0.06667	$6.4{\cdot}10^{6}$	321393
3	860	1	0.25	0.025	$1.693{\cdot}10^{-3}$	0.001667	$1.04{\cdot}10^{5}$	1296
4	25809	30	0.25	0.025	$1.321{\cdot}10^{-4}$	0.05	$2.16{\cdot}10^{8}$	539273

Which of these situations will occur, depends on when the subdomains set their markers (the subdomain's stop number is set to that of the stop event). To avoid either of the situations, stop events have to be defined critical regions, which are at maximum allowed to be executed by one subdomain of the affected group. This region has to include checks of other subdomains, the gathering of subdomains, application of the dependent map, and redistribution of subdomains. Note that the setting of the stop numbers for the stop events on the higher level has to be a critical region as well. It is only to be executed by one subdomain at the same time.

When the code uses Cantera for thermodynamics and kinetics, every subdomain will need its own Cantera object. If there is merely one Cantera object for all subdomains, there would be a competitive situation, i.e. if a Cantera function (from one object) is called more than once at the same time the code will abort.

Furthermore, the organization of the subdomains and all other related vectors with boost's ptr_vector class is recommended. The standard vector class in C++ is made to store values. The ptr_vector class can be used to handle a vector of pointers as if it was a vector of values, as it lowers the level of indirection for iterators and member functions. Using the ptr_vector class simplifies the treatment of vectors of classes, such as the vector of subdomains, and helps prevent memory leaks.

5.4.3. Influence of turbulence parameters on the performance

In this section the performance of the subdomain decomposition algorithm is tested by running simulations with different conditions and varying the number of subdomains. The cases in this section are set to conditions close to the flames investigated later. A lean premixed methane-air flame at an equivalence ratio of 0.6 and preheated to 425 K is considered. The turbulence intensities and integral length scales are varied according to Tab. 5.4.1. The reduced combustion mechanism described in Sec. 5.5 is used and all simulations were run for 0.05 s, except case 4 which was run for 0.01 s. The domain length for all cases is set to 10 integral length scales.

In addition to the turbulence intensity u' and the integral length scale L, the turbulent Reynolds number Re_t, the LEM domain length L_D, the Kolmogorov length scale η, the turbulent diffusivity D_t, the rate parameter λ, and the average number of overall maps are given in Tab. 5.4.1. The Kolmogorov length and turbulent diffusivity are calculated from the relations given in Sec. 5, with C_η and C_λ being 10.76 and 15.

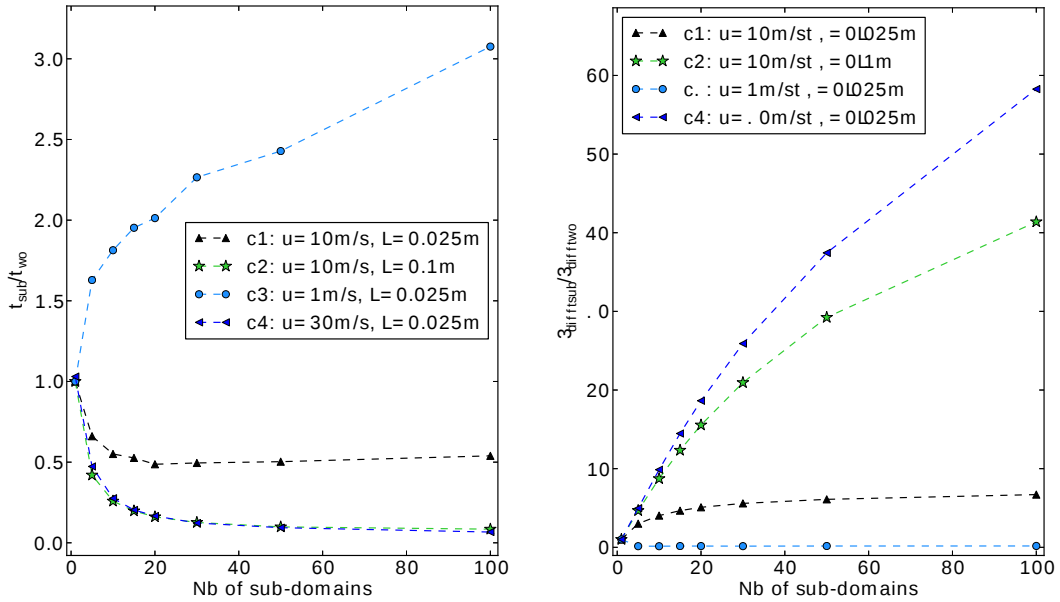

(a) (b)

Figure 5.4.2.: Evaluation of subdomain decomposition for different cases (Tab. 5.4.1), (a) run time normalized with corresponding single-domain run time; (b) average number of diffusion time steps.

The performance of the algorithm is evaluated by considering the run times for the test cases, t_{sub}, normalized by the corresponding run times without subdomain decomposition, t_{wo} (Fig. 5.4.2(a)). Furthermore, Fig. 5.4.2(b) shows the mean time steps for the calculation of the diffusion terms, t_{diff}, normalized by the corresponding single-domain values. t_{diff} is calculated by counting the diffusion steps $N_{ds,i}$ in every subdomain i and normalizing it with the number of subdomains N and the run time t_{sub}:

$$t_{\text{diff}} = \frac{N t_{\text{sub}}}{\sum_i N_{ds,i}} \tag{5.4.4}$$

For the highly turbulent cases (2 and 4) a speed-up of almost 12 can be achieved. Also for case 1, which corresponds to the turbulent conditions investigated in this work, a speed-up of around 2 is possible. For this case a slight minimum establishes around 20 subdomains whereas for cases 2 and 4 no minimum has been reached up to 100 subdomains. For case 3, in contrast, no speed-up can be achieved, and the code is even considerably slowed down by the subdomain decomposition.

The speed-up behavior is inversely coupled with that of the averaged diffusion times. The relative mean diffusion times increase strongly for cases 2 and 4 so that for 100 subdomains the diffusion time steps are 41 respectively 58 times larger than those for the single domain with still rising tendencies. For case 1 an increase in averaged diffusion times of more than 6 can be observed. At $N = 100$ subdomains the curve is close to saturation though. For case 3 the diffusion time steps do not increase and rather stay at a low constant level, slightly lower than for the single-domain application. This indicates that, in contrast to

Table 5.4.2.: Time scales for single-domain simulations.

case	t_{diff} in s	τ in s	t_{wo} in min
1	$2.2{\cdot}10^{-7}$	$2.2{\cdot}10^{-7}$	3434
2	$1.6{\cdot}10^{-7}$	$1.6{\cdot}10^{-7}$	5448
3	$1.1{\cdot}10^{-6}$	$3.8{\cdot}10^{-5}$	633
4	$1.9{\cdot}10^{-8}$	$1.9{\cdot}10^{-8}$	9317

the other cases, the diffusion time step bounded by the CFL criterion here is smaller than the average eddy turnover time. This is confirmed by Tab. 5.4.2, which gives the different time scales, averaged diffusion time step, mean eddy turnover time, and total run time for the single-domain simulations.

To classify the performance behavior in terms of turbulence parameters, a closer look on Tab. 5.4.1 is taken. The performance of subdomain decomposition increases with an increase in integral length scale (case 1 vs. case 2) as well as an increase in turbulence intensity (case 1 vs. case 4). The rate parameter λ, which gives the number of eddies per time and length, in case 3 is smaller than that in case 1 (although it is of the same order of magnitude), whereas the Kolmogorov length η is larger. λ in case 4 on the other hand is two orders of magnitude larger than that in case 1 whereas η is smaller. Despite these differences, the turbulent Reynolds number increases in both cases and is thus responsible for correlating with the speed-up rather than the rate parameter.

Figure 5.4.3 shows the influence of the number of subdomains on the number of maps that are distributed to the subdomains normalized by the total number of maps. The cumulative distribution function of the map/eddy sizes is also shown. As explained in Sec. 5.4.1, all maps are distributed to the subdomains. A single map, which lies within the solution region of one subdomain, is distributed to that one subdomain only. If a dependent map, overlapping the solution regions of two (or more) subdomains, occurs, it is distributed to all affected subdomains. This generally leads to a higher number of distributed maps than overall number of maps. For cases 2 and 4 the increase of distributed maps with the number of subdomains is only weak; for case 1 it is slightly stronger and for case 3 it is considerably stronger (Fig. 5.4.3(a)). This implies that cases 2 and 4 exhibit mainly independent maps up to a high number of subdomains, which indicates very small eddy sizes. For case 3 on the other hand, the number of dependent maps strongly increases with the number of subdomains, which indicates larger eddy sizes. These assumptions are confirmed by Fig. 5.4.3(b) giving the cumulative distribution function (CDF) of eddy sizes. The CDF $F(l)$ is the integral of the eddy size PDF $f(l)$ in Equ. (5.2.2) and thus gives the probability that a random variable will be found at a value less than or equal to l. For cases 2 and 4 most eddies occur at small eddy sizes close to their respective Kolmogorov length whereas the eddy sizes for case 3 are, in comparison, more uniformly distributed between Kolmogorov and integral length.

In summary, for high turbulent Reynolds numbers, which imply high probability of small eddies (close to the Kolmogorov length), and an averaged eddy turnover time much smaller than the CFL time steps, a high speed-up, even in serial mode, can be expected. If the averaged eddy turnover time is larger than the CFL time step, in contrast, the subdomain

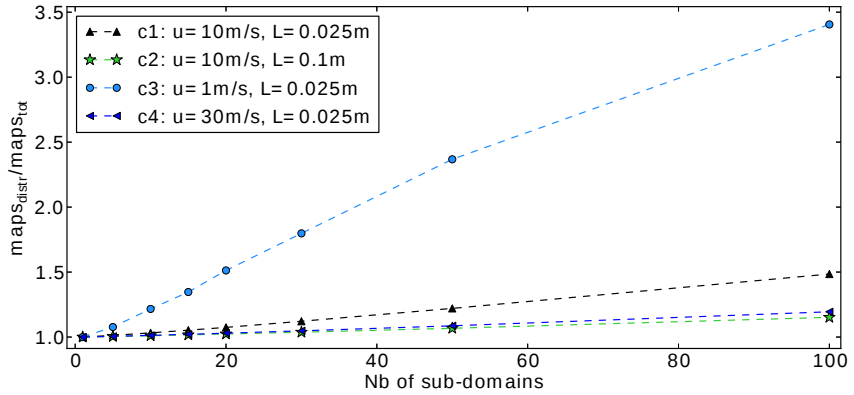

(a)

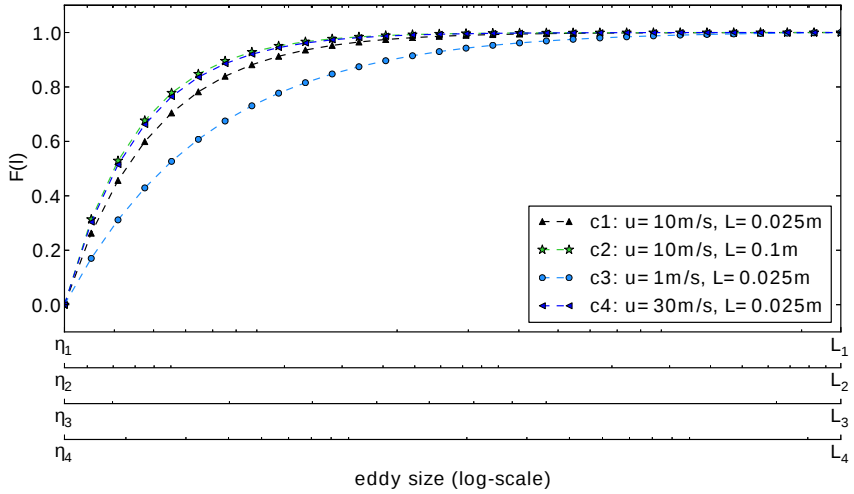

(b)

Figure 5.4.3.: Evaluation of subdomain decomposition for different cases (Tab. 5.4.1), (a) distributed maps normalized with total number of maps; (b) Cumulative distribution function for the eddy sizes.

decomposition algorithm can slow down the calculations.

5.4.4. Validation

The purpose of the validation case presented in this section is to ensure that the subdomain decomposition algorithm does not change the statistics of the scalars. Therefore the mean and rms temperature fields of the baseline case ($u' = 10\,\mathrm{m/s}$, $L = 0.025\,\mathrm{m}$) are compared for the simulations without subdomains and with 20, and 50 subdomains (Fig. 5.4.4).

The overall agreement of the different simulations is good. Small discrepancies can be seen at the mean flame front and a little stronger in the rms-profiles. The distributions are not entirely smooth which can be attributed to too short run times. For longer run times an even better agreement is expected, and it can be assumed that the subdomain decomposition algorithm does not alter the statistics of the scalars.

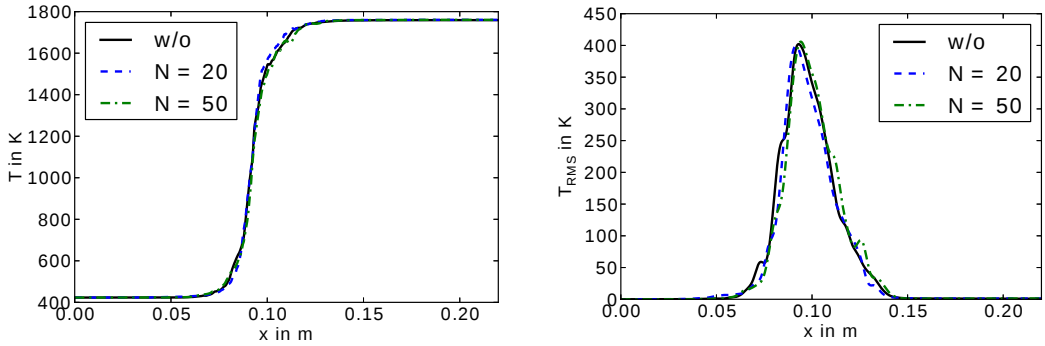

(a) T_{mean} (b) T_{rms}

Figure 5.4.4.: Validation of subdomain decomposition for $N = 20$ and $N = 50$ against original code. Mean temperature and RMS are shown over the one dimensional domain for the cases with and without subdomain decomposition.

5.5. Combustion mechanism

Detailed kinetic mechanisms are necessary to investigate dynamic processes in combustion, especially regarding intermediate species such as the pollutants NO_x and CO. The GRI-Mech 3.0 (Smith et al. 1999) is a standard mechanism for natural gas, which has been validated against a huge number of data sets. It is, however, challenging to apply it in spatially and temporally resolved simulations, as it consists of 325 reaction equations and involves 53 species. The present computations necessitate a smaller mechanism.

The combustion mechanism used in this work is a reduced mechanism derived from the GRI-Mech 3.0. The mechanism was developed within our group for lean methane-air combustion at atmospheric conditions including NO_x and CO formation. All important NO_x formation pathways for lean combustion were retained from the original mechanism. These are the thermal path, the N_2O-path, and the NNH-path. The prompt (CH) path was neglected since its influence in lean premixed combustion up to an equivalence ratio of 0.9 is insignificant.

The GRI-Mech 3.0 has been tuned for lean premixed flames to agree well with experimental data for the major species and formation of pollutants NOx and CO, as well as laminar burning velocities. Cantera's MixMaster was employed to generate reaction path diagrams showing the important formation pathways for lean methane-air flames. Minor, non-relevant species and the reactions in which they occur, were successively neglected. This procedure was repeated as long as the reduction did not negatively affect the results for the predefined properties. Some adaptation of reaction rates, more precisely pre-exponential factors of the Arrhenius equation, was made to comply with the original mechanism. The reduced mechanism consists of 23 species and 76 reactions. Several one dimensional test cases were run, and, in average, the reduced mechanism was found to be more than 5 times faster than the GRI-Mech 3.0 in terms of CPU time. At the same time the error was less than 5 % for the predefined properties (8 % for CO) in comparison to the full mechanism for equivalence ratios in the range of 0.5 to 0.94. The reduced mechanism is given in Appendix A.

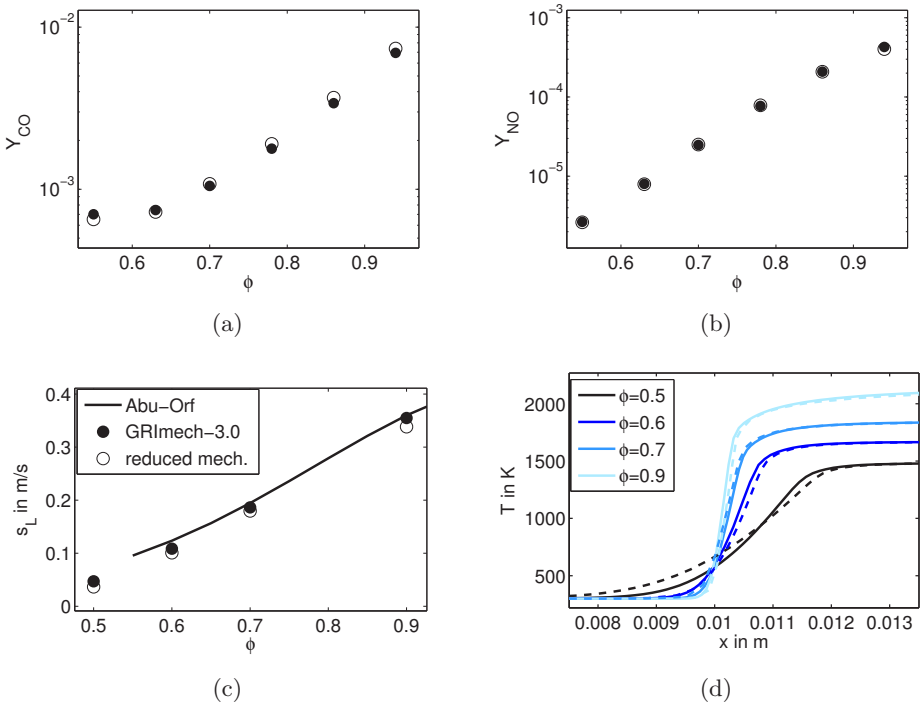

Figure 5.5.1.: Comparison of the considered reduced mechanism with the original one. (a) CO mass fraction vs. equivalence ratio; (b) NO mass fraction vs. equivalence ratio; (c) burning velocity vs. equivalence ratio in comparison with a correlation for laminar burning velocities of methane-air combustion by Abu-Orf & Cant (1996); (d) temperature profiles for different equivalence ratios for a one-dimensional laminar flame; – GRI-Mech 3.0, - - reduced mechanism.

Figure 5.5.1 shows a comparison of the reduced mechanism against the GRI-Mech 3.0. Mass fractions of CO and NO, computed from a zero dimensional perfectly stirred reactor with constant mixture composition inflow and volume outflow conditions, are compared for lean conditions. Furthermore, temperature profiles and laminar burning velocities calculated for one-dimensional laminar flames are displayed. The agreement of the reduced with the original mechanism is very good overall. The burning velocities compare well with an empirical burning velocity model for methane-air flames derived from a compilation of experimental data by Abu-Orf & Cant (1996).

5.5.1. Validation of the reduced mechanism

This section gives a brief validation of the reduced mechanism with experimental and numerical data from literature (Andrews & Bradley 1972, Warnatz 1981, Peters 1991, Smith & Menon 1997). The results for the reduced mechanism were obtained using the one-dimensional LEM-code without turbulent stirring.

Figure 5.5.2 shows the laminar flame thickness respectively the laminar burning velocity for lean premixed methane-air flames at atmospheric pressure and $T_u = 293\,\mathrm{K}$. The flame thickness is evaluated based on the thermal flame thickness ($\delta_{\mathrm{th}} = (T_b - T_u)/(dT/dx)_{\max}$)

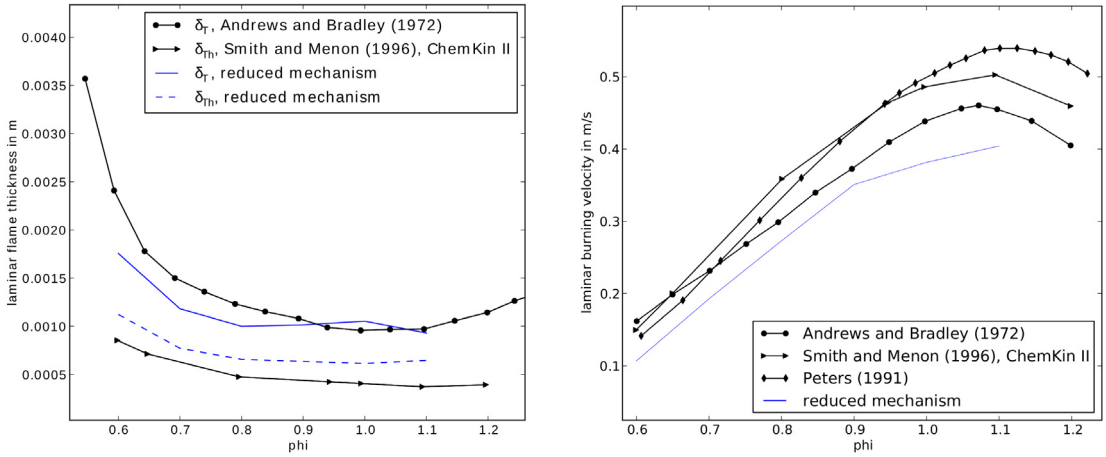

(a) (b)

Figure 5.5.2.: Validation of the considered reduced mechanism. (a) laminar flame thickness; (b) laminar flame speed.

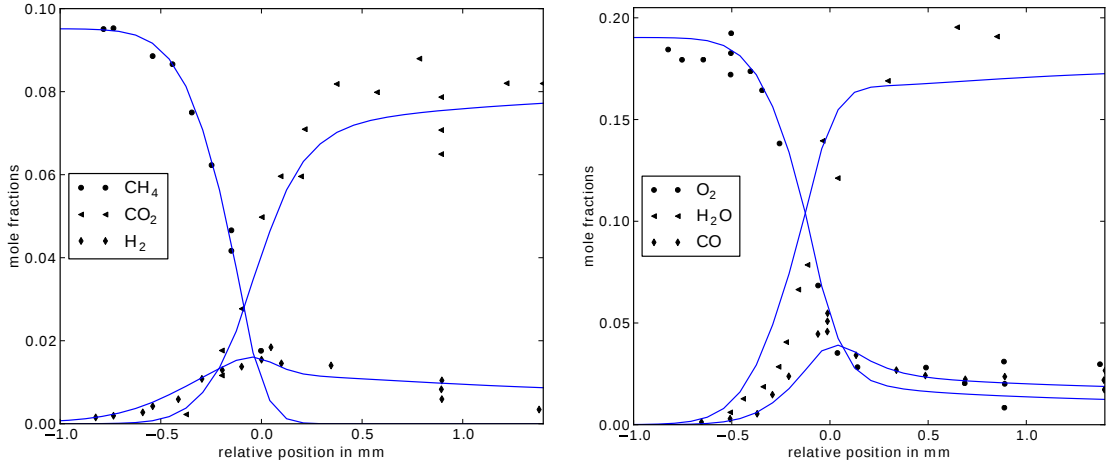

(a) (b)

Figure 5.5.3.: Laminar species profiles for a stoichiometric methane-air flame at atmospheric pressure and $T_u = 293K$; symbols: measurements, lines: reduced mechanism.

and the width of the reduced temperature (δ_T). The GRI-Mech 3.0 and therefore also the reduced mechanism have a relatively thick recombination zone which would lead to too large values for the flame thickness based on the temperature profiles. To establish a better comparability δ_T was determined as the distance of the reduced temperature $((T - T_u)/(T_b - T_u))$ change from 1 % to 85 % along the profile instead of 1 % to 99 %. The simulations are compared to laminar flame bomb experiments by Andrews & Bradley (1972) and calculations by Peters (1991) and Smith & Menon (1997). The predictions with the LEM-code and the reduced mechanism are in good agreement with the previous data. The laminar burning velocity is slightly underpredicted while δ_{Th} is slightly overpredicted.

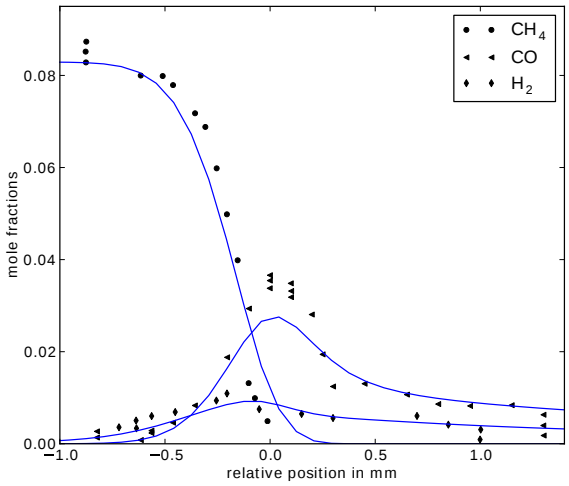

Figure 5.5.4.: Laminar species profiles for a lean methane-air flame at $\phi = 0.86$, atmospheric pressure and $T_u = 293K$; symbols: measurements, lines: reduced mechanism.

One dimensional profiles for major species as well as intermediates CO and H_2 are given in Fig. 5.5.3 for a stoichiometric flame and in Fig. 5.5.4 for a lean flame. The calculated profiles are compared to measurements by Warnatz (1981). All profiles match very well and lie within measurement accuracy.

5.6. Validation of the LEM code

Smith & Menon (1997) investigated numerous quantities of freely propagating flames. One of the flames is chosen here to validate the LEM-code since it matches best with the conditions investigated within this work. The flame properties are given in Tab. 5.6.1.

Table 5.6.1.: Flame properties for the LEM validation case.

T_u in K	ϕ -	Re_t -	u' in m/s	u'/s_L -	L in m	L_{Domain} in m	C_η -	C_λ -
328	0.717	509-15264	0.25-7.5	1-30	0.037	0.305	10.76	15

In contrast to the work by Smith & Menon (1997), which uses a one-step-mechanism and a constant Lewis number, we employ a detailed combustion mechanism (reduced mechanism) and Cantera for thermo-chemical calculations. The turbulence intensity is varied to investigate the influence on the (turbulent) flame propagation speed. The propagation speed is determined from the consumption speeds of the major species (Sec. 5.3), which is also different in the work of Smith & Menon (1997).

In Figure 5.6.1, the predicted normalized turbulent flame propagation speeds are compared to high Re fan-stirred bomb experiments by Abdel-Gayed et al. (1984) and the results of Smith & Menon (1997). The flame propagation speeds are given for different turbulence levels, u', ranging from 0 to 30 times the laminar burning velocity.

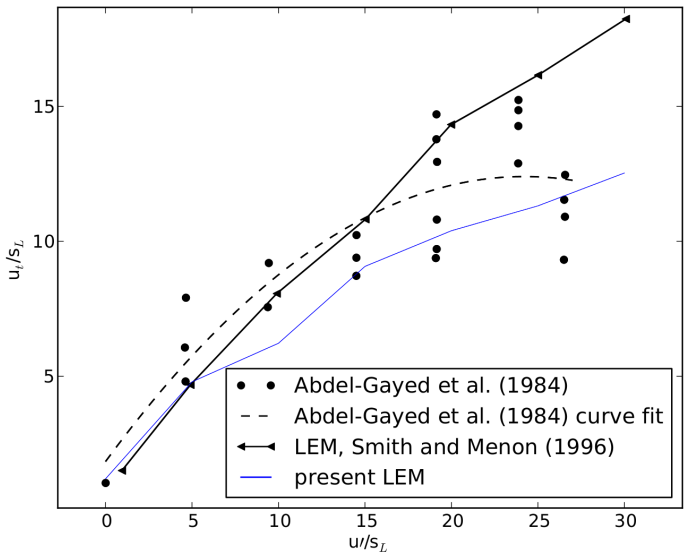

Figure 5.6.1.: Turbulent burning velocity, u_t, over turbulence intensity, u', both normalized by the laminar burning velocity, s_L.

The current LEM simulations are in good agreement with the former calculations by Smith & Menon (1997) and the measurements by Abdel-Gayed et al. (1984). Deviations from the results of Smith & Menon (1997) arise from the different conditions discussed above. The presents results are closer to the experimental data which could result from the physically more realistic conditions employed here.

5.7. Influence of turbulent velocity fluctuations and integral length scale on flame characteristics

This chapter discusses the influence of different turbulent velocity fluctuations u' and integral length scales, used as input parameters in the LEM-code, on turbulent flame characteristics and emissions.

One-dimensional turbulent calculations with different turbulent velocity fluctuations u' and integral length scales ranging around the *baseline* case were conducted. The *baseline* case uses the input parameters of the investigations described in the next chapters, namely $L = 0.025\,\mathrm{m}$ and $u' = 10\,\mathrm{m/s}$. All calculations were performed for a premixed flame at an equivalence ratio of 0.6, preheated to 423 K at atmospheric pressure. Table 5.7.1 lists the parameters of the test cases.

Table 5.7.1.: Turbulence properties for different u' and L.

	u' in m/s	L in m	Re_t -	η in m	D_t in $\mathrm{m^2 s^{-1}}$	L_{Domain} in m
1	10	0.025	8603	$3.011 \cdot 10^{-4}$	0.01667	0.25
2	2	0.025	1721	$1.007 \cdot 10^{-3}$	0.00333	0.25
3	5	0.025	4301	$5.065 \cdot 10^{-4}$	0.00833	0.25
4	15	0.025	12904	$2.222 \cdot 10^{-4}$	0.025	0.25
5	20	0.025	17206	$1.791 \cdot 10^{-4}$	0.03333	0.25
6	30	0.025	25809	$1.321 \cdot 10^{-4}$	0.05	0.25
7	10	0.01	3441	$2.395 \cdot 10^{-4}$	0.00666	0.25
8	10	0.05	17206	$3.581 \cdot 10^{-4}$	0.03333	0.5
9	10	0.075	25809	$3.963 \cdot 10^{-4}$	0.05	0.75
10	10	0.1	34412	$4.259 \cdot 10^{-4}$	0.06666	1.0

5.7.1. Variation of the turbulence intensity

Increasing u' while keeping L constant leads to increased turbulent Reynolds numbers Re_t and turbulent diffusivities D_t, whereas the Kolmogorov length scale decreases. For the LEM this means that we have more eddy events per length and time and that the probability density of eddy sizes is shifted to lower values, although the largest possible eddies remain at the same size (Equs. 5.2.1 and 5.2.2). These characteristics become evident when regarding Fig 5.7.1. It shows an instantaneous temperature profile of cases 2 and 6, i.e. turbulence intensities of 2 and 30 m/s respectively. The temperature profile in Fig. 5.7.1(a) exhibits only few and rather large eddies, while the one in Fig. 5.7.1(b) features clearly more eddies and especially more eddies of smaller sizes. The larger number of eddies leads to a broadened reaction zone, which can be classified as the corrugated or thickened flame combustion. The flame in Fig. 5.7.1(a), on the other hand, shows more attributes of a wrinkled flamelet.

In average the increase of u' decreases the gradient of the mean temperature profiles (Fig. 5.7.2(a)). The RMS profiles (Fig. 5.7.2(b)) indicate a slightly broader extent but a decrease in maximum values, which is due to the drift to smaller eddy sizes.

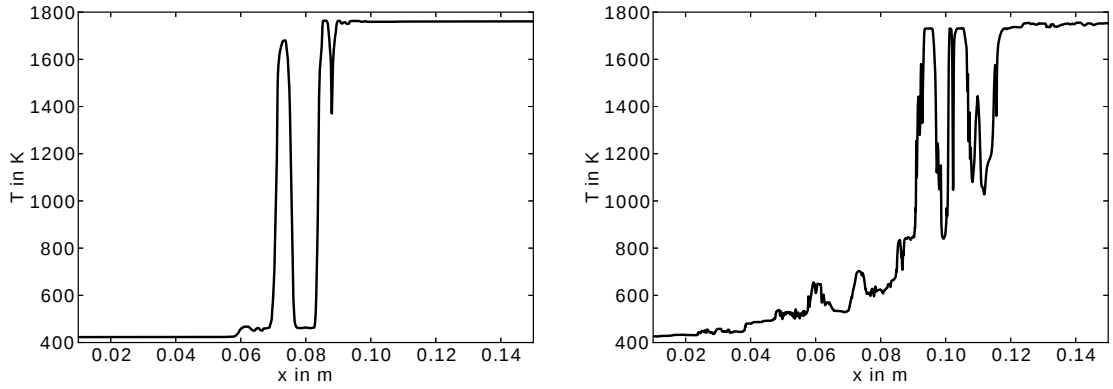

(a) $u' = 2\,\mathrm{m/s}$ (b) $u' = 30\,\mathrm{m/s}$

Figure 5.7.1.: Instantaneous Temperature profiles for different turbulence intensities u' and the same integral length scale $L = 0.025\,\mathrm{m}$.

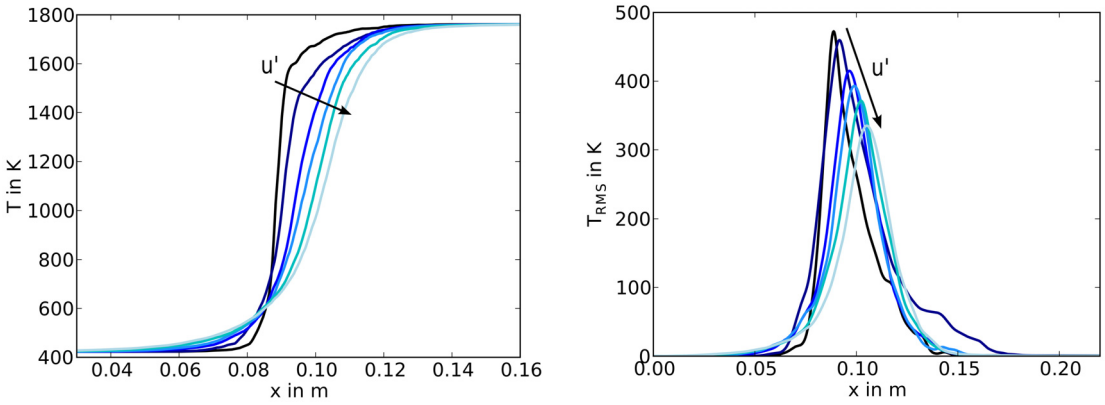

(a) mean temperature (b) temperature RMS

Figure 5.7.2.: Mean and RMS Temperature profiles for different turbulent velocity fluctuations u' and the same integral length scale $L = 0.025\,\mathrm{m}$.

The influence of variations in the turbulent velocity fluctuations on NO and CO emissions can be observed in Fig. 5.7.3. On account of the broadening of the reaction zone in average, it takes more time respectively distance for NO and CO to approach their equilibrium states. The CO mass fractions reach higher maximum values with increasing u' since the formation zone is stretched while the oxidation of CO is delayed.

5.7.2. Variations of the integral length scale

For increasing values of the integral length scale, the turbulent Reynolds number and turbulent diffusivity increase. In contrast to the previous section, the Kolmogorov scale also slightly increases. This means that not only larger eddies occur but also the amount of larger eddies increases. The probability density of eddy sizes is shifted to higher values. These aspects are apparent comparing the two instantaneous temperature profiles with

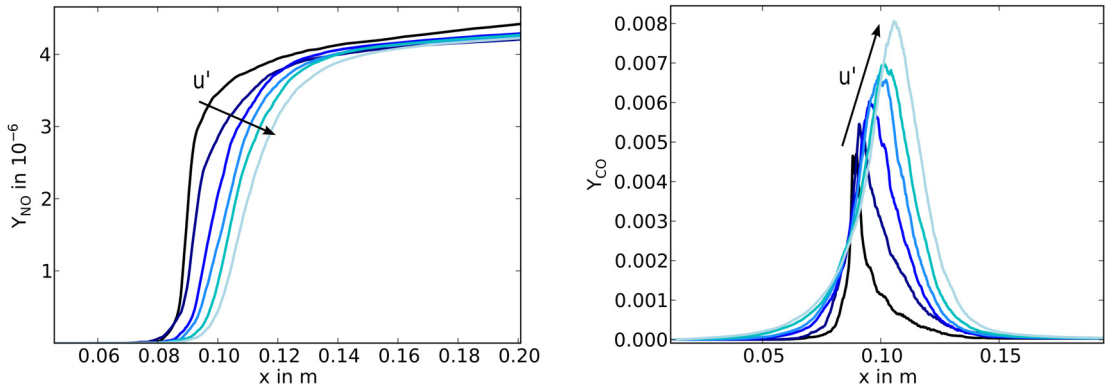

(a) NO mass fraction (b) CO mass fraction

Figure 5.7.3.: Mean species profiles of emissions NO and CO for different turbulent velocity fluctuations u' and same integral length scale $L = 0.025\,\mathrm{m}$.

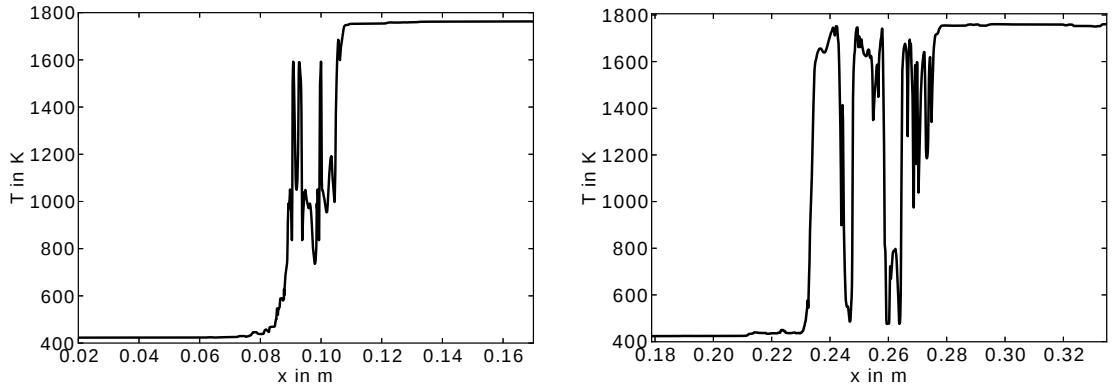

(a) $L = 0.01\,\mathrm{m}$ (b) $L = 0.1\,\mathrm{m}$

Figure 5.7.4.: Instantaneous temperature profiles for different integral length scales L and same turbulent velocity fluctuation $u' = 10\,\mathrm{m/s}$.

$L = 0.01\,\mathrm{m}$ (case 7) and $L = 0.1\,\mathrm{m}$ (case 10) in Fig. 5.7.4. Figure 5.7.4(a) shows a flame with few, small eddies, whereas Fig. 5.7.4(b) depicts a larger number of eddy occurrences and an expanded range of eddy sizes. The larger eddy sizes convert a slightly distributed flame (Fig. 5.7.4(a)) into a more wrinkled flamelet-type structure. Areas of distributed flame type are however still apparent since the smallest eddy sizes only slightly increased.

The influence of the integral length scale on the averaged temperature profiles (Figs. 5.7.5 and 5.7.6) is similar to the effect of u' discussed in the previous section. The reaction zone is stretched and consequently the gradients decrease. The broadening of the reaction zone is though more distinct than in the cases discussed before, and the temperature and species therefore need longer to reach their equilibrium states. The RMS temperature profiles in Fig. 5.5(b) reveal strongly enlarged extents and increasing maximum values with increasing L. This stems from the shifting of the eddy distribution to larger sizes, resulting in larger fluctuations.

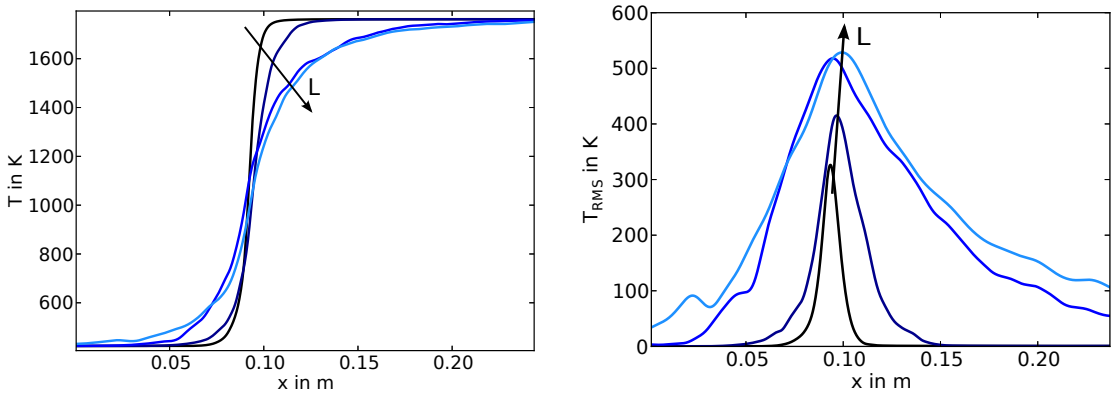

(a) mean temperature (b) temperature RMS

Figure 5.7.5.: Mean and RMS temperature profiles for different integral length scales and same turbulent velocity fluctuations $u' = 10\,\mathrm{m/s}$.

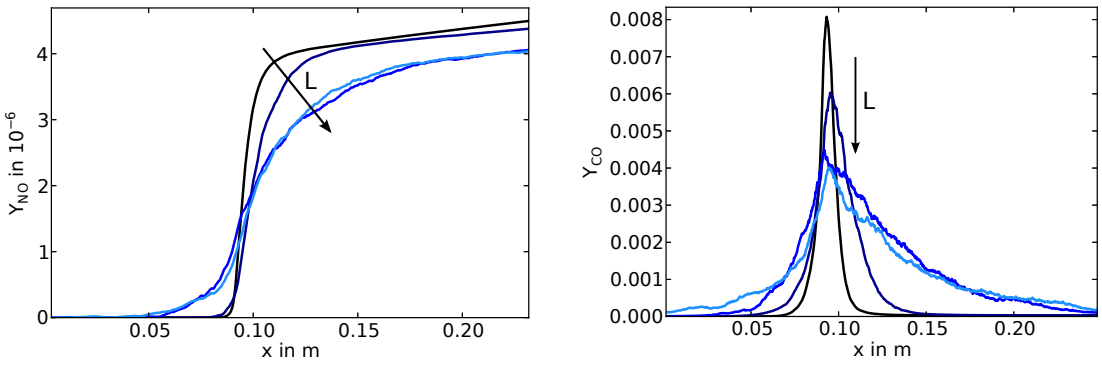

(a) NO mass fraction (b) CO mass fraction

Figure 5.7.6.: Mean species profiles of emissions NO and CO for different integral length scales and same turbulent velocity fluctuations $u' = 10\,\mathrm{m/s}$.

In contrast to the previous section, the maximum in the CO mass fraction distributions decrease with increasing integral length scale L. This is caused by the flamelet-like structure, which corresponds to a folded flame with small thickness. The values of the properties therefore change between unburnt and burnt, which leads to a faster CO oxidation than for a thickened or corrugated flame. On the other hand, size of the reaction zone is increased and thus the domain of CO formation.

5.7.3. Turbulent flame speed

The turbulent flame propagation speeds, u_t, for the different cases have been assembled in Fig. 5.7.7. For means of a better comparison, the propagation speeds are plotted against turbulent Reynolds number. As expected (and already shown in Sec. 5.6), u_t increases mainly linearly with Re_t. However, the increase is different for the two parameters L and

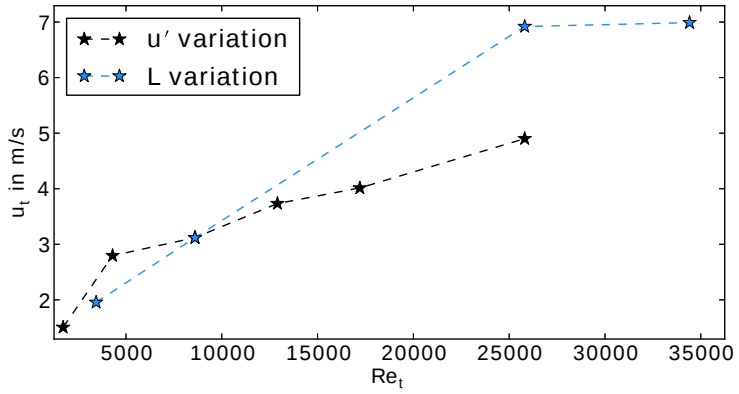

Figure 5.7.7.: Mean turbulent flame propagation speeds for different integral length scales and different turbulence intensities plotted against turbulent Reynolds number Re_t.

u'. For variations in L the gradient is larger, and higher values of turbulent burning velocity are reached for high turbulent Reynolds numbers ($\gtrapprox 8000$). These observations are also consistent with those of the mean profiles, which revealed a stronger broadening of the reaction zone for variations in L compared to that of u'. From this we conclude that, at the same turbulent Reynolds number, the eddy sizes, rather than the turbulence intensity itself, mainly influence the flame broadening and flame propagation speed.

6. Impact of equivalence ratio oscillations on the properties and emissions of a lean premixed flame

Equivalence ratio fluctuations occur due to the imperfect mixing of fuel and air mass flows at the point of fuel injection. Variations in the fuel-air mixture arriving at the flame front lead to heat release rate fluctuations. This mechanism is one of the main drivers for combustion instabilities at lean conditions (Lieuwen & Zinn 1998, Lieuwen et al. 1998). Perturbations in fuel-air ratio affect the heat of reaction, the flame speed, and indirectly the flame area and thus generate oscillations in heat release rate (Cho & Lieuwen 2005, Shreekrishna et al. 2010). This sequence of mechanisms is shown schematically in Fig. 6.0.1.

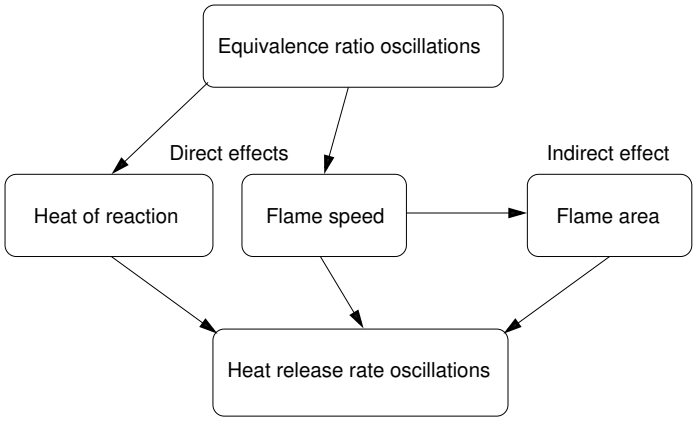

Figure 6.0.1.: Processes generating heat release rate oscillations caused by perturbations in fuel-air ratio.

In the present chapter, we numerically investigate the influence of periodic equivalence ratio oscillations on on strongly turbulent lean premixed flames using detailed chemistry. We compare the results to laminar flames under the same conditions and evaluate pollutant formation of NO_x and CO, heat release rate fluctuations, and species consumption speeds. The flame response is determined for a large range of oscillation frequencies and amplitudes. The benefit of the turbulent approach used for the simulations is that the effect of small scale turbulence is regarded in addition to large scale stratification. The numerical method utilized for the studies is the one dimensional Linear Eddy Model, as presented in the presented in the previous sections. Gas turbine combustors normally operate within the distributed reaction zone, respectively thin reaction zone regime where small scale eddies play an important role. In comparison to other models for premixed combustion, these regimes are fully captured by the Linear Eddy Model. This makes it particularly suitable for the present investigations. Like DNS, LEM resolves all scales but on a one-dimensional

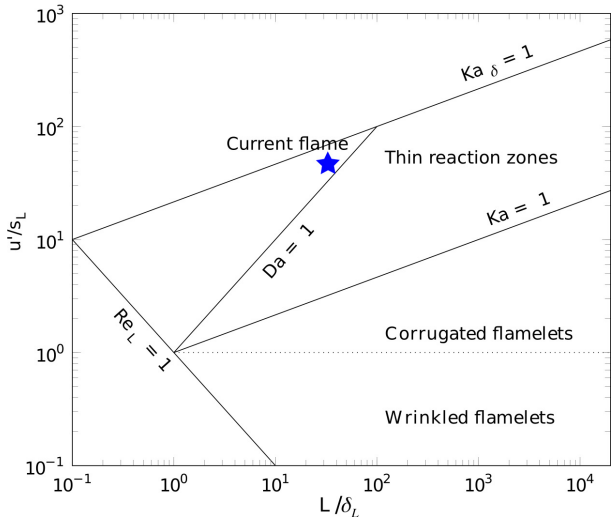

Figure 6.1.1.: Borghi diagram with classification of the investigated flame.

domain and is therefore capable of directly resolving the interaction of turbulence and chemistry at a much lower cost, permitting parametric investigations.

The flame response is determined for a large range of oscillation frequencies and amplitudes. The differences of turbulent and laminar flames are emphasized, and subsequently the flame response to fluctuations in mixture composition is characterized by emissions of CO and NO, heat release rate and consumption speeds.

6.1. Comparison of laminar and turbulent flames at constant equivalence ratio

One-dimensional simulations for the current studies were performed for laminar and turbulent cases. A methane-air mixture with an equivalence ratio of 0.6 preheated to 425 K is investigated. The Kolmogorov and integral scales for the Linear Eddy Model were set to 10^{-4} m and 0.025 m, respectively. The turbulent diffusivity D_t was determined from the relation $D_t = {}^{u'L}/_{C_\lambda}$, with $u' = 10$ m/s. The constant C_λ was taken to be 15, which led to good results for similar flames in previous studies (Smith & Menon 1996). These conditions represent a flame in the thin or distributed reaction zones combustion regime, typical for gas turbine combusters, whose effect on stratified combustion is investigated (Fig. 6.1.1).

Figure 6.1.2 shows the comparison of the laminar and turbulent flames. Mean temperature, heat release rate, and CO and NO mass fraction profiles are given. Furthermore, an instantaneous temperature profile for the turbulent case is shown. It clearly demonstrates that the turbulent flame features characteristics of distributed (eddy size < laminar flame thickness) as well as flamelet (eddy size > laminar flame thickness) combustion regimes. The mean profiles show the difference in flame respectively reaction zone extent, which leads to a decrease of NO_x emissions and an increase of overall heat release rate and burning velocity for the turbulent flame. Due to a thicker flame, the equilibrium state is reached later for the turbulent flame. The burning velocities are on average 0.22 m/s for the lam-

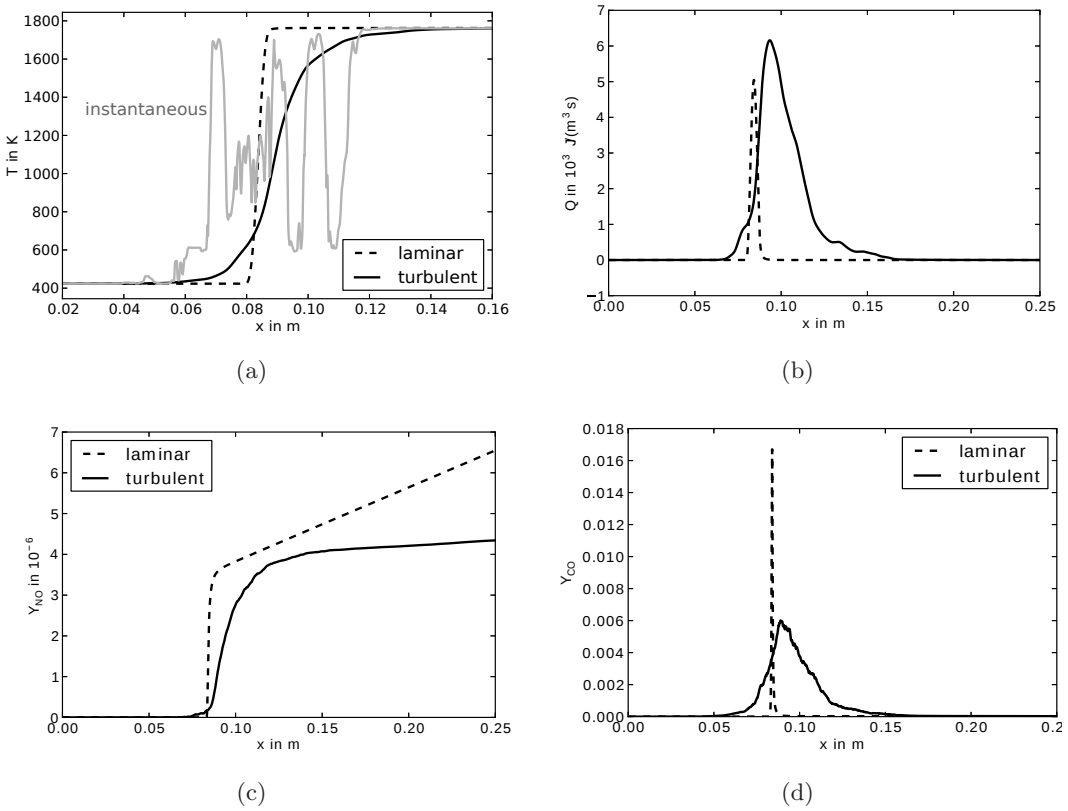

Figure 6.1.2.: Comparison of laminar and turbulent one-dimensional flames. (a) Mean laminar and turbulent, and instantaneous turbulent temperature; (b) mean heat release rate; (c) mean NO mass fraction; (d) mean CO mass fraction.

inar case and 1.7 m/s for the turbulent case. The strong increase in burning velocity for the turbulent case is due to the interaction of small scale turbulence with the flame. This also causes the broadening of the flame. In addition, eddies which are larger than the flame thickness imply the formation of hot pockets within the cold surrounding and increase the burning velocity and heat release rate further.

6.2. Equivalence ratio oscillations

This section describes the conditions set for the equivalence ratio at the inflow boundary, so that the oscillations are consistent for laminar and turbulent cases at different frequencies. We consider a freely propagating flame, thus being able to exclude effects resulting from the anchoring mechanism and vortex interaction. The methane mass fraction at the inflow of the domain is set to a sinusoidal oscillation at constant temperature. The simulations are conducted for a frequency range of 20 Hz to 150 Hz, and the amplitudes are varied in a wide range. The computational domain has a length of 0.25 m for turbulent as well as laminar simulations. The flame is initially located at 0.07 m for the turbulent cases.

The inflow velocity to shift the flame and keep it at the same position was set to the average consumption speed of the product species, H_2O and CO_2, at each time step. The

consumption speed of the products was chosen as it represents the burning velocity accurately (see also discussion in Section 6.5). All simulations were run for 1 s to obtain a sufficient number of oscillation periods for averaging.

Note that the applied shifting approach leads to variations in the mass flow and causes an interaction of equivalence ratio oscillations and shifting speed. However, this procedure allows for an approximately constant flame location within the domain. On the other hand, a constant shifting speed would lead to an oscillating flame front position due to oscillating burning velocities, and to an interaction with the equivalence ratio oscillations, as well.

Due to diffusion effects, the amplitude of the equivalence ratio fluctuations strongly decreases from the inlet to the flame front. This attenuation depends on the perturbation frequency (Fig. 6.2.1(a), top). The distance of the laminar flame from the inlet was set in such a way that the amplitude of the equivalence ratio fluctuations at the flame front corresponds to that of the turbulent case at the same frequency (Fig. 6.2.1(a), bottom).

The attenuation of the equivalence ratio fluctuations was estimated from the frequency response of a one dimensional convection-diffusion process:

$$\frac{\partial \phi}{\partial t} + U\frac{\partial \phi}{\partial x} = D\frac{\partial^2 \phi}{\partial^2 x}. \tag{6.2.1}$$

The transfer function $F(\omega^*)$ for harmonic oscillations of ϕ with dimensionless frequency $\omega^* = 2\pi f \Delta x/U$ over a distance Δx can be obtained from Equ. (6.2.1) as

$$F = \exp\left[\frac{\mathrm{Pe}}{2}\left(1 - \sqrt{1 + 4i\omega/\mathrm{Pe}}\right)\right]. \tag{6.2.2}$$

Here, $\mathrm{Pe} = U\Delta x/D$ is a Péclet number, representing the ratio of diffusion and convection time scales, and U is the convection velocity. The decrease in amplitude of harmonic oscillations is then obtained as the magnitude of the transfer function (6.2.2) evaluated for the corresponding ω^* and Δx.

The relationship between equivalence ratio and dissipation rate for laminar realizations is given in Fig. 6.2.1(b). The scalar dissipation rate χ is in terms of the mixture fraction ξ:

$$\chi = 2D|\mathrm{grad}\,\xi|^2, \tag{6.2.3}$$

where D is a characteristic diffusivity, here taken to be the thermal diffusivity. χ can be interpreted as the inverse of a characteristic diffusion time scale, imposed by the mixture fraction field (Peters 1983). The phase averaged dependence of dissipation rate fluctuations on the equivalence ratio oscillation is plotted for the laminar simulations for three different relative perturbation amplitudes, 0.16, 0.50, and 0.83, for a forcing frequency of 90 Hz, at a position 2 mm downstream of the inlet (Fig. 6.2.1(b)). All curves feature an eight-like shape which is attributed to the quadratic dependence of the scalar dissipation rate on the mixture fraction gradient. It can be observed that the scalar dissipation rate grows strongly with forcing amplitude. For the simulations the described characteristics generally imply that the forcing amplitudes imposed at the inlet will not reach the flame. Diffusive damping increases strongly with frequency so that the oscillation amplitudes in equivalence ratio at the flame front decrease. For turbulent flows the diffusive damping is stronger than for laminar flows since turbulent mixing acts in addition to molecular diffusion.

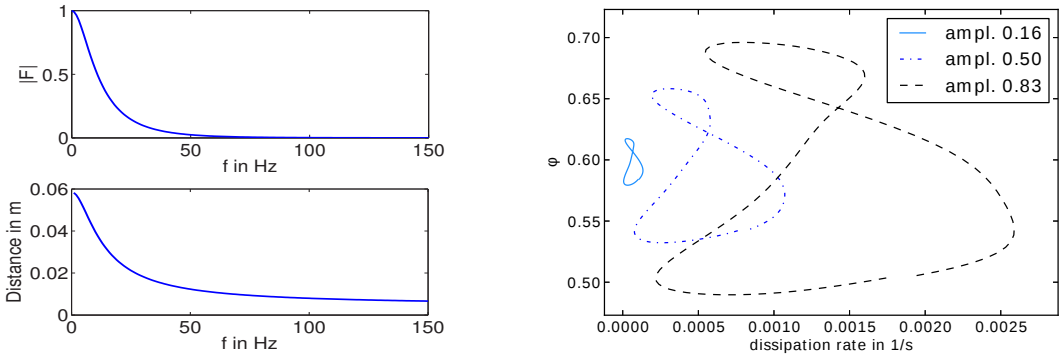

(a) (b)

Figure 6.2.1.: (a) Diffusive amplitude attenuation for the turbulent case (top) and distance between inlet and flame front for the laminar case corresponding to turbulent distance with the same attenuation (bottom); (b) Phase averaged relation between dissipation rate fluctuations and equivalence ratio oscillations 2 mm downstream of the inlet, laminar with variation of relative forcing amplitudes at 90 Hz.

Table 6.2.1.: Relative amplitudes at the flame for different frequencies and relative amplitudes at the inlet.

Ampl. inlet \ f in Hz	20	30	40	50	60	90	120	150
0.16	-	0.016	-	-	0.0021	$4.3{\cdot}10^{-4}$	-	-
0.33	-	0.032	-	-	0.0044	$8.9{\cdot}10^{-4}$	-	-
0.50	-	0.047	-	-	0.0067	0.0014	-	-
0.66	0.144	0.0642	0.031	0.016	0.0088	0.0018	$4.6{\cdot}10^{-4}$	$1.3{\cdot}10^{-4}$
0.83	-	0.081	-	-	0.011	0.0022	-	-
0.99	-	0.096	-	-	0.013	0.0027	-	-

In the following, relative forcing amplitude refers to the amplitude of the equivalence ratio fluctuation at the inlet of the domain divided by mean equivalence ratio. To clarify the meaning of the forcing amplitudes, the relative amplitudes that theoretically reach the flame are given in Tab. 6.2.1 as a function of the forcing frequency and the relative forcing amplitude at the inlet. Furthermore, to illustrate the oscillating conditions at the boundary respectively at the flame, Figure 6.2.2 shows spatial and temporal equivalence ratio distributions for a laminar flame forced at 30 Hz. It can be observed that even for high relative forcing amplitudes at the inlet and low frequencies, the flame will not experience stoichiometric or rich conditions. The Strouhal number which we define here as $\mathrm{St} = \dfrac{\omega \delta_{th}}{s_{L/T}}$, where $s_{L/T}$ is the laminar / turbulent burning velocity, allows for a better comparison of the results. It is given for the considered frequency range in Tab. 6.2.2 for laminar and turbulent cases. The values for δ_{th} and $s_{L/T}$ are taken from the unperturbed flames ($\delta_{th,T} = 0.010$m, $\delta_{th,L} = 0.0008$m, $s_T = 1.7$m/s, $s_L = 0.22$m/s).

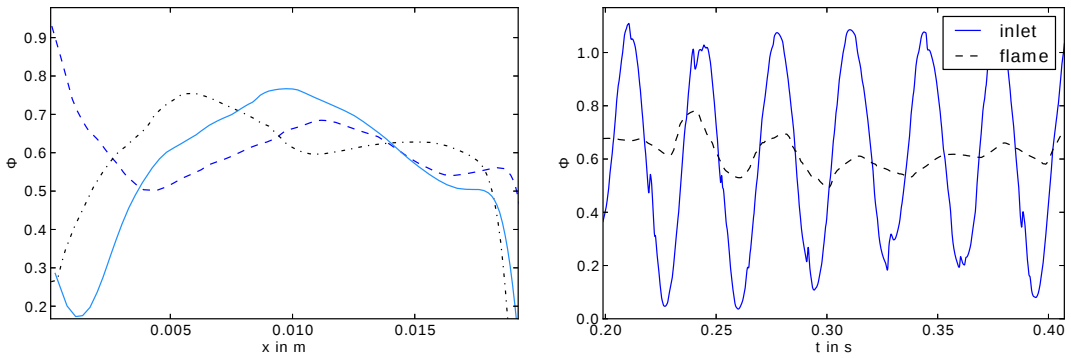

(a) (b)

Figure 6.2.2.: (a) Spatial equivalence ratio distribution from inlet to flame at different times; (b) equivalence ratio history at the inlet and shortly upstream of the flame (case: laminar, 30 Hz, relative amplitude 0.99).

Table 6.2.2.: Strouhal numbers for laminar (L) and turbulent (T) flames.

f in Hz	20	30	40	50	60	90	120	150
St_L	0.46	0.69	0.91	1.14	1.37	2.06	2.74	3.43
St_T	0.74	1.11	1.48	1.85	2.22	3.33	4.44	5.54

6.3. Influence of equivalence ratio oscillations on NO and CO emissions

The emissions of NO and CO underlie strict regulations in modern gas turbine engines. It is therefore essential to be able to control the emissions and to estimate their behavior under unsteady conditions. The qualitative (steady-state) behavior of NO and CO as a function of the equivalence ratio is given in Fig. 6.3.1. The present studies concentrate on the lean combustion regime where modern gas turbines operate due to coexistent low NO and CO emissions. Both pollutants exhibit a nearly exponential growth with increasing equivalence ratio in the lean region. NO reaches its maximum close to stoichiometric conditions and decreases in the rich region whereas CO further increases. In the very lean combustion regime CO grows again due to incomplete combustion. Important for the present studies is to note that NO as well as CO are convex functions of the equivalence ratio for lean conditions.

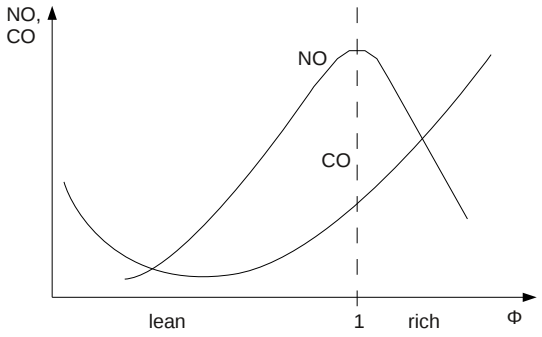

Figure 6.3.1.: Qualitative behavior of NO and CO vs. equivalence ratio.

Figures 6.3.2 and 6.3.3 show the influence of the forcing amplitude and forcing frequency on the emissions of CO and NO for laminar and turbulent cases. The values of the mass fractions of CO and NO for the particular cases are temporal averages taken at a position 10 cm downstream of the mean flame position. Regarding the amplitude dependence in Fig. 6.3.2, it can be observed that for 30 Hz the emissions increase with forcing level up to a relative perturbation amplitude of 0.66 for the laminar and 0.83 for the turbulent flame. This behavior can be attributed to the convex dependence of NO and CO on the equivalence ratio which causes higher mean values of the NO and CO emissions in the presence of sinusoidal equivalence ratio oscillations than for the averaged steady state equivalence ratio. This mechanism is well known and was among others discussed in Paschereit et al. (1999). Similar effects are also found from the measurements conducted on a bluff-body flame (Sec. 8.4). In these experiments, however, other effects were present in addition, and the outcome is not as distinct as for the present simulations.

The strongest increase in emissions is observed for forcing at 30 Hz because the highest amplitudes reach the flame for this forcing frequency. Higher emissions are also found for forcing at 60 Hz and, in weaker form, for 90 Hz. For higher amplitudes at 30 Hz, the emissions decrease again for laminar as well as turbulent simulations. NO and CO emissions follow very similar trends. Comparing laminar and turbulent simulations, the following differences can be observed: for 30 Hz the increase in emissions is less distinct and the decrease for higher amplitudes is stronger for turbulent than laminar cases. The maximum NO emissions are higher for the laminar case whereas the maximum CO emissions are higher for turbulent cases. For forcing at 60 Hz, there is an increase of emissions for both laminar and turbulent simulations and no maximum is reached. For 90 Hz the increase of emissions due to forcing in the laminar case is small. In the turbulent case, the emissions stay more or less at a constant level up to an amplitude of 0.83 (though a slight minimum is observable at around 0.6) and then decay to a value lower than that without forcing.

The frequency dependence in Fig. 6.3.3 shows higher emissions for decreasing frequency. For the turbulent flame and 20 Hz forcing the emissions are again lower than for 30 Hz.

As suggested earlier, the increase in emissions can be related to the convex relation between NO and CO emissions and the equivalence ratio. The non-linear behavior, i.e. the decrease of emissions for high forcing amplitudes, can partly, for NO, be attributed to the dependence of NO emissions on the equivalence ratio as well. When forcing with a sufficiently high amplitude, NO would decrease again as the equivalence ratio extends into the rich combustion region. This is not the case for CO, and also the amplitudes of oscillation at the flame front are for none of the cases sufficiently high to extend into the rich regime (cf. Tab. 6.2.1). The effect seen here is rather caused by the interaction of the burning velocity and the oscillation in equivalence ratio. As mentioned in Sec. 6.2, the velocity and therefore the mass flow at the inlet is not constant since this corresponds to the instantaneous burning velocity. This results in a non-sinusoidal oscillation at the flame front (cf. Fig 6.2.2). Depending on the phase between inflow equivalence ratio oscillation and burning velocity, this may result in amplification or damping. The present observations suggest a dampening effect for high amplitudes at 30 Hz for both turbulent and laminar cases and at 90 Hz for the turbulent case.

The slight minimum at an amplitude around 0.6 in the turbulent cases with forcing at 60 and 90 Hz suggests an additional effect, which is attributed to the damping of turbulent fluctuations when forcing is applied. This behavior will be further discussed in Sec. 6.5

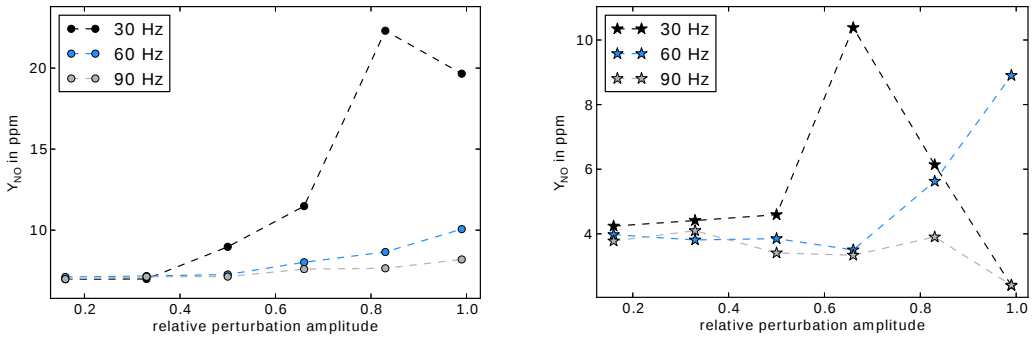

(a) laminar (b) turbulent

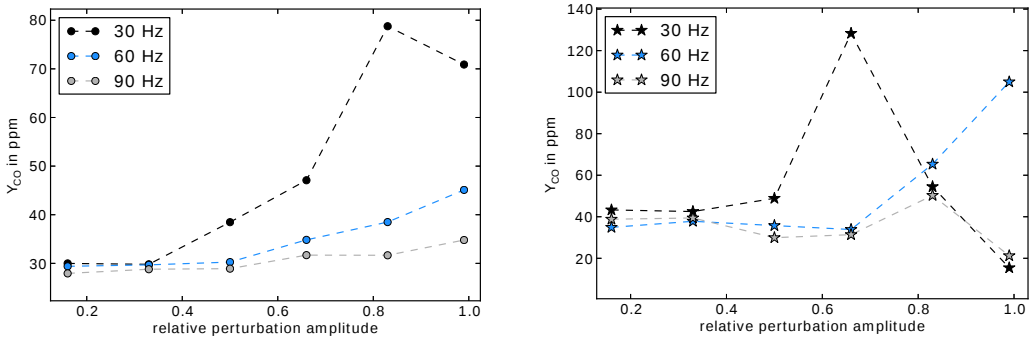

(c) laminar (d) turbulent

Figure 6.3.2.: Influence of forcing amplitude on mean emissions of NO and CO. (a) Mean NO mass fraction, laminar; (b) mean NO mass fraction, turbulent; (c) mean CO mass fraction, laminar; (d) mean CO mass fraction, turbulent

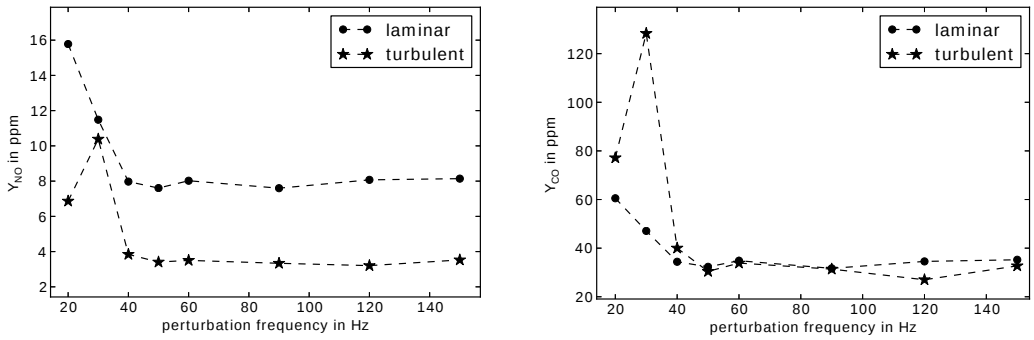

(a) (b)

Figure 6.3.3.: Influence of forcing frequency on mean emissions of NO and CO at a relative forcing amplitude of 0.66. (a) Mean NO mass fraction; (a) mean CO mass fraction

when considering the consumption speeds.

Figure 6.3.4 presents the phase averaged relation between CO fluctuations 10 cm down-

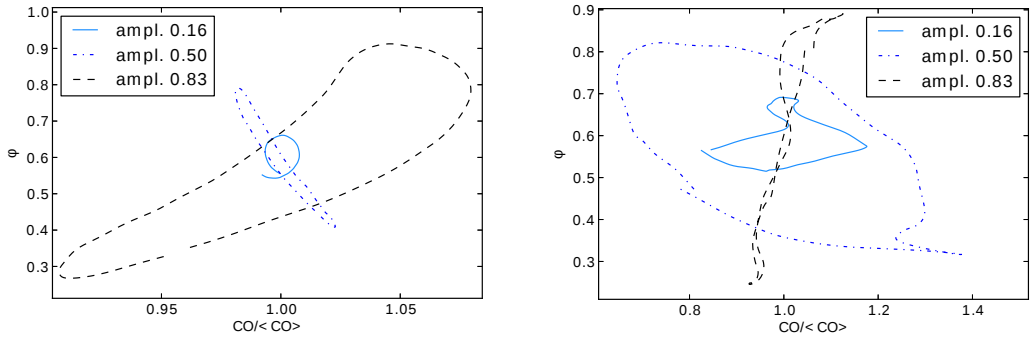

(a) laminar (b) turbulent

Figure 6.3.4.: Phase averaged relation between CO fluctuations 10 cm downstream of the flame and equivalence ratio oscillations at the inlet for 30 Hz and different forcing amplitudes. (a) laminar; (b) turbulent.

stream of the flame and equivalence ratio oscillations at the inlet for 30 Hz and different forcing amplitudes for laminar and turbulent simulations. The results exhibit strongly varying behavior for the different amplitudes and the laminar and turbulent flames. This implies different phase dependencies and is consistent with the explanation given above.

6.4. Influence of equivalence ratio oscillations on the heat release rate

The heat release rate and especially heat release rate fluctuations play an important role in gas turbines since they interact with pressure fluctuations and may enhance thermoacoustic instabilities under certain conditions.

Figure 6.4.1 shows the amplitude and frequency dependence of heat release rate fluctuations for laminar and turbulent simulations and in addition the influence of the forcing amplitude on the mean heat release rate. The heat release rate fluctuations for laminar and turbulent cases show in general a similar behavior. For all frequencies an increase in fluctuation amplitude with forcing amplitude can be observed. For the turbulent cases the heat release rate fluctuation amplitude decreases again for 30 Hz for forcing amplitudes higher than 0.66 and for 90 Hz for forcing amplitudes higher than 0.83. Figure 6.4.1(c) presents the frequency dependence for a relative perturbation amplitude of 0.66 and reveals a strong increase in heat release rate fluctuations for decreasing perturbation frequency. For frequencies higher than 60 Hz, the influence of forcing is negligible.

The non-linear response of heat release rate fluctuations was investigated in experimental studies (Balachandran et al. (2011), Kim et al. (2011) and also in our own studies in Sec. 8.1), where the heat release was determined via CH* and OH*-chemiluminescence. Note that caution is advisable when comparing chemiluminescence and heat release rate especially when the flame is subjected to equivalence ratio modulations since chemiluminescence is not only a function of heat release rate but also of fuel/air ratio (Shreekrishna et al. 2013, Schuermans et al. 2004). In these studies, the non-linear response could be, for

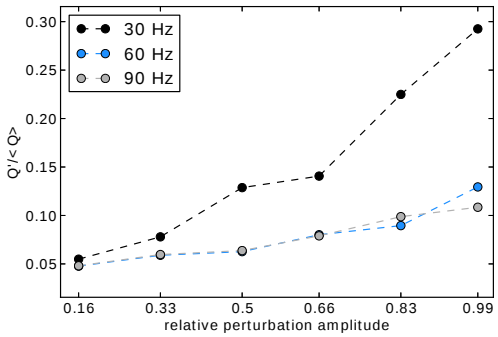

(a) Heat release fluctuation, laminar

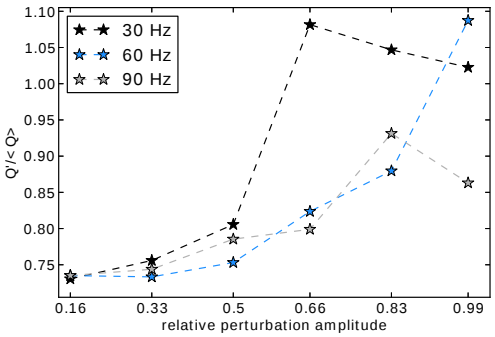

(b) Heat release fluctuation, turbulent

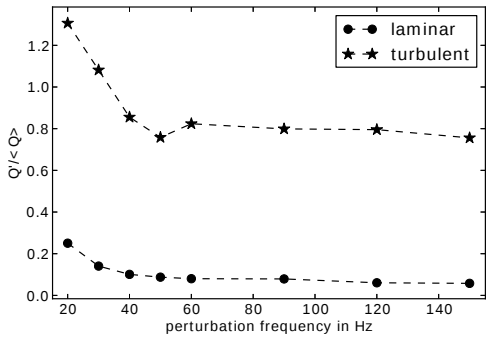

(c) Heat release fluctuation; relative forcing amplitude of 0.66

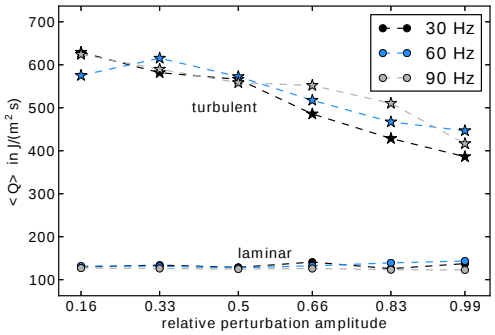

(d) Mean heat release rate

Figure 6.4.1.: Amplitude and frequency dependence of the relative heat release rate fluctuations for laminar and turbulent flames (a)–(c) and the influence of forcing amplitude on the mean heat release rate (d).

certain cases, solely attributed to fluctuations in equivalence ratio. Mechanisms responsible for nonlinear effects in the heat release rate fluctuations were investigated analytically and numerically by Shreekrishna et al. (2010) and Birbaud et al. (2008). They found that the heat release rate saturation for equivalence ratio oscillations at lean conditions is dominated by flame kinematics originating from fluctuations in the flame position associated with oscillations in flame speed. In the present work, the flame is kept at a constant position, the equivalence ratio oscillations induce fluctuations in burning velocity, which in turn alter the inflow velocity. The varying inflow velocity then interacts with the oscillations in equivalence ratio oscillations.

The turbulent simulations exhibit heat release rate fluctuations of about 70% of the mean heat release rate for the unforced case which increase to values of more than 100% when forcing is applied. The laminar flame, in contrast, reaches a maximum fluctuation level of 30% of the mean heat release rate. This is also the reason why in the turbulent case only very high oscillation levels, higher than the incoherent turbulent fluctuations, lead to an increase in heat release rate fluctuations. Corresponding effects were observed in the experiments with a bluff-body flame in Sec. 8.1.

Regarding the mean heat release rate in Fig. 6.4.1(d) it is interesting to note that it

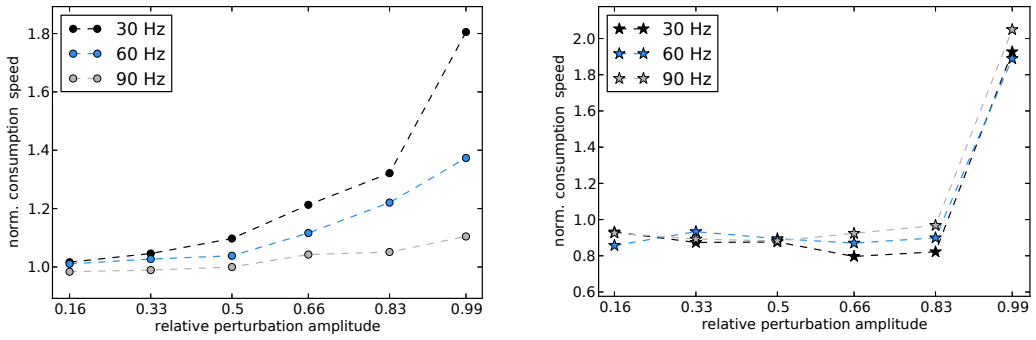

(a) Laminar

(b) Turbulent

Figure 6.5.1.: Consumption speeds for CH_4 and O_2, averaged, for different forcing amplitudes and frequencies, normalized by the unforced burning velocity.

decreases with amplitude in the turbulent case for all considered frequencies. For the laminar case the mean heat release rate increases slightly but remains overall at similar values for all amplitudes and frequencies. The decreasing heat release rate for the turbulent cases is caused by decreasing mass flow rates, which in turn are due to decreasing burning velocities. This will be discussed in detail in Sec. 6.5.

6.5. Influence of equivalence ratio oscillations on the burning velocity

The burning velocity is one of the most important parameters in premixed combustion. It couples directly with the flow field and perturbations in the equivalence ratio. For steady state considerations, the consumption speeds (Equ. 5.3.1) for major species compare quantitatively well and correspond to the burning velocity. In unsteady conditions this does not apply anymore. We will therefore regard consumption speeds of the following species groups, which exhibit similar behavior: reactants (O_2 and CH_4), products (CO_2 and H_2O) and pollutant species (NO). Differences between the consumption speeds of these groups and possible reasons for this will be discussed in this section. The consumption speed groups are averaged, i.e. $s_{C,CH_4+O_2} = 1/2(s_{C,CH_4} + s_{C,O_2})$, and the temporal mean response is plotted against forcing amplitude (Fig. 6.5.1, 6.5.2, and 6.5.4) and frequency (Fig. 6.5.5) for laminar and turbulent simulations. The consumption speeds are normalized by the unforced laminar respectively turbulent burning velocities, 0.22 m/s and 1.7 m/s.

The laminar case in Fig. 6.5.1(a) shows an increase in reactant-consumption speed with forcing amplitude. This is expected as the oscillations were directly imposed on the methane and oxygen mass fractions and there is, as for NO and CO, a convex dependence of the burning velocity on equivalence ratio for the lean regime (around $\phi = 0.6$). The turbulent case in Fig. 6.5.1(b) also shows a growth of reactant-consumption speed but only at a relative forcing amplitude of 0.99.

The influence of forcing on the consumption speed of CO_2 and H_2O (Fig. 6.5.2) is quite different for laminar and turbulent cases. The laminar results exhibit a slight growth

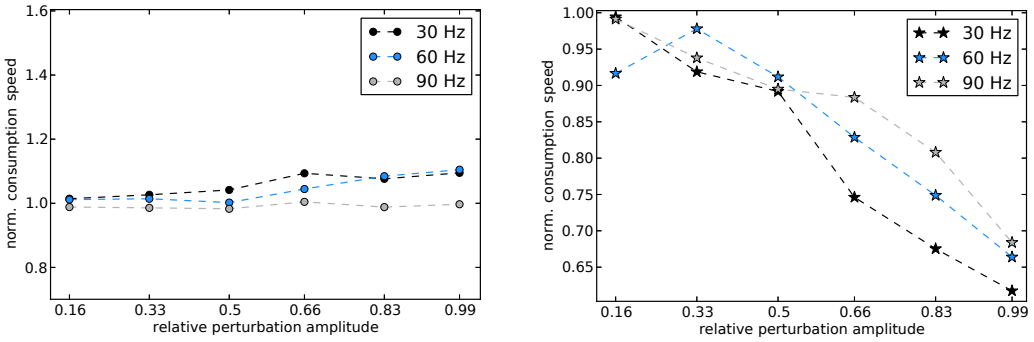

(a) Laminar (b) Turbulent

Figure 6.5.2.: Consumption speeds for CO_2 and H_2O, averaged, for different forcing amplitudes and frequencies, normalized by the unforced burning velocities.

in consumption speeds with increasing forcing amplitude. The turbulent results however show a decrease of consumption speed with increasing forcing amplitudes for all considered frequencies. Since the averaged consumption speeds of CO_2 and H_2O were taken as the inflow velocity, this correlates with the mean mass flow rate and the mean heat release rate (Fig. 6.4.1(d)). Note that it also represents the flame propagation speed which implies a decrease in turbulent burning velocity with forcing. The decrease of CO_2 and H_2O consumption speed with forcing amplitude can be explained by considering the temporal evolution of the consumption speeds of CH_4 and CO_2 for different forcing amplitudes (Fig. 6.5.3). For low forcing amplitudes (Fig. 6.5.3(a)), no distinct periodic but only stochastic behavior can be observed. The histories of the different species consumption speeds agree well. For the higher forcing amplitude (Fig. 6.5.3(b)), periodic patterns are present. It can be observed that turbulent fluctuations in the consumption speeds are suppressed when the forced oscillation is at a minimum. For low values of the methane mass fraction, that is for very lean conditions, the reaction zone broadens and gradients become smaller. For smaller gradients, turbulent eddies have less influence and therefore fluctuations are damped. This damping occurs for all species and is also the reason the mean reactant consumption speeds grow only for very high forcing amplitudes. Similar effects were also observed in the measurements presented in Chapter 8. The damping of turbulent fluctuations could be seen in the heat release rate fluctuations in the presence of forced equivalence ratio oscillations (Sec. 8.1). Furthermore, an evaluation of the turbulent flame thickness and the flame surface density (Sec. 8.3) suggested a decrease of flame propagation speed with forcing, which confirms the findings of this section.

Considering the normalized mean consumption speed for NO (Fig. 6.5.4), the laminar results show an increase with relative perturbation amplitude with saturation at very high forcing amplitudes. This is again caused by the convex dependence of the burning velocity on the equivalence ratio. The turbulent results indicate a superposition of the laminar behavior and the damping of the turbulent fluctuations. It has to be kept in mind here that NO has not reached its equilibrium concentration at the outflow end of the domain. This may be responsible for the differences with respect to the consumption speeds of the other groups considered. However, for steady simulations the NO consumption speeds equal those of the other species for laminar as well as turbulent cases, although the equilibrium

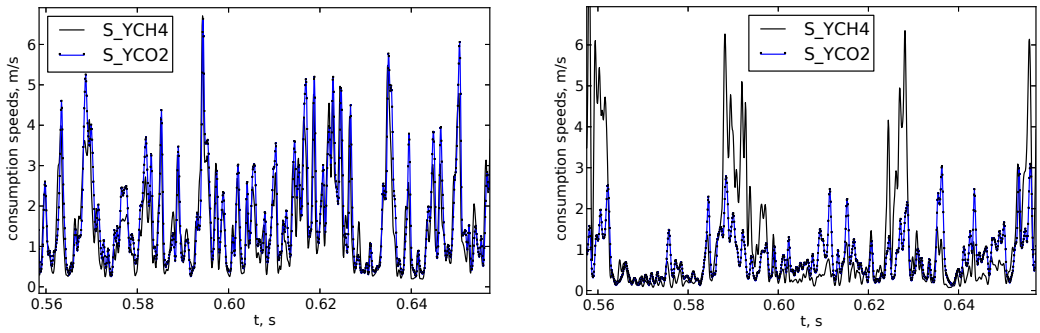

(a) (b)

Figure 6.5.3.: Histories of CH_4 and CO_2 consumption speeds at 30 Hz. (a) relative forcing amplitude of 0.16; (b) relative forcing amplitude of 0.83

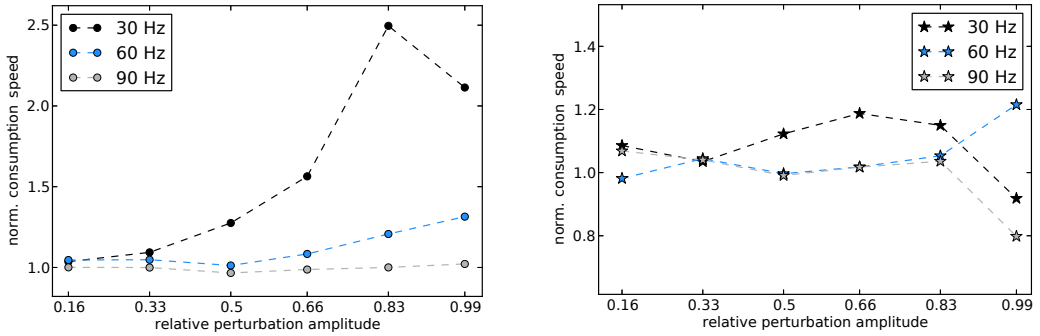

(a) Laminar (b) Turbulent

Figure 6.5.4.: Consumption speeds for NO for different forcing amplitudes and frequencies, normalized by the unforced burning velocities.

is not reached here either.

The frequency dependence of the different groups of consumption speeds at a relative forcing amplitude of 0.66 is given in Fig. 6.5.5. For the laminar case the consumption speed of NO strongly increases with decreasing forcing frequency whereas the consumption speeds of products and reactants do not show major effects. The turbulent results indicate a slight increase in consumption speeds of NO and an in comparison a stronger decrease in consumption speeds of $CO_2 + H_2O$ and $O_2 + CH_4$. The characteristics of the consumption speeds of products and reactants compare well for all considered conditions. The absolute value for the consumption speeds of O_2 and CH_4 are, however, slightly higher than those of CO_2 and H_2O. The frequency dependence is consistent with the explanations given above: the consumption speeds increase with forcing amplitude, strongest for NO, less distinct for the reactants, and almost negligible for the products; the superposed damping of fluctuations increases with amplitude and decreases with frequency in the turbulent flames.

Other computational studies on the impact of equivalence ratio variations on the flame

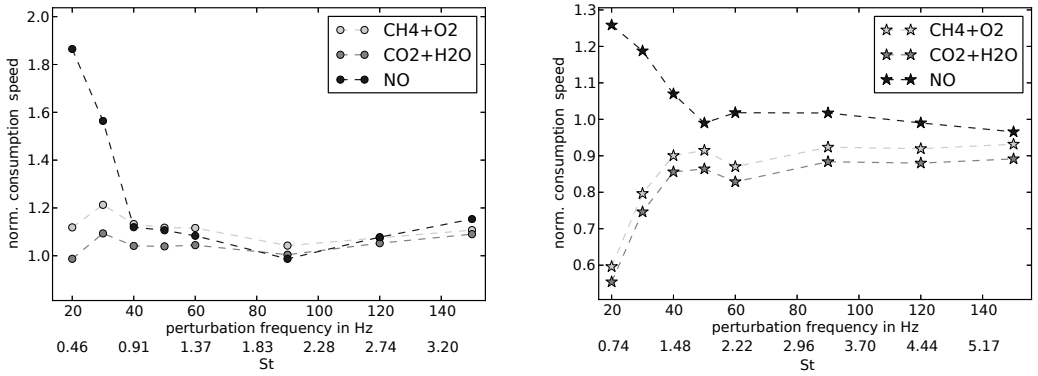

(a) Laminar (b) Turbulent

Figure 6.5.5.: Consumption speeds for different forcing frequencies, divided into CH4 + O2, CO + H2O, and NO, normalized by the unforced burning velocities.

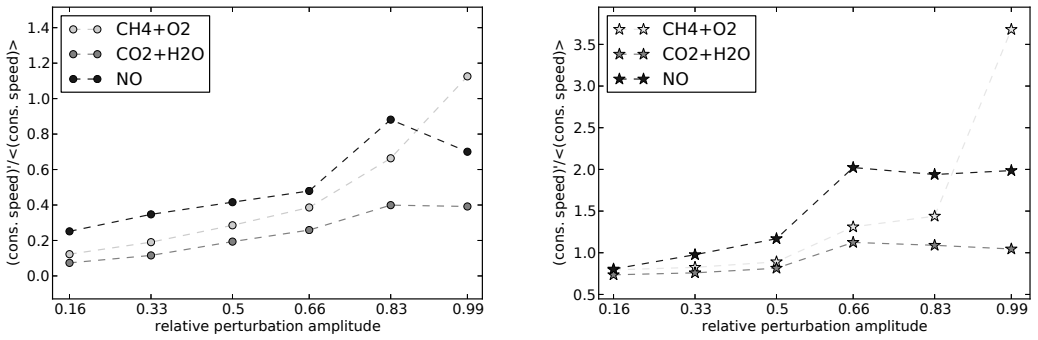

(a) Laminar (b) Turbulent

Figure 6.5.6.: Consumption speed fluctuations for different forcing amplitudes for 30 Hz, divided into reactants (CH_4 and O_2), products (CO_2 and H_2O), and NO

dynamics (Marzouk et al. 2000, Richardson et al. 2010) revealed higher/lower burning rates and heat release rates for back/front supported flames. These effects are intensified for dynamic considerations. The slight increases in burning velocity and heat release rate for the laminar case suggest that the oscillations in equivalence ratio cause a back support of the flame. In the turbulent case it is not clear if the flame is back supported. At first glance the flame rather seems to be front supported regarding the consumption speed of CO_2 and H_2O. However, including the observations on consumption speeds of O_2, CH_4, and NO in the assessment, a back supported flame overlaid with the mechanism of turbulent damping discussed above could apply.

Figure 6.5.6 shows the relative consumption speed fluctuations for 30 Hz plotted against the forcing amplitude. The plots illustrate the dependencies for the different consumption speed groups and for laminar and turbulent cases. As already for the mean results, the fluctuations of the different groups feature different behavior. The product consumption speed fluctuations show characteristics similar to those of the heat release rate fluctuations. The fluctuations grow up to a relative perturbation amplitude of 0.66 and 0.83 for lam-

inar and turbulent cases, respectively, and saturate or even decay for higher amplitudes. The NO consumption speed fluctuations show similar trends but are generally higher than those associated with the product species. As in the case of heat release rate fluctuations, saturation of the consumption speed originates from the nonlinear effects associated with the interaction of oscillations in the inflow velocity and the equivalence ratio. The reactant consumption speed fluctuations directly depend on the equivalence ratio oscillations. Therefore they do not show saturation effects, which in turn will also influence the mean values and contribute to the explanation of the observed characteristics.

6.6. Concluding remarks on the effect of fluctuations in the fuel-air ratio

The influence of equivalence ratio oscillations on the properties of lean partially premixed laminar and turbulent flames was investigated in this chapter. The flame response was characterized by evaluating NO and CO emissions, heat release rate fluctuations, and consumption speeds in dependence on forcing frequencies and amplitudes. The inflow velocity was set to the instantaneous burning velocity.

It was found that emissions of NO as well as CO increase with forcing amplitude up to a certain value. This behavior is related to the convex relation of NO respectively CO and the equivalence ratio. Laminar and turbulent simulations show the same tendencies although differences in absolute values and in the frequency dependence are present. Decreased NO and CO emissions for high forcing amplitudes were attributed to the complex interaction of burning velocity with equivalence ratio oscillations, giving rise to nonlinear effects.

Fluctuations in heat release rate increase with amplitude and saturate for certain frequencies. This is attributed to the convex dependence of the burning velocity on equivalence ratio and the same non-linear effects as for the emissions. The mean consumption speeds were considered separately for reactants, products and the pollutant species NO. A different dependence on the forcing parameters is observed for the different groups. For the laminar case an increase in all consumption speed groups is found, although it is much stronger for reactants and NO.

The turbulent cases exhibit damping of turbulent fluctuations in the consumption speeds when forcing is applied. This becomes more distinct with higher forcing amplitudes and lower forcing frequencies. The damping of turbulent fluctuations leads to a decrease of consumption speeds, which superposes the characteristics found for the laminar case. The burning velocity therefore decreases with forcing amplitude for the turbulent case, and this also results in decreasing mean heat release rates.

Part III.

Experimental investigations

In the present part, the influence of periodic equivalence ratio oscillations on a lean, premixed bluff-body flame is investigated. The flow conditions are strongly turbulent so that the flame is located within the corrugated flamelets / thin reaction zones combustion regime, where gas turbine combustors usually operate. The benefit of this kind of flame is the possibility to study the effect of fuel modulation on the flame and the velocity field and their interaction, separated from effects that are driven by strong coherent flow structures introduced by swirl. To achieve comprehensive insight into the flame dynamics, velocity and OH*-chemiluminescence measurements for periodical fuel mass flow excitation at constant air mass flow were conducted. OH-PLIF measurements provide further insight into the flame front characteristics and exhaust gas analysis gives information on pollutant emissions of NO and CO. Frequencies in the range of 20 Hz–150 Hz and a range of technically relevant amplitudes were considered.

The experimental results presented in this part shed more light on the complex dynamics of turbulent flames subjected to fluctuations in the equivalence ratio. Furthermore, the data is used to support findings from the one-dimensional LEM calculations in Chapter 6 and to validate the simulations in Chapter 10.

Some of the outcomes of this part were published in Schrödinger et al. (2013*a*).

7. Experimental setup

7.1. Burner

The present studies were conducted using a bluff-body stabilized, strongly turbulent, non-swirling flame. The burner consists of a nozzle and a center-body used as flame holder. The nozzle has an upstream diameter of 105 mm and a diameter of 35 mm at the burner exit. The bluff body, which is a cylindrical rod with 10 mm diameter, is mounted on a grid with 90% blockage, 263 mm upstream of the burner exit. The bluff body extends 5 mm downstream the burner exit. The center-body is centered by three 2 mm bars located 14 mm upstream of the burner exit. Fuel is injected through 12 holes with 0.8 mm diameter in the center-body 120 mm upstream of the flame. This allows at the same time for satisfactory mixing and a wide operational range with respect to frequency and amplitude of equivalence ratio perturbations approaching the flame. A sketch of the burner is given in Fig. 7.1.1.

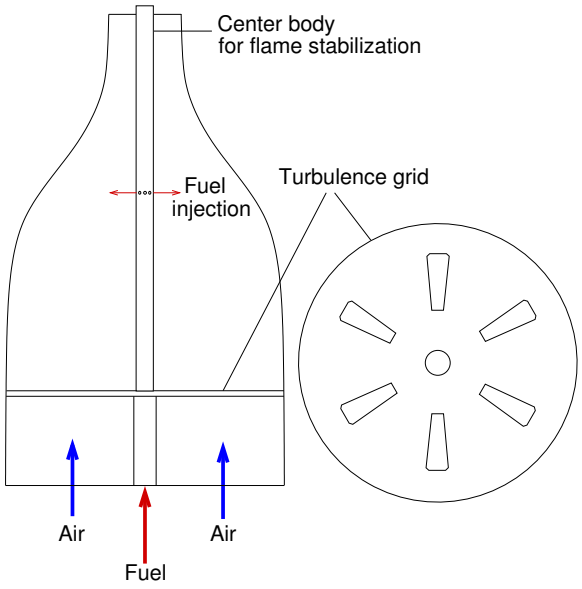

Figure 7.1.1.: Sketch of the burner

The modulation of the fuel massflow was generated with a natural gas injector for automotive applications (Bosch NG12), which was controlled by a square wave voltage signal at the corresponding frequency. Different amplitudes were achieved by employing a bypass parallel to the injector valve where different fuel mass flow rates could be set. The bypass and the injector line were merged before entering the burner. A single line led into the burner and was connected with the center-body tube. Maximum amplitudes up to 60 % at the injection point could be generated this way.

7.2. Measurement techniques

7.2.1. Particle Image Velocimetry (PIV)

A high-speed PIV-system (Quantronix Darwin Duo 100) was used to measure the time resolved velocity field. The system consisted of a dual oscillator/single head diode-pumped Nd:YLF laser and a high-speed CMOS camera (Photron Fastcam SA1.1). A laser sheet of 1 mm thickness was formed in the vertical plane through the burner axis downstream of the center-body with a light sheet optic. A frame rate of 1 kHz in double frame mode was used. A brush based powder disperser was employed to seed zirconium dioxide (ZrO_2) particles with 2 μm nominal diameter into the flow at the burner inlet, approximately 200 mm upstream of the turbulence grid. The delay between the laser pulses was set to 70 μs. The images were post-processed with a final 16 px $\times$ 16 px interrogation area with 50 % overlap, corresponding to a spatial resolution of 1.57 mm. The data was filtered for outliners and interpolated from adjacent interrogation areas.

7.2.2. OH*-chemiluminescence

The spatial distribution of OH*-chemiluminescence intensity was recorded using a high-repetition rate 12-bit, 1024 by 1024 pixel CMOS camera (Photron Fastcam SA1.1) together with an intensifier and a narrow band pass filter at 307 nm, which corresponds to the wavelength of maximum OH chemiluminescent light emission. The resulting image is the integral of light emission intensity along the line of sight. The radial intensity distribution can be reconstructed for axisymmetric flames by means of Abel-deconvolution (Hughey & Santavicca 1982).

The sample rate for image acquisition was set to 1 kHz for cases excited at frequencies up to 110 Hz, and 2 kHz for higher forcing frequencies. 5480, respectively 10920 snapshots were taken at each measurement point for OH*-chemiluminescence as well as PIV.

7.2.3. OH-Planar Laser Induced Fluorescence (OH-PLIF)

A dye laser system in combination with an intensified CCD camera (1376 by 1040 pixel at 12-bit depth, LaVision) equipped with a bandpass filter centered at 308 nm was employed to measure the time-resolved concentration of the OH radical in a plane. The dye used in the dye laser was Rhodamine 6G. The dye was excited using a high energy frequency-doubled Nd:YAG laser (Quantel Dual2) with a wavelength of 532 nm and a pulse energy of 160 mJ. Light at a wavelength of 566 nm was selected from the generated spectrum and amplified by oscillation in the resonator. The amplified light was frequency-doubled to generate a wavelength of 283 nm, which is required for the excitation of OH radicals. When the excited OH molecules fall back to ground level, they emit light at a wavelength of 308 nm. A laser sheet of approximately 1 mm thickness was created in the vertical plane through the burner axis downstream of the center-body. The spatial resolution corresponded to 0.136 mm. 2000 images were recorded with a repetition rate of 5.9 Hz. The gating time of the intensifier was set to 35 ns in order to avoid required for the excitation of OH*-chemiluminescence. Due to effects like re-absorption of the fluorescence, quenching, and laser beam attenuation (Drake & Pitz 1985), the OH-PLIF measurements can only provide qualitative results on

the OH distributions.

7.2.4. Emission analysis

Exhaust gases were measured locally via a probe with a single hole. The probe was traversed so that measurements at different axial and radial positions could be obtained. The probe was water-cooled to 60-70°C to quench further reactions. Downstream of the probe the gas was transported via a heated tube at 180°C to a cold steam trap. The steam was removed to avoid condensation in the tube connecting the steam trap and the gas analyzer and NO_2 absorption in the condensate. The gas analyzer was equipped to measure O_2, CO_2, CO, NO, and NO_2. The analysis for NO and NO_2 is based on UV-absorption, for CO_2 and CO on IR-absorption, and for O_2 on the paramagnetic properties of this species. The recorded data was averaged over a period of 30 s. For uncertainties due to conversion of the species within the probe and measurement uncertainties of the gas analyzer we refer to Göke (2012).

7.2.5. Hot-wire

Velocity fluctuations of the fuel massflow shortly downstream of the injection holes in the center-body were measured with an in-house built hot-wire probe to estimate the excitation amplitudes.

7.3. Measurement conditions

The experiments were conducted at atmospheric pressure for a Reynolds number of 10600 (based on the hydraulic diameter of the nozzle exit) with a constant air mass flow rate of 24 kg/h and a mean fuel (methane) mass flow rate of approximately 1.1 kg/h. This resulted in a mean equivalence ratio of 0.78. A highly turbulent flow was generated using a turbulence grid with 90% blockage. The combustion regime for these conditions is shown in Fig. 7.3.1. The integral length scale and the RMS velocity for different positions in the flame were determined from the time resolved velocity field measurements without excitation. The laminar flame thickness and laminar burning velocities were estimated for a one-dimensional premixed flame at the given conditions.

The fuel mass flow was modulated in a frequency range of 20 to 150 Hz and the influence of varying forcing amplitudes was investigated for 20, 30, 60 and 90 Hz.

As described in the burner setup section, the natural gas injector was positioned outside of the burner so that the forcing amplitudes were damped from injector valve to fuel injection position at the center-body of the burner. The forcing amplitudes at the fuel injection position were measured with a hot wire. The maximum possible forcing amplitude (which is 1 at the natural gas injector) for varying frequencies is shown in Fig. 7.3.2. For 20 Hz an amplitude of more than 0.6 was achieved. The forcing amplitudes decrease with frequency so that the highest possible forcing amplitude for 150 Hz lies around 0.2.

The amplitudes of the equivalence ratio oscillations decay further from fuel injection point to flame front. The decay increases with frequency. Table 7.3.1 gives the relative attenuation

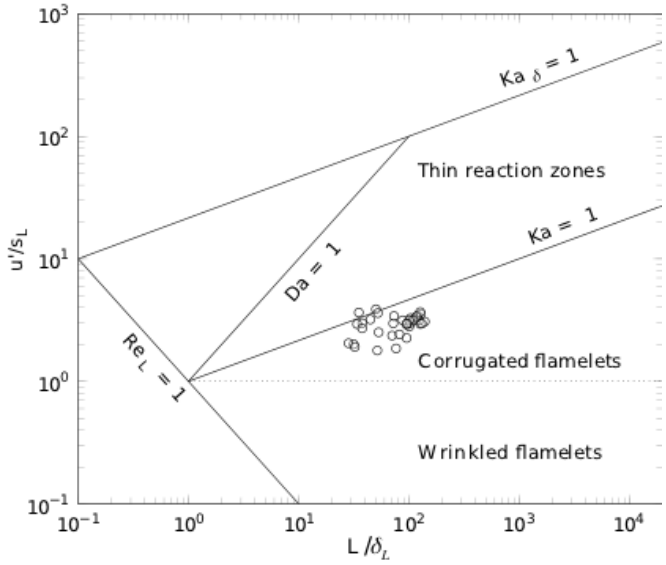

Figure 7.3.1.: Combustion regimes after (Peters 1999) (modified Borghi diagram). Markers indicate the regime of the studied flame.

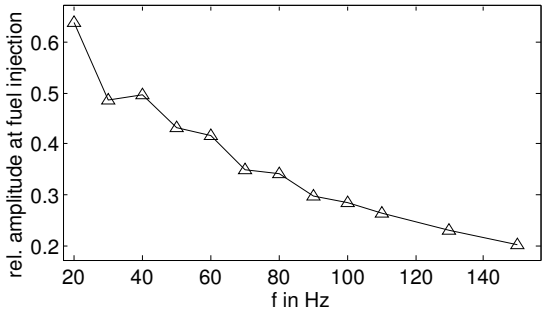

Figure 7.3.2.: Relative fuel flow oscillation amplitudes at fuel injection point (at the centerbody) vs. forcing frequency.

from fuel injection point to flame front, calculated as in Sec. 6.2. The convection velocity, distance, and diffusivity were estimated as the mean bulk velocity ($u = 6.55\,\mathrm{m/s}$), the distance from fuel injection to the end of the bluff body ($d = 0.11\,\mathrm{m}$), and the turbulent diffusivity was calculated from $D_t = {}^{u'L}/_{C_\lambda} = {}^{0.7 \cdot 0.01}/_{3.5}\,\mathrm{m^2/s} = 0.002\,\mathrm{m^2/s}$. Here, u' and L were taken as the maximum values from measurements at the burner exit, and C_λ was set to the smallest value investigated in Smith & Menon (1996), leading to the largest possible diffusivity.

Table 7.3.1.: Relative attenuation from fuel injection to flame and amplitudes at the flame for different frequencies.

f in Hz	20	30	40	50	60	70
attenuation	0.9877	0.9726	0.9518	0.9257	0.8949	0.8597
ampl. at flame	0.62	0.48	0.48	0.40	0.37	0.30
f in Hz	80	90	100	110	130	150
attenuation	0.8210	0.7792	0.7351	0.6893	0.5954	0.5022
ampl. at flame	0.28	0.23	0.21	0.18	0.14	0.10

8. Impact of fuel-air ratio oscillation on a bluff body flame

In this chapter, the effect of periodic equivalence ratio oscillations on a lean, premixed bluff body flame is investigated. Experimental studies on the influence of equivalence ratio oscillations on flame dynamics in literature comprise, among others, investigations on swirl-stabilized flames (Balachandran et al. 2005, Kim et al. 2010, 2011), bluff body flames (Balachandran et al. 2011), weakly turbulent flames (Schwarz et al. 2010) and a backward-facing step combustor (Altay et al. 2009).

Balachandran et al. (2005) investigated the effect of strong acoustic forcing on the response of a lean premixed flame with varying swirl and oscillating mixture composition achieved by choked fuel injection holes. The results suggested that flame kinematics have a major impact on the saturation mechanism at low swirl. In further investigations on a bluff body flame Balachandran et al. (2011) concluded that the response of an acoustically and convectively compact flame is mainly driven by temporal variations in equivalence ratios, whereas for higher frequency (lower wavelength) forcing it is dominated by flame-vortex interaction.

Kim et al. (2010, 2011), studying the response of a partially premixed swirl-stabilized flame subjected to acoustic velocity and equivalence ratio oscillations, found that the linear and nonlinear response is affected by the phase between acoustic velocity and equivalence ratio fluctuations. Furthermore, the amplitude and frequency dependence of the response to equivalence ratio fluctuations was found to be qualitatively similar to that to inlet velocity fluctuations; however, the underlying physics is driven by the nonlinear dependence of the heat of reaction and the burning velocity on equivalence ratio.

Altay et al. (2009) experimentally investigated a lean premixed backward-facing step combustor. They observed that combustion dynamics are primarily governed by flame-vortex interaction and that equivalence ratio oscillations play a secondary role, although they could generate variations in the combustion dynamics and influence the stability of the flame under certain conditions.

Schwarz et al. (2010) analyzed a weakly turbulent conical premixed flame subjected to mixture composition inhomogeneities. Their studies indicate that the flame dynamics are dominated by the velocity perturbations imposed on the mean flow. These results may, however, not be general, as a flame close to stoichiometric conditions was considered. The flame properties are then largely insensitive to perturbations in the equivalence ratio. The importance of the impact of equivalence ratio oscillations is expected higher for laminar flows.

Studies concentrating on non-swirling, fairly turbulent flames and without the excitation of the main flow, as in the present work, are scarce. The current studies focus on the investigation of the effect of oscillations in equivalence ratio on the combustion characteristics.

The flow conditions are fairly turbulent so that the flame is located within the corrugated flamelets / thin reaction zones combustion regime, where gas turbine combustors usually operate. The benefit of this type of flame is the possibility to study the effect of fuel modulation on the flame and the velocity field and their interaction separated from effects that are driven by strong coherent flow structures introduced by swirl.

The studies focus on flame dynamics characterized by OH*-chemiluminescence, which is closely linked to the heat release rate, and the velocity field. The heat release rate and especially heat release rate fluctuations play an important role in gas turbines since they interact with pressure fluctuations giving rise to thermoacoustic instabilities. Furthermore, the impact on flame front characteristics, especially the flame surface density, which is directly related to the heat release rate, is investigated. Finally, burned-gas concentrations of O_2, CO_2, CO and NO under the effect of forcing are discussed.

8.1. Heat release rate

Care has to be taken when chemiluminescent light emission from a flame is to be interpreted in terms of the heat release rate. There is no generally accepted model to relate the chemiluminescence intensity quantitatively to the heat release rate for turbulent flames and varying equivalence ratio. The possibility of correlating chemiluminescence and heat release rate is, for example, discussed in Najm et al. (1998), Lauer & Sattelmayer (2008) and Lauer (2011). Common assumptions for heat release rate measurements based on chemiluminescence are adiabatic systems, temporally and spatially constant equivalence ratio, and low turbulence, strain rate and curvature. Some modeling attempts were made to shed more light on the underlying effects occurring in technical flames (Venkata Nori 2008, Hall & Petersen 2006, Shreekrishna et al. 2013). None of the aforementioned assumptions are met in the present flame (or in any other partially premixed turbulent flame). We will nevertheless refer to the chemiluminescence intensity as heat release rate in the following.

To evaluate the effect of equivalence ratio perturbations on the heat release rate, the OH* chemiluminescence data was spatially integrated for each recorded image. Figure 8.1.1 shows the behavior of heat release rate fluctuations with increasing forcing amplitudes for forcing frequencies of 20, 30, 60, and 90 Hz. Figure 8.1.1(a) presents the results for the original signal whereas Fig. 8.1.1(b) shows the phase-averaged version. The heat release rate fluctuations of the raw signal reveal strongly nonlinear behavior, which can be attributed to different effects. First of all, we will consider the heat release rate fluctuations for the phase-averaged signal to examine their behavior uncoupled from turbulent effects. The heat release rate fluctuations increase approximately linearly with amplitude for all frequencies. Generally, the increase is stronger for lower frequencies, although the 30 Hz and 90 Hz cases show higher levels of oscillation than for 20 Hz respectively 60 Hz forcing at the same amplitude. This indicates a coupling with the flow field through coherent structures around 70 Hz, which will be further discussed in the next section. The 20 Hz and 30 Hz cases further display nonlinear effects for high amplitudes of forcing. As Cho & Lieuwen (2005) pointed out, the heat release response is controlled by three quantities namely heat of reaction, flame speed, and flame area. Naturally, these quantities may interact nonlinearly with each other and with the flow field and the fuel distribution.

Evidently, the forced periodic equivalence ratio oscillations are superposed to turbulent

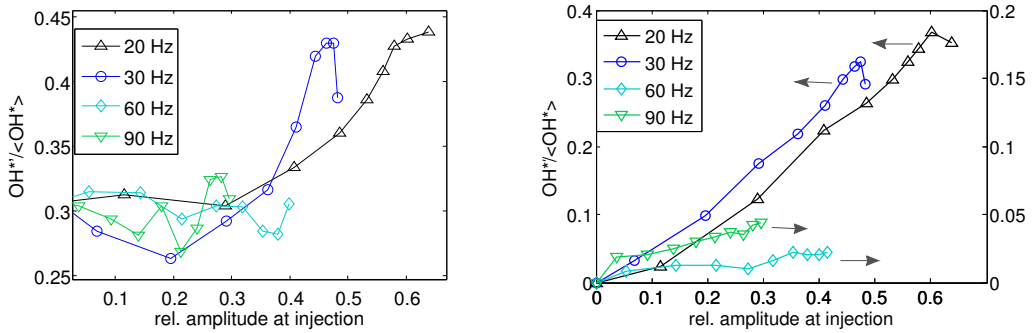

Figure 8.1.1.: Integrated OH* fluctuations vs amplitude for 20, 30, 60, and 90 Hz, normalized by their mean value; (a) rms of original signal, (b) rms of phase-averaged signal.

fluctuations (Fig. 8.1.1(a)). For the unforced case, the level of normalized heat release rate fluctuations is already 0.3 so that only oscillations due to forcing that are fairly high increase the overall heat release rate fluctuations. The results additionally suggest a dampening effect on turbulent fluctuations. This is particularly evident for 30 Hz and 90 Hz at low amplitudes of forcing but also for the other cases and amplitudes when subtracting raw and phase-averaged results. The damping is seen to increase with amplitude (not shown here).

Figure 8.1.2 presents the amplitude of the normalized integrated OH*-chemiluminescence fluctuations and the phase between the OH*-chemiluminescence and the equivalence ratio oscillations versus frequency for maximum amplitudes obtained (see Fig. 7.3.2). The fluctuations attenuate with frequency up to a frequency of 60 Hz and then slightly increase again. A local maximum forms around 70-80 Hz, which relates to the coherent structure of the flow field. The difference between the fluctuations calculated from the raw and the phase-averaged signals increases with frequency, which supports the hypothesis that the periodic oscillations have an attenuating effect on the turbulent fluctuations. It has to be kept in mind here that higher oscillation amplitudes reach the flame at lower forcing frequencies. The phase angle between heat release fluctuation and equivalence ratio oscillation decreases almost linearly with frequency. This is indicative for a time lag in the response, associated with convective transport. The phase angle is virtually independent of the forcing amplitude (not shown here).

Phase-averaged oscillations of heat release rate are plotted against the phase-averaged equivalence ratio oscillations for different frequencies at maximum forcing amplitude in Fig. 8.1.3. The diagram emphasizes the discussed findings and shows that the equivalence ratio perturbations at the point of fuel injection extend far into the lean and also into the rich regime for low forcing frequencies.

8.2. Coupling of the heat release rate and the velocity field

A comparison of forced and unforced cases in terms of the mean chemiluminescence and the mean velocity field is given in Fig. 8.2.1. The forced case corresponds to a frequency of

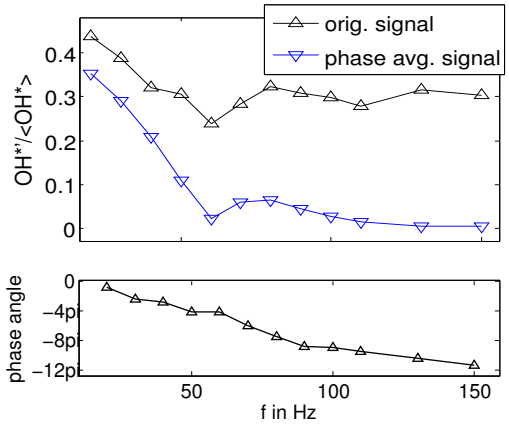

Figure 8.1.2.: Integrated OH* fluctuations vs. frequency for maximum amplitude of forcing, normalized by their mean value.

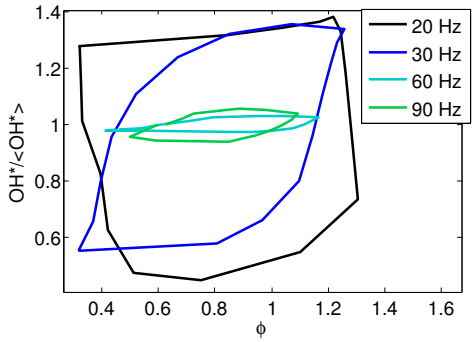

Figure 8.1.3.: Integrated phase-averaged OH* oscillations vs. phase-averaged equivalence ratio oscillations for different forcing frequencies at maximum forcing amplitude.

20 Hz and the maximum possible amplitude. It can be observed that the mean flame shape changes with forcing. The flame length decreases while the flame width increases. This is also visible in the velocity fields. Areas of high velocity move upstream and in positive radial direction.

Figure 8.2.2 presents phase-averaged Abel-deconvoluted OH*-chemiluminescence images and phase-averaged axial velocity fields. For all cases the flame anchors at the bluff body and is located between inner (at anchoring point) and outer shear layer (further downstream). The coupling of velocity field and flame is evident. The flame changes from a short and widely distributed shape at 0° phase angle to a long and thin shape at 135°, until it almost extinguishes at 225°. For the short but widely distributed flame, the velocity field features a strong gradient in axial direction close to the flame holder and a less pronounced variation in radial direction (e.g. 0°). For a strong gradient in radial direction, the flame front is thinner (e.g. 135°), and for a weak gradient in axial direction the flame width is smaller (e.g. 270°).

Phase-averaged signals of equivalence ratio oscillations at fuel injection position, inte-

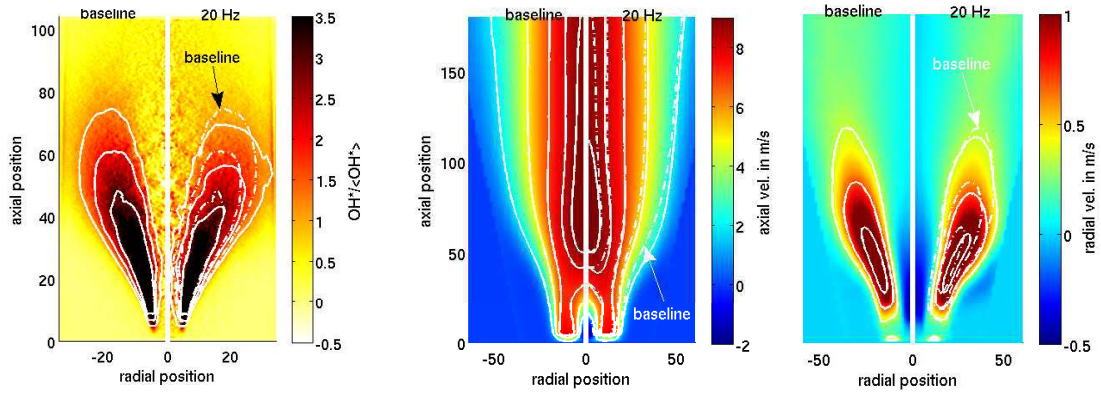

Figure 8.2.1.: Comparison of mean Abel deconvoluted OH*-chemiluminescence (a), axial (b) and radial (c) velocity fields in the axial–radial plane downstream of the burner exit for baseline case without forcing and forcing at 20 Hz and maximum amplitude. Axial and radial positions in mm.

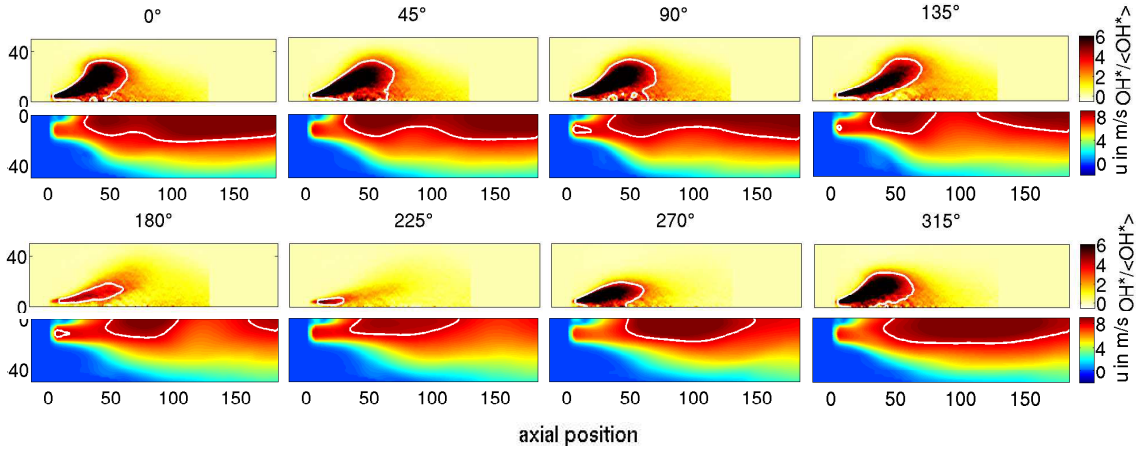

Figure 8.2.2.: Phase-averaged Abel-deconvoluted OH*-chemiluminescence and phase-averaged axial velocity fields for forcing at 20 Hz and maximum amplitude.

grated OH* chemiluminescence, and axial and radial velocities at a point within the flame (axial pos.= 41 mm, radial pos.= 19 mm), all normalized by their means, are given in Fig. 8.2.3 for forcing frequencies of 20 and 60 Hz and maximum forcing amplitude. For the 20 Hz case the oscillation amplitudes of all variables are of the same order of magnitude. For the 60 Hz case, however, oscillations in heat release are negligible while oscillations in radial velocity are almost twice as large as those of the equivalence ratio.

The fluctuating velocities exhibit maxima around forcing frequencies of 30 Hz and 70 Hz (Fig. 8.2.4). The maximum in the axial velocity is most pronounced in the flame. For radial velocity the second maximum is higher than the first one. POD analysis of the isothermal flow field identifies a coherent structure close to 70 Hz. This causes the amplification in velocity fluctuations and leads to the local maximum in the heat release rate fluctuations

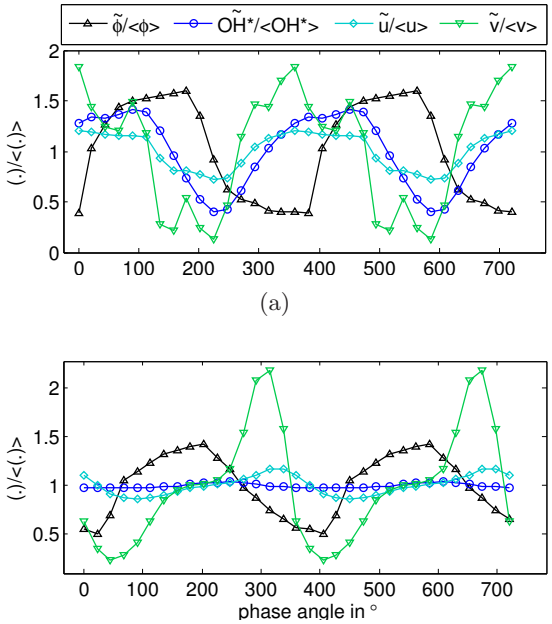

Figure 8.2.3.: Phase-averaged signals of normalized equivalence ratio oscillations at the fuel injection position, integrated OH* chemiluminescence, and axial and radial velocities at (41 mm, 19 mm) vs phase angle for (a) 20 Hz and (b) 60 Hz and maximum forcing amplitude.

around this frequency (see Fig. 8.1.2). The phase angle for both axial and radial velocities decreases with frequency, but weaker than for the heat release rate fluctuations.

To further characterize the axial and radial velocity fluctuations and the coupling with the heat release rate oscillations, the phase-averaged velocity fluctuations are plotted against the phase-averaged equivalence ratio and heat release rate fluctuations for different frequencies and maximum amplitudes (Fig. 8.2.5). The results for different forcing frequencies exhibit varying phase relations between velocities and equivalence ratio as well as heat release rate fluctuations. Again, the high fluctuation amplitudes in the radial velocity are evident.

8.3. Flame front characteristics

The impact of equivalence ratio oscillations on the combustion process is further characterized by investigating the flame front structure. The flame front can be extracted from OH-PLIF as well as Mie scattering images (Steinberg et al. 2012), which are provided by the PIV measurements. Both exhibit a distinct edge at the border of fresh mixture and burnt gas. In the former this is due to strong OH gradient across the reaction zone whereas in the latter the velocity jump across the flame front causes a change in the seeding density. The method for identifying the flame front is similar for both cases. The images were binarized employing global thresholding. For OH-PLIF a fixed threshold was determined iteratively while the threshold for the Mie scattering images was identified with a dynamic algorithm

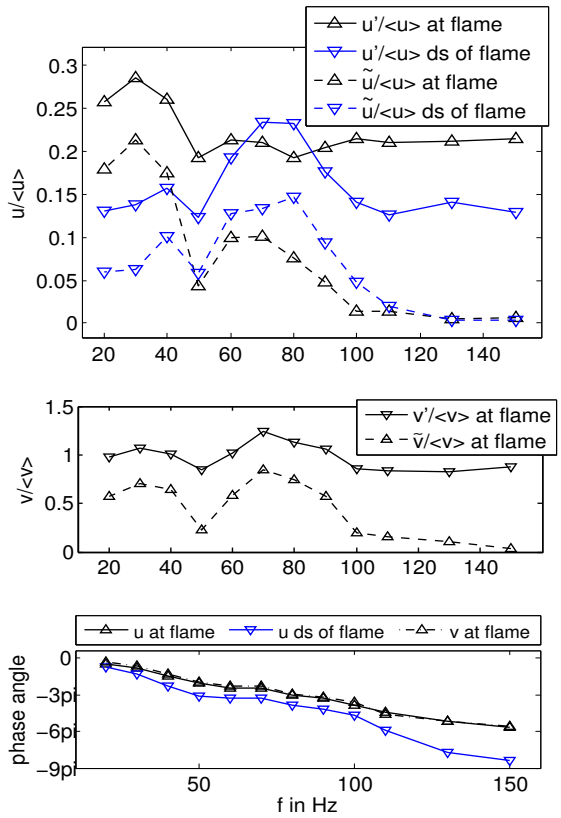

Figure 8.2.4.: Amplitude and phase angle of axial and radial velocity fluctuations for raw and phase-averaged signals vs frequency.

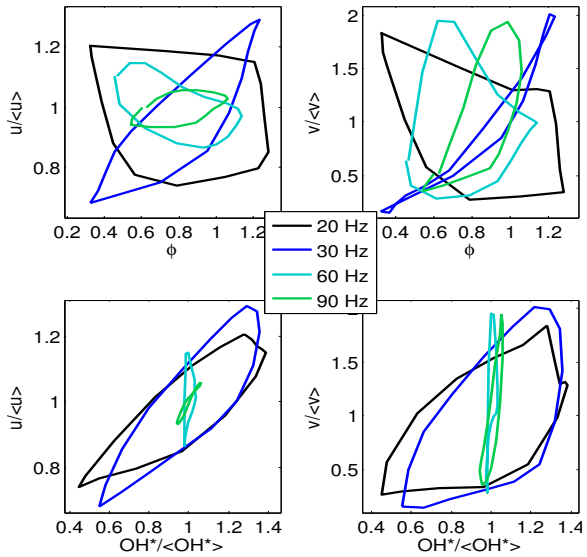

Figure 8.2.5.: Phase-averaged velocity fluctuations versus phase-averaged equivalence ratio and heat release rate fluctuations for different frequencies and maximum forcing amplitudes.

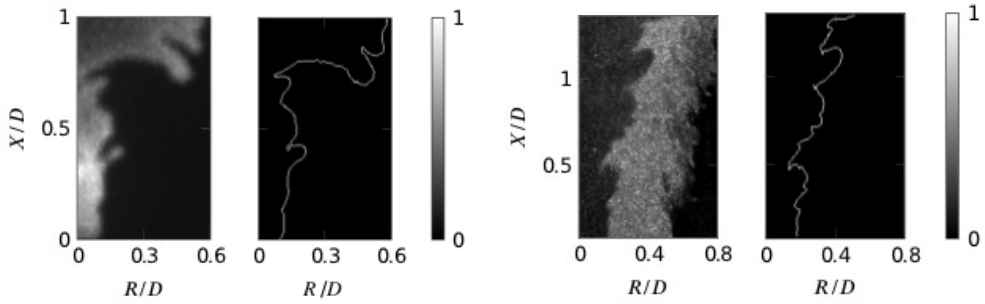

(a) OHPLIF (b) Mie scattering

Figure 8.3.1.: Edge detection for OH-PLIF and Mie scattering. Left figures show the instantaneous intensities and right figures show the detected edges.

(Otsu 1975). A progress variable $c(x,t)$ was introduced, which takes the value 1 in the burnt gas and 0 in the unburnt mixture. The flame front is defined as the interface between $c = 1$ and $c = 0$. Note that this approach only holds for thin flame fronts or flamelets, where the smallest eddies are larger than the reaction layer (Turns 2000). The flame investigated in this work lies within the corrugated flamelets respectively thin reaction zones regime, where turbulent eddies occur that are smaller than the thermal thickness and lead to thickening of the flame. Furthermore strong turbulent fluctuations may cause the formation of pockets of unburnt mixture in the burnt gas and vice versa. Using the described approach to identify the flame front for the underlying flame is therefore questionable. It nevertheless allows to qualitatively classify the studied flames in terms of the flame surface density and the average flame front position.

The edge detection procedure of OH-PLIF and Mie scattering images is shown in Fig. 8.3.1 for intensity distributions from the baseline case at an arbitrary time. Only a cropped half plane of the images was taken into account to avoid areas of blur, disruption or low intensity. D denotes the nozzle diameter at the burner exit. The exemplary intensity distributions for OH-PLIF and Mie scattering show qualitative differences. The Mie scattering image features a strongly cusped and wrinkled flame whereas the OH-PLIF image exhibits a smoother structure. This may originate from the resolution of the intensifier, which is lower than that of the camera, causing reduced effective image quality.

8.3.1. Turbulent flame brush thickness

The turbulent flame brush thickness, δ_T, describes the deviation of the fluctuating flame front from its mean position, that is the area occupied by the time-averaged flame. There are several definition to estimate δ_T (Kheirkhah & Gülder 2013, Lipatnikov & Chomiak 2002), for example, based on the mean progress variable, $\overline{c}$:

$$\delta_T = \left(\max \frac{d\overline{c}}{dx} \right)^{-1}. \tag{8.3.1}$$

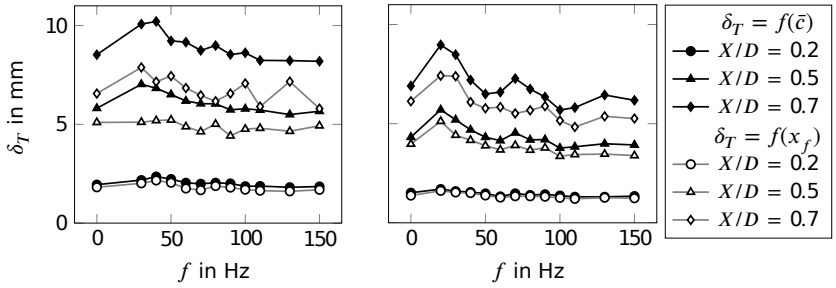

(a) OH-PLIF (b) Mie scattering

Figure 8.3.2.: Turbulent flame brush thickness vs. forcing frequency for three axial positions based on the RMS of the mean progress variable $\overline{c}$ and the flame front position x'_f.

Assuming a Gaussian distribution of the flame front position yields an approximation of δ_T in terms of the RMS flame front position fluctuations, x'_f:

$$\delta_T = \sqrt{2\pi} x'_f. \tag{8.3.2}$$

The results for the flame brush thickness calculated for OH-PLIF and Mie scattering using both definitions of δ_T are given in Fig. 8.3.2. Qualitatively all results show that the turbulent flame brush thickness increases with the distance from the burner, x. The results using the two formulations differ, more pronounced for OH-PLIF than Mie scattering, which suggests that the distribution of the flame front position is not perfectly Gaussian. Furthermore, the values derived from OH-PLIF data are slightly larger than those obtained from the Mie images. This can partly be attributed to the lower quality of the OH-PLIF data and to the fact that strong fluctuations of the fuel mass flow in the fuel line occurred during thee OH-PLIF measurements. They superposed on the coherent oscillations of the fuel mass flow as well as the turbulent fluctuations. δ_T obtained from the Mie scattering data exhibits a second peak around 70 Hz which correlates with the findings in Sec. 8.1 and 8.2 on the heat release rate and the velocity field.

8.3.2. Flame surface density

The flame surface density (FSD), Σ, quantifies the wrinkling of the flame front. It is defined as the area of the flame front per unit volume or, in two dimensions, as the length of the flame per unit area. The flame surface density can be used as a measure of the burning rate (Shepherd 1996) or the flame speed (Bray 1990). It also plays an important role for combustion instabilities since it directly influences the heat release rate (Shreekrishna et al. 2010). In this section we will concentrate on the impact of equivalence ratio oscillations on the flame surface density and its interpretation in terms of flame propagation.

The flame surface density is evaluated employing the approach suggested by Shepherd (1996) which describes the FSD as a function of the mean progress variable:

$$\Sigma(\overline{c}) = \frac{L(\overline{c})}{A(\overline{c})}. \tag{8.3.3}$$

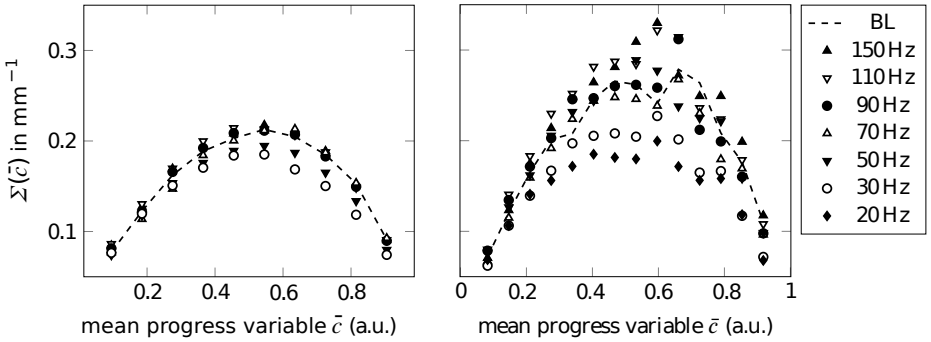

(a) OH-PLIF (b) Mie scattering

Figure 8.3.3.: Flame surface density vs mean progress variable $\bar{c}$.

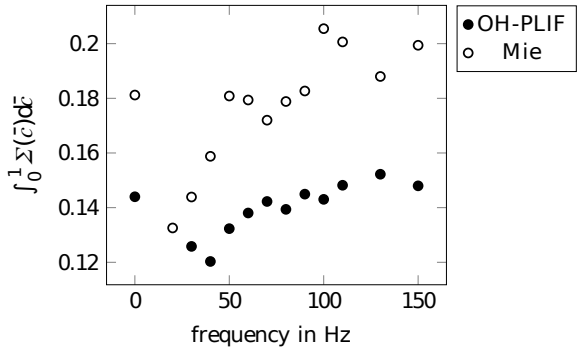

Figure 8.3.4.: Integral of the flame surface density over the mean progress variable space.

As in the previous section a map of the mean progress variable is calculated as the time-average of the instantaneous binary progress variable fields. The resulting mean progress variable field is divided into segments between $\bar{c} = 0.05$ and $\bar{c} = 0.95$. Ten segments are used OH-PLIF and fourteen for Mie scattering. The number of pixels belonging to each segment is determined and multiplied by the corresponding pixel size in square millimeters. This yields the flame area as a function of $\bar{c}$, $A(\bar{c})$. To estimate the flame length, $L(\bar{c})$, each instantaneous flame edge is superposed on the mean progress variable map. The edge is divided into segments of 1 pixel in length. The length as a function of $\bar{c}$ is then calculated with a frequency distribution of $\bar{c}$ values found at the edge segments' coordinates, subsequently multiplied by the segment size in millimeter. Temporal averaging then yields $L(\bar{c})$.

For both measurement techniques, the FSD is evaluated for the same section of the flame ($0.1 < X/D < 1$; $0 < R/D < 0.6$). The FSD as a function of the mean progress variable is given in Fig. 8.3.3. Generally, the values of flame surface densities derived from OH-PLIF are lower than those obtained from Mie scattering. The Mie scattering results exhibit a larger variance for different forcing frequencies. Qualitatively, both measurement techniques indicate a reduction of FSD for low frequency forcing. For OH-PLIF data the FSD for 70 Hz and higher resembles the baseline case. For Mie scattering, in contrast, the flame surface densities for frequencies larger than 90 Hz exhibit higher values than for the baseline case.

To assess the overall effect on FSD, $\Sigma(\overline{c})$ is integrated over the $\overline{c}$ space, and the integrated flame surface density is plotted against the forcing frequency (Fig. 8.3.4). Despite larger absolute values for Mie scattering, the qualitative distrtibutions of the overall FSD for OH-PLIF and Mie scattering are similar. Both feature values smaller than for the baseline configuration at low forcing frequencies and recovery to the baseline level at a frequency of 70 respectively 50 Hz. For higher frequencies (> 100 Hz) the baseline level is exceeded; this is much more pronounced for Mie scattering. It can therefore be concluded that low forcing frequencies, at which high forcing amplitudes reach the flame, lead to a reduction in flame surface density. This could be attributed to effects on the level of flame kinetics, though, more likely this behavior is correlated with the observed damping of turbulent fluctuations. Less turbulence, that is less stochastic motion, results in reduced flame wrinkling and subsequently a reduced flame edge length. At constant or due to coherent motion slightly larger flame area, this causes a lower flame surface density. A lower flame surface density suggests, in turn, a lower burning rate (Kariuki et al. 2012, Shepherd 1996). This agrees with the conclusions drawn from the results of the studies with the Linear Eddy model (Chapter 6).

8.4. Emissions

This section discusses the concentrations of O_2, CO_2, CO and NO with respect to oscillations in fuel-air ratio. The exhaust gas was probed at different axial ($x = 0.02, 0.05, 0.09$ m) and radial positions for the baseline case and 30 Hz forcing and at $x = 0.09$ m on the center axis for all forcing frequencies.

Figure 8.4.1 shows the concentration fields comparing the baseline case with forcing at 30 Hz. The distribution of the emissions in axial and radial direction is consistent with the observations made on the flame shape (Sec. 8.2). Since with forcing the flame is compressed in axial direction and spread in radial direction, compared to the baseline case, the oxygen concentration at the center line increases more distinct and is lower in the outer regions. Naturally, the CO_2 concentration is distributed in an opposite manner. At the centerline mixing with ambient air occurs earlier in the forced case and therefore the concentration of O_2 is larger, the concentration of CO_2 lower, and additionally the temperature is expected to be lower. These effects result in higher CO and lower NO concentration due to quenching; less CO is converted to CO_2 while production of NO via the thermal path is reduced.

The investigation of the impact of oscillations in the fuel mass flow on the pollutant species of NO and CO thus proves to be difficult. Since the flame shape changes with forcing and the measurement field was unconfined, it is impossible to asses the overall emissions and hence to evaluate the effect of periodical equivalence ratio oscillations. The frequency dependence of the concentrations on the center axis 0.09 m downstream of the center-body will be nevertheless discussed (Fig. 8.4.2).

The frequency dependence of O_2 and CO_2 show characteristics that can be attributed to the changing flame shape as discussed before. The O_2 respectively CO_2 concentration gets higher respectively lower with decreasing forcing frequency since the flame becomes shorter in axial direction, and the mixing with ambient air occurs earlier. For higher frequencies the concentrations approach the baseline level. The peak at 80 Hz agrees with the observations of the previous sections; the burner flow is susceptible to instability around this frequency.

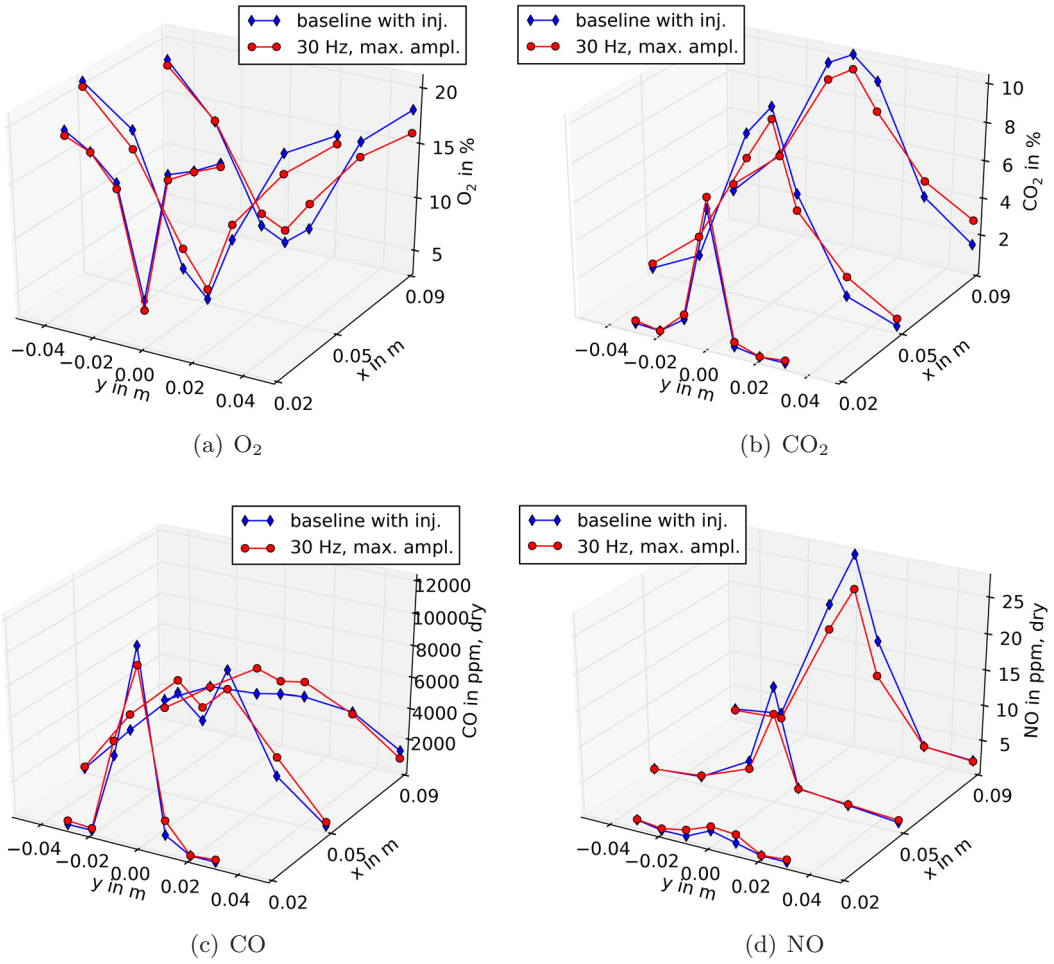

(a) O_2 (b) CO_2

(c) CO (d) NO

Figure 8.4.1.: Molar fractions of emissions for different axial (x) and radial (y) positions.

The distributions of NO and CO concentrations can mostly be explained by those of O_2 and CO_2, and quenching as stated above. The peak of CO at 30 Hz, the adjacent decrease with frequency, as well as the minima of NO at 30 and 80 Hz are consistent with these explanations. There are however features that suggest other effects overlaying the described ones. These features are a less distinct decrease of CO between 30 and 50 Hz in comparison with O_2 and CO_2, the local maximum of CO at 70 Hz, and the maximum of NO at 60 Hz. These characteristics could indicate an increase of CO and NO emissions with forcing, which adds to the above explained effects due to the flame shape. As discussed in Sec. 6.3, CO and NO are both convex functions of the equivalence ratio for lean combustion and therefore their mean increases when subjected to fuel-air ratio oscillations. Thus, this mechanism would explain the irregularities in the CO and NO profiles and verify the results obtained with the Linear Eddy Model.

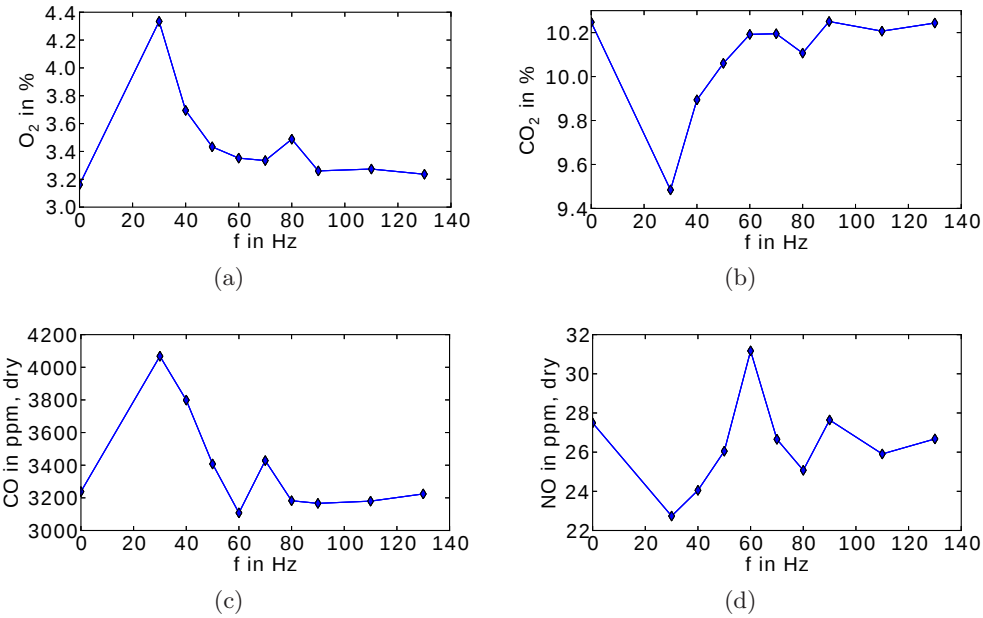

Figure 8.4.2.: Molar fractions of emissions vs. frequency for $x = 0.09\,\mathrm{m}$ and $y = 0.0\,\mathrm{m}$.

8.5. Summary on the experimental investigation of the effect of fuel-air ratio oscillations on a bluff-body stabilized flame

The effect of oscillations in equivalence ratio at constant air mass flow on a bluff body flame was investigated. The flow featured a high level of turbulence so that the flame was located in the corrugated flamelets / thin reaction zones combustion regime, in which also gas turbines operate. The fuel mass flow was modulated in a frequency range of 20 to 150 Hz and a range of amplitudes were investigated to evaluate nonlinear effects. The impact of equivalence ratio oscillations on the heat release rate and the velocity field was examined employing OH*-chemiluminescence and PIV measurements. In addition, the influence on flame front characteristics was studied by means of OH-PLIF and Mie scattering. Concentrations of O_2, CO_2, CO and NO were measured at different positions across the flame.

Nonlinear effects were observed in the heat release rate response. This was attributed to the nonlinear dependence of the burning velocity and the heat of reaction on the equivalence ratio (Cho & Lieuwen 2005) and the superposition of harmonic and turbulent fluctuations. Due to the high level of turbulence, only high amplitudes and low frequencies of forcing lead to an increase of heat release rate fluctuations. The results further suggest a dampening effect of the harmonic oscillations on turbulent fluctuations.

Fluctuations in the flame interact with the flow field and induce velocity fluctuations that feature a maximum around 70 Hz. The amplification of disturbances at this frequency results from a coherent flow structure, which also results in a slight increase in heat release rate fluctuations. Furthermore, the flame shape changes with high forcing amplitudes, which was shown examplarily for a forcing frequency of 20 Hz.

It could be further shown that forcing at low frequencies and high amplitudes causes

an increase in turbulent flame brush thickness and a decrease in flame surface density, indicating a decrease in burning rate. The evaluation of emissions is in line with the flame shape modification for low forcing frequencies and high forcing amplitudes. Irregularities in the CO and NO distributions suggest an increase of these species with forcing.

Many of the outcomes of this chapter encourage the validity of the conclusions drawn from the Linear Eddy Model studies in Chapter 6.3, such as the nonlinear effects in the heat release rate oscillations, damping of turbulent fluctuations via low-frequency, high-amplitude forcing, and the resulting decrease in burning rate.

Part IV.

The Linear-Eddy-subgrid-model

In this part, we introduce a novel coupling strategy for LEM as a subgrid model for LES (LEMLES). The method is based on a predictor-corrector scheme. The thermo-chemical evolution of the LEM is coupled with the velocity and pressure fields of the LES via a divergence constraint. To demonstrate the performance of the coupling in view of physically realistic applications, a strongly turbulent conical V-flame as introduced in Part III is studied. The simulations are run with LEMLES and compared to experimental data and LES simulations using a traditional combustion model.

An introduction to LEMLES, the general LEMLES approach, the novel closure procedure, and a validation of the algorithm for scalar material transport across LES cell boundaries are presented in Chapter 9. Chapter 10 gives results on the V-flame studies, in terms of velocity fields, heat release rate, emissions, and flame front properties.

9. Coupling of LEM and LES

Considering three dimensional reacting flow simulations with RANS or LES, which solely consider the mean respectively large scale motion, reliable (subgrid) models are required, which reproduce the physics on turbulent mixing processes and chemical kinetics of the small – unresolved – scales (Section 9.1). Many commonly used models do not consider the interaction of turbulent mixing, molecular diffusion, and chemical reactions at small scales. A precise description of the dynamics at the small scales might however be crucial for global mixing and combustion processes.

Menon et al. (1992, 1993) first implemented the Linear Eddy Model (LEM) (Kerstein 1989, 1991) as a subgrid model for LES. The Linear Eddy Model describes turbulent mixing processes and molecular diffusion independent of each other on a one dimensional domain. It resolves all relevant physical and chemical scales (see Chapter 5). The LEM subgrid model implementation organizes the diffusion and convection advancement in two processes: 1. Linear Eddy computations are conducted independently in every LES-Cell which advance the diffusion processes on small scales; 2. the transport of scalar information from the subgrid is transported across LES cell borders according to the large-scale resolved velocity field. A further coupling of LEM and LES considers the influence of the subgrid thermo-chemical properties on the LES velocity field. The approach of Menon et al. (1992, 1993) employs a compressible LES solver and solves mass, momentum, and energy equations on the LES side. On the LEM side mass, energy and species equations are solved.

The LEM subgrid model, refereed to as LEMLES, has been applied to several fields of study. The following paragraphs are to give a small overview on the applications to premixed combustion. Menon et al. (1993) showed first results on the modeling of turbulent premixed combustion with the LEMLES approach. They investigated vortex roll-up in a shear layer with predefined velocity field, which was initially calculated analytically with simplifying assumptions. Eventually, they simulated a transient shear layer. For both cases one side of the shear layer consists of a fuel-air mixture and the other side of burned products. The computations showed promising results for future, more practical configurations.

Smith & Menon (1998) presented a transient simulation of a premixed stagnation point flame employing LEMLES. Good qualitative agreement with experimental observations was found. Sankaran & Menon (2005) conducted a 3D-LEMLES of a freely propagating flame in the thin reaction zones regime. Many important characteristics of this regime, for example, the broadening of the flame structure, the statistics of flame curvature, and the vorticity field, agree well with DNS studies.

Stein & Kempf (2009) and Stein (2009) developed a new algorithm for the coupling of LEM and LES for incompressible premixed combustion applications. The algorithm is based on a predictor-corrector method and allows for a mutual temporal advancement of the 3D-LES and 1D-LEM equations. They applied the model to premixed twin flames in turbulent counter flow. The simulations correctly reproduced flame characteristics close to

the flame axis but exhibited deficits further away from the axis. These were attributed to inaccuracies in the 3D convection algorithm (splicing) and a too coarse grid resolution.

For the sake of completeness, a different approach of employing the Linear Eddy Model as a subgrid model introduced by Sannan et al. (2009, 2013) is presented here but will not be considered for our studies. This ansatz regards three fields of one-dimensional LEM domains, which intersect orthogonally. This three dimensional geometric structure can be employed as closure for LES as well as RANS. The scalar fields are computed on each LEM domain, and they are coupled by advective processes. Fluid cells are transported according to the velocity field of the underlying solver. Continuity is thereby presumed in every three dimensional subgrid cell. An additional coupling of the LEM domains is achieved through stochastic rotation of the subgrid cells. This additional coupling ensures the even representation of physical processes in every spatial direction. Since this last approach is fairly new and only few very basic applications are known to the author and moreover the application to complex geometries appears to be challenging, we follow the approaches from Menon et al. (1993), Sankaran & Menon (2005) and Stein & Kempf (2009) for the LEM-LES coupling.

9.1. Large Eddy Simulations (LES)

In large eddy simulations, large scale motion is directly resolved, while small scale motion is modeled. This approach is reasonable since large scale motion is usually much more energetic than small scale motion and thus provides the major transport of conserved properties (Kolmogorov hypothesis). To obtain a velocity field that only contains the large scale components of the total field, a spatial filter is applied. The filtered velocity is defined as

$$\bar{u}_i(\boldsymbol{x}) = \int G(\boldsymbol{x} - \boldsymbol{x'}) u_i(\boldsymbol{x'}) d\boldsymbol{x'}. \tag{9.1.1}$$

The filter kernel $G(\boldsymbol{x} - \boldsymbol{x'})$ is a localized function. A length scale Δ, which distinguishes between large and small eddies, is associated with the filter. Most practical implementations of LES do not perform explicit filtering but use the grid itself as a filter (box filter).

The filtered continuity and momentum equations read

$$\frac{\partial \bar{\rho}}{\partial t} + \frac{\partial \bar{\rho} \tilde{u}_i}{\partial x_i} = 0, \tag{9.1.2}$$

$$\frac{\partial \bar{\rho} \tilde{u}_i}{\partial t} + \frac{\partial}{\partial x_j} \left(\bar{\rho} \tilde{u}_j \tilde{u}_i + \bar{p} \delta_{ij} - \tilde{\tau}_{ij}^{\mathrm{tot}} \right) = 0, \tag{9.1.3}$$

with the filtered respectively subgrid-scale (sgs) stress tensors:

$$\tilde{\tau}_{ij}^{\mathrm{tot}} \equiv \tilde{\tau}_{ij} + \tilde{\tau}_{ij}^{\mathrm{sgs}}, \tag{9.1.4}$$

$$\tilde{\tau}_{ij} = \bar{\rho}\nu \left(\frac{\partial \tilde{u}_i}{\partial x_j} + \frac{\partial \tilde{u}_j}{\partial x_i} - \frac{2}{3}\frac{\partial \tilde{u}_k}{\partial x_k}\delta_{ij} \right) \quad \text{and} \tag{9.1.5}$$

$$\tilde{\tau}_{ij}^{\mathrm{sgs}} \equiv -\overline{\rho u_i' u_j'}. \tag{9.1.6}$$

The tilde denotes a density weighted – or Favre – average, $\overline{\rho u} = \bar{\rho}\tilde{u}$ and $u = \tilde{u} + u'$. The filtered energy and species equations can be derived accordingly. They are not presented here since in the present approach they are not solved within the LES but on the subgrid scale within the LEM (Sec. 9.6).

The subgrid-scale stress tensor requires closure. A well-established closure is based on the eddy viscosity concept, which introduces an artificial turbulent or eddy viscosity, ν_t, analogous to the molecular viscosity.

$$\tilde{\tau}_{ij}^{\mathrm{sgs}} \approx \bar{\rho}\nu_t \left(\frac{\partial \tilde{u}_i}{\partial x_j} + \frac{\partial \tilde{u}_j}{\partial x_i} - \frac{2}{3}\frac{\partial \tilde{u}_k}{\partial x_k}\delta_{ij} \right) - \frac{2}{3}\bar{\rho}k\delta_{ij}, \tag{9.1.7}$$

where k is the turbulent kinetic energy, $k = 1/2\widetilde{u_k' u_k'}$. Its principle intended effects are increased transport and dissipation of the turbulent kinetic energy at the small scales.

The earliest subgrid scale model to calculate the eddy viscosity was introduced by Smagorinsky in 1963. The eddy viscosity is related to the filter length scale and the strain rate of the resolved field. Due to its simplicity it is widely used as a closure in LES, albeit, shortcomings due to the assumption of a constant model parameter, inducing isotropic turbulence, especially in shear layers and boundary regions. To overcome these problems, dynamic models have been proposed, which allow the model parameter to be calculated dynamically and thus vary in space and time. Other models solve additional transport equations. The model employed in the present studies, the one-equation eddy model, computes the eddy viscosity from the filter width in terms of the cell volume $\Delta = V_{\mathrm{LEScell}}^{1/3}$ and the turbulent kinetic energy as $\nu_t = C_\nu \sqrt{k}\Delta$. The turbulent kinetic energy, k, is obtained from an additional transport equation. The advantage of this model is that it is capable of determining the non-equilibrium of the production / dissipation of k on the subgrid scale. Furthermore, the turbulent kinetic energy is required for the LEMLES model to identify the subgrid contribution for the exchange of scalar properties between LES cells (Sec. 9.5).

For quantities other than the velocity, the LEMLES is utilized as a subgrid model. The LEMLES concept and the present implementation will be explained in the following.

9.2. LEMLES: general approach

The LEMLES, as introduced by Menon et al. (1992, 1993), is composed of: 1. independent LEM simulations in every LES cell; 2. scalar transport of Linear Eddy domain information across the LES cell borders, which is governed by the LES velocity field; and 3. the coupling of thermo-chemical properties of the LEM with the LES, which affects the resolved fields.

Within every LES time step several LEM subgrid time steps are computed since the LEM

time steps are generally much smaller than the LES time steps. This is due to the detailed chemistry and small scale eddy events that are treated by the LEM. In our implementation for incompressible flow, species, energy, and mass equations are solved on the LEM side whereas only the momentum and mass equations are solved on the LES side. Convection processes are treated by so called *splicing* events, which will be described in detail in Sec. 9.5. Small scale (subgrid) mixture and scalar diffusion are included in the LEM calculations.

The coupling of LEM and LES is governed by the *splicing* events, which are controlled by the LES velocity field (Sec. 9.5), the transfer of subgrid turbulent information from LES to LEM (Sec. 9.6), and the transfer of mean scalar information of the subgrid LEM to the LES, which in turn influences the flow field. The latter is, in contrast to earlier approaches, realized through a divergence constraint (Sec. 9.3). To enable a simultaneous evolution of LES and LEM equations, we employ an iterative procedure with predictor and corrector steps similar to that of Stein & Kempf (2009).

The splicing algorithm that is implemented in the current studies is face based. This allows for an easy coupling with finite volume LES solvers (we employ OpenFOAM). The major advantage of the face based method is that it works regardless of the type of cell structure or mesh, which can be structured, unstructured, or hybrid.

Furthermore, to reduce the computational effort, only a part of the LEM domains, depending on certain thresholds of temperature, species and heat release rate statistics, are advanced or contribute to the splicing procedure.

9.3. LEMLES closure

The present closure uses a direct coupling of LEM and LES via the divergence condition of the filtered velocity field instead of transferring the thermo-chemical information of the subgrid LEM model to the LES by means of the equation of state as done in conventional coupling procedures (Menon et al. 1992, 1993). The introduced closure relies on the asymptotic analyses of the balance equations according to Klein et al. (2001), Klein (1999). With this procedure no explicit filter operations are needed on the LEM subgrid model.

The governing filtered equations for low Mach numbers on the LES side are:

$$\frac{\partial \overline{\rho}}{\partial t} + \nabla \cdot (\overline{\rho}\tilde{\boldsymbol{u}}) = 0, \tag{9.3.1}$$

$$\frac{\partial \overline{\rho}\tilde{\boldsymbol{u}}}{\partial t} + \nabla \cdot (\overline{\rho}\tilde{\boldsymbol{u}}\tilde{\boldsymbol{u}}) = -\nabla \overline{p} + \nabla \cdot \boldsymbol{\sigma}, \tag{9.3.2}$$

$$\nabla \cdot \tilde{\boldsymbol{u}} = \mathcal{D}, \tag{9.3.3}$$

where $\overline{\rho}$ denotes the filtered density, $\tilde{\boldsymbol{u}}$ the Favre-averaged velocities, $\overline{p}$ the filtered pressure, and $\boldsymbol{\sigma}$ the stress tensor, which consists of molecular as well as turbulent subgrid components.

Equ. 9.3.3 is the divergence constraint which can be determined from the energy equation

for constant pressure:

$$\begin{aligned} \nabla \cdot \boldsymbol{u} &= -\frac{1}{\rho c_p T}\left\{\nabla \cdot \boldsymbol{q} + \sum_s \boldsymbol{j}_s \cdot \nabla h_s\right\} \\ &\quad -\frac{1}{\rho}\sum_s \left\{\frac{M}{M_s}\nabla \cdot \boldsymbol{j}_s\right\} + \frac{1}{\rho}\sum_s \left\{\frac{M}{M_s} - \frac{h_s}{c_p T}\right\}\dot{\sigma}_s. \end{aligned} \tag{9.3.4}$$

The right hand side of Equ. 9.3.4 consists of quantities which are only available in the LEM subgrid model. The equation is unfiltered and holds for every point of the LEM domain. To determine an approximation of the divergence of the filtered velocity field Equ. 9.3.4 is integrated over the whole LEM domain:

$$\nabla \cdot \tilde{\boldsymbol{u}} = \sum_{i=1}^{n_{\mathrm{LEM}}} (\nabla \cdot \boldsymbol{u})_i. \tag{9.3.5}$$

Equation 9.3.5 is only valid for equally sized LEM cells. With a non-uniform mesh, the divergences in the single LEM cells have to be multiplied by the cell size fraction of the domain length.

The discretized equations, when solved implicitly, are of the form:

$$\frac{\rho^{n+1} - \rho^n}{\Delta t} = -\nabla \cdot (\rho \boldsymbol{u})^{n+1}, \tag{9.3.6}$$

$$\frac{(\rho \boldsymbol{u})^{n+1} - (\rho \boldsymbol{u})^n}{\Delta t} = -\nabla \cdot (\rho \boldsymbol{u}\boldsymbol{u})^{n+1} - \nabla p^{n+1} + \nabla \cdot \boldsymbol{\sigma}^{n+1}, \tag{9.3.7}$$

$$\nabla \cdot \boldsymbol{u}^n = \mathcal{D}^n \quad \text{and} \quad \nabla \cdot \boldsymbol{u}^{n+1} = \mathcal{D}^{n+1}. \tag{9.3.8}$$

The tilde and overbar are dropped for convenience.

9.4. Iterative solution procedure

9.4.1. Predictor

The LEM subgrid lines are advanced to time step $n+1$.

The density is calculated in a first step explicitly from the density and velocity from the previous time step n.

$$\frac{\rho^{n+1,\alpha} - \rho^n}{\Delta t} = -\nabla \cdot (\rho \boldsymbol{u})^n. \tag{9.4.1}$$

This predicts the density at time level n+1 and iteration step α.

The velocity is predicted using the implicit momentum equation, yielding $\boldsymbol{u}^{n+1,*}$:

$$\frac{(\rho^{n+1,\alpha}\boldsymbol{u}^{n+1,*}) - (\rho \boldsymbol{u})^n}{\Delta t} = -\nabla \cdot (\rho^{n+1,\alpha}\boldsymbol{u}^n\boldsymbol{u}^{n+1,*}) - \nabla p^{n+1,\alpha(-1)} + \nabla \cdot (\mu \nabla \boldsymbol{u}^{n+1,*}). \tag{9.4.2}$$

At this stage the pressure at time step $n+1$ is not known and instead the pressure at time step n is used.

The velocity divergence constraint before splicing, $\mathcal{D}^{n+1,\text{preSplice}}$, is calculated from the LEM lines. The splicing procedure is carried out and divergence is computed again ($\mathcal{D}^{n+1,\text{postSplice}}$). The divergence at time iteration level $n+1,\alpha$ then assembles to

$$\mathcal{D}^{n+1,\alpha} = \frac{1}{2}(\mathcal{D}^{n+1,\text{preSplice}} + \mathcal{D}^{n+1,\text{postSplice}}). \tag{9.4.3}$$

9.4.2. Corrector

Analogous to Equ. 9.4.2 the momentum corrector can be written as

$$\frac{(\rho^{n+1,\alpha}\boldsymbol{u}^{n+1,\alpha}) - (\rho\boldsymbol{u})^n}{\Delta t} = -\nabla\cdot(\rho^{n+1,\alpha}\boldsymbol{u}^{n+1,*}\boldsymbol{u}^{n+1,*}) - \nabla p^{n+1,\alpha} + \nabla\cdot(\mu\nabla\boldsymbol{u}^{n+1,*}) \tag{9.4.4}$$

Subtracting the momentum predictor (Equ. 9.4.2) from the momentum corrector (Equ. 9.4.4) results in

$$\frac{\rho^{n+1,\alpha}(\boldsymbol{u}^{n+1,\alpha} - \boldsymbol{u}^{n+1,*})}{\Delta t} = -\nabla\cdot(\rho^{n+1,\alpha}\boldsymbol{u}^{n+1,*}(\boldsymbol{u}^{n+1,*} - \boldsymbol{u}^{n+1,\alpha})) - \nabla\delta p^{\alpha}, \tag{9.4.5}$$

with the pressure increment

$$\delta p^{\alpha} = p^{n+1,\alpha} - p^{n+1,\alpha-1}. \tag{9.4.6}$$

Defining

$$\boldsymbol{u}^{n+1,**} = \boldsymbol{u}^{n+1,*} - \frac{\Delta t}{\rho^{n+1,\alpha}}(\rho^{n+1,\alpha}\boldsymbol{u}^{n+1,*}(\boldsymbol{u}^{n+1,*} - \boldsymbol{u}^{n+1,\alpha})), \tag{9.4.7}$$

Equation 9.4.2 can be written as

$$\boldsymbol{u}^{n+1,\alpha} = \boldsymbol{u}^{n+1,**} - \frac{\Delta t}{\rho^{n+1,\alpha}}\nabla\delta p^{\alpha}. \tag{9.4.8}$$

In a first iteration step $\boldsymbol{u}^{n+1,\alpha}$ is set equal to $\boldsymbol{u}^{n+1,*}$ and $p^{n+1,\alpha-1}$ to $p^{n+1,*}$.

Taking the divergence of Equ. 9.4.8, a Poisson equation for the pressure increment δp is obtained:

$$\nabla\cdot\boldsymbol{u}^{n+1,\alpha} = \mathcal{D}^{n+1,\alpha} = \nabla\cdot\boldsymbol{u}^{n+1,**} - \nabla\cdot\left(\frac{\Delta t}{\rho^{n+1,\alpha}}\nabla\delta p^{\alpha}\right). \tag{9.4.9}$$

The pressure and velocity of iteration step α are then given by

$$p^{n+1,\alpha} = p^{n+1,\alpha-1} + \delta p^{\alpha} \quad \text{and} \quad \boldsymbol{u}^{n+1,\alpha} = \boldsymbol{u}^{n+1,**} - \frac{\Delta t}{\rho^{n+1,\alpha}}\nabla\delta p^{\alpha}. \tag{9.4.10}$$

Finally, the corrector splicing procedure is carried out, and the density is updated to the value of the filtered subgrid density ($\overline{\rho} = \overline{\rho}_{\text{LEM}}$).

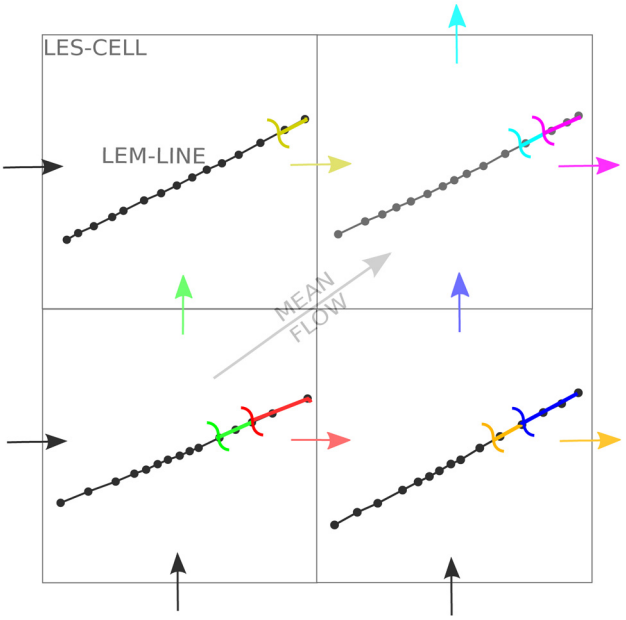

Figure 9.5.1.: Illustration of splicing events.

9.5. Mean and turbulent transport of scalar material across the LES cell boundaries (splicing)

The communication of the scalar information between the LES cells represents the convective transport according to the resolved LES velocity field. In addition, transport due to subgrid turbulence k_{sgs} is considered.

The Linear Eddy subgrid model manages the scalar transport across LES cell borders with *splicing* events. Parts of LEM lines are transferred from one LES cell to another in a Lagrangian fashion. The general splicing procedure is presented in Fig. 9.5.1. It includes the following four steps:

1. Computation of the mass transport across the face of two adjacent LES cells (the overall volume transport, into and out of a cell, is zero due to the continuity condition, if $\nabla \cdot \tilde{\boldsymbol{u}} = 0$).
2. Identification of the donor and receiver cells for the scalar transport according to the LES velocity field and the subgrid turbulent kinetic energy.
3. Extraction of the segment of the LEM domain of the donor cell that is to be transferred.
4. Insertion of the extracted LEM segment of the donor cell into the LEM domain of the receiver cell.

The splicing events occur at a frequency that is governed by the LES time step. Details of the splicing procedure and its physical meaning are explained in the following.

The volume flux across a cell face with cell face area S_k in a time interval Δt_{LES} is given

by

$$dV_k = u_k \Delta t_{\mathrm{LES}} S_k. \tag{9.5.1}$$

u denotes the velocity, which is interpolated on the face, and index k indicates the k-th face. The resolved velocities as well as the subgrid turbulence from the LES contribute to the volume flux. The subgrid contribution to the volume flux is calculated from the turbulence intensity using the subgrid turbulent kinetic energy

$$u_{k,\mathrm{sgs}} = \sqrt{2/3 k_{\mathrm{sgs}}}, \qquad dV_{k,\mathrm{sgs}} = u_{k,\mathrm{sgs}} \Delta t_{\mathrm{LES}} S_k. \tag{9.5.2}$$

The direction of the volume transport in Equ. 9.5.1 directly results from the resolved velocity field. The direction for the subgrid turbulent transport is chosen randomly. It can be in the same or in the opposite direction of the resolved transport. The overall transport in and out of a cell is zero according to the continuity condition so that the volumes of the cells do not change.

The computed volume transfer is normalized by the volume of the donor cell. This results in a segment of the donor cell which is transferred across cell face k to the receiver cell

$$dx_k/L = dV_k/V_{\mathrm{donor}}. \tag{9.5.3}$$

The LEM line elements are distributed to their neighbors according to the segment sizes, in descending order.

The Linear Eddy field is interpreted as a representative linear cut through the LES cell and forms a representative statistical sample of the spatial structure of the thermo-chemical field in the LES cells. We treat the LEM lines with outflow boundary conditions, which allows for virtually aligning the LEM lines along scalar gradients, and do not use periodic boundary conditions as in Menon et al. (1992, 1993).

The LEM-lines are generally organized in such a way that the left side is the unburned and the right side the burned zone. The line elements are donated from the right side of the donor domain and received at the left side of the receiver domain. We do not employ a donation that chooses the sides of donor and receiver cells for splicing according to gradients between donor and receiver cells to avoid artificial diffusion (Stein 2009). This donation approach evaluates a scalar gradient, e.g. temperature gradient, from donor to receiver cell. If it is positive, i.e. the mean temperature of the donor cell is smaller than that of the receiver cell, the line elements are donated from the right side of the donor domain and received at the left side of the receiver domain. If it is negative, the line elements are donated from the left side of the donor domain and received at the right side of the receiver domain. Test computations with this approach exposed problems for applications with a combination of negative and positive gradients across the borders of three adjacent LES cells, which leads to an unphysically fast transport of LEM cells across LES borders, i.e. one LES cell is almost completely skipped. The conventional approach, which we employ here, does not cause these accelerating effects, which we deem worse than the potential artificial diffusion.

As already mentioned in the introduction to Chapter 9, the computational cost is reduced by excluding LEM domains from advancement and LES faces from the splicing procedure. The LEM domains are only advanced if the rms of one of several scalar fields, here we choose temperature and methane as representatives, is larger than a threshold, here 1% of

its minimum respectively mean value, or if heat release occurs. The rms rules hold as well for the splicing procedure, only that here donor as well as receiver cells are considered. In addition, it is checked if the scalar gradient between donor and receiver (again of temperature and methane) is greater than a threshold. Only if all of these criteria are false, the scalar transport across the according cell face is not performed.

9.6. Subgrid Linear Eddy computations

In every LES cell of size Δ an LEM simulation is carried out. The largest eddy size within the subgrid LEM results directly from the LES cell size Δ, which in turn can be calculated from the LES cell volume i as

$$\Delta_i = \sqrt[3]{V_{\mathrm{i,LES}}}. \tag{9.6.1}$$

The smallest eddy size within the LEM is computed from the turbulent Reynolds number Re_t and Kolmogorov's scaling laws. The LEM lines in the subgrid of the LES are not aligned in any direction. The Linear Eddy subgrid model rather gives a characteristic statistic representation of the scalar field within the subgrid.

To execute the LEM computations, the frequency parameter λ and the eddy size pdf $f(l)$ analogous to the stand-alone model have to be determined:

$$\lambda = \frac{54}{5} D_t \Delta^{-3} \frac{\left[1 - (\eta/\Delta)^{-5/3}\right]}{\left[(\eta/\Delta)^{4/3} - 1\right]}, \qquad f(l) = \frac{-5/3}{\Delta^{-5/3} - \eta^{-5/3}} l^{-8/3}. \tag{9.6.2}$$

The turbulent diffusivity D_t and the turbulent scales are extracted from the LES:

$$\eta = C_\eta \Delta \mathrm{Re}_t^{-3/4.} = C_\eta \Delta^{1/4} \left(\frac{\sqrt{2/3 k_{\mathrm{sgs}}}}{\nu} \right)^{-3/4}, \qquad D_t = \frac{1}{C_\lambda} \nu \mathrm{Re}_t = \frac{1}{C_\lambda} \Delta \sqrt{2/3 k_{\mathrm{sgs}}}. \tag{9.6.3}$$

C_η and C_λ are constants determined for a wide range of turbulent premixed flames in Smith & Menon (1996) and taken as 1 and 15, respectively, for the present simulations.

Note that the LEMLES requires a turbulence model that solves an additional equation for the subgrid turbulent kinetic energy. Menon & Kerstein (2011) suggest a localized dynamic subgrid kinetic energy model (LDKM). We employ the OneEqEddy model available in OpenFoam, which is of type k-equation eddy-viscosity model.

9.7. Parallelization

In OpenFOAM a mesh decomposition method is employed for parallel runs, which distributes one decomposed part of the mesh to one processor. The interfaces between the individual parts are treated in the same manner as (external) boundaries. This makes it easy to incorporate the LEM subgrid model in a parallel realization.

The boundary conditions for the LEM computations are set in a Lagrangian manner, similar to that of the splicing algorithm. The size of the inflow respectively outflow segment is calculated from the mass flux across the boundary face which results from the OpenFOAM

boundary conditions:

$$dx_b = \frac{\phi_b \Delta t}{A_{f,b}\rho_b}, \tag{9.7.1}$$

where ϕ_b is the mass flow rate per unit area and index b stands for boundary. ϕ_b, Δt and the boundary face area $A_{f,b}$ are directly taken from the OpenFOAM boundary conditions. ρ_b is calculated from the boundary's thermodynamic state, set by pressure, species mass fractions, and temperature.

For inflow, dx_b is positive, and a new cell of size dx_b with the boundary's thermodynamic state is introduced on the inflow (left) side of the LEM domain. For outflow, dx_b is negative, and a segment of size $|dx_b|$ is cut from the outflow (right) side of the LEM domain. Note that with this procedure the volume of subgrid cells can become larger or smaller than that of the LES cells. This inconsistency will however be compensated after the splicing events.

This ansatz uses interpolated mean values of the subgrid LEM cells, i.e. temperature and species mass fractions. This implies that across the (inner) boundaries of the LES mesh subdomains no splicing takes place and an inaccuracy is introduced. The group of Michael Oevermann at Chalmers University, Gothenburg, currently works on a solution for this problem.

9.8. Validation

To validate the splicing algorithm, a 2D test case with a disk possessing scalar properties different from the surrounding is used (Figs, 9.8.1 and 9.8.2). The disk (temperature is shown in the figures) is convected with constant velocity without solving any transport equations on the LES or LEM domains. The $5 \times 5\,\mathrm{cm}^2$ square is meshed with a uniform cartesian grid with 99 grid cells in x and y direction. The subgrid LEM-lines are initially divided into 20 grid cells.

Figure 9.8.1 shows convection of the disk in x direction along the cartesian grid orientation. The circular shape is almost perfectly preserved and only moved along the coordinate axis.

Diagonal to the cartesian grid orientation the circular shape is fading both in x and y direction (Fig. 9.8.2). The result is similar to that shown by Stein (2009). The observed artificial dissipation is one major drawback of the splicing algorithm. For cases with purely cartesian grids, this problem can be avoided by using operator splitting. However when using unstructured grids, this effect has to be accepted.

The shown examples indicate that the present splicing routine works as intended. It features all known (positive and negative) characteristics that were observed in previous work (Stein 2009, Menon & Kerstein 2011).

Figure 9.8.3 again presents convection of the disk along the x coordinate. In this case, however, a decomposed field with 4 subdomains, as indicated in the plots, is computed in parallel by making use of the procedure introduced in Sec. 9.7. The shape of the disk is preserved, albeit slightly more blurred than in the serial case, and small deformations are apparent. As explained previously, the parallelization routine is only preliminary for the studies within this thesis and will be replaced by a precise routine for future studies.

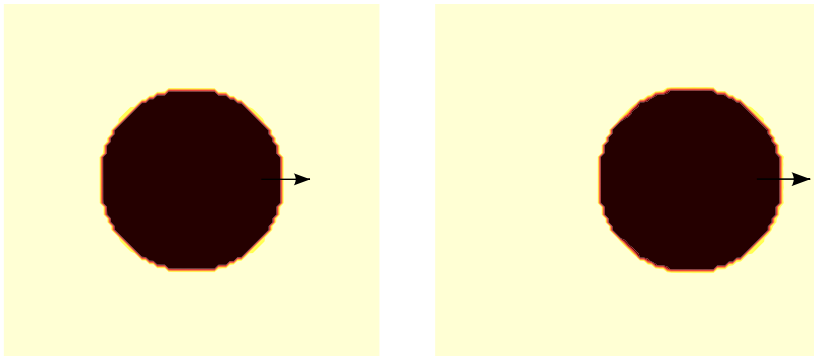

(a) (b)

Figure 9.8.1.: Splicing of disk along grid orientation. (a) Initial field. (b) Convected field.

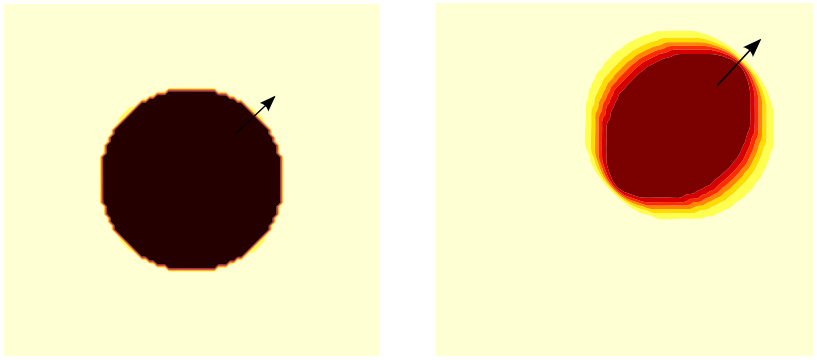

(a) (b)

Figure 9.8.2.: Splicing of disk diagonal to grid orientation. (a) Initial field. (b) Convected field.

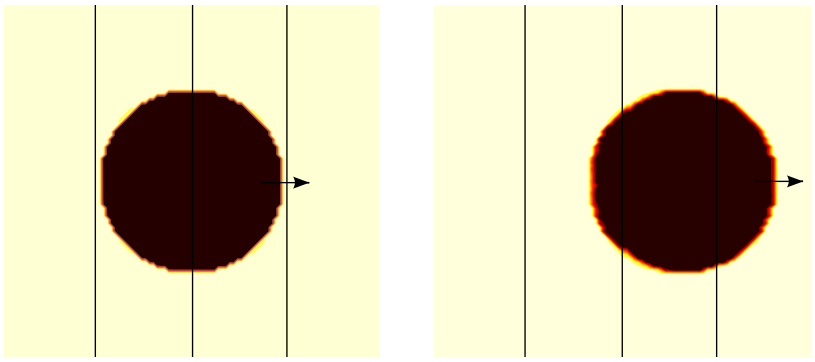

(a) (b)

Figure 9.8.3.: Splicing of circle along grid orientation. Decomposed domain, computed in parallel mode. Domain borders are indicated by lines. (a) Initial field. (b) Convected field.

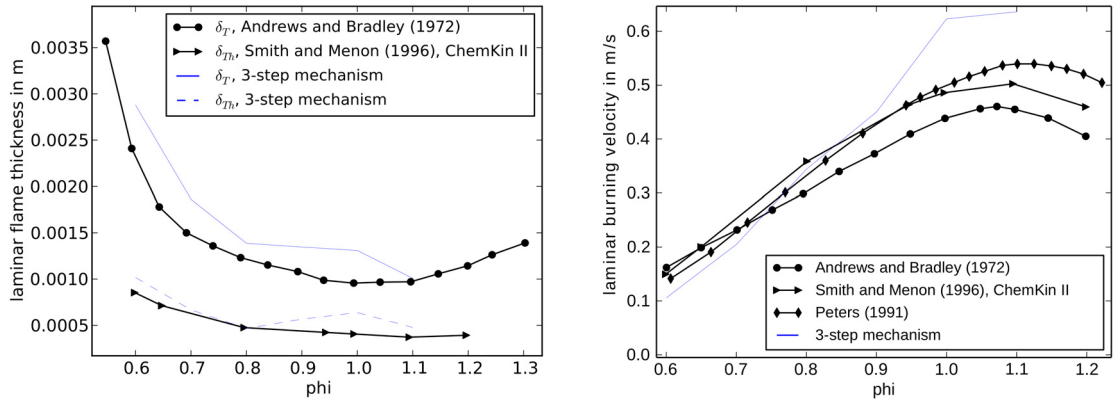

(a) (b)

Figure 9.9.1.: Validation of the employed mechanism. (a) laminar flame thickness; (b) laminar burning velocity.

9.9. Combustion mechanism

The combustion mechanism employed for the LEMLES is a global mechanism consisting of three steps. It is based on the 8-step mechanism by Novosselov & Malte (2008), which includes the formation of NO in addition to methane oxidation. Since test computations did not yield satisfactory results with respect to NO formation, it was neglected. The resulting 3-step mechanism consists of the reactions given in Table 9.9.1.

Table 9.9.1.: 3-step mechanism. Units in cm, s, cal, mol

nb	reaction	A	b	E_A
1	$CH_4 + 1.5\ O_2 \rightarrow CO + 2\ H_2O$	7.2172×10^{14}	0	44118.77
	reaction orders: $[CH_4]^{1.29}[O_2]^{0.0143}[CO]^{0.1987}$			
2	$CO + 0.5\ O_2 \rightarrow CO_2$	5.604×10^{18}	0	44658.69
	reaction orders: $[CO]^{1.348}[O_2]^{0.9037}[H_2O]^{0.1821}$			
3	$CO_2 \rightarrow CO + 0.5\ O_2$	5.5306×10^{15}	0	128356.6
	reaction orders: $[CO_2]$			

Figures 9.9.1 and 9.9.2 show the validation of the 3-step mechanism against measurements of laminar flame thickness, laminar burning velocity and species profiles (Andrews & Bradley 1972, Warnatz 1981, Peters 1991, Smith & Menon 1997). The agreement for lean conditions ($\phi = 0.6 - 0.9$), where the simulations are run, is good overall.

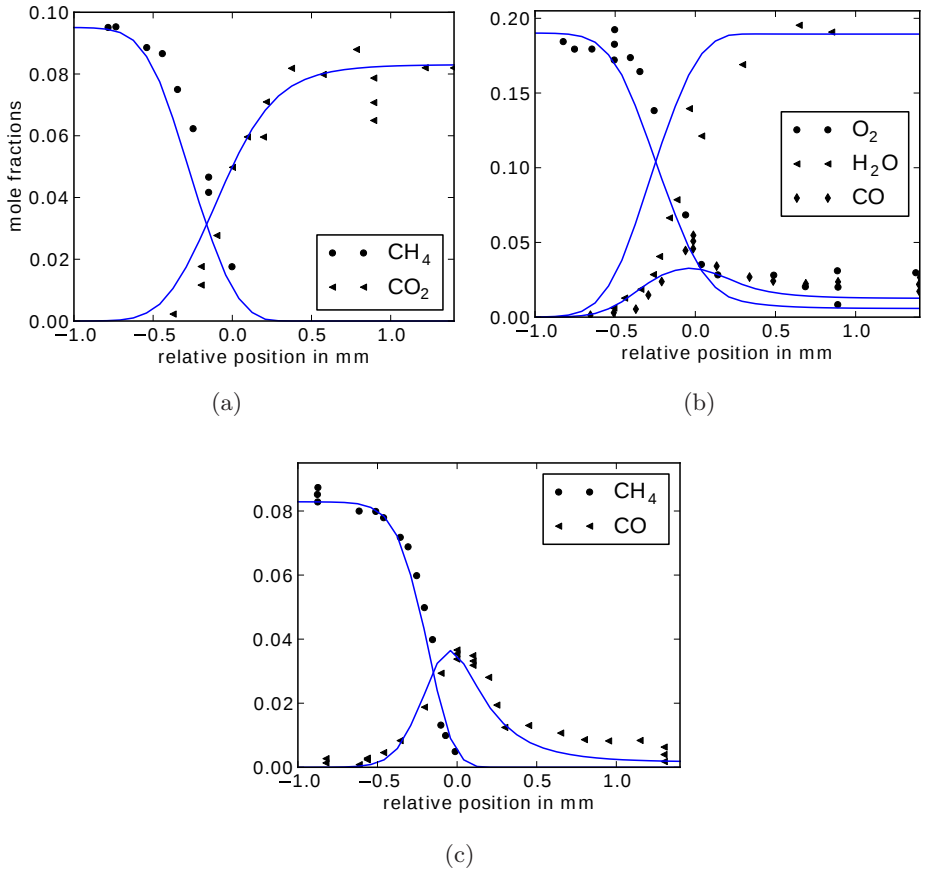

Figure 9.9.2.: Species profiles in a laminar premixed flame at $T_u = 293\,\mathrm{K}$, $p = 1\,\mathrm{atm}$. (a) $\phi = 1$; (b) $\phi = 1$; (c) $\phi = 0.86$.

10. Simulations of a V-flame with LEMLES

An inverted conical flame corresponding to that in Part III with premixing of methane and air will be studied in this chapter by means of LEMLES. The results, evaluated in terms of velocity fields, heat release rate, and flame front characteristics, will be compared to a common combustion model in OpenFOAM (reactingFoam) and to experimental data.

10.1. Computational domain

The computational domain comprises the exit of the burner nozzle with the center-body, the flame area and the direct surroundings. The inlet is positioned approximately 20 mm upstream of the center-body trailing edge. To reduce the computational costs, only one eighth of the circumference is considered. The resulting domain is meshed with tetrahedrons. Refinements are applied in the inlet area and the flame stabilization region. The cell volumes in these areas are smaller than $10^{-9}\,\mathrm{m}^3$. The mesh consists of 135 578 cells. A sketch of the domain is presented in Figure 10.2.1.

10.2. Setup

OpenFOAM-2.1.0 was employed for the present simulations. For both simulations, with LEM and standard combustion model, the oneEqEddy model was used for the subgrid turbulence closure and the 3-step combustion mechanism introduced in Section 9.9 was used for the determination of thermo-chemical properties.

For the LEMLES simulations all thermo-chemical properties were handled within the Linear Eddy Model utilizing Cantera and the mixture-averaged diffusion model, as in the stand-alone studies. Two loops were set for the corrector routine described in Section 9.4.2. The maximum allowed time step was calculated satisfying a maximum exchange of LEM-line fraction of 0.2.

ReactingFoam provides a compressible reacting flow solver. The chemistry model is a Partially Stirred Reactor Combustion Model or PaSR. The PaSR model is a modified version of the Eddy Dissipation Concept (EDC). The psiChemistryCombustionModel, with turbulent reactions turned on, the ODE chemistry solver, and the hsPsiMixtureThermo type for thermophysical properties were employed. Three outer corrector loops, five Piso corrector loops, and four non-orthogonal corrector loops were applied. The maximum Courant number was set to a 0.4.

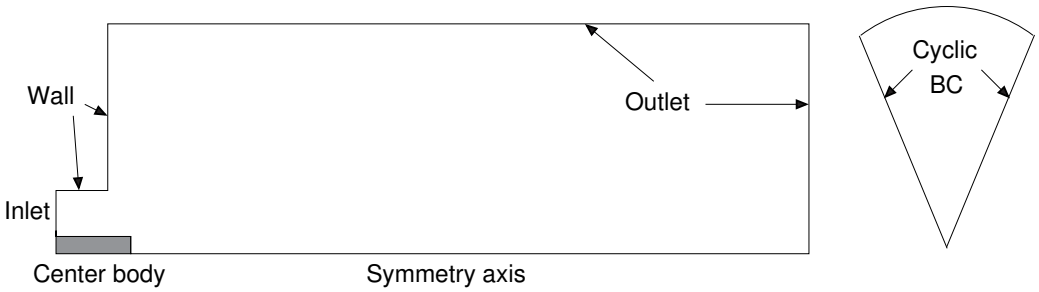

Figure 10.2.1.: Sketch of computational doamin.

10.2.1. Boundary conditions

The computational domain with its boundaries is given in Figure 10.2.1. The cyclic boundary patches of the eighth domain is set to cyclicAMI for rotational transformation. The outlet boundaries are set to patch type with inletOutlet boundary condition except for pressure which is set to constant (ambient) pressure.

The inlet is assigned with fixed values for all but pressure, which is calculated with zero gradient boundary condition, and velocity, which is computed via the groovyBC routine. groovyBC allows for user specified profiles and functions. In the current studies the velocity inlet conditions are set to a polynomial of degree 10 to approximate the profile at the inlet axial position. The polynomial was adapted to the velocity profile from a LES simulation including the whole burner geometry (nozzle, turbulence grid, fuel-injection, center-body):

$$u_{\text{in}} = 2.13 \cdot 10^{23} r^{10} - 2.43 \cdot 10^{22} r^{9} + 1.24 \cdot 10^{21} r^{8} - 3.704 \cdot 10^{19} r^{7} + 7.23 \cdot 10^{17} r^{6}$$
$$-9.59 \cdot 10^{15} r^{5} + 8.73 \cdot 10^{13} r^{4} - 5.37 \cdot 10^{11} r^{3} + 2.13 \cdot 10^{9} r^{2} - 4.88 \cdot 10^{6} r + 4.89 \cdot 10^{3},$$

with u_{in} in m/s and r in m. Additionally, random fluctuations for all velocity components, with the appropriate rms values, were superposed. The mass fractions of methane and air at the inlet were set according to an equivalence ratio of 0.78 as in the experiments. The temperature was set to 293 K.

All other boundaries were assigned as adiabatic walls.

10.3. Velocity fields

The velocity fields were measured in the vertical plane downstream of the burner exit via PIV (see Sec. 7.2.1). The axial and radial velocity components in that plane, their mean and rms values, will be compared to the simulation results. The mean velocity profiles are given for different axial positions in Fig. 10.3.1, whereas the rms velocity profiles are presented for $x = 0.005$ m in Fig. 10.3.2.

The origin of the coordinate system is located in the center of the center-body trailing edge. The computed mean axial velocity profiles at the burner exit ($x = 0.004$ m) are similar and are in reasonable agreement with the measurements (Fig. 10.3.1(a)). The radial component is overpredicted by the LEMLES simulations within the inner jet region (Fig. 10.3.1(b)). Directly downstream of the center-body, the reactingFoam results show

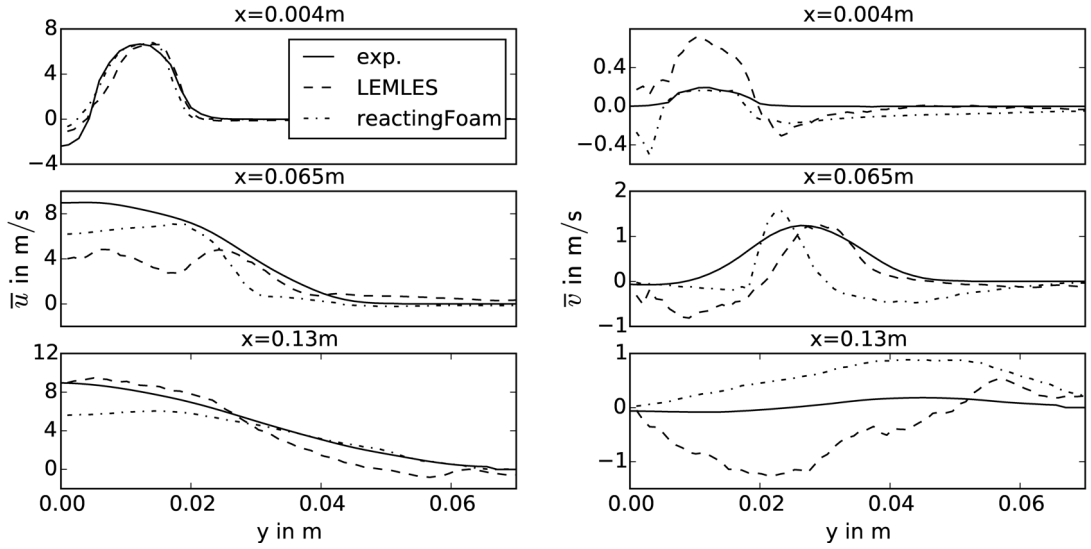

(a) Mean axial velocity, $\overline{u}$

(b) Mean radial velocity, $\overline{v}$

Figure 10.3.1.: Mean axial and radial velocities for different axial positions.

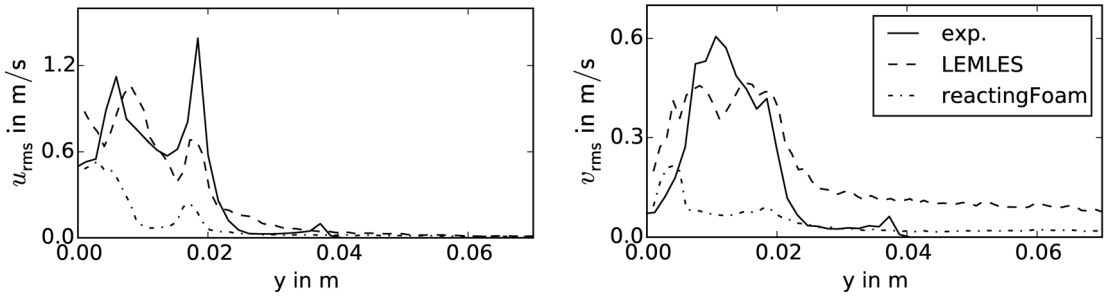

(a) RMS axial velocity, u_{rms}

(b) RMS radial velocity, v_{rms}

Figure 10.3.2.: RMS axial and radial velocities for $x = 0.005\,\mathrm{m}$.

significant radial inflow, which does not agree with the experimental results. In the outer shear layer, both simulations underestimate the radial velocity compared to the measurements. Further downstream, at $x = 0.065\,\mathrm{m}$, the LEMLES is in good agreement with the measurements in the outer shear layer but underpredicts the velocities in the inner region for both axial and radial velocities. The reactingFoam profiles show too steep gradients and too low axial velocities in the inner jet region. For $x = 0.13\,\mathrm{m}$ the axial velocity for both simulations is in reasonable agreement with the measurements, although the reactingFoam profile exhibits too low values in the inner region here as well. The radial velocity profiles show discrepancies from experimental results for both simulations.

The absolute values for the rms velocities shortly downstream the bluff-body agree well for the LEMLES and experiments. They are underpredicted by the reactingFoam simulations, although the same inlet conditions were used for both simulations.

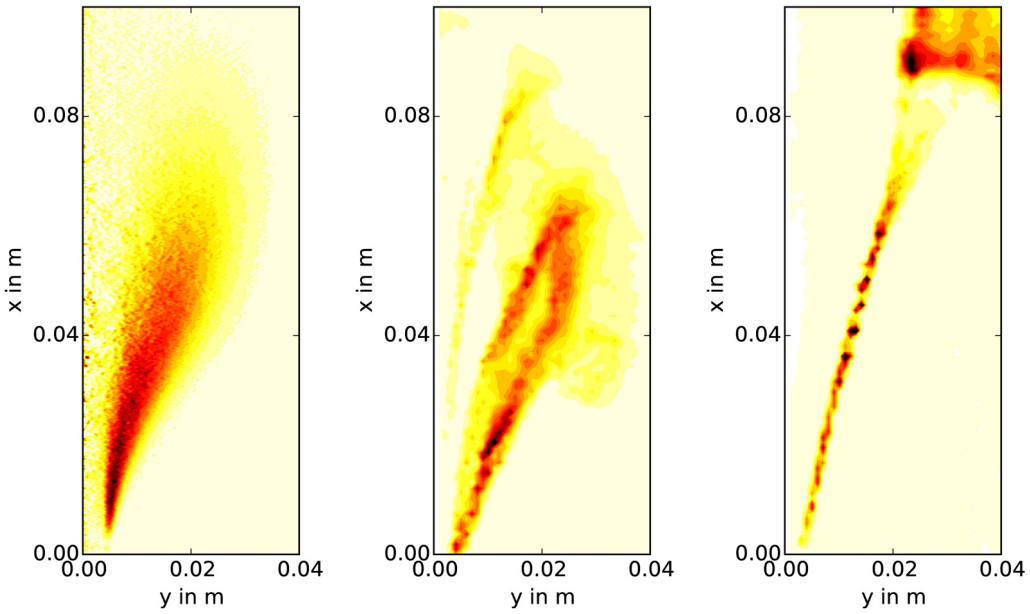

(a) OH chemiluminescence from experiment (b) heat release rate from LEMLES (c) heat release rate from reactingFOAM

Figure 10.4.1.: Mean OH*-chemiluminescence respectively heat release rates in xy-plane.

10.4. Heat release rate

The simulated heat release rates are compared to measurements of OH*-chemiluminescence. Chemiluminescence is a reasonably appropriate marker for the heat release rate although one should be aware of its limitations (see discussion in Section 8.1). The OH*-chemiluminescence respectively heat release rate gives a good indication of the flame position and extent. The measurements provide a two-dimensional projection of the three-dimensional OH*-chemiluminescence field. To allow for a comparison between measurements and simulations, the measured images are post-processed (Abel-deconvolution) to obtain the radial distribution of the OH*-chemiluminescence intensity in the vertical plane. Figure 10.4.1 shows a comparison of the mean chemiluminescence respectively heat release rate distribution in one half of the xy-plane.

For all three, experiment and both simulations, the angle and the radial and axial extent of the flame agree well. The reactingFoam distribution, however, exhibits high values of heat release rate in the upper right corner of the presented domain, in contrast to the experiment and the LEMLES solution. The mean flame shape is well reproduced by the LEMLES but not by the reactingFoam simulation. The latter only shows a very thin line where heat release occurs. This is caused by the lack of the model to describe flame-turbulence interaction. Flame wrinkling leading to blurring of the mean heat release rate field (the flame brush) is therefore not accounted for. The LEMLES on the other hand captures these effects and reproduces the flame shape in satisfactory agreement with the measurement results.

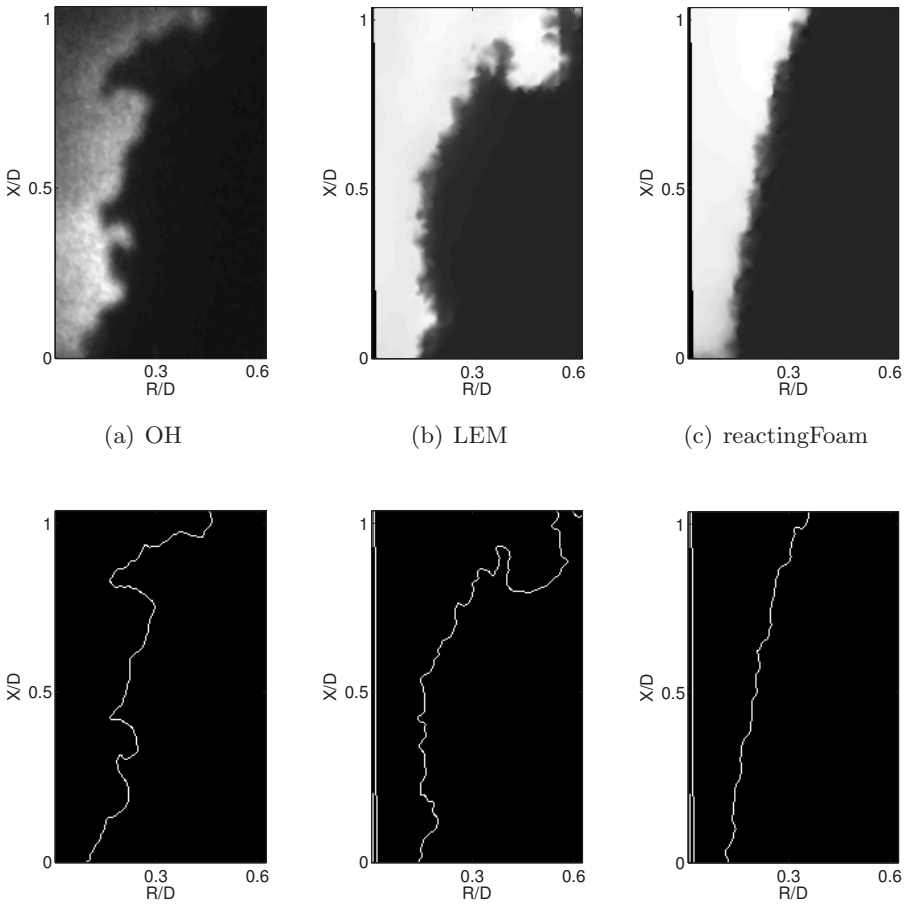

(a) OH (b) LEM (c) reactingFoam

(d) OH (e) LEM (f) reactingFoam

Figure 10.5.1.: Instantaneous OH resp.temperature distributions (a-c) and detected edges (d-f).

10.5. Flame structure

Figure 10.5.1 presents images of instantaneous temperature distributions and OH concentration, measured via OH-PLIF, in the axial plane for simulations and measurements. The edges detected from these images are also shown (procedure according to Sec. 8.3).

The edge determined from the OH image is quite wrinkled, as is the one determined from the LEMLES planar temperature distribution. Both of them exhibit very different shapes over time. The flame edge detected from the reactingFoam simulations however exhibit only little wrinkles and do not vary much over time. As in Sec. 8.3, the instantaneous edge images are processed to calculate the turbulent flame brush thickness and the flame surface density. The turbulent flame brush thickness is determined from the definitions based on the mean progress variable (see Equ. (8.3.1)) and based on the RMS flame front position fluctuations (see Equ. (8.3.2)). It is plotted for the experiment and the simulation over the axial position in Fig. 10.5.2(a). The LEMLES captures the turbulent flame brush thickness well for $x/D = 0.2$ and reproduces the increase with axial position, although for

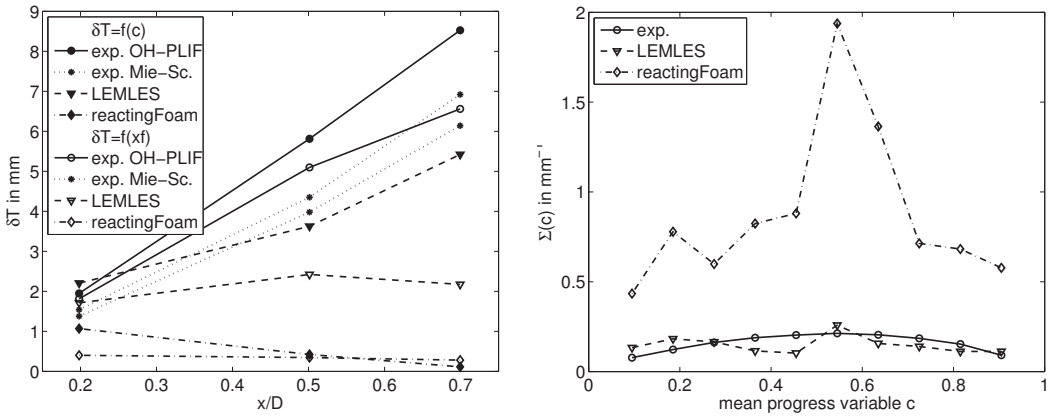

(a) flame brush thickness

(b) flame surface density

Figure 10.5.2.: Flame brush thickness (a) and flame surface density (b).

higher x/D, the turbulent flame brush thickness is underpredicted in comparison with the experimental results. The LEMLES as well as the measurements exhibit lower values for the turbulent flame brush thickness determined from the RMS flame front position fluctuations. The reactingFoam simulations underpredict the turbulent flame brush thickness and are not able to capture the increase with axial position. The flame surface density, plotted in Fig. 10.5.2(b), is well reproduced by the LEMLES simulation. The reactingFoam calculations however overpredict the flame surface density significantly. This is due to the static behavior of the flame, resulting in a small area occupied over time and thus too high values for the flame surface density, which is determined from Equ. (8.3.3).

10.6. Concluding remarks on the LEMLES simulations of a bluff-body burner

In this part, we introduced a novel coupling approach of LEM as a subgrid model for LES. The application of the LEMLES to a premixed lean methane-air turbulent bluff-body flame was presented and compared to experimental results as well as to simulations with a standard combustion model.

The abilities of the LEMLES were evaluated on the basis of mean and RMS velocity profiles, heat release rate distribution, and flame front characteristics. The mean axial velocity was well predicted by the LEMLES, although it was underpredicted within a region in the wake of the bluff body. The reactingFoam simulations show similar deficits that prolong even further downstream. The mean radial velocity profiles feature more discrepancies. The level of turbulence intensity shortly downstream of the center-body, presented by axial and radial RMS velocity profiles, agrees well for LEMLES and measurements but is underpredicted by the reactingFoam results.

The calculated mean heat release rate distribution in the axial plane was compared to the mean Abel-deconvoluted OH* intensities in the same plane. The images visualize the mean flame shape and size. The LEMLES reproduces these characteristics in very good

agreement with the experimental results while the reactingFoam simulation is not able to capture the extent respectively the flame brush thickness. The results were further discussed regarding flame front characteristics. Edges were detected for planar temperature profiles and OH-PLIF images for simulations and measurements. Both experimental and LEMLES results show wrinkling of the flame at different scales, featuring a strongly changing shape over time. The reactingFoam results only exhibit minor wrinkling of the flame front not altering significantly over time. The edge images were further processed to determine the turbulent flame brush thickness and flame surface density. LEMLES was found to reproduce the flame surface density well. The turbulent flame brush thickness is well predicted just downstream of the bluff-body but underpredicted further away. The increase of turbulent flame brush thickness with axial position is, however, captured. ReactingFoam does not caputure the flame wrinkling well and therefore fails to accurately predict the turbulent flame brush thickness and the flame surface density.

Summing up, the LEMLES is a promising model to represent flame-turbulence interaction, which plays an important role in many technical combustion systems. The major drawback of the model is, however, its high computational cost, which is 30 times higher than for reactingFoam. Nevertheless, with the rapid advance in computer technology, it could become a reliable tool in the future.

11. Conclusion and outlook

The focus of this thesis is the effect of mixing and fuel-air ratio perturbations on the properties of lean premixed flames. The mixing in a burner affects combustion properties such as the heat release rate, the burning velocity, pollutant emissions, and the convective time delay distribution. Some of these attributes are essential for the occurrence of combustion instabilities, arising from the coupling of unsteady heat release rate and the acoustic modes of the combustor. Combustion instabilities must be avoided because they can lead to increased emissions, flame extinction, and – in extreme cases – mechanical failure. It is thus crucial to understand the underlying fundamental mechanisms and to be able to predict properties relevant for the applications (such as NOx emissions).

Mixing in a swirl burner was studied with RANS and LES for different fuel injection configurations in the presence of periodic inflow excitation. These studies examined the capability of conventional CFD tools to capture important features of the mixing process. Furthermore, oscillations in fuel-air ratio were studied based on one-dimensional laminar as well as turbulent simulations and experiments with a bluff-body flame. The impact of mixing and fuel-air ratio perturbations on flow, mixing, and flame properties was analyzed. A new coupling method for the Linear Eddy subgrid model was introduced, which shows great potential for future investigations. It fully resolves turbulence–flame interaction in a one-dimensional manner and includes feedback from the subgrid to the large scale hydrodynamic field via a divergence condition. These effects play a crucial role in gas turbine type flames. The methodology was tested on a generic partially premixed flame to validate it on the basis of experimental data.

The first part concentrated on the simulation of mixing and flame position in an industrial-type swirl burner for different fuel-injection configurations (Chapter 3). The simulations were based on RANS methods employing Ansys CFX with the SST-turbulence model and the combined Eddy Dissipation / Finite Rate Chemistry (EDM/FRCM) combustion model. The steady RANS simulations were shown to be able to capture the mixing behavior for different fuel injection positions when adjusting the turbulent Schmidt number to a value of 0.2. The shift in flame position observed in corresponding measurements could be reproduced on a qualitative level with turbulent Schmidt and Prandtl numbers of 0.55.

The investigations of the effect of periodical flow forcing on the mixing fields in a swirl burner with URANS and LES in Chapter 4 showed many aspects in agreement with experimental studies, such as a helical wave associated with the unforced flow being replaced by an axisymmetric structure when forcing is applied and improved mixing with forcing. Moreover, an influence of the two-half-cone burner geometry on the mode structure could be identified. URANS as well as LES showed these characteristics although the mean velocity fields, turbulence properties, and modal energy distributions were much better captured by LES than URANS.

The effect of oscillations in fuel-air ratio on flame properties and emissions was presented

in Part II. The studies were conducted using the Linear Eddy Model. This one-dimensional turbulence model resolves all relevant spatial and temporal scales on a one-dimensional domain. The implementation of the model was discussed, and a new subdomain decomposition method, which significantly speeds up the code, was introduced.

Results of the investigations of the effect of fuel-air ratio fluctuations at representative frequencies and amplitudes were presented in Chapter 6. The parametric studies revealed an increase in CO and NO emissions as well as in heat release rate fluctuations with increasing amplitude at the flame front (corresponding to increasing inlet amplitudes and decreasing frequency). Nonlinear effects and saturation at fairly high forcing amplitudes could be attributed to the interaction of flame propagation and fuel-air ratio oscillations. Furthermore, the investigations indicated a dampening effect of the oscillations on turbulent fluctuations, leading to a decrease in burning velocity.

The impact of oscillations in fuel-air ratio was studied experimentally in Part III. A bluff-body burner with a lean partially premixed flame was used for the investigations so that effects of fuel-air ratio oscillations could be investigated mostly independent of effects related to coherent structures. Similar to the LEM computations, various amplitudes and frequencies of forcing were studied. PIV, OH*-chemiluminescence, OH-PLIF, and exhaust gas analysis gave information on the velocity field, the heat release rate, the flame front structure, and the emissions. The results (Chapter 8) show characteristics such as increasing heat release rate fluctuations for high forcing amplitudes and low frequencies and a change of the mean flame shape. In addition, the findings suggest a damping of turbulent fluctuations by harmonic oscillations, as observed in the numerical results. This was also supported through the evaluation of the flame surface density, extracted from OH-PLIF and Mie scattering images. The flame surface density characterizes flame propagation, indicating a decrease of burning velocity with increased forcing amplitude at the flame front. Forcing at high amplitudes or low frequencies also affected the concentration fields. The results of this part show agreement with, and thus also confirm, the outcome of the LEM studies.

Finally, in Part IV, a novel coupling approach for the Linear Eddy Model with an LES code was introduced. The advantage of using the LEM as a subgrid combustion model compared to other models is its applicability to any turbulent combustion regime. The coupling is face based and can thus be used with any kind of grid. Furthermore, the effect of the subgrid LEM on the supergrid velocity and pressure fields is given by the velocity divergence determined from the LEM solution.

Application of the LEMLES on a turbulent bluff-body flame was presented in Chapter 10, showing promising results regarding the prediction of the turbulent reaction zone and flame front properties. In contrast to a standard combustion model implemented in OpenFoam, the LEMLES reproduces the mean flame shape, instantaneous flame wrinkling, the flame brush thickness, and the flame surface density in good agreement with experimental results. The major drawback of the LEMLES is its high computational effort. However, with a further advance in computer technology, it could become an immensely useful turbulent combustion model in the near future, taking into account turbulence–chemistry interaction on a fundamental level.

Appendices

A. Reduced methane–air reaction mechanism

Table A.0.1.: Reduced mechanism for lean premixed methane combustion, derived from GRI-mech 3.0. Units in cm, s, cal, mol

nb	reaction	A	b	E_A
1	$2\ O + M \leftrightarrow O_2 + M$	1.20E+17	-1	0
	efficiencies: AR:0.83, C_2H_6:3, CH_4:2, CO:1.75, CO_2:3.6, H_2:2.4, H_2O:15.4			
2	$O + H + M \leftrightarrow OH + M$	5.00E+17	-1	0
	efficiencies: AR:0.7, C_2H_6:3, CH_4:2, CO:1.5, CO_2:2, H_2:2, H_2O:6			
3	$O + H_2 \leftrightarrow H + OH$	3.87E+04	2.7	6260
4	$O + HO_2 \leftrightarrow OH + O_2$	2.00E+13	0	0
5	$O + CH_2 \leftrightarrow H + HCO$	8.00E+13	0	0
6	$O + CH_2(S) \leftrightarrow H + HCO$	1.50E+13	0	0
7	$O + CH_3 \leftrightarrow H + CH_2O$	5.06E+13	0	0
8	$O + CH_4 \leftrightarrow OH + CH_3$	1.02E+09	1.5	8600
9	$O + HCO \leftrightarrow H + CO_2$	3.00E+13	0	0
10	$O + CH_2O \leftrightarrow OH + HCO$	3.90E+13	0	3540
11	$H + O_2 + M \leftrightarrow HO_2 + M$	2.80E+18	-0.86	0
	efficiencies: AR:0, C_2H_6:1.5, CO:0.75, CO_2:1.5, H_2O:0, N_2:0, O_2:0			
12	$H + 2\ O_2 \leftrightarrow HO_2 + O_2$	2.08E+19	-1.24	0
13	$H + O_2 + H_2O \leftrightarrow HO_2 + H_2O$	1.126E+19	-0.76	0
14	$H + O_2 + N_2 \leftrightarrow HO_2 + N_2$	2.60E+19	-1.24	0
15	$H + O_2 \leftrightarrow O + OH$	2.65E+16	-0.6707	17041
16	$2\ H + M \leftrightarrow H_2 + M$	1.00E+18	-1	0
	efficiencies: AR:0.63, C_2H_6:3, CH_4:2, CO_2:0, H_2:0, H_2O:0			
17	$2\ H + H_2 \leftrightarrow 2\ H_2$	9.00E+16	-0.6	0
18	$2\ H + H_2O \leftrightarrow H_2 + H_2O$	6.00E+19	-1.25	0
19	$2\ H + CO_2 \leftrightarrow H_2 + CO_2$	5.50E+20	-2	0
20	$H + OH + M \leftrightarrow H_2O + M$	2.20E+22	-2	0
	efficiencies: AR:0.38, C_2H_6:3, CH_4:2, H_2:0.73, H_2O:3.65			
21	$H + HO_2 \leftrightarrow O_2 + H_2$	4.48E+13	0	1068
22	$H + HO_2 \leftrightarrow 2\ OH$	8.40E+13	0	635
23	$H + CH_3\ (+ M) \leftrightarrow CH_4\ (+ M)$			
	kf	1.39E+16	-0.534	536
	kf0	2.62E+33	-4.76	2440
	falloff: Troe(A = 0.783, T3 = 74, T1 = 2941, T2 = 6964)			
	efficiencies: AR:0.7, C_2H_6:3, CH_4:3, CO:1.5, CO_2:2, H_2:2, H_2O:6			
24	$H + CH_4 \leftrightarrow CH_3 + H_2$	6.60E+08	1.62	10840
25	$H + CH_2O \leftrightarrow HCO + H_2$	5.74E+07	1.9	2742
26	$H_2 + CO\ (+ M) \leftrightarrow CH_2O\ (+ M)$			
	kf	4.30E+07	1.5	79600

Table A.0.1.: Reduced mechanism for lean premixed methane combustion, derived from GRI-mech 3.0. Units in cm, s, cal, mol

nb	reaction	A	b	E_A
	kf0	5.07E+27	-3.42	84350
	falloff: Troe(A = 0.932, T3 = 197, T1 = 1540, T2 = 10300)			
	efficiencies: AR:0.7, C_2H_6:3, CH_4:2, CO:1.5, CO_2:2, H_2:2, H_2O:6			
27	$OH + H_2 \leftrightarrow H + H_2O$	2.16E+08	1.51	3430
28	$2\ OH \leftrightarrow O + H_2O$	3.57E+04	2.4	-2110
29	$OH + HO_2 \leftrightarrow O_2 + H_2O$	1.45E+13	0	-500
30	$OH + CH_2 \leftrightarrow H + CH_2O$	2.00E+13	0	0
31	$OH + CH_3 \leftrightarrow CH_2 + H_2O$	5.60E+07	1.6	5420
32	$OH + CH_3 \leftrightarrow CH_2(S) + H_2O$	6.44E+17	-1.34	1417
33	$OH + CH_4 \leftrightarrow CH_3 + H_2O$	1.00E+08	1.6	3120
34	$OH + CO \leftrightarrow H + CO_2$	4.76E+07	1.228	70
35	$OH + HCO \leftrightarrow H_2O + CO$	5.00E+13	0	0
36	$OH + CH_2O \leftrightarrow HCO + H_2O$	3.43E+09	1.18	-447
37	$CH_2 + O_2 \rightarrow OH + H + CO$	5.00E+12	0	1500
38	$CH_2(S) + N_2 \leftrightarrow CH_2 + N_2$	1.50E+13	0	600
39	$CH_2(S) + O_2 \leftrightarrow H + OH + CO$	2.80E+13	0	0
40	$CH_2(S) + O_2 \leftrightarrow CO + H_2O$	1.20E+13	0	0
41	$CH_2(S) + H_2O \leftrightarrow CH_2 + H_2O$	3.00E+13	0	0
42	$CH_2(S) + CO \leftrightarrow CH_2 + CO$	9.00E+12	0	0
43	$CH_2(S) + CO_2 \leftrightarrow CH_2 + CO_2$	7.00E+12	0	0
44	$HCO + M \leftrightarrow H + CO + M$	1.87E+17	-1	17000
	efficiencies: C_2H_6:3, CH_4:2, CO:1.5 CO_2:2, H_2:2, H_2O:0			
45	$HCO + O_2 \leftrightarrow HO_2 + CO$	1.345E+13	0	400
46	$N + NO \leftrightarrow N_2 + O$	3.20E+13	0	355
47	$N + O_2 \leftrightarrow NO + O$	9.00E+09	1	6500
48	$N + OH \leftrightarrow NO + H$	3.36E+13	0	385
49	$N_2O + O \leftrightarrow N_2 + O_2$	1.40E+12	0	10810
50	$N_2O + O \leftrightarrow 2\ NO$	2.90E+13	0	23150
51	$N_2O + H \leftrightarrow N_2 + OH$	5.00E+14	0	18880
52	$N_2O\ (+\ M) \leftrightarrow N_2 + O\ (+\ M)$			
	kf	7.91E+10	0	56020
	kf0	6.37E+14	0	56640
	efficiencies: AR:0.625, C_2H_6:3, CH_4:2, CO:1.5, CO_2:2, H_2:2, H_2O:6			
53	$HO_2 + NO \leftrightarrow NO_2 + OH$	2.80E+12	0	-480
54	$NO + O + M \leftrightarrow NO_2 + M$	1.06E+20	-1.41	0
	efficiencies: AR:0.7 C_2H_6:3, CH_4:2, CO:1.5, CO_2:2, H_2:2, H_2O:6			
55	$NO_2 + O \leftrightarrow NO + O_2$	3.90E+12	0	-240
56	$NO_2 + H \leftrightarrow NO + OH$	1.32E+14	0	360
57	$NH + O \leftrightarrow NO + H$	4.00E+13	0	0
58	$NH + H \leftrightarrow N + H_2$	3.20E+13	0	330
59	$NH + OH \leftrightarrow HNO + H$	2.00E+13	0	0
60	$NH + OH \leftrightarrow N + H_2O$	2.00E+09	1.2	0
61	$NH + O_2 \leftrightarrow HNO + O$	4.61E+05	2	6500

Table A.0.1.: Reduced mechanism for lean premixed methane combustion, derived from GRI-mech 3.0. Units in cm, s, cal, mol

nb	reaction	A	b	E_A
62	$NH + O_2 \leftrightarrow NO + OH$	1.28E+06	1.5	100
63	$NH + H_2O \leftrightarrow HNO + H_2$	2.00E+13	0	13850
64	$NH + NO \leftrightarrow N_2O + H$	3.65E+14	-0.45	0
65	$NNH \leftrightarrow N_2 + H$	3.30E+08	0	0
66	$NNH + M \leftrightarrow N_2 + H + M$	1.30E+14	-0.11	4980
	efficiencies: AR:0.7, C_2H_6:3, CH_4:2, CO:1.5, CO_2:2, H_2:2, H_2O:6			
67	$NNH + O \leftrightarrow NH + NO$	7.00E+13	0	0
68	$H + NO + M \leftrightarrow HNO + M$	4.48E+19	-1.32	740
	efficiencies: AR:0.7, C_2H_6:3, CH_4:2, CO:1.5, CO_2:2, H_2:2, H_2O:6			
69	$HNO + H \leftrightarrow H_2 + NO$	9.00E+11	0.72	660
70	$HNO + OH \leftrightarrow NO + H_2O$	1.30E+07	1.9	-950
71	$NH + CO_2 \leftrightarrow HNO + CO$	1.00E+13	0	14350
72	$N + CO_2 \leftrightarrow NO + CO$	3.00E+12	0	11300
73	$O + CH_3 \rightarrow H + H_2 + CO$	3.37E+13	0	0
74	$OH + HO_2 \leftrightarrow O_2 + H_2O$	5.00E+15	0	17330
75	$CH_2 + O_2 \rightarrow 2\ H + CO_2$	5.80E+12	0	1500
76	$CH_2 + O_2 \leftrightarrow O + CH_2O$	2.40E+12	0	1500

Bibliography

Abdel-Gayed, R. G., Al-Khishali, K. J. & Bradley, D. (1984), 'Turbulent burning velocities and flame straining in explosions', *Proceedings of the Royal Society of London. A. Mathematical and Physical Sciences* **391**(1801), 393–414.

Abu-Orf, G. M. & Cant, R. S. (1996), Reaction rate modelling for premixed turbulent methane-air flames, *in* 'Joint Meeting of the Portuguese, British, Spanish and Swedish Sections of the Combustion Institute', Madeira, Portugal.

Altay, H. M., Speth, R. L., Hudgins, D. E. & Ghoniem, A. F. (2009), 'The impact of equivalence ratio oscillations on combustion dynamics in a backward-facing step combustor', *Combustion and Flame* **156**(11), 2106 – 2116.

Andrews, G. & Bradley, D. (1972), 'The burning velocity of methane-air mixtures', *Combustion and Flame* **19**(2), 275 – 288.

Balachandran, R., Dowling, A. & Mastorakos, E. (2005), Response of turbulent premixed flames subjected to inlet velocity and equivalence ratio perturbations, *in* 'Proceeding of the European Combustion Meeting', Louvain-la-Neuve, Belgium.

Balachandran, R., Dowling, A. & Mastorakos, E. (2011), Dynamics of bluff-body stabilised flames subjected to equivalence ratio oscillations, *in* 'Proceedings of the European Combustion Meeting', Cardiff, UK.

Biagioli, F. (2006), 'Stabilization mechanism of turbulent premixed flames in strongly swirled flows', *Combustion Theory and Modelling* **10**(3), 389–412.

Biagioli, F., Pascale, A. D. & Güthe, F. (2005), Modelling NOx emissions from lean partially premixed flames in industrial burners, *in* 'Proceedings of the European Combustion Meeting', Louvain-la-Neuve, Belgium.

Birbaud, A., Ducruix, S., Durox, D. & Candel, S. (2008), 'The nonlinear response of inverted "V" flames to equivalence ratio nonuniformities', *Combustion and Flame* **154**(3), 356 – 367.

Bobusch, B., Ćosić, B., Moeck, J. P. & Paschereit, C. O. (2013), 'Optical measurement of local and global transfer functions for equivalence ratio fluctuations in a turbulent swirl flame', *Journal of Engineering for Gas Turbines and Power* **136**, 021506 (8 pages).

Bray, K. N. C. (1990), 'Studies of the turbulent burning velocity', *Proceedings of the Royal Society of London. Series A, Mathematical, Physical and Engineering Sciences* **431**.

Bulat, G., Jones, W. & Marquis, A. (2014), 'NO and CO formation in an industrial gas-turbine combustion chamber using LES with the Eulerian sub-grid PDF method', *Combustion and Flame* **161**(7), 1804 – 1825.

Bulat, G., Skipper, D., McMillan, R. & Syed, K. (2007), Active Control of Fuel Splits in Gas Turbine DLE Combustion Systems, *in* 'Proceedings of ASME Turbo Expo 2007, May 14-17, 2007, Montreal, Canada. ASME Paper GT2007-27266'.

Cho, J. H. & Lieuwen, T. (2005), 'Laminar premixed flame response to equivalence ratio oscillations', *Combustion and Flame* **140**(1-2), 116 – 129.

Cohen, S. D. & Hindmarsch, A. C. (1996), 'CVODE, a Stiff/Nonstiff ODE Solver in C', *Computers in Physics* **10**(2), 138–143.

Cosic, B., Terhaar, S., Moeck, J. P. & Paschereit, C. O. (2015), 'Response of a swirl-stabilized flame to simultaneous perturbations in equivalence ratio and velocity at high oscillation amplitudes', *Combustion and Flame* **in press**.

Danckwerts, P. V. (1952), 'Continuous flow systems and Distribution of Residence Times', *Chemical Engineering Science* **2**, 1–13.

Drake, M. & Pitz, R. (1985), 'Comparison of turbulent diffusion flame measurements of OH by planar fluorescence and saturated fluorescence', *Experiments in Fluids* **3**(5), 283–292.

Düsing, M., Sadiki, A. & Janicka, J. (2003), 'LES of a confined configuration using oscillating inflow conditions', *PAMM* **2**(1), 348–349.

Duwig, C., Fuchs, L., Lacarelle, A., Beutke, M. & Paschereit, C. O. (2007), Study of the vortex breakdown in a conical swirler using LDV, LES and POD, *in* 'Proceedings of ASME Turbo Expo, May 14-17, 2007, Montréal, Canada'.

Echekki, T., Kerstein, A. R. & Sutherland, J. C. (2011), *Turbulent Combustion Modeling: Advances, New Trends and Perspectives*, Vol. 95 of *Fluid Mechanics and Its Applications*, 1st edn, Springer, chapter 11 The One-Dimensional-Turbulence Model, pp. 249–276.

Eggels, R. (2001), Modelling of Nox Formation of a Premixed Dle Gas Turbine Combustor, *in* 'Proceedings of ASME Turbo Expo, June 4-7, 2001, New Orleans, Louisiana, USA, 2001-GT-0069'.

Emara, A., Lacarelle, A. & Paschereit, C. (2009), Planar Investigation of Outlet Boundary Conditions Effect on Isothermal Flow Fields of a Swirl- Stabilized Burner, *in* 'Proceedings of ASME Turbo Expo, June 8-12, 2009, Orlando, FL, USA'. GT2009-59948 and Proceedings of ASME Turbo Expo 2009 and June 8-12 and 2009 and Orlando and Florida and USA.

Ferrand, P., Boudet, J., Caro, J., Aubert, S. & Rambeau, C. (2006), 'Analyses of URANS and LES capabilities to predict vortex shedding for rods and turbines', *Unsteady aerodynamics, aeroacoustics and aeroelasticity of turbomachines* pp. 381–393.

Flohr, P., Paschereit, C. O., van Roon, B. & Schuermans, B. (2001), Using CFD for Time-Delay Modeling of Premix Flames, *in* 'Proceedings of ASME Turbo Expo, June 4-7, 2001, New Orleans, LA, USA'. ASME Paper 2001-GT-0376 and Proceedings of ASME Turbo Expo 2001 and June 4-7 and 2001 and New Orleans and Louisiana and USA.

Flohr, P., Schmitt, P. & Paschereit, C. O. (2002), Mixing Field Analysis of a Gas Turbine Burner. ASME IMECE paper IMECE2002-39317.

Fröhlich, J., Garcia-Villalba, M. & Rodi, W. (2008), 'Scalar mixing and large-scale coherent structures in a turbulent swirling jet', *Flow, Turbulence and Combustion* **80**, 47–59.

Garcia-Villalba, M., Fröhlich, J. & Rodi, W. (2007), 'Numerical simulations of isothermal flow in a swirl burner', *Journal of Engineering for Gas Turbines and Power* **129**(2), 377–386.

Göke, S. (2012), Ultra Wet Combustion: An Experimental and numerical Study, PhD thesis, Technische Universität Berlin.

Goodwin, D. (2009), 'Cantera: An object-oriented software toolkit for chemical kinetics, thermodynamics, and transport processes', http://code.google.com/p/cantera.

Güthe, F., Lachner, R., Schuermans, B., Biagioli, F., Geng, W., Inauen, A., Schenker, S., Bombach, R. & Hubschmidt, W. (2006), Flame Imaging on the ALSTOM EV-burner: Thermo Acoustic Pulsations and CFD-Validation. AIAA Paper 2006-437.

Hall, J. M. & Petersen, E. L. (2006), 'An optimized kinetics model for OH chemiluminescence at high temperatures and atmospheric pressures', *International Journal of Chemical Kinetics* **38**(12), 714–724.

He, G., Guo, Y. & Hsu, A. T. (1999), 'The effect of Schmidt number on turbulent scalar mixing in a jet-in-crossflow', *International Journal of Heat and Mass Transfer* **42**, 3727–3738.

Holmes, P., Lumley, J. & Berkooz, G. (1998), *Turbulence, coherent structures, dynamical systems and symmetry*, Cambridge Univ Pr.

Huang, Y. & Yang, V. (2009), 'Dynamics and stability of lean-premixed swirl-stabilized combustion', *Progress in Energy and Combustion Science* **35**, 293–364.

Hughey, B. J. & Santavicca, D. A. (1982), 'A comparison of techniques for reconstructing axisymmetric reacting flow fields from absorption measurements', *Combustion Science and Technology* **29**(3-6), 167–190.

ITTC (2008), Uncertainty Analysis Particle Image Velocimetry, recommended procedures and guidelines, *in* 'Proceedings of the 25th International Towing Truck Conference'.

Iudiciani, P. & Duwig, C. (2011), 'Large eddy simulation of the sensitivity of vortex breakdown and flame stabilisation to axial forcing', *Flow, Turbulence and Combustion* **86**, 639–666.

Ivanova, E., Noll, B. & Aigner, M. (2010), Unsteady Simulations of Turbulent Mixing in Jet in Crossflow, *in* '40th Fluid Dynamics Conference and Exhibit, 28 June - 1 July 2010, Chicago, Illinois, AIAA 2010-4724'.

Jella, S., Gauthier, P. & Paraschivoiu, M. (2010), CFD Predictions of CO Emission Trends in an Industrial Gas Turbine Combustor, *in* 'Proceedings of ASME Turbo Expo 2010: Power for Land, Sea and Air, GT2010, June 14-18, 2010, Glasgow, UK'.

Jiang, L.-Y. & Campbell, I. (2008), 'Reynolds analogy in combustor modeling', *International Journal of Heat and Mass Transfer* **51**, 1251–1263.

Kariuki, J., Dawson, J. R. & Mastorakos, E. (2012), 'Measurements in turbulent premixed bluff body flames close to blow-off', *Combustion and Flame* **159**(8), 2589 – 2607.

Kerstein, A. R. (1989), 'Linear-eddy modeling of turbulent transport. II: Application to shear layer mixing', *Combustion and Flame* **75**(3-4), 397–413.

Kerstein, A. R. (1991), 'Linear-eddy modelling of turbulent transport. Part 6 Microstructure of diffusive mixing fields', *J. Fluid Mech.* **231**, 361–394.

Kerstein, A. R. (2010), 'Personal communication'.

Khalil, S., Hourigan, K. & Thompson, M. C. (2006), 'Response of unconfined vortex breakdown to axial pulsing', *Physics of Fluids* **18**, 038102 (4 pages).

Kheirkhah, S. & Gülder, O. L. (2013), 'Turbulent premixed combustion in V-shaped flames: Characteristics of flame front', *Physics of Fluids (1994-present)* **25**(5).

Kim, K., Lee, J., Quay, B. & Santavicca, D. (2010), 'Response of partially premixed flames to acoustic velocity and equivalence ratio perturbations', *Combustion and Flame* **157**(9), 1731 – 1744.

Kim, K. T., Lee, J. G., Quay, B. D. & Santavicca, D. A. (2011), 'Experimental Investigation of the Nonlinear Response of Swirl Stabilized Flames to Equivalence Ratio Oscillations', *Journal of Engineering for Gas Turbine and Power* **133**, 833–842.

Klein, R. (1999), Numerics in Combustion, *in* L. V. D. Veynante, ed., 'Introduction to Turbulent Combustion', von Karman Institute for Fluid Dynamics, Brussels, Belgium.

Klein, R., Botta, N., Hofmann, L., Meister, A., Munz, C., Roller, S. & Sonar, T. (2001), 'Asymptotic Adaptive Methods for Multiscale Problems in Fluid Mechanics', *Journal of Engineering Mathematics* **39**, 261–343.

Kokanovic, S., Guidati, G., Torchalla, S. & Schuermans, B. (2006), Active Combustion Control System for Reduction of NOx and Pulsation Levels in Gas Turbines, *in* 'Proceedings of the ASME Turbo Expo, Spain, May 8-11, 2006. ASME paper 2006-GT-90895'.

König, K., Bykov, B. & Maas, U. (2009), 'Investigation of the dynamical response of methane-air counterflow flames to inflow mixture composition and flow field perturbations', *Flow, Turbulence and Combustion* **83**, 105–129.

Lacarelle, A., Faustmann, T., Greenblatt, D., Paschereit, C. O., Lehmann, O., Luchtenburg, D. M. & Noack, B. R. (2009*c*), 'Spatiotemporal Characterization of a Conical Swirler Flow Field under Strong Forcing', *Journal of Engineering for Gas Turbines and Power* **131**, 031504 (12 pages).

Lacarelle, A., Gelbert, G., King, R. & Paschereit, C. O. (2008), Control of Emissions and Pulsations in a Premix Combustor using Fuel Staging, *in* '46th AIAA Aerospace Sciences Meeting and Exhibit, 7 - 10 January 2008, Reno, Nevada. AIAA paper 2008-1060.'.

Lacarelle, A., Moeck, J. P., Konle, H. J., Vey, S., Nayeri, C. N. & Paschereit, C. O. (2007), Effect of Fuel/Air Mixing on NOx Emissions and Stability in a Gas Premixed Combustion System, *in* '45th AIAA Aerospace Sciences Meeting and Exhibit, 8 - 11 January 2007, Reno, Nevada'.

Lacarelle, A., Moeck, J. P., Paschereit, C. O., Gelbert, G. & King, R. (2009*b*), Model Based Control of Emissions and Pulsations in a Premixed Combustor using Fuel Staging, *in* 'ASME Paper GT2009-59300, Proceedings of ASME Turbo Expo 2009:Power for Land, Sea and Air, GT2009, June 8-12, 2009, Orlando, Florida, USA'.

Lacarelle, A., Moeck, J. P., Tenham, A. & Paschereit, C. O. (2009*a*), Dynamic Mixing Model of a Premixed Combustor and Validation with Flame Response Measurements, *in* '47th AIAA Aerospace Sciences Meeting and Exhibit, 5 - 8 Jan 2009, Orlando, Florida. AIAA paper 2009-0986.'.

Lauer, M. (2011), Determination of the Heat Release Distribution in Turbulent Flames by Chemiluminescence Imaging, PhD thesis, Technische Universität München.

Lauer, M. & Sattelmayer, T. (2008), Heat release calculation in a turbulent swirl flame from laser and chemiluminescence measurements, *in* '14th Int Symp on Applications of Laser Techniques to Fluid Mechanics Lisbon, Portugal, 7-10 July, 2008'.

Lieuwen, T., Neumeier, Y. & Zinn, B. T. (1998), 'The Role of Unmixedness and Chemical Kinetics in Driving Combustion Instabilities in Lean Premixed Combustors', *Combustion Science and Technology* **135**, 193–211.

Lieuwen, T., Torres, H., Johnson, C. & Zinn, B. T. (2001), 'A Mechanism of Combustion Instability in Lean Premixed Combustion', *Journal of Engineering for Gas Turbine and Power* **123**, 182–189.

Lieuwen, T. & Zinn, B. T. (1998), The role of equivalence ratio oscillations in driving combustion instabilities in low NOx gas turbines, *in* '27th Symposium (International) on Combustion', pp. 1809–1816.

Lignell, D., Kerstein, A., Sun, G. & Monson, E. (2013), 'Mesh adaption for efficient multiscale implementation of one-dimensional turbulence', *Theoretical and Computational Fluid Dynamics* **27**(3-4), 273–295.

Lipatnikov, A. & Chomiak, J. (2002), 'Turbulent flame speed and thickness: phenomenology, evaluation, and application in multi-dimensional simulations', *Progress in Energy and Combustion Science* **28**(1), 1 – 74.

Lucca-Negro, O. & O'Doherty, T. (2001), 'Vortex breakdown: a review', *Progress in Energy and Combustion Science* **27**, 431–481.

Marzouk, Y., Ghoniem, A. & Najm, H. (2000), 'Dynamic response of strained premixed flames to equivalence ratio gradients', *Proceedings of the Combustion Institute* **28**(2), 1859 – 1866.

Menon, S. & Kerstein, A. R. (2011), *The Linear-Eddy Model*, Vol. 95 of *Fluid Mechanics and its Application*, Springer, chapter 10, pp. 221–247.

Menon, S., McMurtry, M. A., Kerstein, A. R. & Chen, J. Y. (1994), 'Prediction of NOx production in a turbulent hydrogen-air jet flame', *Journal of Propulsion and Power* **10**, 161–168.

Menon, S., McMurtry, P. A. & Kerstein, A. R. (1992), A Linear-Eddy Mixing Model for LES of Turbulent Combustion, *in* 'LES of Complex Engineering and Geophysical Flows', B. Galperin and S. A. Orszag, Cambridge University Press.

Menon, S., McMurtry, P. A. & Kerstein, A. R. (1993), A Linear Eddy Subgrid Model for Turbulent Combustion: Application to Premixed Combustion, *in* '31st Aerospace Sciences Meeting & Exhibit, January 11-14, 1993, Reno, NV'.

Miller, P. L. (1991), Mixing in High Schmidt Number Turbulent Jets, PhD thesis, California Institute of Technology.

Moeck, J. P., Bourgouin, J.-F., Durox, D., Schuller, T. & Candel, S. (2012), 'Nonlinear interaction between a precessing vortex core and acoustic oscillations in a turbulent swirling flame', *Combustion and Flame* **159**(8), 2650–2668.

Najm, H. N., Paul, P. H., Mueller, C. J. & Wyckoff, P. S. (1998), 'On the adequacy of certain experimental observables as measurements of flame burning rate', *Combustion and Flame* **113**(3), 312 – 332.

Nicoud, F. & Ducros, F. (1999), 'Subgrid-scale stress modelling based on the square of the velocity gradient tensor', *Flow, Turbulence and Combustion* **62**(3), 183–200.

Novosselov, I., Malte, P., Yuan, S., Srinivasan, R. & Lee, J. (2006), Chemical Reactor Network Application to Emissions Prediction for Industial DLE Gas Turbine, *in* 'Proceedings of GT2006, ASME Turbo Expo 2006: Power for Land, Sea and Air, May 8-11, 2006 Barcelona, Spain'.

Novosselov, I. V. & Malte, P. C. (2008), 'Development and application of an eight-step global mechanism for [CFD and CRN simulations of lean-premixed combustors', *Journal of Engineering for Gas Turbines and Power* **130**(2), 9.

Oberleithner, K., Sieber, M., Nayeri, C. N., Paschereit, C. O., Petz, C., Hege, H.-C., Noack, B. R. & Wygnanski, I. (2011), 'Three-dimensional coherent structures in a swirling jet undergoing vortex breakdown: stability analysis and empirical mode construction', *Journal of Fluid Mechanics* **679**, 383–414.

Oevermann, M., Schmidt, H. & Kerstein, A. (2008), 'Investigation of Autoignition under Thermal Stratification using Linear Eddy Modeling', *Combustion and Flame* **155**, 370–379.

Oevermann, M., Schrödinger, C. & Paschereit, C. (2015), Investigation of equivalence ratio fluctuations on the dynamics of turbulent lean premixed methane/air flames with a linear-eddy model, *in* R. King, ed., 'Active Flow and Combustion Control 2014', Vol. 127 of *Notes on Numerical Fluid Mechanics and Multidisciplinary Design*, Springer International Publishing, pp. 213–227.

Otsu, N. (1975), 'A threshold selection method from gray-level histograms', *Automatica* **11**(285-296), 23–27.

Palies, P., Schuller, T., Durox, D., Gicquel, L. Y. M. & Candel, S. (2011), 'Acoustically perturbed turbulent premixed swirling flames', *Physics of Fluids* **23**(3), 037101 (15 pages).

Pan, G. & Meng, H. (2001), 'Experimental study of turbulent mixing in a tee mixer using PIV and PLIF', *AIChE Journal* **47**(12), 2653–2665.

Panda, J. & McLaughlin, D. K. (1994), 'Experiments on the instabilities of a swirling jet', *Experiments in Fluids* **6**(1), 263–276.

Paschereit, C. O., Gutmark, E. J. & Weisenstein, W. (1999), 'Coherent structures in swirling flows and their role in acoustic combustion control', *Physics of Fluids* **11**(9), 2667–2678.

Paschereit, C. O., Gutmark, E. J. & Weisenstein, W. (2000), 'Excitation of Thermoacoustic Instabilities by Interaction of Acoustics and Unstable Swirling Flow', *AIAA Journal* **38**(6), 1025–1034.

Paschereit, C. O., Schuermans, B. & Büchey, D. (2003), Combustion Process Optimization using Evolutionary Algorithm, *in* 'Proceedings of the ASME Turbo Expo 2003, June 16-19, 2003, Atlanta, USA. ASME paper 2003-GT-38393'.

Peters, N. (1983), 'Local quenching due to flame stretch and non-premixed turbulent combustion', *Combustion Science and Technology* **30**(1-6), 1–17.

Peters, N. (1991), Reducing mechanisms, *in* M. Smooke, ed., 'Reduced Kinetic Mechanisms and Asymptotic Approximations for Methane-Air Flames', Vol. 384 of *Lecture Notes in Physics*, Springer Berlin Heidelberg, pp. 48–67.

Peters, N. (1999), 'The turbulent burning velocity for large-scale and small-scale turbulence', *Journal of Fluid Mechanics* **384**, 107–132.

Poinsot, T. & Candel, S. M. (1988), 'A Nonlinear Model for Ducted Flame Combustion Instabilities', *Combustion Science and Technology* **61**(4-6), 121–153.

Richardson, E. S., Granet, V. E., Eyssartier, A. & Chen, J. H. (2010), 'Effects of equivalence ratio variation on lean, stratified methane-air laminar counterflow flames', *Combustion Theory and Modelling* **14**(6), 775–792.

Sankaran, R. & Im, H. G. (2002), 'Dynamic Flammability Limits of Methane/Air Premixed Flames with Mixture Composition Fluctuations', *Proceedings of the Combustion Institute* **29**(1), 77–84.

Sankaran, V. & Menon, S. (2005), 'Subgrid Combustion Modeling of 3-D Premixed Flames in the Thin-Reaction-Zone Regime', *Proceedings of the Combustion Institute* **30**, 575–582.

Sannan, S., Kerstein, A. & Weydahl, T. (2009), A 3D geometrical substructure based on LEM-LES, *in* 'European Combustion Meeting ECM, Vienna, Austria, April 14-17, 2009'.

Sannan, S., Weydahl, T. & Kerstein, A. R. (2013), 'Stochastic simulation of scalar mixing capturing unsteadiness and small-scale structure based on mean-flow properties', *Flow, Turbulence and Combustion* **90**(1), 189–216.

Sattelmayer, T., Felchlin, M. P., Haumann, J., Hellat, J. & Styner, D. (1992), 'Second Generation Low-Emissions ABB Combustors for Gas Turbines: Burner Development and Tests at Atmospheric Pressure', *Transactions of the American Society of Mechanical Engineers* **114**, 118–125.

Scarinci, T., Freeman, C. & Day, I. (2004), Passive Control of Combustion Instability in a Low Emissions Aeroderivative Gas Turbine, *in* 'Proceedings of ASME Turbo Expo 2004, June 14-17, Vienna, Austria. ASME Paper GT2004-53767'.

Schlüter, J. & Schönfeld, T. (2000), 'LES of jets in cross flow and its application to a gas turbine burner', *Flow, Turbulence and Combustion* **65**, 177–203.

Schmitt, P., Poinsot, T., Schuermans, B. & Geigle, K. P. (2007), 'Large-eddy simulation and experimental study of heat tranfer, nitric oxide emissions and combustion instability in a swirled turbulent high-pressure burner', *Journal of Fluid Mechanics* **570**, 17–46.

Schmitz, I., Scherer, V., Wirtz, S. & Carroni, R. (2007), CFD based development of a fuel-air premixer for a retrofittable catalytic combustion system, *in* 'Proceedings of GT2007, ASME Turbo Expo 2007: Power for Land, Sea and Air, May 14-17, 2007, Montreal, Canada, GT2007-27326'.

Schrödinger, C., Krüger, O., Lacarelle, A., Oevermann, M. & Paschereit, C. O. (2010), CFD Modeling of the Influence of Fuel Staging on the Mixing Quality and Flame Characteristics in a Lean Premixed Combustor, *in* 'ASME Turbo Expo 2010: Power for Land, Sea and Air, June 14-18, 2010, Glasgow, Scotland, UK', GT2010-22910.

Schrödinger, C., Lacarelle, A., Oevermann, M. & Paschereit, C. O. (2011*c*), The Impact of Periodical Flow Forcing on the Mixing Quality in a Staged Premixed Burner: Numerical and Experimental Studies, *in* 'AIAA Joint Propulsion Conference and Exhibit 2011, 31 Jul - 3 Aug 2011, San Diego, CA'.

Schrödinger, C., Moeck, J. P., Oevermann, M. & Paschereit, C. O. (2012*a*), Numerical studies on the influence of periodical flow forcing on mixing quality and flow structure of a swirl burner, *in* 'Proceedings of ASME Turbo Expo 2012, June 11-15, 2012, Copenhagen, Denmark', GT2012-69843.

Schrödinger, C., Nolte, D., Oevermann, M. & Paschereit, C. (2013*a*), Experimental investigations of the impact of equivalence ratio oscillations on a bluff body flame, *in* 'Proceedings of the European Combustion Meeting, June 25-28, 2013, Lund, Sweden'.

Schrödinger, C., Paschereit, C. O. & Oevermann, M. (2014), 'Numerical studies on the impact of equivalence ratio oscillations on lean premixed flame characteristics and emissions', *Combustion Science and Technology* **186**(10-11), 1392–1409.

Schrödinger, C., Paschereit, C. & Oevermann, M. (2011*a*), Linear Eddy Modeling of the Influence of Turbulence and Coherent Structures on Pollutant Emissions in Lean Premixed Combustion, *in* 'European Combustion Meeting 2011, Cardiff University from 28th June - 1st July 2011'.

Schrödinger, C., Paschereit, C. & Oevermann, M. (2011*b*), Numerical studies of the Influence of Turbulence and Coherent Structures on Flame and Emission Characteristics in Lean Premixed Combustion, *in* '23rd ICDERS, July 24-29, 2011, Irvine'.

Schrödinger, C., Paschereit, C. & Oevermann, M. (2012*b*), Numerical studies on the impact of equivalence ratio oscillations on lean premixed flame characteristics and emissions, *in* 'Seventh International Conference on Computational Fluid Dynamics (ICCFD7), Big Island, Hawaii, July 9-13, 2012', ICCFD7-3401.

Schrödinger, C., Paschereit, C. & Oevermann, M. (2013*b*), Numerical investigations of the impact of temperature fluctuations on lean premixed flames, *in* '24rd ICDERS, July 28 – August 2, 2013, Taipei, Taiwan'.

Schuermans, B., Bellucci, V., Guethe, F., Meili, F., Flohr, P. & Paschereit, C. O. (2004), A Detailed Analysis of Thermoacoustic Interaction Mechanisms in a Turbulent Premixed Flame. ASME Turbo Expo '04, 2004-GT-53831, June 14–17, Vienna, Austria.

Schwarz, H., Zimmer, L., Durox, D. & Candel, S. (2010), 'Detailed measurements of equivalence ratio modulations in premixed flames using laser rayleigh scattering and absorption spectroscopy', *Experiments in Fluids* **49**(4), 809–821.

Shepherd, I. (1996), 'Flame surface density and burning rate in premixed turbulent flames', *Symposium (International) on Combustion* **26**(1), 373 – 379.

Shreekrishna, Acharya, V. & Lieuwen, T. (2013), 'Flame response to equivalence ratio fluctuations - relationship between chemiluminescence and heat release', *International Journal of Spray and Combustion Dynamics* **5**, 329–358.

Shreekrishna, Hemchandra, S. & Lieuwen, T. (2010), 'Premixed flame response to equivalence ratio perturbations', *Combustion Theory and Modelling* **14**(5), 681–714.

Smith, G. P., Golden, D. M., Frenklach, M., Moriarty, N. W., Eiteneer, B., Goldenberg, M., Bowman, C. T., Hanson, R. K., Song, S., Jr., W. C. G., Lissianski, V. V. & Qin, Z. (1999), 'GRI-Mech 3.0, The Gas Research Institute', `http://www.me.berkeley.edu/gri-mech/`.

Smith, T. & Menon, S. (1996), 'Model simulations of freely propagating turbulent premixed flames', *Symposium (International) on Combustion* **26**(1), 299–306.

Smith, T. & Menon, S. (1997), 'One-Dimensional of Freely Propagating Turbulent Premixed Flames', *Combust. Sci. and Tech.* **128**, 99–130.

Smith, T. & Menon, S. (1998), Subgrid Combustion Modeling for Premixed Turbulent Reacting Flows, *in* '36th AIAA Aerospace Sciences Meeting and Exhibit'.

Stein, O. (2009), Large Eddy Simulation of Combustion in Swirling and Opposed Jet Flows, PhD thesis, Department of Mechanical Engineering, Imperial College London.

Stein, O. T. & Kempf, A. M. (2009), An LEM-LES Method for Incompressible Reacting Flows eith Finite-Rate Chemistry, *in* 'Proceedings of the European Combustion Meeting 2009'.

Steinberg, A. M., Driscoll, J. F. & Swaminathan, N. (2012), 'Statistics and dynamics of turbulence-flame alignment in premixed combustion', *Combustion and Flame* **159**(8), 2576 – 2588. Special Issue on Turbulent Combustion.

Syed, K. J., Roden, K. & Martin, P. (2007), 'A Novel Approach to Predicting NOx Emissions From Dry Low Emissions Gas Turbines', *Journal of Engineering for Gas Turbines and Power* **129**, 672–679.

Syred, N. (2006), 'A review of oscillation mechanisms and the role of the precessing vortex core (PVC) in swirl combustion systems', *Progress in Energy and Combustion Science* **32**, 93–161.

Turns, S. R. (2000), *An introduction to combustion: Concepts and Applications*, 2nd edn, McGraw-Hill Boston.

Venkata Nori, J. S. (2008), Evaluation of chemiluminescence as a combustion diagnostic under varying operating conditions, *in* '46th AIAA Aerospace Sciences Meeting and Exhibit', number AIAA 2008-953.

Vicente, W., Salinas, M. & Barrios, E. (2004), 'Pdf Modeling of CO and NO Formation in Lean Premixed Methane Flames', *Combust. Sci. andTech.* **176**, 585–601.

Wang, P., Bai, X. S., Wessman, M. & Klingmann, J. (2004), 'Large eddy simulation and experimental studies of a confined turbulent swirling flow', *Physics of Fluids* **16**(9), 3306–3324.

Wang, S. & Yang, V. (2005), 'Unsteady flow evolution in swirl injectors with radial entry. II. External excitations', *Physics of Fluids* **17**, 045107 (12 pages).

Warnatz, J. (1981), 'The structure of laminar alkane-, alkene-, and acetylene flames', *Symposium (International) on Combustion* **18**(1), 369 – 384. Eighteenth Symposium (International) on Combustion.

Wegner, B., Gruschka, U., Krebs, W., Egorov, Y., Forkel, H., Ferreira, J. & Aschmoneit, K. (2010), CFD Prediction of Partload CO Emissions using a TWO-Timescale Combustion Model, *in* 'Proceedings of ASME Turbo Expo 2010: Power for Land, Sea and Air, GT2010, June 14-18, 2010, Glasgow, UK'.

Wegner, B., Maltsev, A., Schneider, C., Sadiki, A., Dreizler, A. & Janicka, J. (2004), 'Assessment of unsteady RANS in predicting swirl flow instability based on LES and experiments', *International Journal of Heat and Fluid Flow* **25**(3), 528 – 536.

Zhou, R. & Hochgreb, S. (2013), 'The behaviour of laminar stratified methane/air flames in counterflow', *Combustion and Flame* **160**(6), 1070 – 1082.